A Study of Combustion Augmentation in Supersonic Flows via a Pulsed-Detonation Device

by

Yasin Mohammad Abul-Huda

A dissertation submitted in partial fulfillment
of the requirements for the degree of
Doctor of Philosophy
(Aerospace Engineering)
in The University of Michigan
2017

Doctoral Committee:

Assistant Professor Mirko Gamba, Chair
Professor James F. Driscoll
Dr. Timothy Ombrello, Air Force Research Laboratory
Professor Venkat Raman
Professor Margaret Wooldridge

Yasin M. Abul-Huda

yasinma@umich.edu

ORCID iD: 0000-0001-5625-4091

Noor

ACKNOWLEDGEMENTS

All praise is for Allah, the king and author of all existence, the all-compassionate, the all-compelling...

A sincere thank you to all those who interacted with me as a brother and friend in humanity, not with preconceived misconceptions.

A sincere thank you to everyone who encouraged and supported me, whether it was through a single kind gesture, or years of unwavering support.

A sincere thank you to my family, teachers, colleagues, and friends. There are too many of you and examples to mention individually. I can never repay you for the impact and direction you have given my life.

Professor Mirko Gamba, thank you for your patience and support. You have provided me with both freedom and opportunities to pursue my scientific interests, while taking the time to expand my ability to think and ask the right questions. It has been my privilege to take part in your vision and I am deeply honored to have been a student of yours.

We are all merely travelers through this life, and what a truly beautiful *opportunity* it is for us to share our feelings, ideas, and time with one another.

TABLE OF CONTENTS

LIST OF FIGURES

Figure

LIST OF TABLES

Table

LIST OF APPENDICES

Appendix

ABSTRACT

Robust ignition and stable flame holding are challenging feats in scramjet combustors because of their susceptibility to large variations in flow, pressure, temperature, and composition. In an effort to help resolve some of these challenges, the development of the Michigan Hypersonic Expansion Tube (MHExT) Facility was undertaken. The 14 meter long expansion tube provides an experimental platform for well controlled studies of various supersonic mixing and combustion phenomena. MHExT was designed with the capability of generating a wide range of aerothermal flow properties representative of combustor entry conditions for flight Mach numbers ranging between 4 and 11. More specifically, the theoretical range of achievable conditions with air as the test gas is as follows; $80 < T$ [K] < 2500, $0.5 < H_0$ [MJ/kg] < 8.1, $0.6 < P$ [kPa] < 180, $1 < M < 11.2$, and $600 < U$ [m/s] < 3800. A portion of this dissertation analyzes the capacity of the facility through a combined experimental, analytical, and computational analysis, providing the necessary foundational groundwork for future supersonic mixing and combustion studies.

New and creative solutions are crucial in achieving robust control of supersonic combustion devices. Since the fluid residence times within non-premixed supersonic combustion devices are short, ignition typically cannot be achieved by solely relying on diffusion and heat conduction alone. The work of this dissertation explores a new technique of active combustion augmentation, where a H_2-O_2 detonation is used to generate and deliver a high-temperature radical-rich exhaust to the wake of a (pri-

mary) reacting jet in supersonic crossflow (JISCF), here taken to be representative of a scramjet combustion system. The new technique provides several advantages over conventional forms of energy deposition such as those produced by deflagration waves, spark igniters, and plasma discharges, which are localized and therefore have a limited spatial influence on the reacting system. By forming intermediate species of combustion through a detonation wave (constant volume process) as opposed to a deflagration wave (isobaric process), larger temperatures and pressures are achieved, providing additional opportunities and mechanisms for combustion enhancement. The elevated temperatures (temperature ratio across detonation wave $T_{\mathrm{CJ}}/T_1 = 11.8$) of the post-detonation products (as compared to deflagrations) enhance a number of thermal and kinetic mechanisms that are experimentally and theoretically observed to increase the reactivity of a system. The elevated pressures (pressure ratio across detonation wave $P_{\mathrm{CJ}}/P_1 = 18.2$) cause the post-detonation gases to exhaust into the flow field as a high momentum flux ratio jet, penetrating deep into the core flow and significantly altering the flow field pressure distribution and subsequent entrainment and mixing processes.

The impact of the transient blowdown process on the JISCF system, which takes place over a 300 μs period, is studied using schlieren imaging, OH* chemiluminescence imaging, and OH PLIF imaging. The imaging techniques provide insight to several hydrodynamic and chemical processes, by revealing properties such as shear layer penetration, modification in shock structures and recirculation regions, stability of reactions along the shear layer, net (enhanced) heat release distribution, and the evolution of the instantaneous reaction and post-reaction zone structures. During early portions of the blowdown process the shear layer penetration is observed to increases by a factor of 2. The post-detonation products pre-heat the primary jet fuel, increasing extinction strain rates, and thereby stabilizing reactions along the shear layer. Within the field of view, the OH* images reveal how the post-detonation

products increase the heat release of the primary jet fuel by more than 350 %, by augmenting ignition and fuel-oxidation.

With requisite concentrations of radical addition, macroscopic properties such as ignition delay and reaction time are shown to be reduced by several orders of magnitude, while extending the flammability limits over a significantly wider range of mixture equivalence ratios. The consequences are of critical significance in non-premixed compressible flow environments which rely heavily on the autoignition mode of combustion. A combined theoretical and experimental analysis, intended to decouple the complex interplay between chemical and hydrodynamic effects, is conducted to elucidate the governing processes. A series of analytical models are developed to understand the experimental observations, and thereby shed light on the potentials and limitations of the technique.

CHAPTER I

Introduction

1.1 Motivation

The development of hypersonic propulsion systems is perplexed by our inadequate understanding of the highly complex and coupled nature of multiple physical and chemical phenomena. Robust ignition and stable flame holding are challenging to control in high-speed air-breathing propulsion systems because of their susceptibility to large variations in flow, pressure, temperature, and mixture composition. The processes of mixing, initiating reactions, and achieving complete fuel-oxidation are restricted by short flow residence times, which can be of the same order of magnitude as the chemical time scales. Traditional methods of augmenting ignition, flame stabilization, and extraction of the total potential chemical heat release, are inadequate in such constrictive and highly-dynamic environments. Therefore, new and creative solutions are crucial in achieving robust control of supersonic combustion devices.

Supersonic combustion is a challenging regime of combustion since a universal understanding, independent of any specific physical configuration, requires a coherent understanding of the complex coupling between turbulence, chemistry, compressibility, nonequilibrium, and heat transfer. Sufficiently instrumenting a flight-test vehicle to understand the individual role of each of the highly coupled physical and chemical processes is an insurmountable task. Recently, there have been efforts to advance

hypersonic flight technology through a number of flight experimentations using instrumented ballistic re-entry vehicles to study several hypersonic flow phenomena. Collaborative efforts such as the HIFiRE and HyShot programs have successfully tested sub-scale scramjet vehicles in true-flight environments [16–19]. However, the data acquired from experimental flight tests are limited to a system-level understanding of vehicle performance. On the other hand, ground testing provides a means to decouple these effects while replicating the relevant and required flight conditions, in order to elucidate the governing physics of processes such as mixing and combustion. The utilization of ground test facilities remains the workhorse for the advancement of hypersonic propulsion technology because they provide a platform to test and develop new concepts, repeat and vary test conditions, perform well-controlled fundamental level experiments, as well as system-level testing of models, with advanced experimental methods and diagnostics.

To this end, a hypersonic impulse facility was developed to support the advancement of future hypersonic propulsion systems. The 14 meter long Michigan Hypersonic Expansion Tube (MHExT) Facility, was designed with the capability of generating a wide range of aerothermal flow properties representative of combustor entry conditions for flight Mach numbers ranging between 4 and 11. The use of such a ground test facility provides an opportunity to access relevant and meaningful information through a platform that allows for well controlled studies of various supersonic mixing and combustion phenomena. However, extracting meaningful test data with such a facility must be preceded by a comprehensive understanding of the generated flow characteristics, range of facility operability, and defining which and how flow properties are scaled between experiments and true-flight conditions. A portion of this dissertation provides the necessary detailed assessment of the facility through a combined experimental, computational, and analytical analysis.

Over the past several decades, numerous techniques employing *passive* and *active*

methods have been explored to overcome the challenges in mixing and combustion that exist under high-speed, compressible conditions with short residence times, low-pressures, and low-temperatures [20, 21]. These methods are designed to assist in distributing fuel to the core flow, increase the flow residence time, or provide a region of high energy to the flow to help initiate chemical reactions. The physical mechanism behind most passive methods relies on the generation of streamwise vorticity, leveraging self-excited resonance, or acoustic excitation. Examples include cavity flame-holders, hypermixers, transverse injection, and shock/shear layer interactions [22, 23]. On the other hand, active methods primarily rely on forced excitation of large scales and include methods such as pulsed jets, piezoelectric actuation, and plasma discharge [24, 25]. Each of these methods have been shown to have certain strengths but are ultimately limited by certain deficiencies such as stagnation pressure losses, combustion confinement near walls, limited range of operation, and significant amounts of input energy required to be effective. The underlying mechanisms that traditional techniques exploit are intrinsically susceptible to the dynamic nature of the combustor environment. In other words, these mechanisms and their impact are subject to change based on the aerothermodynamic properties of the flow entering the combustor. Therefore, their effectiveness and efficiency is subject to the wide range of inflow conditions encountered over the course of a hypothetical flight envelope. For these reasons, it is necessary to explore new methods of controlling the increasingly demanding and restrictive nature of future combustion systems.

Recently, pulsed detonators (PDs) have been examined as an active technique of enhancing jet mixing and penetration into a supersonic crossflow [26, 27]. The PD device was used to enhance the mixing characteristics of an exemplar supersonic fuel-injection system, taken to be the transverse jet in supersonic crossflow (JISCF). The PD device was used to exhaust a transient high-momentum flux gas into the wake of a primary transverse jet in Mach 2 crossflow, as is shown schematically in Fig. 1.1.

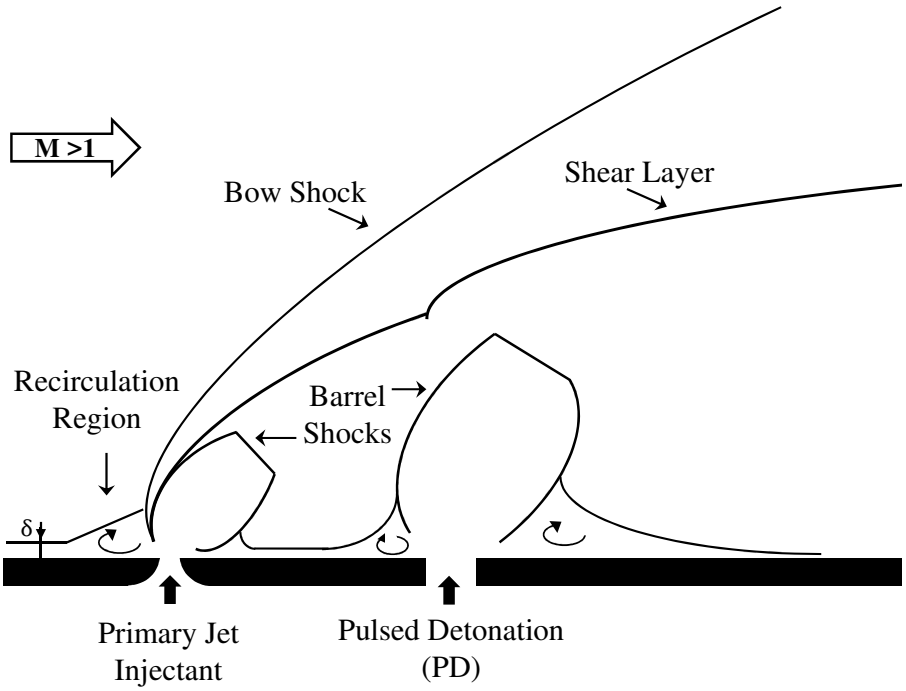

Figure 1.1: Center-plane schematic of the staged transverse jet and pulsed detonation (PD) in supersonic crossflow.

The blowdown process of the PD had a significant impact on the flow field pressure distribution. The investigation showed that the global interaction helped distribute and penetrate the primary jet fluid deeper into the core flow, as well as increase the jet-freestream interface by a factor of 6. As the PD blowdown process continued, the primary jet injectant was observed to be entrained into the wake and counter-rotating vortex pairs (CVP) of the PD exhaust. From a combustion standpoint, these observations of the highly coupled interaction have the potential to provide a number of mechanisms of combustion augmentation to a reacting system. A series of preliminary numerical studies which have attempted to provide an understanding of the combustion effects of such a configuration [28, 29], have only left more questions unanswered.

The work of this dissertation assessed the performance of a PD device in enhancing the combustion characteristics of a JISCF system. The configuration, shown in Fig. 1.1, involved staging a H_2-O_2 PD downstream of a primary transverse underex-

panded H_2 jet in supersonic crossflow, representative of combustor entry conditions for Mach 7 flight ($M = 2.35$, $P = 40$ kPa, $T = 1330$ K, and $U = 1660$ m/s). The PD provided a short-duration (approximately 300 μs), high temperature and momentum flux, radical-rich gas to the wake of the primary jet. The mechanisms of combustion augmentation were identified by leveraging three imaging techniques. These techniques were used to visualize several properties of the complex and transient interaction, both in the vicinity and far-field wake. High-speed schlieren imaging was used to visualize changes in flow field structures such as shocks, vortices, and the trajectories of the primary jet and PD exhausts. High-speed OH^* chemiluminescence imaging was used to visualize the temporal evolution of the global heat release distribution. The OH^* signal was used as a proxy for heat release, and therefore provided a means of quantifying the extent and locations of enhancement in heat release of the primary jet fuel. Lastly, planar laser-induced fluorescence (PLIF) of OH was used to mark the distribution of OH on the center-plane and several cross-sectional planes of the flow field in order to infer the instantaneous local structures of the reaction zones and post-combustion regions. For example, the data provided insight of the stability and nature of the reaction zones as they evolved in time.

The complex nature of the staged JISCF and PD exhibits a combination of several flow and chemical processes that have been previously studied. It combines components of several flow configurations such as transverse jet injection, staged jet injection, and pulsed jet injection. Moreover, it contains elements from research areas such as plasma assisted combustion, radical farming, and flame holding and combustion in reacting transverse jets in crossflow. Therefore, in order to analyze the use of a PD as a combustion augmentation device, an understanding of the individual and combined role of these components is required. The work of this dissertation provides a comprehensive understanding and evaluation of the use of a pulsed detonation (PD) device for combustion augmentation within the context of a supersonic

reacting system. The combined experimental and theoretical analysis provides a coherent description of the governing chemical (thermal and kinetic) and fluid mechanic mechanisms that are responsible for the observed combustion enhancement.

1.2 New Contributions of Dissertation

1.2.1 Expansion Tube Development and Characterization

A portion of the dissertation is dedicated to the development and characterization of a hypersonic expansion tube facility for supersonic combustion studies. The range of accessible conditions were theoretically computed and were shown to overlap well with conditions required to properly replicate combustor entry conditions of a hypothetical scramjet. A number of flow conditions were generated and studied extensively to understand their characteristics and compare their properties with analytical models. The effect of boundary layer growth and unsteady expansion on the generated flows is investigated. In addition, a combined analytical, computational, and experimental study is carried out to understand the implications of improper test model mounting in impulse facilities. A one-dimensional model was formulated to accurately predict the extent of test gas contamination that results from protruding a test model into the expansion section. Development and characterization of the MHExT facility provides the necessary ground work for future supersonic combustion/mixing studies, by providing the necessary information needed to isolate non-ideal facility induced effects from the combustion/mixing phenomena being studied.

1.2.2 Combustion Augmentation

The work of this dissertation provides the first-ever experimental and analytical analysis of using a PD to augment combustion in supersonic flows. The use of a PD device to enhance the combustion properties of a supersonic reacting system is

innovative for a number of reasons. From a practical standpoint, unlike other active combustion augmentation techniques, the system is simple and compact. It does not require large, heavy, or expensive equipment, and can use the fuel stored on board of the aircraft as the energy source. The impact of the detonation wave and subsequent exhaust of post-detonation products on the global flow field chemistry and dynamics can be greater than conventional techniques of energy deposition such as those produced by deflegration waves (pilot flames), spark igniters, and plasma discharges. The impact of conventional techniques are typically confined to small regions of the flow field, and generally rely on the natural flow dynamics and processes such as flow expansion, entrainment, and mixing to propagate their influence away from the source. The disruptive and spatially extensive impact of the exhausting PD on the flow field is attributed to the constant volume (non-isobaric) combustion process provided by the detonation wave, which generates large post-detonation gas pressures. The PD products issue into the flow field as a high momentum flux ratio underexpanded jet, penetrating deep into the supersonic crossflow, generating vortical structures similar to a JISCF system, and significantly modifying the flow field pressure distribution which augments entrainment and mixing. Similarly, the detonation wave generates larger post-combustion gas temperatures, as compared to deflagration waves. The CJ-state temperatures for a stoichiometric H_2-O_2 detonation wave is approximately 3600 K, and therefore nearly half of the equilibrium gas composition is composed of combustion intermediates. The elevated temperatures and large concentration of radicals provide thermal and kinetic mechanisms of combustion enhancement to a reacting system.

Ultimately, the PD device is an effective and efficient means of both *generating* and *delivering* high-temperature post-combustion gases to a supersonic reacting system. To illustrate this point on the most basic level, and provide an understanding of the potential that can be harnessed with PDs, a simplified comparison between

Mixture	Wave Process	Pressure Ratio	Temperature Ratio	Percent Intermediates
H_2-O_2	Deflagration	1	10.0	43.1
	Detonation	18.2	11.8	48.2
CH_4-Air	Deflagration	1	7.4	50.8
	Detonation	28.5	12.0	55.6
C_3H_8-O_2	Deflagration	1	10.1	56.4
	Detonation	35.1	12.3	61.0

Table 1.1: A comparison of post-combustion product properties generated by detonations and deflagrations. The initial conditions for all cases were $\Phi = 1$, T = 300 K , and P = 0.5 atm. The properties for the detonations refer to the equilibrium values of the CJ-state. The properties of the deflagrations refer to the equilibrium values after a constant enthalpy and pressure combustion process.

deflagrations and detonations can be made. Table 1.1 summarizes a comparison of the pressure and temperature ratios across several detonation and deflagration waves propagating through premixed mixtures ($\Phi = 1$) with an initial pressures and temperatures of 0.5 atm and 300 K, respectively. The deflagration waves are taken to be representative of a pilot flame that can be used to augment combustion in a supersonic reacting system, and the indicated properties refer to the equilibrium values after a constant enthalpy and pressure combustion process. The properties of the detonations refer to the equilibrium values of the CJ-state. The table shows how the detonation wave can provide larger post-combustion temperatures and concentrations of intermediate species, as compared to deflegrations. Furtermore, since reaction rates have a non-linear dependence on temperature and species composition, detonations have a greater potential to significantly increase the reaction progress of a system. Moreover, the detonation waves generate significantly larger post-combustion gas pressures. If exploited in a proper manner, this can provide an opportunity to significantly enhance the mixing properties of a supersonic reacting system. Moreover, it provides a means of delivering and dispersing the high-temperature post-combustion gases deep into the crossflow. This extends the spatial influence of the high temperature exhaust to greater regions of the flow field, rather than being confined to the locality of the

source.

1.3 Dissertation Objectives and Outline

Given the complexity of the challenges within the supersonic combustion regime, the scope of this dissertation is to develop an experimental platform for carrying out well controlled and characterized studies of supersonic combustion phenomena. A hypersonic impulse facility was developed to access a wide range of high-enthalpy flow conditions required to study various aspects of supersonic mixing and combustion. Furthermore, a technique to enhance the reactivity of a supersonic reacting system is explored. The technique takes advantage of several kinetic and thermal mechanisms to increase reaction rates, and modify reaction pathways. In practice, the PD device is used to enhance the reaction progress of a jet in supersonic crossflow (JISCF) system. The work of this dissertation develops an understanding that elucidates the governing phenomena that lead to the experimentally and theoretically observed enhancement. A series of models are developed to understand the underlying mechanisms that control the increased reactivity, and thereby shed light on the strengths and limitations of the technique.

The goals of this dissertation can be summarized as follows:

1. Develop an expansion tube facility capable of generating tractable supersonic/ hypersonic high-enthalpy test gas flows. This work provides a comprehensive understanding of expansion tube performance, proper test model mounting, and effects of non-idealities such as boundary layer growth over a range of operating conditions relevant to supersonic combustion studies. This includes evaluating the theoretical range of achievable flow conditions, how they scale with full-scale flight environments, and assessing the achievable test times with respect to the required flow establishment times for several relevant unit flow processes.

Among others, this work quantifies properties such as shot-to-shot repeatability, spatial and temporal uniformity, deviation of predicted and measured properties, and test gas flow disturbances induced by primary diaphragm rupture.

2. Develop a comprehensive understanding of the operating principles and properties of a practical pulsed detonation device. An analysis on the extent of impact of energy loss mechanisms on the trailing post-detonation gas is carried out to understand the transient characteristics and properties of an ideal and sub-ideal detonation tube blowdown process. This model is then used to understand the heating potential of PD devices and serve as a guide in their design and use for combustion augmentation applications.

3. Develop an understanding of the extent of combustion enhancement that is attained by staging a PD downstream of a primary transverse jet in supersonic crossflow. This is accomplished by measuring, quantifying, and describing metrics such as shear layer penetration, stability of reactions along the shear layer, changes in shock structures and recirculation regions, heat release distribution, and characteristics of the reaction and post-reaction zones. Further more, this work develops a comprehensive understanding of the fundamental governing mechanisms which control enhancement in combustion, by decoupling the hydrodynamic and chemical effects that lead to combustion enhancement. This information is then used to evaluate the use of a pulsed detonation device for combustion augmentation of a practical supersonic combustion device.

In chapter 2, a number of relevant flow and combustion systems are reviewed. This chapter serves to form a foundation for the current study by providing a background of several relevant and critical topics. Chapter 3 of the dissertation describes the experimental platforms that were developed over the course of this work. This includes an overview of the design and operation of the Michigan Hypersonic Expan-

sion Tube (MHExT) Facility, and a description of the components of the primary test model that was used. A description of the experimental techniques that were used as well as a brief overview of their principles is also provided. Chapter 4 provides an analysis of the MHExT facility and its ability to generate conditions that accurately represent those of a practical scramjet combustor. The dissertation then provides an experimental characterization of a number of important flow properties through a few exemplar flow conditions. The remainder of the chapter brings to light the significance of proper test-model mounting in such impulse facilities. A combined experimental, numerical, and theoretical study was undertaken to understand and predict a test-model induced test gas interference effect.

Chapter 5 describes a one-dimensional model used to compute the properties of the post-detonation products issued from the pulsed-detonation (PD) device. The model includes the inhibitive effects of heat and momentum losses to the PD walls, which can significantly alter the exhaust properties in a practical device. Chapter 6 provides a number of experimentally observed effects of the staged JISCF and PD system. The influence of the PD on the system is analyzed by decoupling hydrodynamic effects from chemical effects. Chapter 7 provides a theoretical analysis of the use of a practical PD device to enhance the reactvity of a supersonic reacting system. Chapter 8 provides a unified description of the processes governing the staged JISCF and PD configuration investigated in this work. Finally, chapter 9 provides a summary of the dissertation as well as recommendations for future work.

CHAPTER II

Overview of Relevant Flow and Combustion Systems

2.1 Introduction

The complex nature of the configuration being studied requires an understanding of several flow and combustion processes. This chapter is designed to serve as a foundation for the work of this dissertation by reviewing a number of important concepts and configurations related to transverse jets in crossflow, detonations, combustion enhancement techniques, and ground test facilities. A sufficient understanding of the effects of the pulsed detonation device on a supersonic reacting system is contingent upon understanding the physics governing the individual components before they are combined.

The significance of the topics that are discussed in the following chapter can be described by referencing Fig. 1.1. The simplified schematic outlines the presence of various flow features such as a bow shock, boundary layer, barrel shocks, recirculation zones, and a shear layer. It is essential to understand the properties and roles that each of these features have in governing mixing and flame stabilization. Moreover, the presence of vortical structures that are formed by the interaction of the crossflow with the transverse jets are known to significantly influence the entrainment and mixing

properties. Understanding how and where these structures form will provide an understanding of the interplay and coupling between the primary jet and PD exhaust. Moreover, it is important to understand what parameters govern the trajectory of the jet fluid or presence and size of recirculation regions. Among other things, these properties may reveal where chemical reactions are being stabilized, and whether or not they are confined to the walls or far into the crossflow.

Since the secondary (downstream) jet is in the form of a detonation tube, it is important to understand properties of detonation waves and their propagation through channels. Understanding the processes that govern a PD exhaust process is essential to extracting the full potential of the generated detonation and post-detonation products. Furthermore, since the detonation device issues high-temperature radicals into the reacting flow field and alters the reactivity of the JISCF system, a brief review of what is already known about combustion enhancement through radical addition will help guide our understanding of the complex interaction. Lastly, the experimental campaigns of the current study were carried out by leveraging a hypersonic expansion tube facility. A description of impulse facilities and expansion tube theory is provided to give a better understanding of the capabilities of the experimental platform. The information that is provided in this chapter is not intended to be comprehensive, but rather to outline a number of important aspects and provide references.

2.2 Transverse Jets in Supersonic Crossflow

The jet in crossflow is a canonical flow configuration that has been studied extensively over the past several decades [3, 30, 31, 31–37]. Numerous experimental, theoretical, and numerical studies have been conducted to study transverse gas and liquid phase injection into both subsonic and supersonic flows. Their relevance spans a number of practical applications in the areas of both propulsion and energy systems [38]. For example, they are commonly observed in systems with dilution air jets, tur-

bine film cooling systems, thrust vector control, and more. The interaction of the jet and cross flow forms a unit physics problem of interest in the areas of both turbulent mixing and combustion [1, 39]. The components of the unit problem include the formation of a number of vortical structures, recirculation regions, shock-boundary layer interactions, two-stream mixing, Kelvin-Helmholtz and Rayleigh Taylor instabilities, and wall confinement effects.

2.2.1 Penetration

Despite the complexities of such a flow field, a number of important characteristics of transverse jets in supersonic crossflow have been found to be strongly correlated with the jet-to-crossflow momentum flux ratio J_j [35, 40, 41], defined as

$$J_j = \frac{\rho_j U_j^2}{\rho_\infty U_\infty^2} = \frac{P_j \gamma_j M_j^2}{P_\infty \gamma_\infty M_\infty^2} \tag{2.1}$$

where the subscript j and ∞ refer to the jet exit and free stream conditions upstream of the bowshock, respectively. The trajectory of a jet is determined by two components where the first is associated with the motion carrying fluid into the crossflow, and the second with the entrainment of crossflow fluid. The mean global trajectory of the jet penetration can be defined in terms of the jet-to-crossflow momentum flux ratio, and is typically given by a correlation of the form

$$\frac{y}{J_j d} = c \left(\frac{x}{J_j d} \right)^m \tag{2.2}$$

where y and x refer to the wall normal and axial coordinates respectively, and d is the jet exit diameter. The values of c and m are fitting parameters. The effects of boundary layer thickness, flow Mach number, and jet density are inherently neglected by using this correlation. It is important to note that the published values of the premultiplicative (c) and exponential (m) factors depend significantly on how the jet

penetration is defined. Therefore, there is a large discrepancy between the published values where the range is $1.1 < c < 2.6$ and $0.28 < m < 0.34$. The definitions can range from being the contour of the local maximum jet concentration, the contour of the 0.5% jet concentration, the contour of the freestream 90% concentration, or even by the locus of maximum velocity on the centerplane. Moreover, these studies can either be of reacting or non-reacting jets in crossflow, where the basis of the flow tracers used to visualize the jet or freestream introduces additional causes for discrepancy. Lastly, they have been shown to depend largely on the range of J_j for which they were measured. Generally however, in the range where $J_j > 1$, the premultiplicative and exponent factors asymptote to values of $c \approx 1$ and $m \approx 0.3$. This scaling best follows the jet penetration definition based on the 0.5% contour of the jet concentration.

2.2.2 Flow Structures

A number of prominent flow features are observed from the complex interaction between the transverse jet, incoming boundary layer, and crossflow [1, 37]. Figures 2.1 and 2.2 are three dimensional schematics illustrating some of these flow features. In the typical configuration used in the supersonic regime, an underexpanded jet issues into the freestream generating a barrel shock structure that is terminated by a Mach disk. The barrel shock is deflected by the hydrodynamic forces imposed by the incoming flow. A shear layer is formed between the deflected barrel shock and the crossflow. The induced flow blockage from the jet generates a bow shock that wraps around the jet boundary. The bow shock is nearly normal to the crossflow just upstream of the jet, and decays in strength as it wraps around the jet boundary. Under certain conditions, the presence of the bow shock can impose an adverse pressure gradient that is sufficient to separate the upstream subsonic boundary layer. In this case, a separation shock is formed upstream of the bowshock and causes a high-

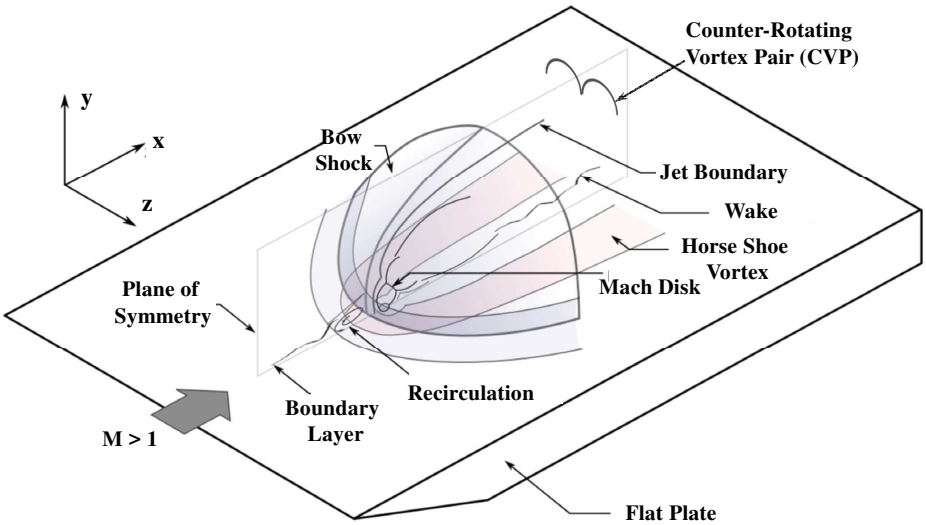

Figure 2.1: Three dimensional schematic of the canonical transverse jet in supersonic crossflow.

pressure recirculation region to exist upstream of the jet. As the flow expands around the jet, a low-pressure wake is formed, where the boundary layer is also separated and a second recirculation region exists.

Several vortical structures are formed during the interaction of the two fluid streams [1, 42]. Jet shear-layer vortices form from the Kelvin-Helmholtz instability associated with the annular shear layer of the jet separating from the orifice. In the near-field, horseshoe vortices wrap around the base of the jet and extend downstream through the wake. A series of folded vortex sheets forming a counter-rotating vortex pair (CVP) is developed a few jet diameters downstream. They are caused by the aerodynamic forces of the jet onto the crossflow and contributes largely to the entrainment of the crossflow into the wake of the jet. Finally for high J_{j} , wake vortices which take place in the form of intermittent and localized separation events, originate in the boundary layer and stretch towards the jet boundary. They are caused by the adverse pressure gradient in the wake of the jet. While the shear-layer and wake vortices are essentially unsteady in nature, the horseshoe and CVP vortices maintain well-defined mean-flow structures.

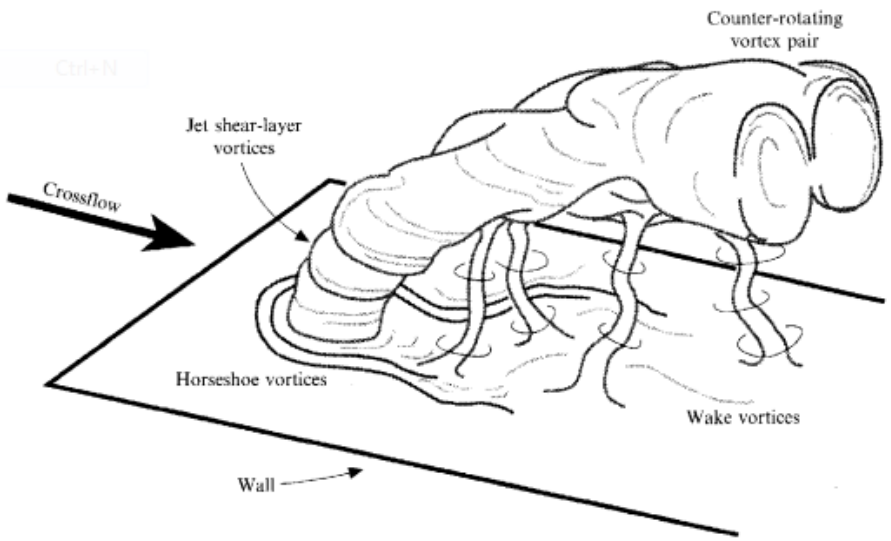

Figure 2.2: Illustration of four prominent types of vortical structures that are formed with a transverse jet in crossflow. Image was taken from Ref. [1].

The interaction between the transverse jet and cross flow produces a significant modification to the pressure field in the near-jet region [2, 43]. The pressure modification is complex and varies in a nonuniform manner around the injector. Fig. 2.3 is an experimentally acquired image revealing the mean pressure distribution in the near-field of a jet in supersonic crossflow. The pressure upstream of the jet and along the centerline, increases due to the formation of a separation shock and bowshock. The magnitude and size of the resulting separation region is observed to depend on J_j. Immediately downstream and along the centerline, the pressure is significantly lower than the freestream value. The effects of the presence of the jet is similar to that of a bluff body, and causes the expanding flow around it to separate. Similarly, the magnitude of the low-pressure wake and extension downstream and laterally also depends on J_j. As the flow along the centerline continues farther downstream, it is recompressed until it gradually asymptotes to the freestream value.

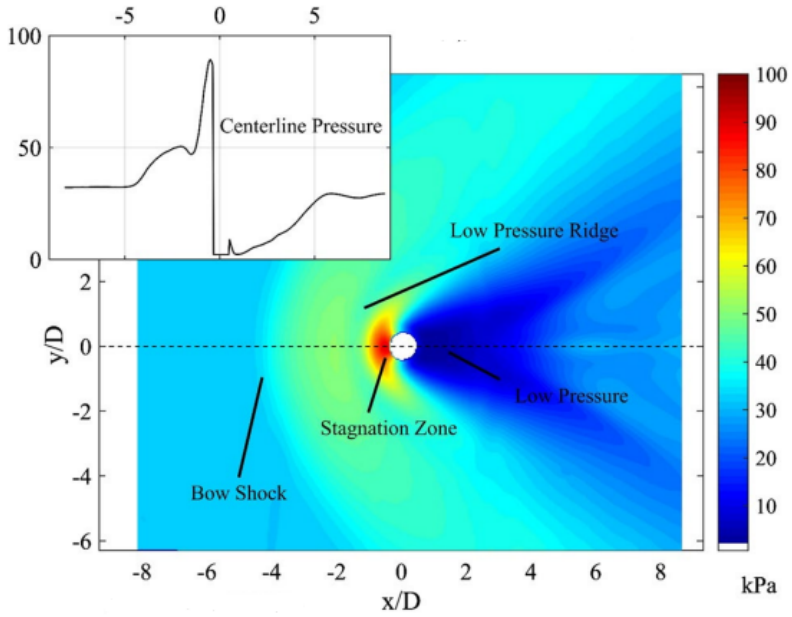

Figure 2.3: Example of the mean pressure distribution in the near-field of a jet in supersonic crossflow. Image was taken from Ref. [2].

2.2.3 Mixing and Flame-Holding

The mixing and flame-holding characteristics of a JISCF system are complex because of their coupled nature [3, 44]. The mechanisms governing ignition and stable flame-holding are governed by the nature and levels of flow turbulence and compressibility. The observed simultaneous existence of two combustion regimes, being thin corrugated reaction layers and distributed reactions, is indicative of the large variations in flow properties and features that control mixing and combustion. This can be seen in Fig. 2.4, which is an image of the instantaneous reaction zone of a reacting jet in supersonic crossflow. The effects of compressibility can have a dominant role in determining the governing mechanisms of ignition as well as stable flame-holding. To this end, varying J_j has been shown to span several dominant flame-stabilization mechanisms.

As J_j is increased to values greater than approximately 3, the jet penetration increases and the effects of compressibility become more dominant as the strength of

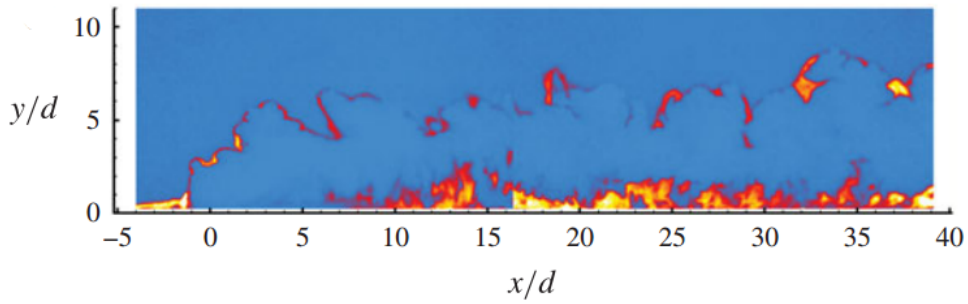

Figure 2.4: Center-plane OH PLIF image of a reacting jet in supersonic crossflow from Ref. [3].

the induced bow shock increases. Increased shock heating as well as the presence of larger recirculation regions exists with larger momentum flux ratios. The recirculation region increases the flow residence time and provides a region for fuel and air to sufficiently mix under relatively high temperature and pressure conditions. The reacting shear layer is anchored just upstream of the injection location, and is believed to be stabilized by the chemical reactions occurring within the recirculation regions. In addition to increased shock heating, the formation of intermediate species within these regions is believed to promote and stabilize reactions.

On the other hand, when the value of J_j is less than unity, the effects of compressibility imposed by substantial jet flow blockage are no longer dominant. Instead, the flame stabilization mechanism is believed to be similar to that of a lifted flame. In this regime of low momentum flux ratios, the jet penetration is similar to the boundary layer height. Therefore, mixing between high temperature air and low temperature fuel streams occurs primarily within the boundary layer while the local mixture is simultaneously subjected to what can be drastic variations in temperature and pressure. It is believed that the stabilization mechanism in this case can be reduced to an autoignition process where the integrated path of a locally varying mixture of fuel and air determines the location where the flame is stabilized.

Near the wall, burning has been shown to exist over broad regions (Fig. 2.4). The

reaction zone structure better resembles the reaction zones of premixed or partially premixed flames, as compared to the relatively thin reaction layers of non-premixed flames. This further supports the belief that the flame stabilization mechanism in low J_j jets is autoignition dominated. On the other hand, burning along the shear layer takes place within thin reaction layers. In this case, it is believed that the stabilization of the thin strained reaction layers are taking place through diffusion dominated processes [45].

Jets in crossflow are known for their superior mixing characteristics when compared to free jets issuing into quiescent media [46]. However, the work of Ref. [37] show how the enhanced mixing rates are only present within the near-field of the JICF system. They evaluated a number of mixing properties of incompressible jets in crossflow for $10 < J_j < 25$. Acetone PLIF was used to acquire quantitative images of the scalar concentration field. They found that the jet centerline concentration decays at a rate of $s^{-1.3}$ in the near field, and decreases to a rate of $s^{-2/3}$ in the far field, where the variable s is the arclength along the jet trajectory. Based on their work, the distinction between the near-field and far field was at approximately $s/J_j^2 d = 0.3$. Furthermore, their work showed that it is the formation process itself of the CVP, which occurs in the near field, that is responsible for the enhanced mixing. However after the CVP has fully developed, it does not contribute to any further enhancement in mixing when compared to a free jet issuing into quiescent media.

Compressible shear layer growth rates are known to be less than those of their incompressible counterparts [47]. The extent of shear layer growth rate decay is observed to increase rapidly with convective Mach number and is found to asymptotically approach a value of 0.2 when normalized by the growth rate of its incompressible counterpart. A number of explanations are given for this observation. First, significant energy removal from the shear layer may cause any interactions responsible for shear layer growth to decrease. Alternatively, the observed decrease in spreading

rate may be given by a vortex sheet amplification affect. At higher convective Mach numbers, disturbances penetrate further into the surrounding fluid and thus act less in perturbing the flow in the vicinity of the vortex sheet itself.

These considerations have significant implications on the use of transverse jets as methods of fuel delivery for supersonic combustion devices. Considering the short residence times through a hypothetical combustor ($\sim$ 1 ms), a lack of mixing will lead to reduced chemical heat release, and a decrease in thrust and efficiency. In most cases, supersonic combustion is a mixing-limited process since the chemical time scales are usually much smaller than the flow transport time scales. However, increasing J_j to enhance the jet penetration and mixing rates must be limited because of undesirable stagnation pressure losses. To help resolve this issue, a number of alternative techniques of fuel injection and combustion augmentation, employing both passive and active methods, have been studied over the years [20, 21]. These methods are designed to assist in distributing fuel into the core flow or increase the flow residence time. The physical mechanism behind most passive methods relies on the generation of streamwise vorticity, leveraging self-excited resonance, or acoustic excitation. Examples include cavity flame-holders, hypermixers, transverse injection, and shock-shear layer interactions [3, 22, 23, 48–51]. On the other hand, active methods primarily rely on forced excitation of large scales and include methods such as, pulsed jets, piezoelectric actuation, and plasma discharge [24, 25, 52–56]. Each of these methods have been shown to have certain strengths but are ultimately limited by deficiencies such as stagnation pressure losses, combustion confinement near walls, limited range of operation, susceptibility to combustor inflow conditions, and significant amounts of input energy required to be effective.

2.2.4 Staged Jets

Staged transverse jet injection into a supersonic crossflow has been a topic of research through several experimental and numerical investigations [4, 57, 58]. The presence of a staged secondary jet has been shown to significantly modify the flow field by altering mixing rates, penetration, and stagnation pressure losses. The additional interactions between the primary (upstream) and secondary (downstream) jets as well as crossflow, create an even more complex flow field. The nature and extent of these interactions are affected by additional parameters such as the spacing between the jets, and the distribution of momentum flux ratios and mass flow rates among the jets.

The experimental study of Ref. [4] investigated the mixing properties of two staged underexpanded air jets issuing into a Mach 2 crossflow. PLIF measurements were carried out to measure the scalar concentration field by seeding both jets with iodine. Both jets were approximately 2 mm in diameter, placed 6 diameters apart, and were each operated at a momentum flux ratio of one. The results revealed a strong upstream influence of the secondary jet on the primary. This was due to the existence of a subsonic recirculation region that spanned the distance between them. As a consequence, the mixing rate immediately downstream of the primary jet was enhanced by this interaction. Moreover, the rapid expansion of the crossflow around the wake of the secondary jet was observed to help generate streamwise vortices that dominated the near-field mixing mechanisms.

Compared with single jet injection, the staged jets were capable of mixing twice as much total injectant to a lower concentration over the same distance. This is shown graphically in Fig. 2.5. Furthermore, the staged jets are shown to enhance the near-field mixing, but have little effect on the mixing rates and dominant mixing mechanism after a distance of approximately 10 jet diameters. This is shown in Fig. 2.6, where the slopes of different configurations and conditions resulted in similar

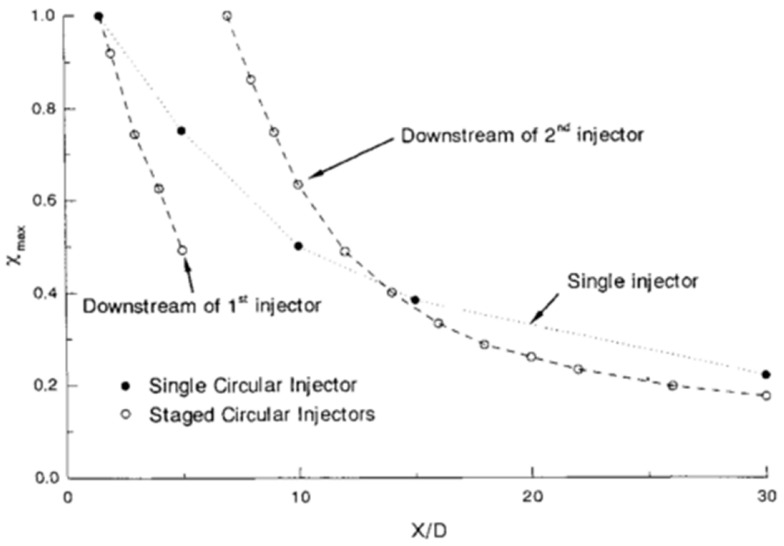

Figure 2.5: Downstream decay of the maximum injectant mole fraction from Ref. [4].

injectant concentration decay rates in the far-field. The slope of the decay rates on a logarithmic plot were approximately 0.75 for all cases, and compares well with that of Refs. [59, 60], who measured a slope of 0.8 under different flow conditions. This implies that the rate of small-scale turbulent mixing, believed to be the dominant far-field mixing mechanism, is insensitive to the injection configuration. This suggests that the best way to increase jet mixing is by increasing the initial vortex generation as well as jet-vortex interaction in the near-field.

One may conceive that there lies an optimal spacing between the jets for a given distribution of jet momentum flux ratios and mass flow rates. The degree of coupling between the two jets will depend on these parameters. The optimal spacing should maximize jet penetration and mixing, while minimizing stagnation pressure losses. For example, a large spacing will allow the flow around the primary injector to recover back to supersonic speeds. This will cause an additional bow shock to form around the secondary jet, and generate a drastically different flow field than in the case of small jet spacing. The upstream influence of the secondary jet on the primary will no longer be present if the flow between them is provided enough distance to recover past

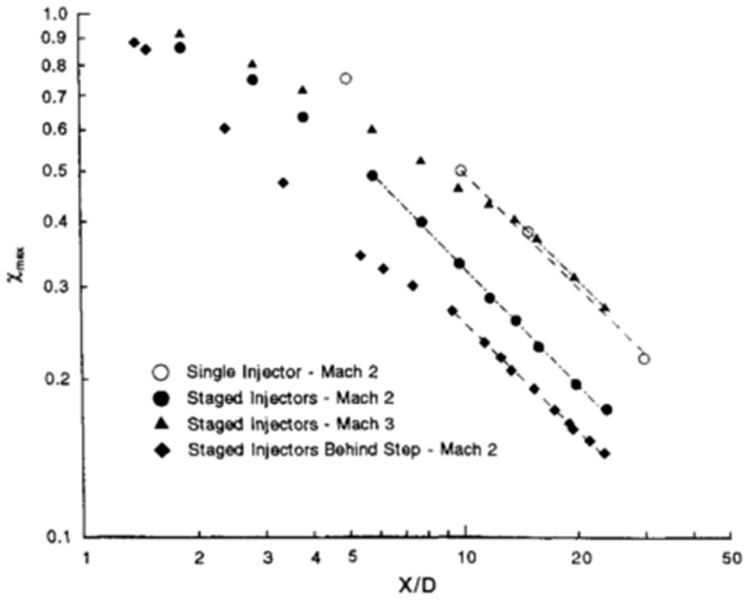

Figure 2.6: Downstream decay of the maximum injectant mole fraction for four different injection configurations from Ref. [4].

sonic speeds. Moreover, as was discussed in Section 2.2.2, the modified flow pressure distribution generated by the primary jet interaction with the crossflow will affect the expansion and penetration of the secondary jet. In fact, if the spacing between the jets is sufficiently small, the additional flow blockage of the secondary jet can enhance the penetration of the primary [57].

2.2.5 Pulsed Jets

An injection scheme that leads to fuel primarily burning in regions confined to the combustor walls may cause large and intolerable thermal loads. In practice, the extent of transverse jet penetration and mixing into a crossflow by increasing the momentum flux ratio is limited because it comes at the cost of increased pressure losses. However, active pulsation can help reduce the amassed penalty of stagnation pressure losses and favorably influence a number of characteristics of the resulting flow field such as the spread, penetration, and mixing of the jet into the crossflow [5, 61–64].

Unlike a steady jet, a pulsed jet consists of a sequence of puffs or vortex rings that individually penetrate into the flow. The characteristics and nature of these structures depend on a few parameters such as the stroke length, duty cycle, strouhal number, and impulsive force of the jet. The impulsive force F generated by a pulsating jet is given by the rate of change in momentum as

$$F = \frac{\mathrm{d}(mu)}{\mathrm{d}t} \tag{2.3}$$

where m and u are the mass and speed of the injectant at the exit plane, respectively. Changing the force of the jet is accomplished by modifying the terms in the numerator, that is; by increasing the jet density (increasing stagnation pressure) or by using a nozzle to expand the jet flow past sonic speeds. Alternatively, the force can be increased by decreasing the time interval of injection.

The spatial separation between successive structures, controlled by the duty cycle, dictates the degree of interaction between them [5]. The duty cycle is simply the fraction of time that the jet is on during each period. For jets operating at lower duty cycles, the flow field consists of well-separated individual vortical structures that penetrate further into the flow than a steady jet. As the duty cycle is increased, successive structures begin to interact with one another, resulting in destruction of the ring structures and decreased penetration.

The slug length determines the nature of the structures, where longer pulses lead to puff-like structures, and shorter pulses lead to compact vortex rings. The stroke length L for a pulse of temporal width τ, is given by

$$L = \int_0^{\tau} u_j \, dt \tag{2.4}$$

where u_j is the temporally varying jet exit velocity.

The combination of the jet fluid slug length of each pulse and the spatial separa-

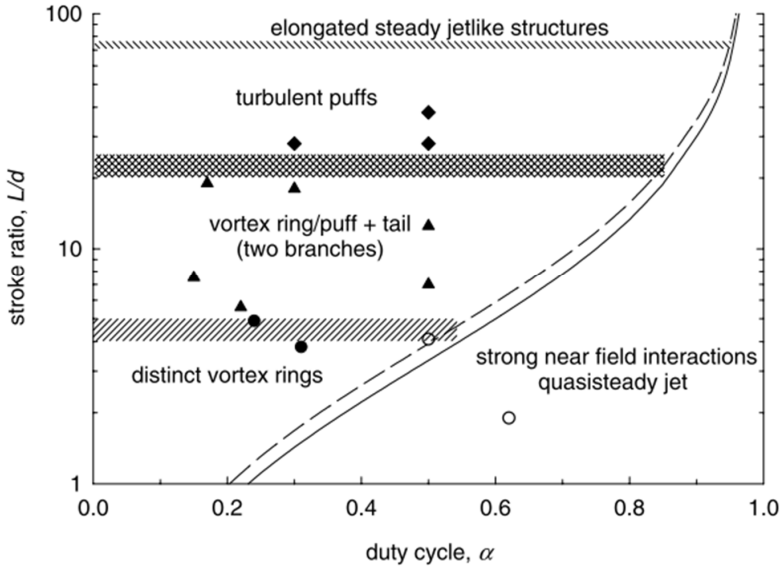

Figure 2.7: Regime diagram for pulsed jets as a function of duty cycle and stroke ratio, from Ref. [5].

tion between successive flow structures are fundamental in determining the governing dynamics of the pulsed fluid. Figure 2.7 is a regime diagram of the various types of flow structures that can be generated with strongly pulsed jets. Strongly pulsed jets are defined as when the root-mean-square velocity is substantially greater than the time averaged velocity at the exit, and the slug of jet fluid associated with each pulse is relatively short. By having sufficiently short duty cycles (less than 0.2), the pulsed jet may consist of distinct vortex rings, vortex rings followed by a fluid column, turbulent puffs, or a segment of a steady jet structure.

The maximum penetration is observed when the pulsed jet consists of individual non-interacting vortex rings [5]. This leads to substantially deeper penetration of the fluid as compared to steady injection. Moreover, even when operating a pulsed jet within a regime that does not enhance penetration, the mixing rate can still be increased [63]. The mixing rate has been shown to have an additional dependence on to the jet-crossflow veolcity ratio, which is not the case for steady jets. In supersonic flows, enhanced mixing has been attributed to fluctuations of the large-scale eddies

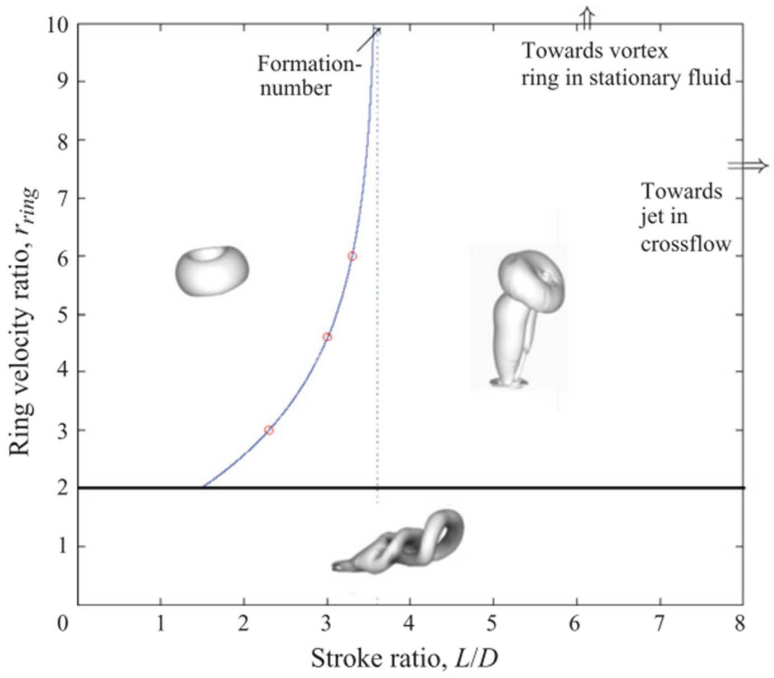

Figure 2.8: Regime diagram for pulsed jets as a function of stroke length and velocity ratio, from Ref. [6].

in the jet fluid, which are correlated with fluctuations of the bow shock in front of the jet.

The work of Ref. [6] provides a regime diagram for pulsed jets as a function of stroke length and velocity ratio. The work shows how the ratio of the jet exit velocity to the crossflow velocity is an important parameter that governs the regime of operation. The regime diagram is shown in Fig. 2.8. For velocity ratios greater than 2, two regimes exist. Lower stroke ratios yield distinct vortex rings that are tilted upstream, while higher stroke ratios yield a downstream tilted vortex ring with a trailing column of vorticity. However, when the velocity ratio is less than approximately 2, vortex rings are not generated. Instead, a hairpin vortices are formed and shed periodically in a similar manner to steady jets in crossflow. The issuing jet exhibits an elongated structure resembling the penetration and structure of a steady jet, regardless of the stroke ratio or duty cycle.

Although, the detonation tube used in this study is referred to as a "pulsed"

device, it is not expected to provide the mixing and penetration benefits of pulsed jets in supersonic crossflows. This is because the exit velocity of the post-detonation gases will be limited by the local sound speed, since the outflow will at most reach sonic speeds. Over the course of a hypothetical scramjet vehicle flight envelope, the exit velocity (exit sound speed) of a PD device will never exceed twice the value of the combustor freestream velocity. This can be shown even after considering a wide range of reactive mixtures for a PD device.

2.3 Detonation Waves

Chapman [65] and Jouguet [66] were the first to propose a theory for detonation waves. The one-dimensional model treats the wave as a stationary hydrodynamic discontinuity across which energy is released. The mass, momentum, and energy equations

$$\rho_1 u_1 = \rho_2 u_2 \tag{2.5}$$

$$P_1 + \rho_1 u_1^2 = P_2 + \rho_2 u_2^2 \tag{2.6}$$

$$h_1 + \frac{u_1^2}{2} = h_2 + \frac{u_2^2}{2} \tag{2.7}$$

are applied across the discontinuity, to obtain the Raleigh and Hugoniot relations:

$$P_2 - P_1 = -(\rho_1 u_1)^2 \left(\frac{1}{\rho_2} - \frac{1}{\rho_1} \right) \tag{2.8}$$

$$h_2 - h_1 = -\frac{1}{2}(\rho_1 u_1)^2 \left(\frac{1}{\rho_2^2} - \frac{1}{\rho_1^2} \right) \tag{2.9}$$

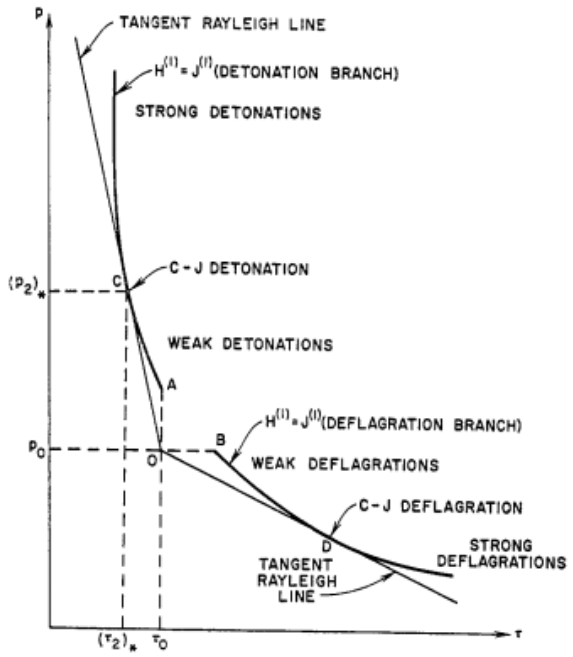

Figure 2.9: Rayleigh-Hugoniot curve of reaction products. Sections corresponding to strong, Chapman-Jouguet, and weak detonations and deflagrations. Figure is taken from Ref. [7].

States 1 and 2 correspond to the reactants upstream and downstream of the wave, respectively. The locus of all solutions along these curves is shown in Fig. 2.9 on a pressure-specific volume diagram. For a given heat release, the upper point (labeled as C) in which these curves are tangent is referred to as the Chapman-Jouguet (CJ) state for detonations. This CJ state solution corresponds to the the point of minimum entropy for the combustion products along the Hugoniot curve, and where the flow behind a detonation wave is sonic relative to the wave ($M_2 = 1$). The detonation travels at one particular velocity (U_{CJ}), and is the minimum velocity of the locus of solutions along the detonation branch of a Hugoniot curve.

The properties at the CJ point can be determined by considering equilibrium calculations of a relevant gas mixture in the unburnt ① and burnt ② states. An analytical solution at the CJ state can be obtained by imposing that $M_2 = 1$, and combining the conservation equations 2.8 - 2.9 and heat of combustion defined as

$$q_c = h_1^0 - h_2^0 \tag{2.10}$$

which is the difference in enthalpy of formations of the burnt and unburnt mixtures. From this, the so-called two-γ solution [67] is obtained

$$M_{CJ} = \sqrt{\tilde{H} + \frac{(\gamma_1 + \gamma_2)(\gamma_2 - 1)}{2\gamma_1(\gamma_1 - 1)}} + \sqrt{\tilde{H} + \frac{(\gamma_2 - \gamma_1)(\gamma_2 + 1)}{2\gamma_1(\gamma_1 - 1)}} \tag{2.11}$$

where the subscript CJ refers to the detonation in the Chapman-Jouguet state and the nondimensional heat of combustion $\tilde{H}$, is given by

$$\tilde{H} = \frac{(\gamma_2 - 1)(\gamma_2 + 1)q_c}{2\gamma_1 \mathcal{R}_1 T_1} \tag{2.12}$$

Through substitution into the conservation equations and using an equation of state, other CJ state properties can be determined:

$$U_{CJ} = M_{CJ} a_1 \tag{2.13}$$

$$\frac{P_2}{P_1} = \frac{\gamma_1 M_{CJ}^2 + 1}{\gamma_2 + 1} \tag{2.14}$$

$$\frac{\rho_2}{\rho_1} = \frac{\gamma_1(\gamma_1 + 1)M_{CJ}^2}{\gamma_2(\gamma_1 M_{CJ}^2 + 1)} \tag{2.15}$$

$$\frac{T_2}{T_1} = \frac{\mathcal{R}_1 P_2 \rho_1}{\mathcal{R}_2 P_1 \rho_2} \tag{2.16}$$

$$u_2 = U_{CJ}\left(1 - \frac{\rho_1}{\rho_2}\right) \tag{2.17}$$

In order to gain an understanding of the structure of a detonation, one needs to adopt the description provided by the ZND theory. In this model, a detonation wave

is a self-sustaining supersonic combustion wave composed of a shock wave coupled with a reaction zone. The one-dimensional ZND model originated from Zeldovich [68], von Neumann [69], and Döring [70], who each independently arrived at the same theory. Based on this theory, a planar shock wave (modeled as a discontinuity) travels at the Chapman-Jouguet velocity, compressing an unburnt reactive mixture and increasing its temperature and pressure to what is referred to as the von Neumann state. Just after the shock, the high-temperature mixture begins to react by generating radicals, in a thermally neutral state known as the induction zone. After an induction period (Δ) where sufficient chain-branching species are produced, heat is released from chemical reactions. The heat release causes the temperature to rise, while the pressure and density decrease as a result of expansion of the products. The expansion process is what helps sustain the propagation of the shock wave. The reaction zone encompasses the induction and energy release zones, and is terminated at the Chapman-Jouguet state. This plane is where chemical equilibrium is reached and the flow is sonic relative to the detonation wave.

An example of a ZND profile of the properties and composition across a stoichiometric H_2-O_2 detonation is given in Figs 2.10(a) and 2.10(b). The profiles were computed with Cantera [71], using the GRI 3.0 mechanism [72]. In this example, the initial pressure and temperature were $P = 0.5$ atm and $T = 300$ K. The leading shock is located at $x = 0$ and is where the induction zone begins. The end of the induction zone (Δ) corresponds to a rapid increase in radical species, and where majority of the energy is released. The properties and composition asymptote to their equilibrium values as the end of the reaction zone is reached.

In reality, the ZND theory is an idealized model of the structure of a detonation wave that does not consider its three-dimensional nature. Coupling between the shockwave, turbulence, and reaction zone provokes an unstable dynamic behavior of the detonation [73]. The exponential dependence of reaction rates on temperature

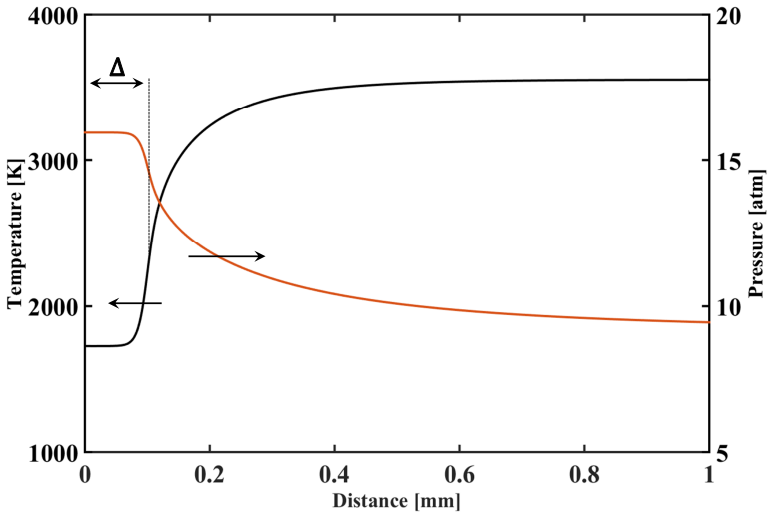

(a)

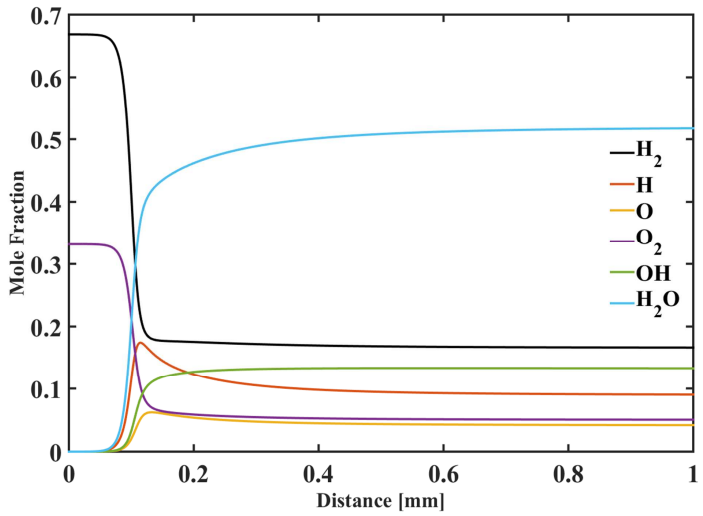

(b)

Figure 2.10: Calculated ZND profile for stoichiometric H_2-O_2 detonation initially at $P_1 = 0.5$ atm and $T_1 = 300$ K. The leading shock is located at $x = 0$. (a) Pressure and temperature profiles. (b) Species composition profiles.

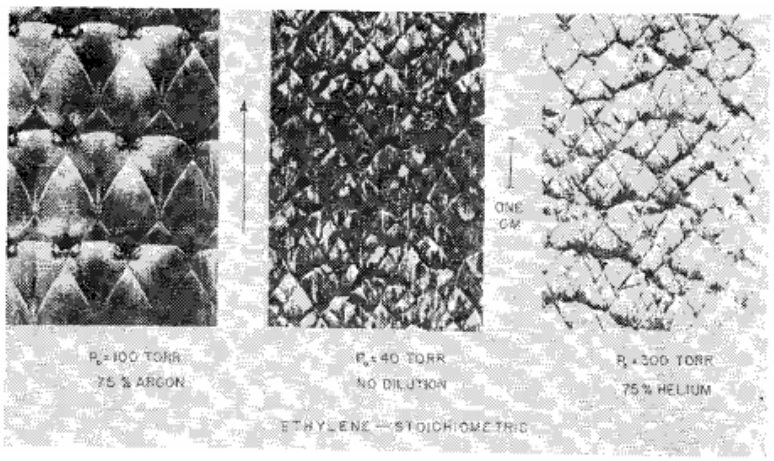

Figure 2.11: Smoked foil record of transverse structure in ethylene-oxygen detonations from Ref. [8].

leads the reaction zone to be highly susceptible to small perturbations in the flow and shock wave strength. The feedback between the shock wave and reaction zone causes the detonation to be oscillatory in nature and produces transverse waves. The transverse waves of a detonation have a characteristic spacing referred to as the cell width λ, which essentially is indicative of the chemical properties of the reactive mixture [10]. Specifically, the cell width represents the sensitivity of a reactive mixture to the detonation wave system. Smaller cell widths imply that the chemical time scale is short, and therefore are less sensitive to perturbations in the detonation wave system. In fact, λ has been shown to be proportional to the induction length Δ [74], which is indicative of the chemical reaction rates and chemical time scale. Figure 2.11 shows smoked foil records that reveal the multi-dimensional structure of several detonation waves.

2.3.1 H_2-O_2 Detonations

The cell width λ is known to be a fundamental property and length scale of a given reactive mixture [73]. Failure or successful propagation of a detonation can be determined by comparing this length scale with the diameter of the tube. A physical

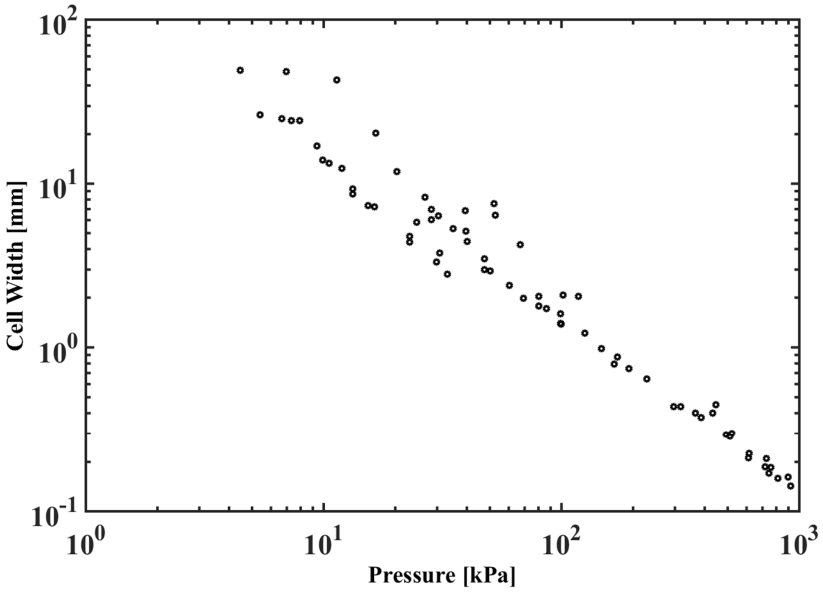

Figure 2.12: Experimentally measured cell widths of stoichiometric H_2-O_2 detonations as a function of initial pressure. Data is from Refs. [8–12].

understanding of this can be given by a time-scale argument. Sufficient time for the reactive mixture to react and release heat is required in order for the gas to expand and drive the shockwave forward. If this time (or space) is not available because the transport time scales to the wall are smaller, the full potential heat release and expansion of the gas will not take place to sustain the shockwave.

There is an abundance of experimental data available on various reactive mixture cell widths as a function of equivalence ratio and initial conditions [8–12]. Fig. 2.12 is a compilation of experimentally measured cell widths for a stoichiometric H_2-O_2 mixture over a range of initial pressures. The cell width is observed to decrease with increasing initial pressure. This is consistent with the fact that the time to initiate and complete reactions decreases with increasing molecular collision frequency, and hence pressure. In order to sustain a stable detonation wave, the tube diameter is required to be approximately three to four times larger than the cell width. However, satisfying this criterion alone is insufficient in determining the nature of the detonation wave as well as the trailing post-detonation products. As will be discussed in Chapter

V boundary layer growth as well as heat transfer effects can place more restrictive demands on the tube diameter required for ideal detonation wave propagation.

2.3.2 Description of Ideal Blowdown Process

A number of wave processes are present as a detonation wave propagates through and is transmitted out of a channel. The features of the wave processes that control the detonation and the resulting blowdown period are essential in interpreting and assessing the performance of the pulsed detonator (PD) in the current study. A number of studies [75, 76] have previously characterized the blowdown process for single-cycle detonation tubes. Figure 2.13 is a space-time diagram of the wave processes present in the detonation tube upon generating a detonation wave at the closed end. This figure neglects the effects of heat and momentum losses to the wall, and only represents the wave processes under ideal conditions. In reality, for tubes with small diameters such as the one used in the current study, these effects can have significant consequences on the characteristics of the detonation wave, the processed gas, and hence the blowdown process. These effects and their implications will be discussed in detail in Chapter V.

After a detonation wave is initiated near the closed end of the tube, it consumes the reactive mixture initially in state ① to ②. Because of the closed end of the tube, an expansion wave (referred to as the Taylor wave) follows the detonation in order to satisfy the kinematic constraint at the closed end and bring the detonated gas to rest (i.e. $U_3 = 0$). This wave is represented by the C_+ characteristics originating at the closed end. Experimentally, properties such as pressure in state ② are difficult to measure directly because of the large convective speeds of the waves and the limited response time of the sensors. However, they can be readily computed with the formulation given in Section 2.3.

The blowdown period begins when the detonation wave reaches the open end of

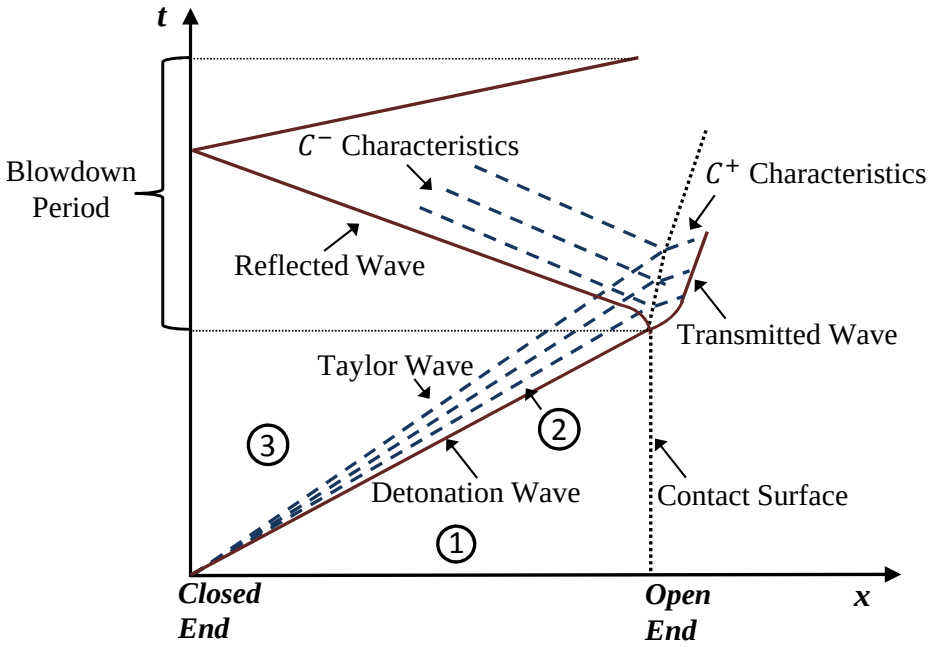

Figure 2.13: Space-Time diagram of wave processes present during the operation of a pulsed detonator tube.

the tube, where it is then partially transmitted and reflected. The transmitted wave diffracts radially and decreases in strength as it propagates outside of the tube. This is a consequence of the combined effect of the sudden change in area and a decoupling of the shock and reaction layer that sustained the detonation. Because of the higher pressure at the tube exit compared to the external ambient pressure and since the gas in state ② is subsonic in the lab reference frame, the reflected wave (referred to as the exhausting wave) propagates back into the tube through a non-simple region, further expanding the gas within the Taylor wave and in state ③ out of the tube. The expanded post-detonation gas exhausting out of the tube is what is referred to as the PD exhaust in this study. After several wave reflections off the ends of the tube, the pressure inside the PD reaches ambient conditions, marking the end of the blowdown.

2.4 Combustion Enhancement with Radical Addition

Combustion enhancement through the addition of free radicals has been explored extensively by several research communities [77–81]. The underlying principles can be seen through a simple kinetics review. It is well known that any given chemical reaction proceeds through a series of coupled elementary reactions. The accessibility of these elementary reactions, which includes chain initiation, chain branching, chain propagation, and chain termination pathways, ultimately determines the initiation and progress of a combustion process. To identify the different ways these pathways are activated or suppressed, we take an arbitrary forward elementary reaction and express it as

$$\sum_{i=1}^{n} \nu_i' C_i \xrightarrow{k_f} \sum_{i=1}^{n} \nu_i'' C_i \tag{2.18}$$

where n is the number of species, ν' and ν'' are the stoichiometric coefficients of the reactants and products, and C_i is the concentration of species i. From the law of mass action, the rate in which reactants are converted to products is proportional to the product of the concentrations of the reactants, as

$$R_f = k_f \sum_{i=1}^{n} C_i^{\nu_i'} \tag{2.19}$$

The proportionality factor k_f is the reaction constant and is generally only a function of temperature. If the activation energy E_a of a reaction is independent of temperature, then the reaction constant can be expressed in an Arrhenius form as such,

$$k_f = A T^{\beta} e^{(-E_a/\mathcal{R}T)} \tag{2.20}$$

where A is the collision frequency or pre-exponential factor. From this elementary analysis, we can see that there are primarily two ways of modifying the reaction rate of

an elementary reaction. The first is through the exponential temperature-dependence of the reaction constant, k_f. This is referred to as *thermal enhancement*, since the translational mode of energy of the molecules is increased. The second is through the power-law dependence of the reaction rate, R_f, on the reactant concentrations. This method is referred to as *kinetic enhancement*. One can conceivably imagine that by purely adding radicals in requisite concentrations, one can enhance the reaction progress of a system by modifying the availability of key branching reaction pathways.

The reaction between hydrogen and oxygen is typically described by 8 major species and at least 16 elementary reactions. The following are several reaction pathways of a H_2-O_2 oxidation mechanism [82]. The chain branching reaction given by Eqn. 2.21b has a dominant role in producing radicals and controlling radical explosion. The reaction rate of this pathway must exceed the rate of removal of radicals to the combustor walls or through competition with the dominant chain termination pathway given by Eqn. 2.21d. These criterion are what define the first two explosion limits of a stoichiometric H_2-O_2 mixture [82].

$$\text{Chain Initiation}: \ H_2 + O_2 \longrightarrow HO_2 + H \tag{2.21a}$$

$$\text{Chain Branching}: \ H + O_2 \longrightarrow OH + O \tag{2.21b}$$

$$\text{Chain Propagation}: \ H_2 + OH \longrightarrow H_2O + H \tag{2.21c}$$

$$\text{Chain Termination}: \ H + O_2 + M \longrightarrow HO_2 + H \tag{2.21d}$$

The addition of radicals provide a means of bypassing endothermic chain initiation reactions (Eqn. 2.21a), and provide a means of accessing chain branching (Eqn.

2.21b) and exothermic chain propagation (Eqn. 2.21c) reactions. However, it is important to note that the pure addition of H or OH to enhance the reaction rate of Eqn. 2.21b, is not sufficient at low temperatures. This is because this pathway is endothermic by approximately 71 kJ/mol, and is therefore not favored at low temperatures. Therefore, the pure addition of radicals to enhance reaction rates must be accompanied by sufficiently high temperatures to sustain the propagation of the intermediate species.

2.4.1 Plasma-Assisted Combustion

Plasma assisted combustion is a very complex yet intriguing technique that relies on both thermal and kinetic mechanisms to alter the reaction progress of a system. The plasma assisted combustion community has been developing a better understanding of the fundamental mechanisms of plasma-chemistry interaction and non-equilibrium initiation of combustion [77, 79, 83, 84]. In this case, an electric discharge is used to simultaneously excite, dissociate, and ionize a gas mixture. This process forms a pool of chemically active species, and therefore, several interaction mechanisms that can accelerate the kinetics of a reacting system.

One of the most important distinctions between plasma discharges is whether or not they are in thermodynamic equilibrium. In the case of equilibrium, the energy between the translational, rotational, vibrational, and electronic energy modes is equilibrated among one another. However, in the case when the energy distribution among the energy modes is not equal, an additional mechanism for energy transfer between the radicals and reactive mixture is available. In other words, besides the effect that free radicals have on the kinetics, an additional complex transfer of energy takes place from vibrationally and electronically excited species and the reacting mixture. Under certain conditions, the addition of these processes has been observed to help augment ignition.

By using a shock tube to generate a range of thermodynamic conditions (pressures between 0.3-2.4 atm and temperatures between 1000 and 2250 K), the work of Ref. [79] showed that the ignition temperatures of several hydrocarbon mixtures were reduced by several hundreds of Kelvin by using a non-equilibrium plasma discharge. The main mechanism believed to affect the flame parameters that were studied (flame speed and ignition delay), was the initial mixture composition. Energy transfer between electronically excited nitrogen and oxygen lead to the production of atomic oxygen. This was believed to provide additional chain reactions in the pre-heat zones which accelerated the processes governing the combustion rate and flame propagation velocity.

2.4.2 H_2O_2 Addition

A number of experimental and theoretical investigations have shown that the addition of hydrogen peroxide (H_2O_2) in small concentrations ($5\% - 10\%$ by volume) can substantially enhance a number of combustion properties such as ignition delay, flammability limits, and flame speed [85, 86]. Since it is stable under room conditions, hydrogen peroxide is delivered to the reacting system by initially premixing it with the fuel. As the fuel/H_2O_2 mixture approaches a preheat zone or a region in the flow with elevated temperatures ($\sim$600 K), the hydrogen peroxide dissociates to form hydroxyl radicals (OH). One of the attractive aspects of this method is that it resolves the challenge of delivering radicals to key locations of a flame since the OH radicals are only formed at elevated temperatures. This is a means of overcoming radical quenching in colder parts of the flow before they have a chance to affect the kinetics of the system.

The addition of H_2O_2 has been observed to have several macroscopic effects on ignition delay, flame speed, as well the limits/boundaries of ignitable mixtures [87, 88]. These studies have shown that OH promotes the oxidation of hydrocarbon

fuels. The increase in burning velocity was determined to be proportional to the radical concentration. Furthermore, the ignition delay was significantly reduced for ($CH_4 - O_2 - Ar$) mixtures in the pressure range between 2.55-13.01 atm and temperature range of 1525- 2025 K. The dominant mechanism for the enhnanced ignition acceleration was attributed to the dissociation reaction $H_2O_2 + M \longrightarrow OH + OH + M$.

2.5 Hypersonic Ground Test Facilities

For over 50 years, the development of scramjet technology has relied heavily on ground test facilities. Recently, there have been efforts to advance hypersonic flight technology through a number of flight experimentations using instrumented ballistic re-entry vehicles to study several hypersonic flow phenomena. Collaborative efforts such as the HIFiRE and HyShot programs have successfully tested sub-scale scramjet vehicles in true-flight environments [16–19]. Some of the objectives of these flights were to test the performance of dual-mode to scramjet-mode transition, demonstrate Mach flight numbers ranging between 6 and 8, the use of hydrocarbon fuels, laminar to turbulent boundary layer transition, steady and unsteady combustion, and more. The complexity of these flight tests and advanced propulsion systems cause them to be expensive and risky. By their nature, they cannot be used to perform parametric studies, nor explore new concepts and ideas. Therefore, in spite of these successful missions, the utilization of ground test facilities remains the workhorse for the advancement of hypersonic technology for many reasons including their relatively simpler and lower cost of operation [89, 90].

Impulse facilities such as shock tunnels, expansion tubes and expansion tunnels, allow the replication of high Mach number and high enthalpy flows. A number of these facilities have been constructed in the effort of studying supersonic flows over several applications such as those of re-entry vehicles or scramjet combustors. Several of these facilities include the Large Energy National Shock Tunnel Facilities at CUBRC

[91], NASA's HYPULSE facility at GASL [92, 93], the X-series and T4 facilities at the University of Queensland [94–96], the free-piston shock tunnel T5 [97] and the Hypervelocity Expansion Tube (HET) at GALCIT [98], the JX-1 in Tohoku, Japan [99], the HIEST facility in Kakuda, Japan [100, 101], and the HEG facility at the German Aerospace Center (DLR) [102].

As a part of this research effort, the development of a new hypersonic expansion tube facility was undertaken at the Gas Dynamics Imaging Laboratory. The impulse facility, referred to as the Michigan Hypersonic Expansion Tube (MHExT), provides an experimental platform for well controlled studies of various supersonic mixing and combustion phenomena. It also provides the capacity for the application and development of advanced non-intrusive diagnostic techniques for measuring critical flow properties. MHExT was designed with the capability of generating a wide range of aerothermal flow properties representative of combustor entry conditions for flight Mach numbers ranging between 4 and 11. The facility scale is capable of producing test times ranging between hundreds of microseconds to several milliseconds, while minimizing the turnaround time between shots.

2.5.1 Expansion Tube Theory

The operation of an expansion tube was originally proposed and analyzed theoretically by Trimpi [14]. It is a short-duration impulse facility that is capable of accessing a wide range of aerothermal conditions with considerable gains in both stagnation enthalpy and pressure. The underlying principle relies on processing the test gas through a series of unsteady waves to generate a desired high-enthalpy supersonic/hypersonic aerothermal test gas flow. In essence, an expansion tube can be thought of as two shock tubes being operated in series, where the first shock tube is comprised of the driver and driven sections, and the second shock tube is comprised of the shock-processed driven section and the expansion section. Moreover, the gen-

erated test gas may be designed to replicate a wide range of flow regimes such as those found in supersonic combustors or re-entry vehicles.

An expansion tube is comprised of three main parts referred to as the driver, driven, and expansion sections. Before each test run, the sections are separated by diaphragms and filled with various gases to predetermined pressures. The driven section is filled with the test gas, which can be any mixture of interest. The pressure and sound speed ratios across each diaphragm prior to rupturing determines the strengths of the generated waves, and therefore the final test gas properties. What differentiates an expansion tube from other impulse facilities such as reflected shock tunnels is the process used to reach the final aerothermodynamic state of the test gas. In particular, after being compressed by the incident shock wave generated by the rupture of the primary diaphragm, the test gas is further processed by an unsteady expansion wave generated by the rupture of the secondary diaphragm. This results in further acceleration of the test gas to higher Mach numbers as well as an increase in its total enthalpy and pressure. In contrast to reflected shock tunnels which rely on a steady expansion of the shock-processed gas through a nozzle, the unsteady expansion processes of an expansion tube contributes a large portion of final test gas energy.

The considerable gains in total enthalpy due to the unsteady expansion process can be seen by analysis of the energy equation. For a flow with negligible heat loss and body forces, the differential form of the energy equation is given by,

$$\frac{\mathrm{D}H_0}{\mathrm{D}t} = \frac{1}{\rho}\frac{\partial P}{\partial t} \tag{2.22a}$$

For a steady expansion process, like that attained by a converging-diverging nozzle, the change in total enthalpy is zero, or $\frac{\mathrm{D}H_0}{\mathrm{D}t} = 0$. On the other hand, for an unsteady expansion process the total enthalpy changes, or $\frac{\mathrm{D}H_0}{\mathrm{D}t} \neq 0$. In particular, the process

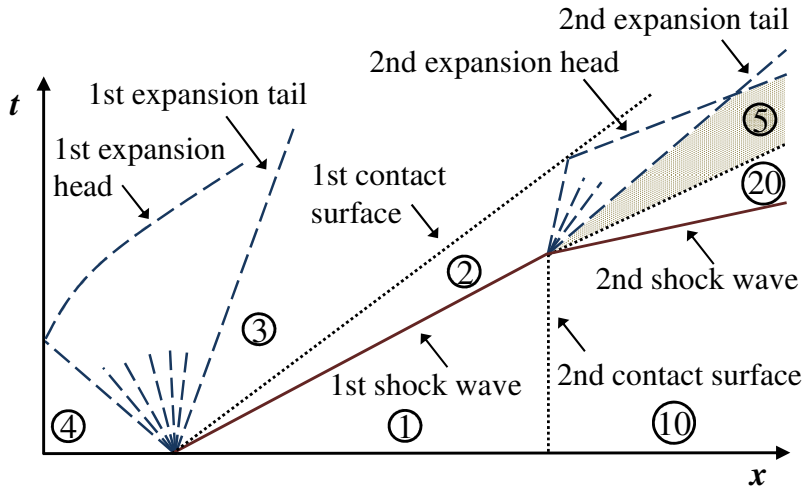

Figure 2.14: Illustration of the generated wave processes during the operation of MHExT.

can be described by,

$$\mathrm{d}u + \left.\frac{\mathrm{d}h}{a}\right|_s = 0 \tag{2.22b}$$

From this follows the relation,

$$\mathrm{d}H_0 = -(M-1)\mathrm{d}h \tag{2.22c}$$

Since for an expanding flow $\mathrm{d}h < 0$, this implies that H_0 increases across an unsteady expansion wave by a factor equal to the Mach number. Moreover, the total pressure attainable in the final test gas exceeds that of the initial fill pressure of the driver section.

An illustration of the wave processes that are present during the operation of an expansion tube is shown as a space-time diagram in Fig. 2.14. The labeling of the various states of gas follows the convention of Trimpi [14]. The figure shows how a second pair of waves is formed at the secondary diaphragm upon arrival of the incident shock wave. The second shock wave continues propagating through the expansion gas (region ⑩), while the expansion wave processes the test gas to its final state (region ⑤). Since the induced bulk motion of the test gas after the incident shock

wave (region ②) is usually supersonic (for high enthalpy operation), the secondary expansion wave is swept downstream as shown in the figure. The test time begins with the arrival of the second contact surface and is limited by the arrival of either of the following three waves: 1) the tail of the second expansion wave; 2) the reflection of the second expansion wave head off the first contact surface; or 3) the reflection of the first expansion wave head off the driver end wall. In general, the available test time scales with the overall length of the facility. However, for a given facility length, the test times can be maximized by altering the lengths of each section (driver, driven, expansion) such that the arrival of each of the test-time terminating waves at the test section occurs simultaneously.

Expansion tubes are typically free-jet facilities where the test model under investigation is mounted inside of a test section at the end of the expansion section. The generated test gas then flows around the test model in manner that is similar to actual flight. The size of the usable region of the flow is limited by the size of the generated core flow. The core flow region is free of any expansion waves emanating from the tube and is conical in shape. To first order, the diameter of the base of the conical region is limited by the internal diameter of the expansion tube, while the length scales with the issuing flow Mach number. Free-jet facilities differ from direct-connect facilities which directly attach an internal flow path of interest, such as a supersonic combustor, to the facility itself. Both techniques have their share of advantages. For example, direct-connect facilities provide an increased capacity for control over the quality and properties of the flow entering the test chamber. However, they generally cannot be used to test external flow phenomena.

There are a number of advantages that expansion tubes have over other impulse facilities such as reflected shock tunnels. First, expansion tubes can be operated over a wide range of conditions by only varying the compositions and fill pressures of each section. This eliminates the requirement of replacing a nozzle to alter the test gas

Mach number. Secondly, the process never involves stagnating the test gas, but rather does work on the test gas as it is moving through the secondary unsteady expansion wave. For a wide range of conditions relevant to supersonic combustion, the flows will have negligible amounts of dissociation and thermochemical non-equilibrium, and are thus more representative of the desired flight conditions being replicated. This is of particular importance in high-speed combustion studies as the chemical composition of the test gas is a significant parameter that must be replicated accurately [90, 103, 104]. Furthermore, higher stagnation pressures and temperatures are achieved in the test gas with an expansion tube for the same initial driver fill pressure and gas sound speed as a shock tunnel. This is a further benefit of the unsteady expansion processes.

Nevertheless, the advantages of using an expansion tube do come at a cost as they are inherently limited by short test times and limited core flow sizes. Furthermore, non-ideal effects such as flow disturbances and boundary layer growth which cause spatial and temporal non-uniformity can have significant effects on the final test gas flow properties. The work of this dissertation identifies the nature of these non-ideal effects and provides insight on their extent of impact on the final test gas properties.

CHAPTER III

Experimental Setup

3.1 Design and Operation Overview of MHExT

The MHExT facility is composed of a 14 m long schedule 120 stainless steel (SS 304/304L) pipe, capable of withstanding pressures of up to 80 bar. The internal surface of the pipe was honed and polished to a diameter of $2R = 144$ mm. A schematic of the completely assembled facility is shown in Fig. 3.1. The facility is comprised of three main sections referred to as the driver, driven, and expansion sections. The length of the tube is comprised of seven interchangeable subsections that allow for the modification of the lengths of each main section. This modular design feature is a means of maximizing test times for varying flow conditions. In its primary configuration, the driver, driven and expansion sections are 2.9 m, 8 m, 3 m long, respectively. This setup is intended to maximize test times for flows representative of combustor entry conditions of flight Mach numbers ranging between 6 and 8. The entire tube rests on rollers to allow diaphragm changing as well as an easier way to interchange the subsections. Three steel pipe shoes are used to clamp the facility down to the structural I-beam that runs along its length. The dump tank and driver section each rest on their own independent structural carriages. These components can be detached to provide easy access to the interior of the tube for routine inspections and cleaning.

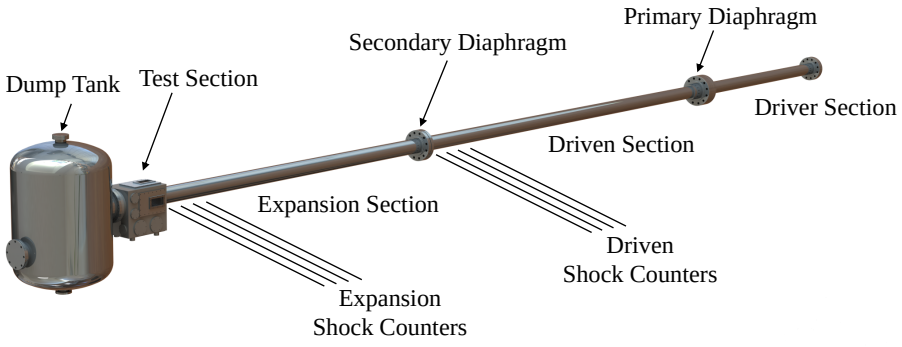

Figure 3.1: Schematic diagram of the MHExT facility.

The driver and driven sections are separated by the primary diaphragm which employs a double diaphragm design. This configuration shown schematically in Fig. 3.2, uses an intermediate section (buffer) to better control rupture initiation, leading to increased repeatability of test conditions between individual runs. This is accomplished by isolating the buffer between two individual diaphragms (usually one or more scored polycarbonate sheets) and filling it with an intermediate pressure relative to that of the driver and driven sections. Upon evacuating the buffer, the upstream diaphragm rapidly ruptures due to the increase in pressure differential across it and is shortly followed by the rupture of the downstream diaphragm. These sheets are typically pre-scored with a cross pattern such that upon rupture, the diaphragms open into four petals that fold and conform to the interior walls of the buffer section. The buffer section has a square inner cross-section to facilitate the complete opening of the diaphragm petals, and is followed by a constant-area transition to a round cross-section. This design serves to minimize flow disturbances originating from the primary diaphragm rupturing process.

The driven and expansion sections are separated by a thin polyester film, which is 2 μm in thickness. Previous studies [105] have shown that the secondary diaphragm thickness had no measurable effect on the final test gas properties for conditions similar to what are considered here. However, using thinner membranes can help

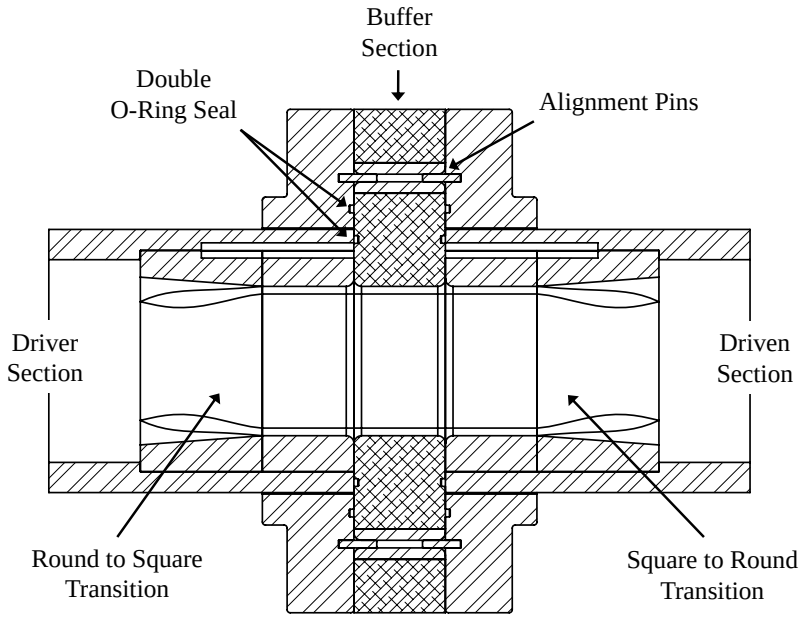

Figure 3.2: Cross-sectional schematic of the primary double-diaphragm, which uses an intermediate buffer section to control the initiation of a test.

reduce measurement noise of the test gas static pressure. The parameter used to compare our study to others is the secondary diaphragm acceleration [106], which is a measure of the extent in which the secondary diaphragm influences the pressure distribution of the flow. The diaphragm acceleration can be approximated to be,

$$a_d = \frac{P_6 - P_{10}}{\rho_d \delta_d} \tag{3.1}$$

where ρ_d and δ_d are the diaphragm density and thickness, respectively. P_6 is the post-reflected-shock pressure of the gas initially in state ②. The secondary diaphragm accelerations for the three flow conditions of this study are tabulated in Table 4.4. The work of Ref. [106] showed that the use of thinner secondary diaphragms increases the diaphragm acceleration and therefore minimizes the formation of a reflected shock wave. This in turn minimizes any alteration of the test gas due to the diaphragm rupturing process. In particular, they have shown that by using polyester film diaphragms 3 μm in thickness, the strength of the reflected wave can be reduced to

that of a Mach wave.

A test section and dump tank are located at the end of the expansion section and are mated with one another through a rubber expansion joint. This allows the dump tank to recoil relative to the test section during each test run, while maintaining the required sealing. The test section is a stainless steel rectangular chamber 45.7 cm $\times$ 48.3 cm $\times$ 34.3 cm in size. Three UV-grade quartz windows provide optical access through the test section. The wall panels in which the windows are mounted can be rotated to shift the field of view further downstream. Several feed-through ports as well as access panels are distributed along the sides of the test section to provide a means of supplying piping, electrical cables, or fiber optics. The test section is independently anchored to the laboratory's floor and it is joined to the expansion section through dynamic o-rings to allow for relative movement of the tube while providing vacuum-tight sealing. The dump tank is approximately 1 m^3 in volume and was designed to be sufficiently large to maintain a nearly constant dump tank pressure during the usable test time as well as maintain a sub-atmospheric pressure within the facility at the end of each test run.

Data acquisition and control of the system is carried out using a computer-based system. The system is comprised of a National Instrument 9-Slot PXIe-1078 Chassis which houses two NI PXI-6133 DAQs, one NI PXI-2521 relay module, and a PXIe-PCIe8381 controller. The system is instrumented with analog and digital input/output modules operated by a Labview program and interfaced with a multi-trigger digital delay generator to provide timing and synchronization to external instrumentation, such as solenoid valves, MKS Baratron vacuum transducers, PCB sensors, lasers, and cameras. Data acquisition of pressure transducers, is typically carried out at a rate of 2 MHz.

Over seventy side-wall ports and plugs are located along the tube to provide access for instrumentation such as pressure transducers, and optical access for non-intrusive

Figure 3.3: Three-dimensional rendering of the MHExT facility.

laser diagnostic measurements. To measure the speed of the primary and secondary shock waves, eight PCB Piezotronics 113B27 pressure sensors are used as time-of-arrival shock counters. Four of the sensors are mounted into ports spaced 30.5 cm apart located just upstream of the secondary diaphragm. A similar four-sensor set up is used just upstream of the test section to measure the secondary shock speed. The shock speeds U_{s1} and U_{s2} are computed from the time of flight between sensors, and are then used to determine the bulk test gas conditions using a solver (described in appendix A) that models expansion tubes and includes equilibrium temperature-dependent properties constructed after the analysis of Trimpi [14]. Before operation, each section of the tube is evacuated with its own designated vacuum pump. During the fill and evacuation processes, the pressures in the driven and expansion sections are monitored using Baratron 627D temperature regulated capacitance manometers. These sensors have a resolution of 20 mtorr, and are regularly monitored using thermocouple gauge tubes.

3.2 Test Models

The primary configuration of study was that of a PD staged downstream of a primary underexpanded jet transverse to a supersonic crossflow. The test model used to generate the desired injection scheme is shown as a cross-sectional schematic in Fig. 3.4. It was comprised of a flat plate with a sharp leading edge, and housed a PD exit port 9.6 mm downstream of a primary transverse jet injector. The flat plate was 2 cm thick and made of anodized aluminum, so as to minimize the amount of elastically diffuse scattered light from its surface. The face of the plate spanned approximately 10 cm in width and provided a sufficient area along the center of the plate that was unaffected by any three-dimensional flow around the model. The plate was approximately 10 cm in length (along the flow direction) to extend the field of view as far downstream as the established core flow existed. The leading edge

was machined out of A2 tool steel and was subsequently hardened and polished. The hardening process was necessary to extend the life of the part as it sustained repeated collisions with diaphragm fragments during each test run. All electrical cables and fuel supply lines were housed underneath the plate and protected from the harsh environment by surrounding them with an aluminum shield.

3.2.1 Primary Transverse Jet

Gaseous hydrogen or helium were used as the primary jet injectants and were delivered from pressurized gas cylinders, through high-pressure stainless steel tubing. The tubing was attached to a fast-response solenoid valve that was mounted directly to the plenum of the injector. The injector plenum was housed within the flat plate of the test model so as to minimize latency in the injection system. Injection was initiated well in advance to ensure a fully-developed and steady jet prior to the arrival of the test gas flow. The valve was found to have a response time of approximately 1 ms, and required approximately 3 ms to achieve a steady and fully developed jet. The plenum conditions were set through a pressure regulator that was placed between the high-pressure fuel cylinder and the fast-response solenoid valve and was capable of maintaining a nearly constant pressure upstream of the injection valve.

Between different experimental runs, the plenum temperature was always nominally 298 K while the pressure was varied to generate jets with different values of momentum flux. By knowing the stagnation conditions of the primary jet, quantities such as momentum flux and mass flow rate can be determined by assuming that the gas is isentropically expanded to sonic conditions at the 2 mm diameter exit port. An indirect method of calibration was used to determine the losses across the fast-response solenoid valve. This provided a means of inferring the jet plenum pressure as a function of the regulator pressure that was manually set upstream of the valve. Indirect calibration was carried out by using the established relations between

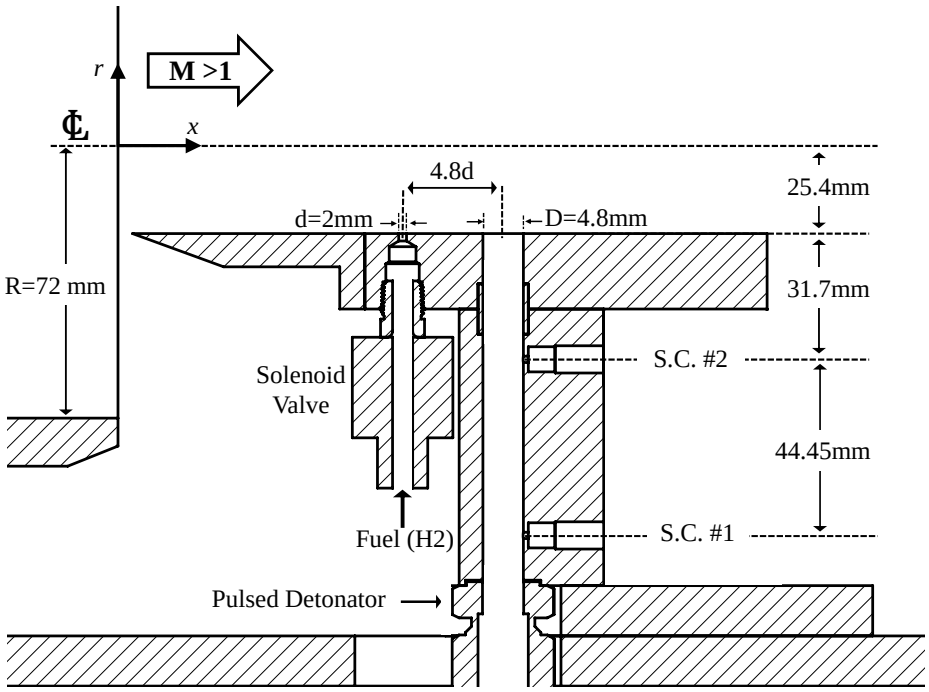

Figure 3.4: Cross-sectional schematic of experimental test model fixed inside of the MHExT test section.

Mach-disk stand-off distance and the jet plenum-to-ambient pressure ratio, P_{0j}/P_a.

The work of Refs. [107] and [108] determined empirical relations between the Mach disk stand-off distance y/D and the jet pressure ratio P_{0j}/P_∞ over a wide range of conditions and geometric configurations. The relation is of the form

$$\frac{P_{0j}}{P_\infty} = A\left(\frac{y}{D}\right)^2 \tag{3.2}$$

where A is a constant between 2.25 and 2.4 based on their results. The empirical relations are shown in Fig. 3.5. By acquiring schlieren images of the underexpanded jet (example shown in Fig 3.6), the Mach disk stand-off distance was measured over a wide range of regulator back-pressures. The resulting jet plenum-to-ambient pressure ratios, if the pressure losses across the solenoid valve were negligible, are represented by the symbols in Fig 3.5. A best-fit of the experimental data results in a value of 8.5 for the constant A of Eqn. 3.2. On the bases of the correlation given by

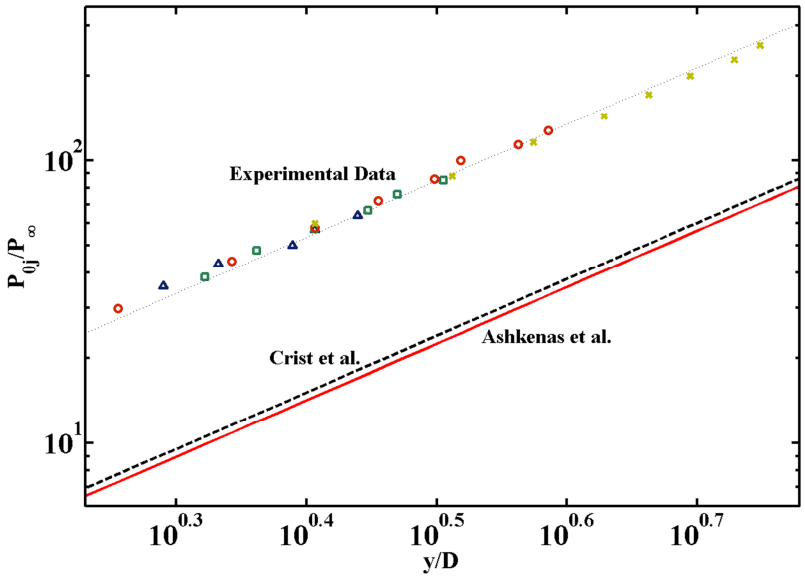

Figure 3.5: Comparison of measured Mach disk stand-off distance as a function of jet pressure ratio. The difference identifies the pressure loss across solenoid valve, and a means of calibrating the system.

equation 3.2, and by using a value of $A = 2.25$, the measurements imply that there is an approximate 74% pressure loss across the solenoid valve. Furthermore, the losses across the solenoid valve were confirmed through previous experiments which directly measured the jet plenum pressure P_{0j} with a piezoelectric sensor as a function of regulator pressure. The results of that study agree very well with the constant value $A = 2.25$ found by Ashkenas. Therefore, the jet plenum pressure as a function of regulator pressure used in the present study was $P_{0j} = 0.26P_{regulator}$. The estimated stagnation (plenum) pressures of the primary jet considered over the course of this study are summarized in Table 6.1. The primary jet-to-crossflow momentum flux ratios, denoted as J_j and given by equation 2.2, were varied between values of 0.5, 2.7 and 5. These values were chosen to span a range of flame stabilization regimes [3].

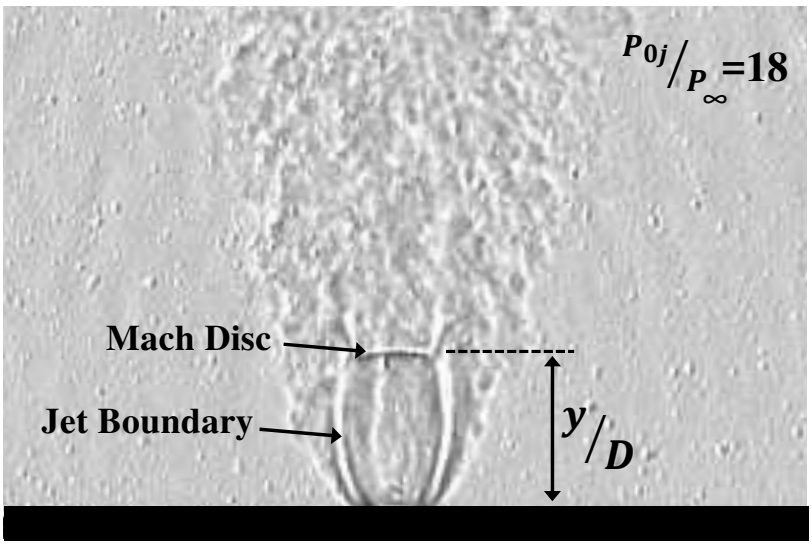

Figure 3.6: Schlieren image of an underexpanded hydrogen jet exhausting into quiescent air.

3.2.2 Pulsed Detonation Tube

The pulsed detonator was comprised of a 0.75 m long stainless steel pipe with an inside-diameter of 4.8 mm. Gaseous hydrogen and oxygen were delivered through separate automotive-style port fuel injectors at the closed end. The injectors were sized appropriately to completely fill the PD with an appropriate mixture before the arrival of the test gas, while being opened and closed at the same time. Upon filling the tube, an automotive spark plug located at the closed end of the tube was used to ignite the mixture with approximately 100 mJ/pulse of energy. Deflagration-to-detonation transition (DDT) was achieved through the use of a 25.4 cm long shchelkin-like spiral with an area blockage of approximately 50%. While the surface roughness along the inner surface of the PD tube was sufficient to cause DDT, it was found that the shchelkin-like spiral lead the DDT process to be more consistent. This was observed as a significant reduction in the observed jitter, or variability in the time of arrival of the detonation at the open end from the time the mixture was ignited. The measured jitter was found to be ± 15 μs, and represents the combined effect of shot-to-shot variations in measured detonation speed as well as the time for DDT to occur. A

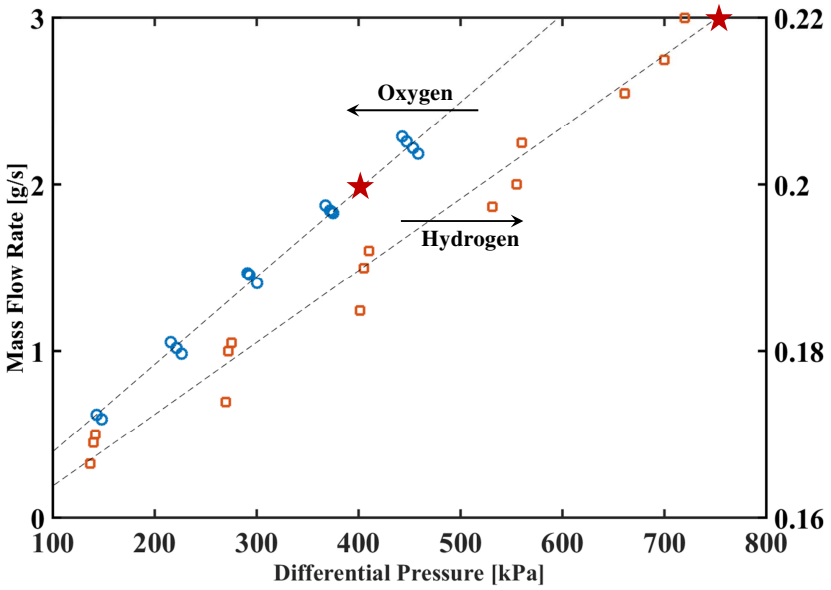

Figure 3.7: Measured mass flow rates of oxygen and hydrogen with the 150 lb/hr and 36 lb/hr Black-ops M-series fuel injectors, respectively. The x-axis refers to the differential pressure across the injector. The star symbols indicate the operating differential pressures used during the experimental campaigns.

schematic of how the PD is incorporated with the test model near the open end is shown in Fig. 3.4.

The equivalence ratio of the mixture obtained through the port-fuel injectors was determined through separate experiments that were designed to measure the flow rates of each fuel injector. The flow rates were determined by measuring the pressure drop across a choked orifice for a wide range of pressure ratios using an absolute pressure sensor (Kulite EMT-375-500A). The results of these experiments are shown in Fig. 3.7, where the left and right axes are for oxygen and hydrogen flow rates, respectively. The star symbols denote the differential pressures that were used during the experiments. These measurements show that the flow rates that were used during the experimental campaigns of this study formed a lean mixture along the PD tube ($\Phi = 0.85$). Moreover, by simple mass conservation, the mass-averaged bulk flow speed of the gaseous H_2-O_2 mixture while the PD was being filled was computed to be approximately 150 m/s.

Two piezoelectric (PCB 113B26) sensors spaced 4.45 cm apart were fixed along the tube 3.17 cm from the PD exit plane and were used to measure the detonation speed and pressure of the subsequent exhaust process (Fig. 3.4). The acquired signal from the sensors also allowed for temporal synchronization with other devices and for identifying the time of arrival of the detonation within the test time. The measured detonation wave speed is (ideally) equivalent to the CJ detonation speed superimposed over the bulk flow speed of the gas it is propagating through ($U_{measured} = U_{CJ}+U_{flow}$). In the experiments, the gaseous mixture of H_2-O_2 filling the PD tube does not come to rest before arrival of the detonation wave, because it is ignited well within 500 μs of the injectors being closed. Therefore, the actual speed of the detonation (U_{CJ}) was taken to be 150 m/s less than what was inferred through the PCB sensor measurements. The distribution of the generated detonation wave speed over 200 shots is shown in Fig. 3.8(a), where the standard deviation was approximately 40 m/s. The mean detonation speed of 2650 m/s corresponds to the Chapman-Jouguet (CJ) speed for a slightly lean ($\Phi = 0.85$) hydrogen-oxygen mixture as shown in Fig. 3.8(b). This agrees very well with the equivalence ratio value that was measured directly (Fig. 3.7).

Only experiments with measured detonation speeds within $\pm 3.8\%$ of 2650 m/s were used for analysis since the resulting jump conditions across the detonation, as well as the production of OH, were predicted to be weakly sensitive to Φ within this range. This is illustrated in Fig. 3.9 where the pressure and temperature jump across the detonation, detonation wave Mach number, and CJ state mole fraction of OH are plotted as a function of equivalence ratio. The grey regions in each figure indicate the predicted range of property variations that were tolerated due to the shot-to-shot variations in the measured detonation speed. The properties of Fig. 3.9 were computed using the chemical equilibrium code CEA [109, 110]. Therefore, we approximate any variations within this range to have a negligible global effect on the

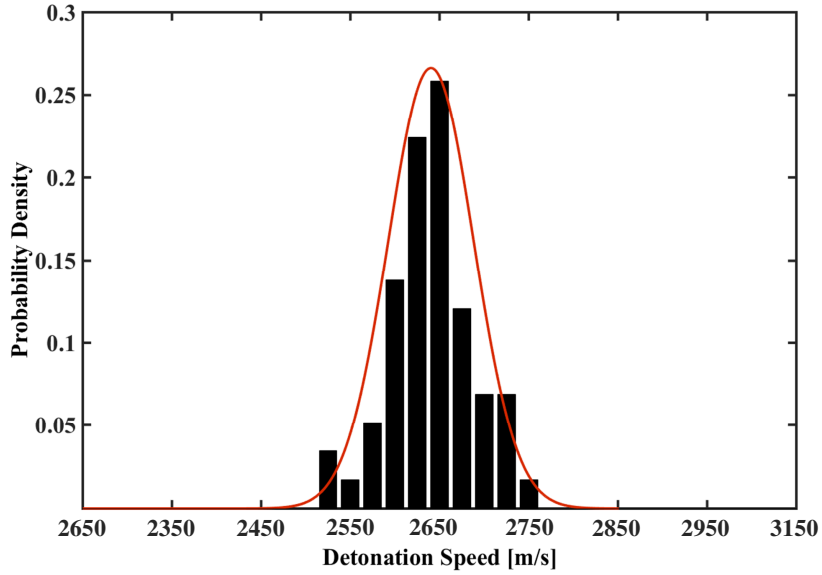

(a)

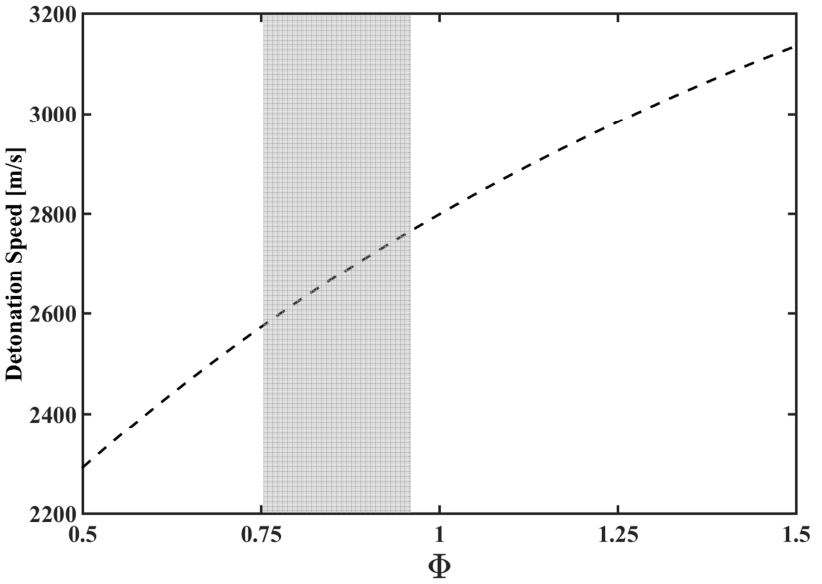

(b)

Figure 3.8: (a) Experimentally measured detonation wave speed distribution over 200 shots with a standard deviation of $\sigma = 40$ m/s. (b) Theoretical CJ detonation speed of a H_2-O_2 detonation as a function of equivalence ratio for initial conditions (P_1 and T_1) of this study. The grey region between $0.75 \leq \Phi \leq 0.95$ indicates the range of Φ in which test data was acceptable.

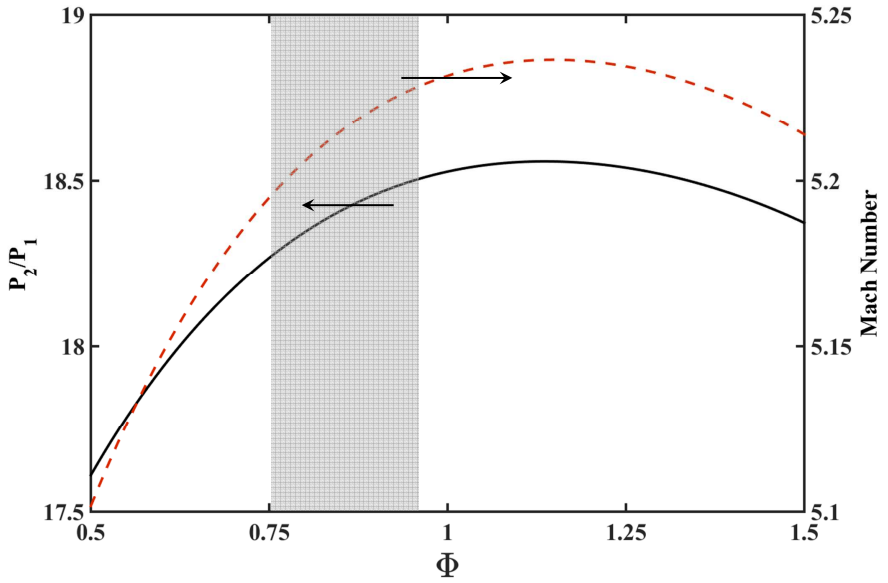

(a)

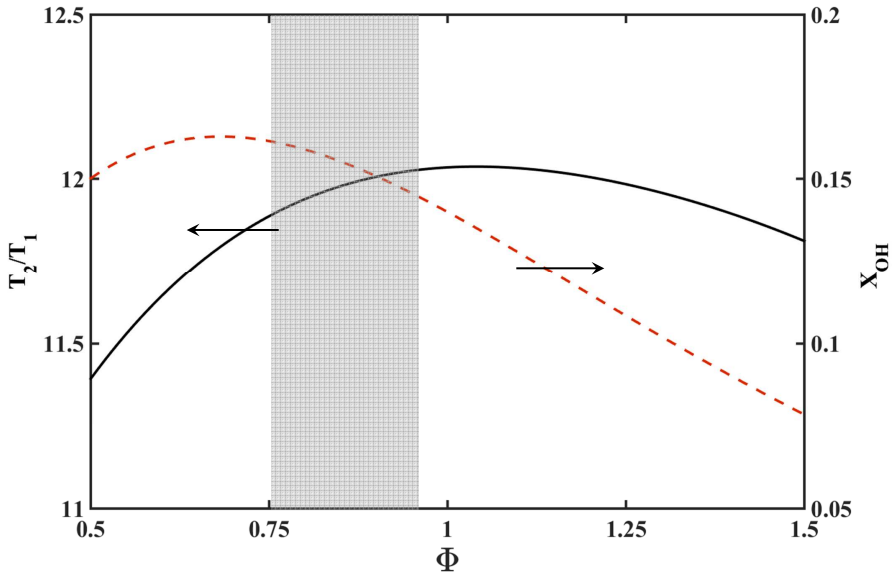

(b)

Figure 3.9: Various properties of a theoretical H_2-O_2 detonation as a function of equivalence ratio for initial conditions (P_1 and T_1) of this study. The grey regions between $0.75 \leq \Phi \leq 0.95$ indicate the range of Φ in which test data was used and their resulting effects on several CJ state properties. (a) Theoretical pressure jump and detonation Mach number. (b) Theoretical temperature jump and equilibrium CJ state OH mole fraction.

interaction being studied.

During an experimental run, the initial pressure inside the PD during the filling process was greater than the crossflow pressure ($P/P_\infty \approx 1.6$). This was experimentally verified and the results are summarized in Fig. 3.10. These results were obtained by mounting an absolute pressure sensor (Kulite EMT-375-500A) in place of the second (downstream) detonation counter to measure the pressure near the open end of the PD. The PD was filled with the same flow rates and hence, reactive mixture used in the study at varying ambient pressures (P_∞). When using a 4.8 mm inner diameter pipe, the combined mass flow rates of both automotive fuel injectors was sufficient to generate a pressure drop across the tube during the filling stages as long as the ambient pressure was approximately 50 kPa or less. This however, is not the case when a larger inner diameter pipe of 10.3 mm was used. In this case, the pressure near the open end of the PD remained equal to ambient regardless of how low the ambient pressure was set. The larger pressure within the PD tube during the filling process was an important requirement in this study, in order to isolate the PD tube from the unsteady wave processes and hence varying pressures, that occur in the test section before the arrival of the test gas slug. This is an inherent effect in the operation of the expansion tube facility that stems from the impulsive unsteady nature used to generate the test gas flow. Initially, experiments using a 10.3 mm inner diameter pipe revealed inflow of the shocked expansion gas (state ⑳) into the PD, and diluting the reactive mixture along the length of the PD. The resulting measured detonation speeds were lower than that of the CJ state. However, for all cases presented in this work, a 4.8 mm inner diameter pipe was used for the PD ensuring that it was choked during the filling process, and therefore the reactive mixture was never contaminated or diluted by any freestream gas. Since the pressure inside the test section never exceeded 50 kPa during the process used to generate the test gas, no inflow was observed to occur.

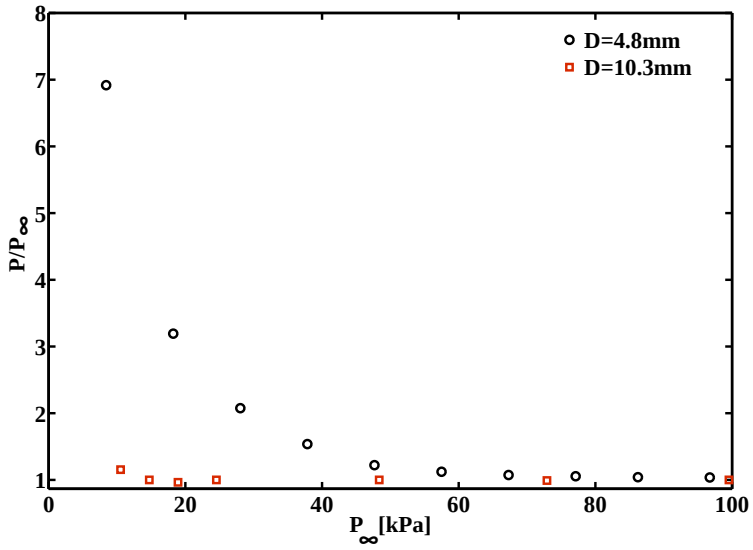

Figure 3.10: Measured pressure near PD exit after filling process as a function of ambient pressure outside of PD. Circle and square symbols indicate inner pipe diameters of 4.8 mm and 10.3 mm, respectively.

3.3 Diagnostic Techniques

Several measurement techniques including intrusive and non-intrusive methods, were adopted over the course of the experimental campaigns of this work. Since an expansion tube is an impulse facility that generates test gas flows with relatively short test times, it is crucial that the facility was capable of repeatably generating flows with nominally identical properties between test runs. In chapter IV, the ability of the MHExT facility to fulfill this requirement will be shown in detail. Because of this limitation and in order to ensure that the observations being made through the use of these diagnostic techniques were indeed a manifestation of the process being studied and were not random, all measurements were repeated over multiple shots.

During each experimental run, the generated shock speeds were monitored to ensure that the mean bulk-flow properties were identical. Therefore, the different measurements of this work were acquired in separate runs under nominally identical conditions. The data was then used to either construct a pseudo-time-series of a transient process, or compute an average quantity of interest over several test runs.

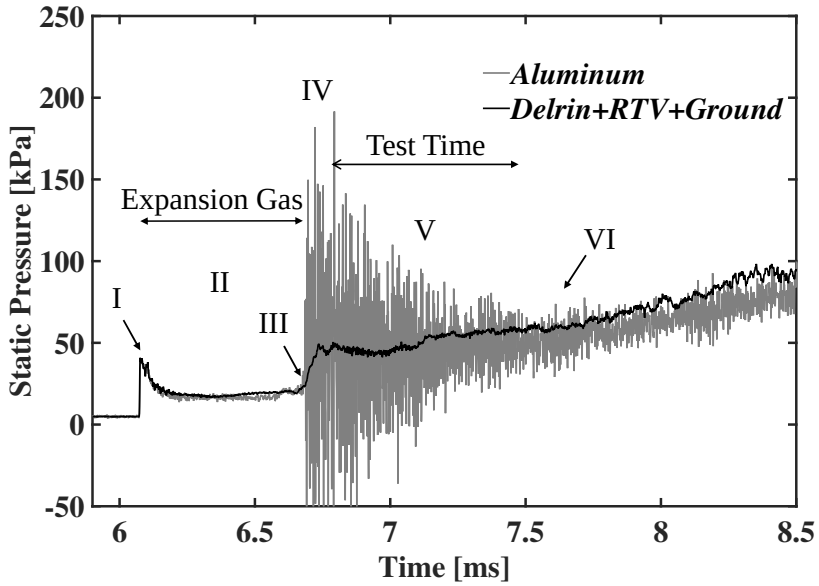

Figure 3.11: Flow condition B pressure measurements taken with and without the modified sensor mounting configuration.

3.3.1 Static Pressure

The use of fast-response piezoelectric pressure sensors are a favored method for dynamic pressure measurements with impulse facilities such as expansion tubes [89, 98, 105, 111, 112]. This is because of their ability to survive in harsh environments and to respond within microseconds to step changes in pressure, while providing measurements with high signal-to-noise ratios (SNR). However, a series of experiments revealed a shortcoming in the ability of the sensor to accurately measure static pressure in such environments. Upon arrival of the test gas, the voltage output from the sensor is overwhelmed by high amplitude noise which renders the pressure measurement useless.

An example of a pressure signal with overwhelming amounts of noise is shown by the grey trace in Fig. 3.11. This pressure trace is a typical example of a measurement acquired with the original mounting configuration of the sensor, which consisted of flush-mounting it in a manner specified by the manufacturer, directly into an aluminum plate with a sharp leading edge. The sensor was located approximate 70 mm

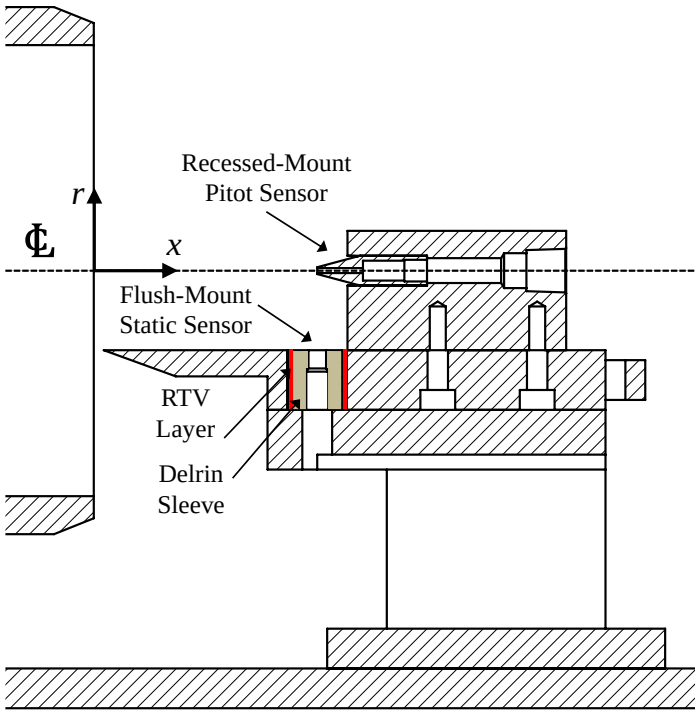

Figure 3.12: Schematic of assembly used to simultaneously measure pitot and static pressure with modified static sensor mounting.

downstream of the exit plane of the expansion tube, and was well within the core flow region of the test gas. The active area of the transducer was approximately 4 mm in diameter, which limits its spatial resolution. Upon arrival of the test gas (III), the signal clearly failed to provide usable data as the pressure trace registered a negative value of pressure, and a standard deviation of $P_{std} = 56$ kPa.

The cause of the deficient pressure measurements were thought to be due to vibrations in the test model assembly, which can cause high frequency oscillations in the pressure measurement. The test gas flow imparts a large stagnation pressure on the assembly and the effects of its arrival can be approximated as an impulsive force. The piezoelectric sensors used in this work were not designed to compensate for lateral force loadings on the sensing element, rather they were designed to only measure axial forces. Moreover, due to the nature of such facilities, the time required for the system to dampen out such vibrations may very well exceed the test times.

The first attempt to reduce the noise was to test different PCB sensor models

with varying sensitivities (ranging between 14.5 mV/kPa and 1.45mV/kPa) in hopes of finding a model that was less susceptible to the flow induced noise. After a series of experiments with three different sensors, no improvement in the SNR was observed since the acquired signal standard deviations normalized by the mean pressures, P_{std}/P_{mean}, ranged between 0.2 and 1.5 regardless of which sensor was used. The results were in agreement with the fact that the PCB sensors tested only differed in the electrical components used to amplify the output, and did not differ in the mechanical stiffness of the sensing element or casing which may have had the potential to dampen the vibrations by a varying extent.

The second attempt was to design an alternative method of mounting the static sensor that extends the work of Ref. [105]. The modified design is shown schematically in Fig. 3.12. With this configuration, the static sensor is flush-mounted into a delrin sleeve with a diameter approximately equal to three sensor body diameters, in a manner specified by the manufacturer. The aluminum plate was bored with a diameter 2 mm larger than that of the delrin sleeve. The sleeve was flush-mounted into the plate while high-temperature RTV silicone was used to fill the space between the parts. The motivation behind this design was to provide a way for the subassembly holding the sensor to dampen the vibrations induced by the strong pressure waves resulting from the arrival of the test gas, while electrically insulating it from the rest of the assembly. Thus, the combination of delrin and RTV silicone were chosen to independently and collectively dissipate the mechanical energy in the form of vibrations by acting as a visco-elastic dampener. In addition, Delrin was a material that was easily machinable. Lastly, the pressure sensor was electrically grounded by attaching a ground strap from the sensor to the inside wall of the test section. This provided a pathway for any charge build-up to move away from the sensor, instead of contaminating the charge going to the signal conditioner.

An example of the static pressure trace with the modified configuration is shown

by the black line in Fig. 3.11. As a result of this alternative mounting strategy, there was a significant improvement in the quality of the measured pressure trace. The amount of noise, P_{std}/P_{mean}, was reduced by 70% for the pitot-static assembly. The static pressure measurements reported in this work were all acquired with the modified sensor mounting configuration discussed in this section.

3.3.2 Pitot Pressure

The pitot pressure was measured with a conical pitot probe. A fast-response pressure transducer was recessed mounted in the cavity at the stagnation point of the probe. The orientation of the pitot probe as it was mounted into the pitot-static assembly, is shown in Fig. 3.12. This assembly was used to acquire a simultaneous measurement of the pitot and static pressures. The pitot probe was located at the same downstream location as the static sensor, and displaced away from the flat plate by approximately 2 cm such that it would not interfere with the static pressure sensor. The measured pitot-static pressures were used to infer the time history of the local Mach number using the Rayleigh pitot relation.

The pitot tubes were also used to measure the radial distribution of properties by instrumenting them into a pitot rake assembly mounted inside the test section. The pitot rake assembly is shown schematically in Fig. 3.13. The rake was originally designed by Örley [113] to measure a total of 25 evenly distributed positions spanning the diameter of the tube ($2R = 144$ mm). This was done by instrumenting the rake with 5 pitot tubes evenly spaced 28.8 mm apart. The rake was then traversed across 5 evenly spaced positions 5.8 mm apart. The tip of the pitot tubes were approximately 3 mm from tube exit plane of the expansion tube to ensure that the sensors were always within the test gas core flow.

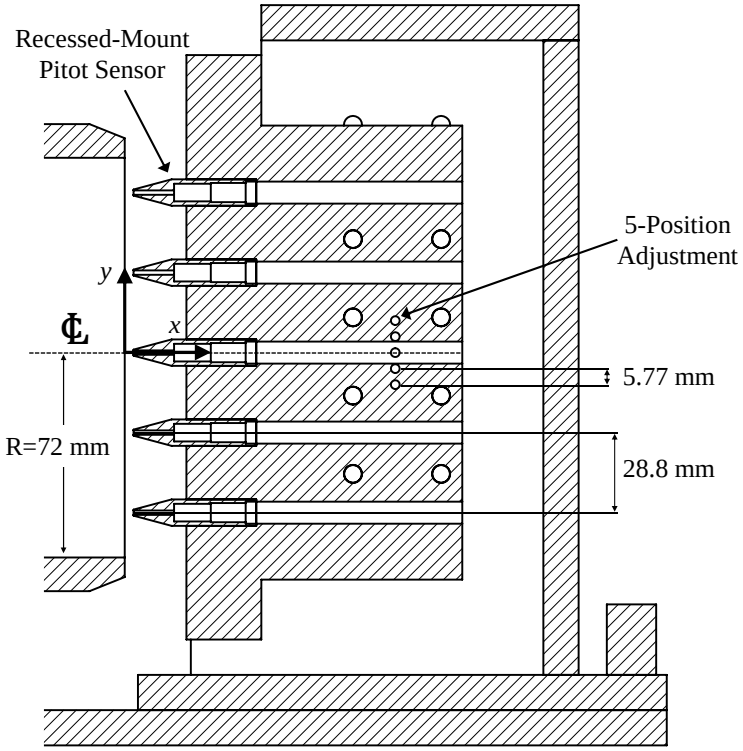

Figure 3.13: Schematic of pitot rake assembly in the test section. In this configuration the rake is in its radially centered position.

3.3.3 Schlieren Imaging

The schlieren technique is an extensively used visualization method in the gas dynamics field. It provides a convenient and non-intrusive means of imaging flow structures where large density gradients are present. The speed of light, and therefore index of refraction, is to first order directly proportional to the local density of the media that it propagates through. Therefore, the schlieren technique is sensitive to variations in the first derivative of density. In principle, the schlieren technique provides line-of-sight and (typically) temporally integrated information about the flow gradients in the index of refraction field.

A standard Z-type schlieren system was set up to acquire kHz frame-rate schlieren images of the various flow fields studied over the course of this research. The setup is shown schematically in Fig. 3.14. The illumination was provided by a continuous

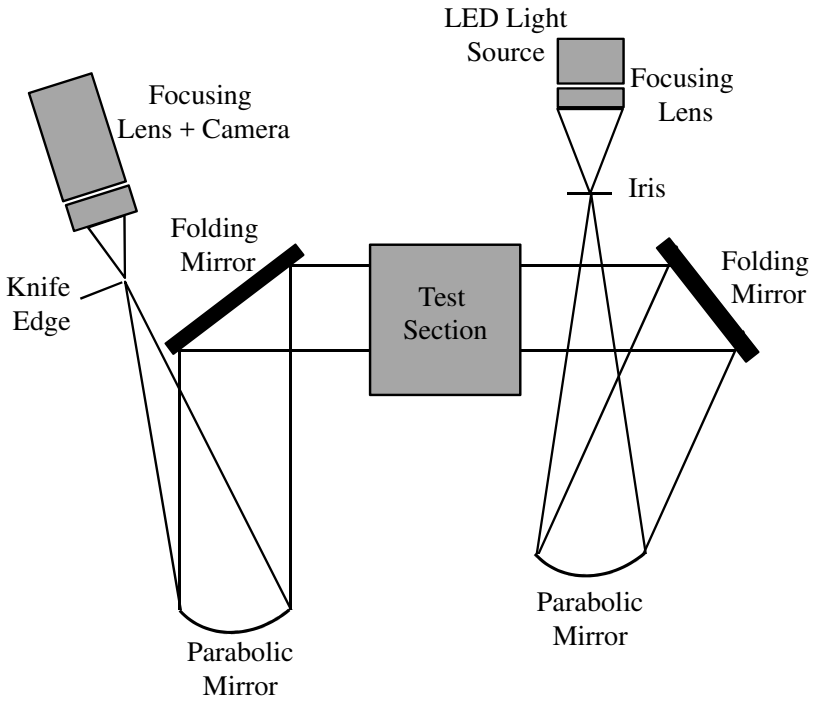

Figure 3.14: Top-view schematic of Z-type schlieren setup.

LED light source (Luminus SBR-70) which was initially focused to a point, one focal length (2 m) away from the first parabolic mirror. An iris is used to adjust the size of the point light source, and therefore the amount of light that is uncovered. The light is then collimated with the first parabolic mirror where it then passed through the test section with a folding mirror. After passing through the test section, the light is re-focused with a second parabolic mirror, before being collected by an optical lens and camera.

A knife edge is placed at the second focal point, which is found by traversing it along the axis of light propagation. By placing the knife edge within the focal point, a uniform reduction of light intensity of the image is obtained. When the knife edge is upstream or downstream of the focal point, the acquired image will have an inverted or non-inverted shadow of the knife edge, respectively. The orientation of the knife edge determines the direction of density gradients that are visualized. For example, a horizontal knife edge will provide sensitivity to the vertical density gradients of the

flow.

The sensitivity s of a system, defined as the fractional deflection of light obtained at the knife edge per unit angular deflection of a light ray at the test section can be evaluated by inspection of [114],

$$s = \frac{f}{h} \tag{3.3}$$

where f is the focal length of the parabolic mirror and h is the amount of light that is unblocked by the knife edge. Therefore the sensitivity of the system can be increased by increasing the focal length of the parabolic mirrors or by increasing the amount of light blocked at the second focal point. In practice, there are a number of considerations that limit or bound the sensitivity of the schlieren system.

The schlieren images acquired over the course of this research were captured with a Phantom v771 CMOS. The exposure time was set to the smallest value that provided sufficient signal (typically 310 ns). This was done to freeze the flow and acquire images that captured the instantaneous structures of the flow. Subsequently, the captured images were reduced by removing dark noise and normalizing by the mean illumination field.

3.3.4 OH* Chemiluminescence

The principle of chemiluminescence imaging relies on the collection of spontaneously emitted light originating from a chemically formed and excited intermediate species of combustion. The formation and excitation of the intermediate species is solely due to the chemical reaction itself. In the case of OH* chemiluminescence, the naturally forming hydroxyl radicals spontaneously emit light as they decay from the $A^2\Sigma^+$ excited electronic state to the $X^2\Pi$ ground state. The emission intensity is proportional to the concentration of the excited species, and is limited by the effects of quenching.

Chemiluminescence has been shown to be a direct indicator of the global heat release rate. However, this is limited to premixed combustion processes, for a constant equivalence ratio and unburnt mixture temperatures. Furthermore, the interpretation of the heat release rate depends on many parameters such as turbulent fluctuations, strain rates, and mixedness [115–117]. Since the combustion processes being studied in this work are non-premixed and strongly coupled with the fluid mechanic processes, the chemiluminescence imaging used in this study served only as an approximate indicator of the characteristics of the chemical reactions.

Chemiluminescence imaging provides a line-of-sight and (typically) temporally integrated representation of the reacting flow field. The OH* chemiluminescence images were acquired with a high-speed Phantom v771 CMOS camera extended with a high-speed image intensifier (LaVision HS-IRO). Emission was collected through a 100 mm f/2.8 UV lens and 310 nm bandpass interference filter (FWHM = 10 nm). Images were acquired at a rate of 41 kHz with an exposure time of 24.4 μs to minimize the loss of information between frames. This allowed for the transient behavior of the processes being studied to be captured as well as collect almost all of the emitted light from the chemically excited OH within the flow field. As was mentioned earlier, this was necessary since the OH* signal was used as an approximate indicator of the global heat release distribution.

3.3.5 OH Planar Laser Induced Fluorescence (PLIF)

Laser-induced fluroescence (LIF) is a spectroscopic technique that relies on a resonant electronic transition to detect the presence of a chemical species of interest. In principle, LIF is a two-step process where stimulated absorption is followed by spontaneous emission of a photon [118]. The LIF process is illustrated graphically in Fig. 3.15. The absorption process occurs when the radiation of light with a wavelength resonant between two distinct electronic energy levels is absorbed by a molecule (or

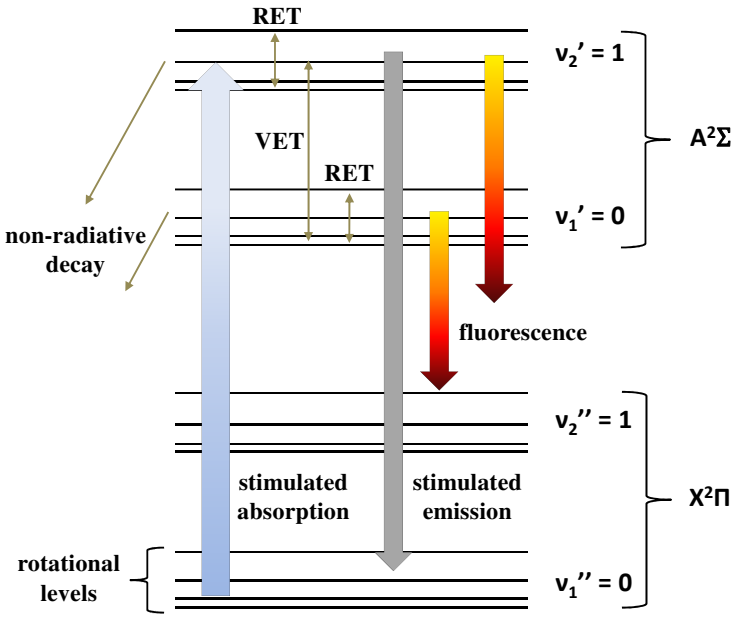

Figure 3.15: Energy level diagram for OH excitation of the $A^2\Sigma^+ \leftarrow X^2\Pi(v' = 1, v'' = 0)$ electronic transition. RET and VET refer to rotational and vibrational energy transfer, respectively.

atom). Upon absorbing the photon, the molecule is brought to an excited electronic state, where it can then undergo a number of processes. The possible processes are; 1) stimulated emission back to the ground state, 2) stimulated absorption to higher energy states, 3) dissociation, 4) non-radiative collisional transfer of energy between rotational and vibrational modes referred to as quenching, 5) spontaneous emission from the laser induced populated state and nearby levels (indirectly populated through collisions). The fourth possibility generates radiation of spontaneously emitted light and is the method of energy transfer that is exploited in PLIF. The radiation is subsequently collected by an imaging lens and detector.

The collected fluorescence signal is proportional to the number density of the tracer species within the ground state. However, it is very challenging to interpret the collected LIF signal in a quantitative manner. This can be seen by inspection of the fluorescence equation. In the linear fluorescence regime with weak excitation, negligible beam attenuation and radiative trapping, the total number of photons collected by a photodetector is given by,

$$N_p = E\ V\ \chi_{OH}\ \frac{P}{kT}\ f_B\ B_{12}\ \frac{A_{21}}{A_{21}+Q_{21}}\ g\ C\ \frac{\Omega}{4\pi} \tag{3.4}$$

where E is the spectral fluence of the laser beam [J cm^{-2}Hz^{-1}], V is the volume over which fluorescence is collected, $\chi_{OH}\ \frac{P}{kT}$ is the total number of OH molecules present per unit volume, f_B is the fractional population of the lower energy level being pumped, B_{12} is the Einstein coefficient for stimulated absorption, $\frac{A_{21}}{A_{21}+Q_{21}}$ is the fluorescence quantum yield, g is the spectral overlap integral between the laser spectrum and the transition of interest, C is the transmission efficiency of the collection options, and $\frac{\Omega}{4\pi}$ is the solid angle subtended by the collection volume to the imaging optics.

The LIF signal has implicit and explicit dependencies on temperature and pressure which make it very challenging to use as a quantitative technique in compressible reacting flows. The pressure dependence is implicit through the g and Q_{21} terms. Variations in pressure can cause the transition features to shift and broaden. The quenching rate Q_{21} varies linearly with pressure, however, in the quenching dominated regime ($Q_{21} >> A_{21}$) this dependence cancels with the explicit dependence in Eqn. 3.4.

The implicit temperature dependencies arise from the f_B, g, and Q_{21} terms. These dependencies are what make it difficult to extract quantitative information such as temperature or tracer number density from the collected fluorescence signal. For example, the quenching rates are coupled to the composition of the perturbing species and temperature. Therefore, the composition of the gas needs to be known. In some cases this can be accomplished, however the accuracy of the technique will heavily rely on how well the composition is modeled or measured. The OH PLIF images presented in this research are therefore only intended to provide qualitative markers of the instantaneous reaction zone.

The excitation laser light source was generated by the frequency-doubled output

of an Nd:YAG-pumped tunable dye laser, operated at 10 Hz. The output of the dye laser was further frequency doubled with a WEX system to produce UV light near 283 nm. The pumping Nd:YAG laser provided approximately 330 mJ per pulse of energy at 532 nm, while the frequency doubled output of the dye laser (283 nm) was measured to be approximately between 5 and 10 mJ per pulse. The $Q_1(N'' = 7)$ line near 283.2 nm of the $A^2\Sigma^+ \leftarrow X^2\Pi(v' = 1, v'' = 0)$ electronic transition was used. The laser beam was formed into a thin sheet through a combination of UV-grade cylindrical lenses. The beam was first expanded and subsequently collimated to form a sheet that was approximately 5 cm wide. A 1 m long cylindrical focusing lens was used to focus the beam into a thin sheet over the region of interest.

The tunable dye laser was equipped with a wavelength tuning mechanism. It was determined that the system had degraded over time, causing it to no longer be accurate. Furthermore, it was determined that the output wavelength of the dye laser drifted throughout the course of a day, even if the system was given time to warm up and reach a steady state of operation. A separate set of experiments were carried out to calibrate the system and determine what the laser wavelength output was as a function of the tuning mechanism setting. It was determined that the system exhibited a hysteresis effect, where the wavelength of light output depended on the direction in which it was engaged. Further uncertainty in setting the desired output wavelength was a result of having to tune the mechanism manually which provided a limited resolution. In order to circumvent these issues, before each test run a candle flame was placed in the field of view, and the laser wavelength was finely tuned to the center of the intended transition by locating where the peak signal was observed and comparing it to data from the spectral simulation software *LIFBASE* [119].

Single-shot OH PLIF images were taken with an Andor iStar (1024 x 1024 pixels) equipped with a 100 mm f/2.8 UV lens. A 310 nm bandpass interference filter (FWHM = 10 nm) was used to reject unwanted light. The CCD array was set to acquire images

with a 2 x 2 binning, effectively resulting in a 512 x 512 array to enhance the signal to noise ratio. The ICCD was gated to 200 ns to prevent interference with background illumination. The acquired images were processed in three steps: 1) subtracting dark noise and background light scattering; 2) normalizing by the average laser sheet energy profile; 3) dewarping to correct for image distortion.

First, the combined signal from dark noise and background light scattering are acquired by averaging 100 images with the camera shutter open and the laser beam present. These images are acquired with the same filter, gain, integration time, and readout time as in the experiments. Dark noise is generated in the absence of incident light and is due to thermally induced charged carriers within the CCD. Since the scattering medium (OH) is not present, the background light scattering is due to reflections of the incident laser beam off of surfaces.

Second, an average of 100 laser sheet profile images were acquired in static flow conditions. This was done to correct for the average spatial non-uniformity in the generated laser sheet. Shot-to-shot variations in energy or spatial non-uniformity were not considered in this study. The sheet profile images were obtained by first evacuating the expansion tube facility to approximately 100 mtorr, filling to several torr with nitrogen, and then repeating several times. This is done to ensure that no oxygen is present, which is known to be a strong quencher of toluene fluorescence. Toluene vapor was seeded into the expansion tube by the use of a bubbler/seeder. While the expansion tube was under vacuum, nitrogen was injected into the bottom of the bubbler which contained a bath of toluene. The vapor is used to fill the expansion tube with a uniform concentration of toluene vapor. An average of 100 images are acquired with an appropriate combination of filters (WG-300 and UG-11) as well as with the same gain, integration time, and readout time as in the experiments.

Finally, the experimentally acquired images are corrected for distortion that primarily results from imaging off-axis, or when the imaging plane is not exactly parallel

with the object plane. Dewarping of the images involves computing a transformation function which is then applied to the experimental image being processed. The transformation function is obtained by imaging an aluminum block that is placed at the location of the laser sheet. The face of the block was machined with an appropriately spaced and sized grid of dots. A desk lamp, or any source with sufficient UV light, is used to illuminate the surface of the aluminum block. An average of 100 images of the block are acquired using the same filter used in the experiments, however with an appropriate (larger) gain, integration, and readout time. An in-house code is then used to compute the transformation function by using the acquired image of dots and knowing (inputting) the target dimensions/spacing of the grid if it were viewed straight-on.

CHAPTER IV

Characterization of the MHExT Facility

4.1 Introduction

Considering all of the potential that high-enthalpy ground test facilities offer, they are notoriously challenging to characterize and control. Instrumentation not only needs to survive the harsh environments, but also provide data that is meaningful. Moreover, a thorough characterization of the generated test gas flows is a crucial pre-requisite to study, in order to isolate non-ideal facility-induced effects from the phenomena being studied. To this end, a series of experiments utilizing three low-to-mid enthalpy conditions were used to characterize and assess the extent of impact that flow-nonidealities have on the final test gas properties. Aspects such as shot-to-shot repeatability, temporal and spatial test gas uniformity, boundary layer properties, and the presence of flow disturbances were analyzed. Furthermore, a study on the capability of using the facility for supersonic combustion studies was performed.

4.2 Theoretical Range of Achievable Conditions

The solution of all possible achievable test gas aerothermodynamic properties is evaluated by using the expansion tube solver outlined in appendix A. The solution is specific to helium, air, and helium as the driver, driven and expansion gases, respec-

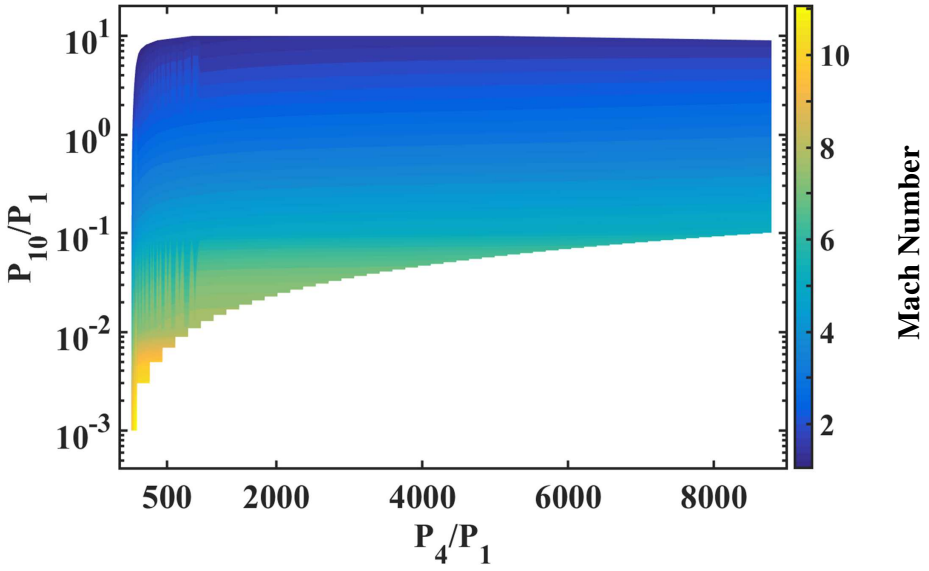

Figure 4.1: Computed range of achievable test gas Mach number as a function of driver to driven (P_4/P_1) and driven to expansion (P_{10}/P_1) pressure ratios. The solution is specific to helium, air, and helium as the driver, driven, and expansion gases, respectively.

tively. The fill pressures spanned the capability of the facility while being limited by practical considerations, and were as follows; $0.013 < P_4$ [MPa] < 11.75, $10 < P_1$ [torr] < 1000, $1 < P_{10}$ [torr] < 150. Only solutions with test times greater than 100 μs were considered. Moreover, since the MHExT facility has a modular design, the solutions correspond to only one of its three configurations, which is intended to maximize test times for conditions representative of flight Mach numbers ranging between 6 and 8.

The solutions for flow Mach number, total enthalpy, temperature, test time, and speed, are given in Figs. 4.1-4.5 respectively. The solutions are provided as semi-logarithmic contour plots where the x and y axes represent the driver to driven (P_4/P_1) and expansion to driven (P_{10}/P_1) pressure ratios, respectively. The results show the vast range of accessible aerothermodynamic properties. More specifically, the theoretical range of achievable conditions with air as the test gas is as follows; $80 < T$ [K] < 2500, $0.5 < H_0$ [MJ/kg] < 8.1, $0.6 < P$ [kPa] < 180, $1 < M < 11.2$, and $600 < U$ [m/s] < 3800. The achievable test times with this configuration can exceed

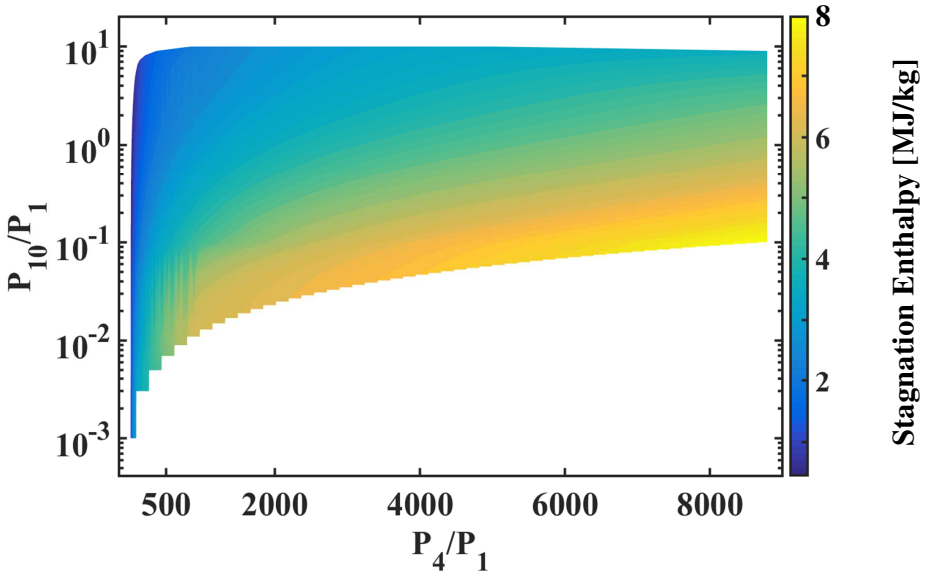

Figure 4.2: Computed range of achievable test gas total enthalpy as a function of driver to driven (P_4/P_1) and driven to expansion (P_{10}/P_1) pressure ratios. The solution is specific to helium, air, and helium as the driver, driven, and expansion gases, respectively.

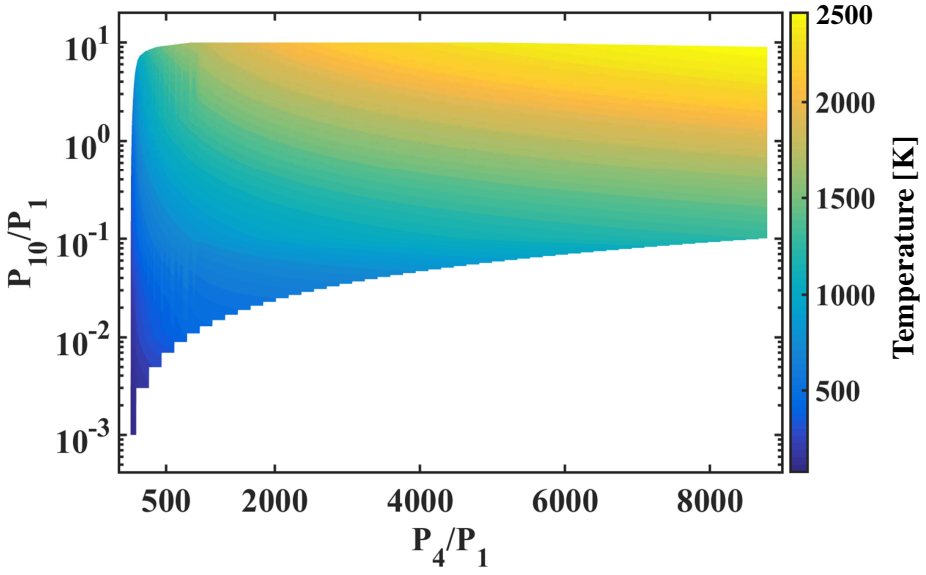

Figure 4.3: Computed range of achievable test gas temperature as a function of driver to driven (P_4/P_1) and driven to expansion (P_{10}/P_1) pressure ratios. The solution is specific to helium, air, and helium as the driver, driven, and expansion gases, respectively..

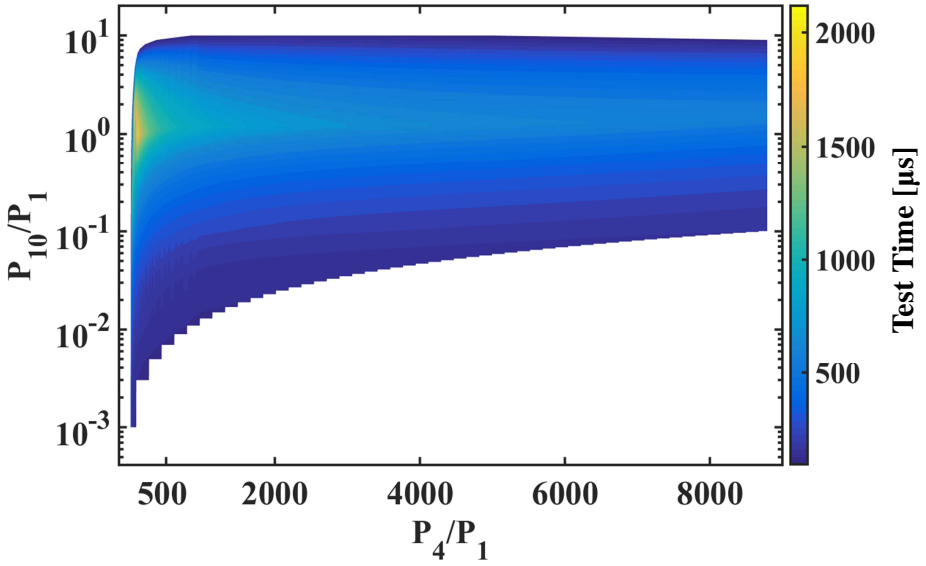

Figure 4.4: Computed range of achievable test gas test time as a function of driver to driven (P_4/P_1) and driven to expansion (P_{10}/P_1) pressure ratios. The solution is specific to helium, air, and helium as the driver, driven, and expansion gases, respectively.

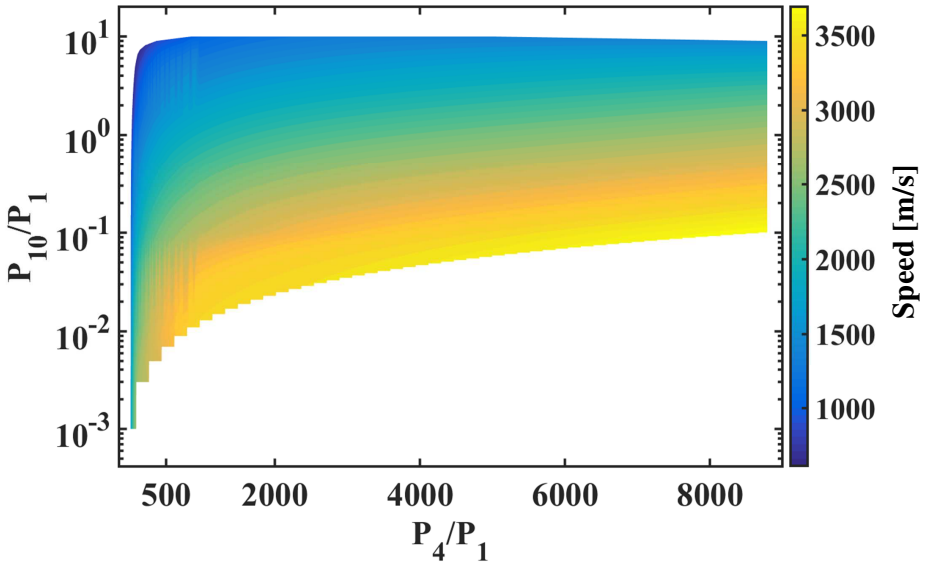

Figure 4.5: Computed range of achievable test gas flow speed as a function of driver to driven (P_4/P_1) and driven to expansion (P_{10}/P_1) pressure ratios. The solution is specific to helium, air, and helium as the driver, driven, and expansion gases, respectively.

2000 μs. In reality, the generated test gas flow properties can be altered by boundary layer growth and additional wave processes arising from non-ideal rupturing of the diaphragms. Furthermore, the test gas quality can be hindered beyond use by flow disturbances originating from the driver gas or from improper test model mounting. In the end, the range of useable test gas conditions are a subset of the theoretically achievable range shown in Figs. 4.1-4.5 and obtained using the solver outlined in appendix A. The work of sections 4.4 and 4.5 provide a detailed analysis of these effects and how they impact several exemplar flow conditions.

Impulse facilities generate a wide range of aerothermodynamic conditions by primarily leveraging unsteady wave processes. They are generally comprised of two or more sections that are separated by diaphragms. The final test gas conditions rely on the initial pressure and sound speed ratios between the sections. In the simplest case, the initial fill temperatures are equivalent to room conditions, leaving only the initial fill pressures and compositions as the free parameters that determine the final test gas properties. This means that the difference in achievable aerothermodynamic conditions from one facility to the next is limited by mechanical (pipe schedule, flange schedule, bolt sizing, welds, etc.) and material considerations as long as the same compositions are available. The only way to extend the range of achievable conditions is to modify the initial fill temperatures. Numerous facilities achieve this by pre-heating the driver gas through electrical heating [91], free-piston compression [97], or combustion/detonations [120, 121]. These techniques can more than double the achievable test gas total enthalpies and in some cases achieve total enthalpies on the order of 100s of MJ/kg. However, they come at a cost as they further complicate the operation of the facility, and generate additional non-ideal effects that alter test gas properties. Since the MHExT facility was not designed to take advantage of any of these techniques, it is therefore capable of generating the same range of conditions of any other expansion tube facility that does not pre-heat the driver gas and is capable

of withstanding equivalent fill pressures.

4.3 Requirements for Supersonic Combustion Studies

The flight envelope of a scramjet vehicle requires operation over a wide range of flow conditions, such as temperature, pressure and Mach number. An expansion tube facility provides an effective means to replicate a wide range of aerothermodynamic conditions in order to study phenomena such as mixing and combustion. The following section provides an analysis of the capability of the MHExT facility in satisfying the requirements needed to generate flows which properly replicate conditions for supersonic combustion studies. Unless otherwise stated, the combustor entry conditions were computed using a generic two-shock inlet, shown schematically by the inset of Fig. 4.6, to process ambient air over the course of a predetermined flight envelope. The details of the solution process are provided in Appendix B. The flight envelopes follow constant dynamic pressure trajectories of either $q = 50$ kPa or $q = 100$ kPa, which represent the limiting operational bounds for hypersonic aircraft [103]. The solver used to compute the post-shock properties assumes that the gas is in equilibrium and considers real gas effects. The inlet is chosen to have an inward turning angle of 20 degrees so as to keep the combustor entry temperature, $T_c < 1500$ K [103] at a flight Mach number of 10. This however, results in a fairly low combustor entry temperature of approximately 700 K at a flight Mach number of 6. The implication on the analysis is a lower than desired flow enthalpy at the early stages of the flight envelope. Nevertheless, since the inlet compression ratio remains a function of flight Mach number, the analysis has a certain degree of consistency and provides valuable insight, while not impacting the conclusions.

4.3.1 Enthalpy Requirements

The analysis of the previous section is extended to assess the capability of the facility in generating the flow enthalpy required to properly replicate conditions for hypersonic flight. We use two methods to compute the combustor entry conditions for a hypersonic vehicle flying along a constant dynamic pressure envelope. The analysis of the first method (also outlined in Appendix B) is limited in scope, as it assumes a constant compression ratio T_c/T_f across the inlet for a range of flight Mach numbers. In reality, this ratio is a function of flight Mach number for a fixed inlet design/geometry. Therefore, we extend our analysis through a second method which uses a generic two-shock inlet, and was described in the previous section.

The results of both methods are shown in Fig. 4.6. The circle symbols ($q = 50$ kPa) and solid lines ($q = 100$ kPa) correspond to the first method. The curves on the right hand side of the figure indicate the expected total flow enthalpy as a function of flight Mach number. The curves on the left hand side of the figure show the corresponding combustor entry Mach number following the inlet compression process, which reduces the Mach number while maintaining a constant total enthalpy. The various circle and solid curves pertain to varying degrees of compression across the inlet (constant T_c/T_f value for each curve). The square symbols correspond to the second method for a constant $q = 50$ kPa flight envelope. As expected, with the two-shock inlet we observe an increasing inlet compression ratio (T_c/T_f) with increasing flight Mach number. We also observe that the enthalpy requirements increase rapidly with flight Mach number where approximately 5 MJ/kg is required for a flight Mach number of 10.

Superimposed on Fig. 4.6 is a color contour plot of the range of achievable test gas conditions with the MHExT facility, which should be compared with the combustor entry condition curves. The contour indicates the achievable test times for varying flow Mach numbers and stagnation enthalpies. Because MHExT has a modular de-

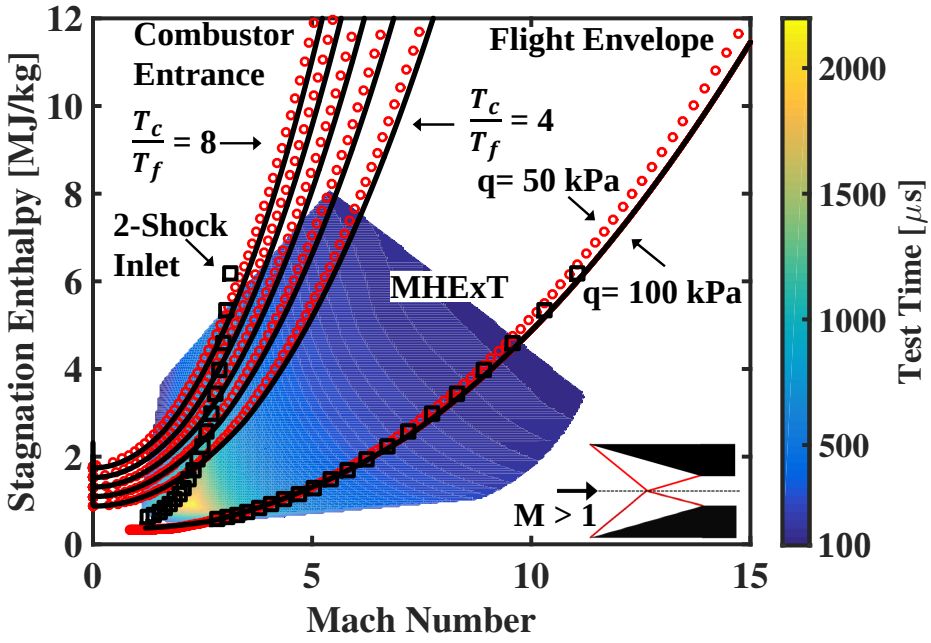

Figure 4.6: Enthalpy requirements to properly replicate conditions for supersonic flight superimposed over the range of achievable conditions with MHExT.

sign, the color contour plot shown indicates the test times achievable with only one of its three configurations, which is intended to maximize test times for conditions representative of flight Mach numbers ranging between 6 and 8. Based on these results, we can see that the MHExT facility is capable of generating a wide range of test gas conditions which satisfy the enthalpy requirements of hypersonic flight. Furthermore, the test times range from the order of hundreds of microseconds to several milliseconds.

4.3.2 Combustion Scaling

Ground test facilities are typically incapable of testing full-scale models. Therefore, we rely on scaling laws to accurately replicate governing parameters which control processes such as mixing, ignition delay, reaction time, etc. Combustion scaling laws allow us to understand how to properly design experiments, interpret ground test data, and relate the results to actual full-scale flight conditions. By manipulating several flow properties such as pressure, temperature, speed, and gas composition

we can scale several important flow parameters. For the purpose of supersonic combustion studies, some of these parameters include the flow Mach number, Reynolds number, Damköhler number, and Stanton number.

An analysis outlined by Ref. [122] is used to relate several flow properties to parameters. We arrive at a slightly different result with the following procedure. From their definitions, M and Re depend on flow properties as,

$$M \backsim \frac{U}{\sqrt{T}} \tag{4.1}$$

$$Re \backsim \frac{\rho L M}{T^{\beta}} \tag{4.2}$$

The value for β arises from combining the temperature dependence of viscosity of the gas, which is sufficiently approximated by $\mu \sim T^k$ where $k = 0.65$ for air, with that of the speed of sound in the definition of Mach number. The combination leads to $\beta = k - 0.5 = 0.15$. Although the value of β depends on the expected dependence of viscosity on temperature (i.e., on k), in general, the temperature dependence of Re is expected to be fairly weak since k is nearly 0.5. The two non-dimensional quantities describe the fluid dynamic properties of the process. To describe the relative importance of the combustion-related properties, we can use a Damköhler number, which is generally defined as the ratio of a flow to chemical time scale. Here, we define an effective Damköhler number (Da_e) to be proportional to the ratio of a flow through time and ignition delay time. This quantity depends on aerothermodynamic properties as,

$$Da_e \backsim \frac{L}{U\tau_{ig}} \backsim \frac{\rho L U T^{\frac{3}{2}+\beta} e^{-\frac{\theta}{T}}}{T^{\frac{1}{2}+\beta} A U^2} \backsim Re \frac{T^{\frac{3}{2}+\beta} e^{-\frac{\theta}{T}}}{A U^2} \tag{4.3}$$

where the value of ignition delay, τ_{ig}, is based on an Arrhenius form given by,

	A [s]	α	θ [K]	P [kPa]	T [K]	Φ
Hydrogen	8×10^{-9}	-1	9600	20 - 500	1000 - 3000	0.4 - 2
Jet-A / JP-8	1.1×10^{-9}	-1	16700	50 - 100	1200 - 2000	1
Jet-A / JP-8	3.3×10^{-8}	-1	10100	50 - 100	2000 - 2500	1

Table 4.1: Coefficients for the Arrhenius equation where combustion is with air.

$$\tau_{ig} = AP^{\alpha}e^{\frac{\theta}{T}} \tag{4.4}$$

and it is assumed that ignition delay is controlled by binary reactions. Eqn. 4.3 is the effective flow Damköhler number cast in terms of its explicit dependence on Reynolds number, temperature and flow speed. The significance of this expression is that it shows how the chemical requirements for a binary reaction can be satisfied by directly replicating several flow parameters. By simultaneously replicating the flow speed, temperature, and Reynolds number of an actual system, one can replicate the Damköhler number. However in most cases, it is challenging if not impossible to replicate the intended model length scale L. In this case, the Reynolds number can be replicated through its implicit dependence on density to compensate for limitations in model length scales; thus preserving the required value of Da_e.

Table 4.1 shows the values of the coefficients in the Arrhenius equation for hydrogen and Jet-A / JP-8 combustion with air. The table also shows the range in which the values are valid. The values for hydrogen are based on the work of Pergament [123] while the values for Jet-A / JP-8 were computed through a linear regression analysis using CHEMKIN and the mechanism by Wang et al. [13] and agrees well with values available in the literature [124–126]. The linear fit for the parameters of Eqn. 4.4 (shown in Fig. 4.7) were done over two temperature ranges since the ignition characteristics were observed to change at approximately 2000 K. Moreover, the ignition delay is expected to increase significantly for temperatures below the

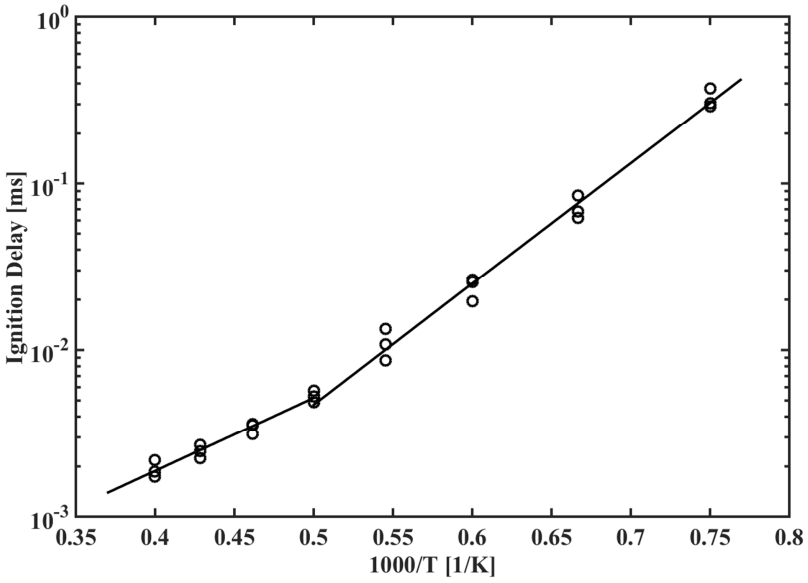

Figure 4.7: Ignition delay times for JP8 / Jet-A combustion with air computed with the mechanism by Wang et al. [13].

specified ranges. This results from a significant increase in the activation energy required to initiate reactions. This is an important aspect to consider since a portion of our analysis, during the early portions of the flight envelope, involves initial mixture temperatures that are below the specified ranges. However, this effect does not alter our conclusions in the assessment of the facility since the facility is capable of generating enthalpies much larger than what is required during early portions of a flight envelope. Lastly, the ignition delay times of Jet-A and JP-8 are identical, as the small amount of additives present in JP-8 does not seem to significantly impact the ignition characteristics.

An assessment is made of the capability of the MHExT facility in generating flows that have equivalent values of Da_e to those of a hypersonic vehicle flying between flight Mach numbers of approximately 5 and 10 along constant dynamic pressure trajectories. Following a similar procedure used to generate the contour plot of Fig.4.6, Da_e was computed from the range of aerothermodynamic properties that can be generated by MHExT. The length scale used for all of the calculations was equivalent to the

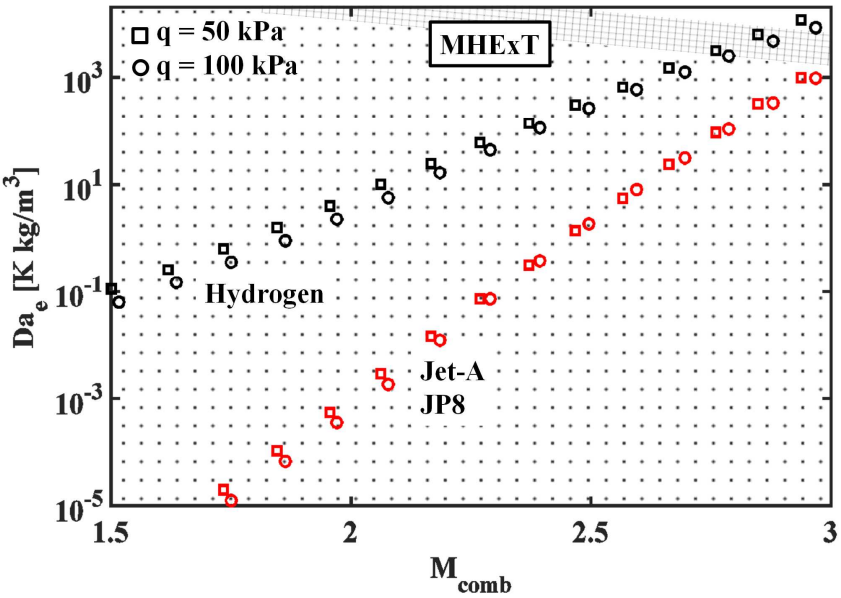

Figure 4.8: Effective Damköhler number as a function of combustor inlet Mach number. Regions with a grid and dot pattern correspond to accessible conditions with MHExT.

inner diameter of the tube. However, since Da_e depends linearly on a length scale, the solution can be scaled accordingly to accommodate different-scale systems.

The results are presented in Fig. 4.8, where Da_e is given as a function of combustor entry Mach number. The regions with a grid and dot pattern correspond to the range of conditions achievable by the MHExT facility. The combined dot and grid regions correspond to hydrogen-air combustion, while the dot patterned region alone corresponds to Jet-A / JP-8 - air combustion. The square and circle symbols correspond to flight envelopes along constant $q = 50$ kPa and $q = 100$ kPa trajectories, respectively, assuming a hypothetical vehicle with the same generic two-shock inlet discussed previously. The results show that for a vehicle with a characteristic length scale equivalent to the tube inner diameter, the MHExT facility is capable of replicating Da_e for combustor entry Mach numbers up to approximately 2.8 and 3 for hydrogen-air and Jet-A / JP-8 - air combustion, respectively. This roughly translates to flight Mach numbers of approximately 9 and 10 for hydrogen-air and Jet-A / JP-8

- air combustion, respectively

4.3.3 Flow Establishment Time

The flow establishment process around a test model will further reduce the inherently short test times of impulse facilities. The complex regions of flow dominated by separation, viscous interaction, or shocks rely on several mechanisms such as acoustic propagation and molecular diffusion, to adjust local properties to their test gas steady state values. As a result, the flow establishment process inevitably consumes a portion of the available test time. In order for the useful test time to exceed the required flow establishment time, the test gas (state ⑤) slug length ($L_{ts} = U_5 t_{ts}$), which is the distance the slug of test gas travels over the test time, must satisfy,

$$L_{ts} > K L_e \tag{4.5}$$

K is a factor that depends on the flow process of interest, and is greater than or equal to one. Empirically found values of K for various flow processes are available in the literature and are provided in Table 4.2 for convenience [127–131]. L_e is a characteristic length scale equivalent to the size of a relevant fluid or geometric region and is equivalent to,

$$L_e = U t_e \tag{4.6}$$

where t_e is the establishment time and U is a characteristic flow speed and can be taken to be equivalent to U_5 or a_5, depending on the flow process.

Before we can assess how well the MHExT facility can satisfy the criterion of Eqn. 4.5, we first explain our reasoning in choosing the values of L_e. Table 4.2 shows the characteristic length scales L_e chosen in this study for five relevant unit flow processes.

Flow Process	Laminar Boundary Layer	Turbulent Boundary Layer	Bluff Body Separated Flow	Shock-Induced Shear Layer	Separated Shock
L_e [mm]	$R\tan\left[\frac{\pi}{2} - \sin^{-1}\left(\frac{1}{M_5}\right)\right]^{\ddagger}$		30	15	$1.1d\frac{\rho_5}{\rho_{5s}}$
K	3.33	2	30	1	$\left(\frac{\rho_{5s}}{\rho_5} - 1\right)\ln\left(1 - \frac{L'_e}{L_e}\right)^{-1}$
Reference	[127]	[127]	[128, 129]	[128, 131]	[130, 132]

Table 4.2: Summary of characteristic lengths L_e used in this study and the corresponding values of K taken from literature data. ‡ Expression applies to both laminar and turbulent boundary layers.

For a laminar and turbulent boundary layer on a flat plate, L_e is equal to the length of the expansion cone emanating from the exit of the expansion tube. This length is then a function of M_5 and represents the approximate length of the boundary layer which can be contained inside of the useful core flow. In the case where a separated flow is present in the aft region of a bluff body, a length of 30 mm was chosen as an arbitrary yet typical test-model diameter. The characteristic length for the case of a shock-induced shear layer was chosen based on the size of boundary layer separation observed upstream of a transverse jet in supersonic crossflow [3]. Separation results from the adverse pressure gradient induced by the bow shock that wraps around the jet. The presence of this region of relatively stagnant gas forms a shear layer with the supersonic free stream. Schlieren images were used to measure the size of a recirculation region in the case of a transverse jet with a momentum flux ratio of 5.0 and was found to be approximately 15 mm in length. Lastly, in the case of a separated shock that forms around a blunt body, the characteristic length scale L_e is equivalent to the asymptotic value of the shock stand-off distance, and it is given by the empirical correlation of Farris et al. [132]. ρ_{5s} is the fluid density behind a normal shock at state ⑤ conditions. In our study, the length d, which is the diameter of the geometric body, was taken to be 30 mm because it is a practical and representative size for a test model. Lastly, the bow shock was considered to be fully established

when the value of L_e' was equivalent to 95% of L_e.

The establishment times for the five cases were computed for a range of combustor entry conditions using Eqn. 4.6, where $U = U_5$ for all cases except for the shock-induced shear layer process, in which case $U = a_5$. This is because the underlying establishment process relies on acoustic propagation to generate the dimensions and flow topology within the separated region. The value of a_5 is computed at an intermediate temperature such as the Eckert reference temperature. The results are shown in Fig. 4.9, where the solid curve corresponds to the left axis and represents the total enthalpy for a flight Mach number range between approximately 5 and 10. The symbols for different flow processes correspond to the right axis. $\widetilde{t}$ is the ratio between the available test time and the required establishment time of a unit flow process for an equivalent flow condition. The test time duration capable of being generated with the facility is extracted from the contour plot of Fig. 4.6, along the "two-shock inlet" curve.

The results of Fig. 4.9 show that the facility is capable of generating values of $\widetilde{t}$ greater than unity for all flow processes over the range of conditions considered. However, care needs to be taken for studies involving bluff body separated flows, as the values of $\widetilde{t}$ lie between 1.3 and 1.8. This requires data acquisition to be limited to the very end of the test gas slug. All other flow processes have values of $\widetilde{t} > 2.3$ for the range of conditions considered. This implies that more than half of the test gas slug will convect over the test model under fully-established steady conditions. It is also important to note that the correlated values of K were developed in a shock tube environment where the flow was impulsively started after the passage of a shock. An expansion tube differs in that after the passage of the secondary shock, the arrival of the test gas flow is preceded by the expansion gas. This effectively reduces the flow establishment times of expansion tube flows to as much as 2/3 of that predicted by the shock tube experiments [122].

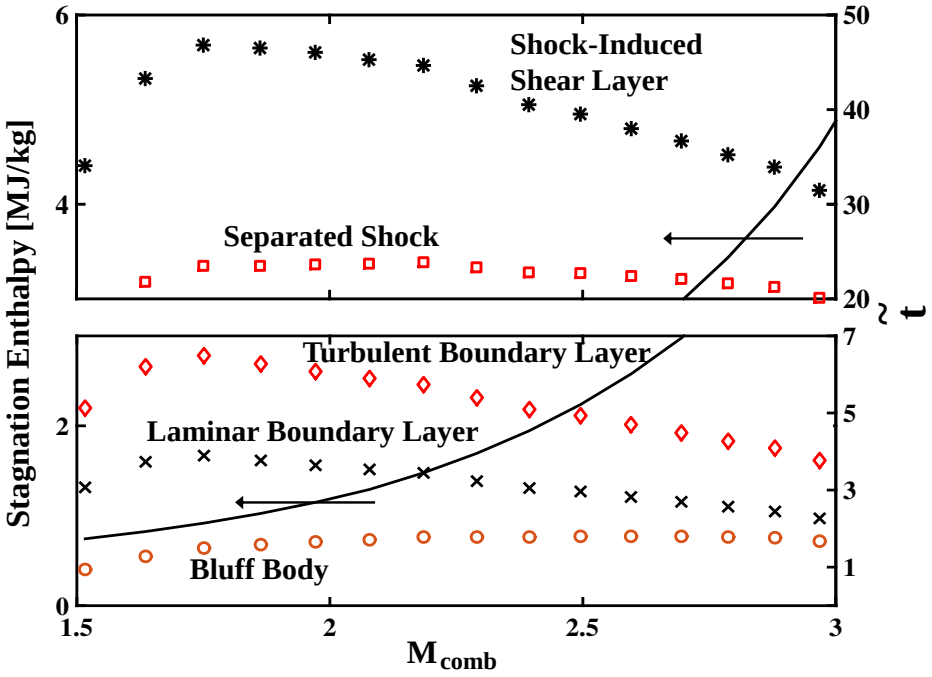

Figure 4.9: Flow establishment time (symbols) and stagnation enthalpy (solid curve) over a range of combustor inlet Mach numbers.

Typically, the flow over a test model will involve a combination of the unit flow processes. Therefore, the total flow establishment time can be conservatively approximated to be a linear combination of all of the individual relevant unit flow processes. The total establishment time, t_{total} would then be,

$$t_{total} = \sum_i C_i t_{e_i} \tag{4.7}$$

where $0 < C_i \leq 1$. Values of C_i would be very challenging to measure experimentally, and the most conservative value would be one. The reasoning behind this expression is based on the idea that the individual unit flow processes will affect one another while simultaneously adjusting to the ideally impulsively started test gas flow.

4.4 Facility Characterization

The use of ground test facilities to replicate flight conditions is an effective means to understanding governing processes controlling scramjet performance. However, in order to accurately interpret any experimental test data, a sufficient understanding of the generated test flow properties and characteristics is required to isolate facility induced effects on processes being studied such as mixing, ignition, and flame-holding. Therefore, an investigation and subsequent evaluation of the aerothermal properties and impact of expansion tube non-idealities on the generated flows was carried out. In particular, a series of experiments were carried out to analyze shot-to-shot repeatability, temporal and spatial test gas uniformity, boundary layer properties, and the presence of flow disturbances. Furthermore, we define properties such as the core flow size and useful test time. Therefore, the present study provides the foundational groundwork necessary for future supersonic mixing and combustion experiments.

A total of three conditions were designed to span a range of properties accessible by the facility while maintaining relevance to the study of supersonic combustion. The first two are referred to as conditions A and B and correspond to Mach 6 and 8 flight, respectively. These flows have aerotherodynamic properties similar to the combustor entry conditions of the hypersonic test-vehicle in the recent HIFiRE Flight-2. During the test window of this experiment, the flight envelope consisted of flight Mach numbers ranging between 6 and 8.5 at a constant dynamic pressure of 86.2 kPa. Using this information, a method discussed in Appendix B was followed to estimate the resulting combustor entry properties used in this study. The third condition referred to as C, is a relatively lower enthalpy flow with a longer test time. It is of interest to the studies of processes that do not require high static temperatures and/or require longer test times. The longer test time was achieved by increasing the ratio of sound speeds a_1/a_4, which generates a relatively weaker set of incident waves and increases the time before the second expansion head is reflected off of the first

contact surface.

A detailed summary of various aerothermal flow properties, such as a comparison of those which were experimentally measured and computed based on the expansion tube solver, is given in Table 4.4, and will be discussed further in the subsequent sections. A representative set of the experimental results for all of the three conditions are presented to provide a relative comparison of their characteristics.

4.4.1 Time-History Measurements of Flow Properties

Since the test gas convects a considerable distance before reaching the test section, the growth of the boundary layer will cause non-uniform, axial variations in the test gas properties. According to the work of Mirels [133, 134], until the limiting distance between the shock and contact surface is reached, the effects that result from boundary layer growth are a function of both time and axial location along the tube. Since the limiting distance is not reached in any of the conditions of the present study, the measurements taking place in the test section during the test gas flow are affected by a combination of both temporal and axial variations within the test gas slug. In order to understand how these combined effects alter the test gas properties, pitot and static pressure measurements were simultaneously carried out to directly measure the test gas pressure and infer the flow Mach number.

An example of a simultaneous pitot-static pressure measurement for flow condition B is shown in Fig. 4.10. P_a is the mean static pressure over the useful test time and has a value of 49.1 kPa. The portion labeled I shows an increase in both static and pitot pressures, and corresponds to the arrival of the secondary shock. The portion labeled II corresponds to the flow of the expansion gas over the sensors. Since the Mach number of region (20) is nearly sonic before exiting the tube with $P_{20} > P_{10}$, the gas entering the test section behaves as a sonic underexpanded jet. Thus, the sensor is effectively located within the expansion fan of the underexpanded jet. The decrease

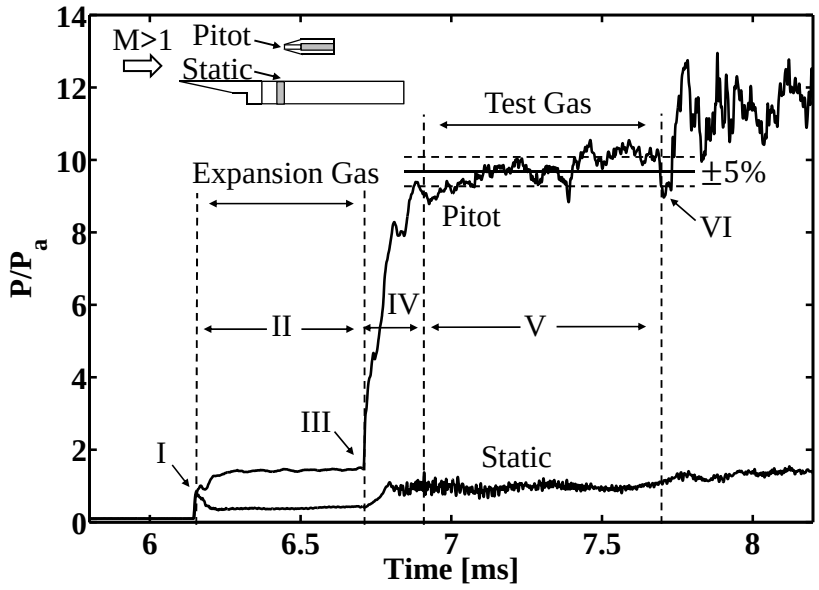

Figure 4.10: Time-history of simultaneous pitot-static pressure measurements. Data pertains to condition B.

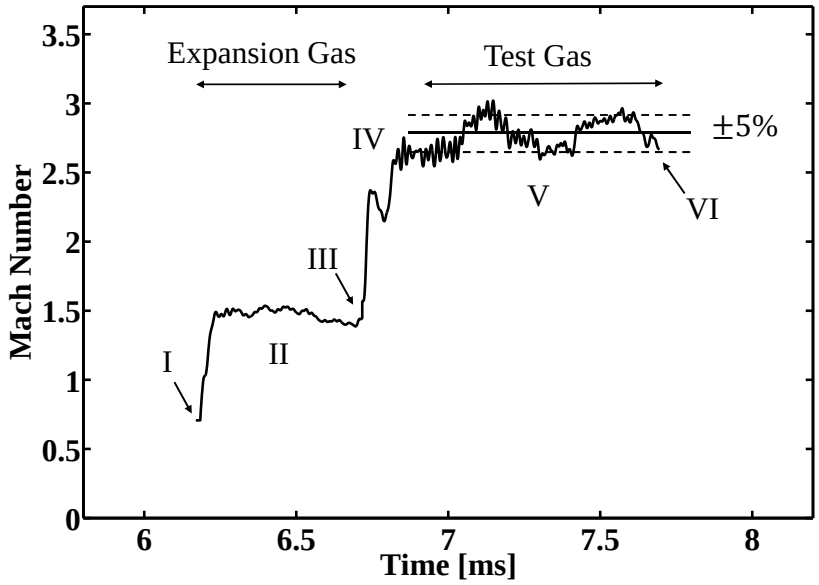

Figure 4.11: Inferred Mach number from pitot-static pressure measurements of Fig. 4.10. Data pertains to condition B.

in static pressure in location II compared to I is consistent with the expected lower pressure in the barrel shock of a sonic underexpanded jet[107, 108].

Since the Mach number of the expansion and test gas are different while pressure and flow speed are the same, the pitot traces allow us to more accurately identify the different regions of the flow. The increase in the measured pitot pressure indicated by the label III marks the arrival of the supersonic test gas. An increase in the static pressure is also observed and it results from the change in Mach angle of the expansion fan of the underexpanded jet, as the flow Mach number increases across the contact surface. The Mach angle decreases and creates a conical region of constant test gas properties (state ⑤) that envelops the sensor. This region of the flow outside of the expansion tube is referred to as the test gas core flow. The location of IV corresponds to a period of non-uniform flow over the sensors. During this time, we observe a number of coupled effects: 1) the effect of the finite thickness of the contact surface as it convects downstream [135–137]; 2) the transient process associated with the change in wave structure from the barrel shock of the initial sonic underexpanded expansion gas to the final underexpanded supersonic test gas flow; 3) the establishment process of the test gas flow; and 4) the limited response time of the pressure sensors. The pitot trace in region IV is an artifact of the combination of all these transient processes in addition to the delayed response time associated with the recessed mounted sensor in the pitot tube. This can be shown by considering the acoustic time through the pitot tube cavity, which can be approximated as the post-normal shock freestream sound speed divided by the length of the pitot tube cavity. For example, the acoustic time scale of the cavity is approximately 20 μs for condition B. Based on the duration of region IV from the pitot trace of Fig. 4.10, the time required for the pitot pressure to reach the test gas value is approximately 10 acoustic time scales. Following the transient flow of region IV is the uniform test gas flow labeled as V. This is the region of flow which we define as the useful test time and is specified as the region of the

flow in which the pitot trace remains to within ±5% of its average value. The test time is terminated by the arrival of any of the rarefaction waves labeled VI.

The increase in both pitot and static pressure over the test gas slug is evident from the measurements. The effect that this trend has on the test gas Mach number was found by using the Rayleigh pitot tube formula to infer the flow Mach number. An average value of γ between the pre- and post-normal shock values was used because of the weak dependence on gamma within the temperature ranges being studied. Figure 4.11 shows the time-history of the approximate flow Mach number as inferred by the simultaneous pitot-static pressure measurements of Fig. 4.10 for flow condition B. We postulate that the combined increase in static pressure and total pressure results in a flow with a nearly constant inferred Mach number. The increasing trend in measured pitot pressure is possibly the result of the secondary expansion wave processing a non-uniform gas in state ②, which results in an increase in total and static pressure in state ⑤. The non-uniformity in the shocked test gas in state ② results from the initial boundary layer growth induced by the primary shock-wave.

The temporal non-uniformity of the fluid in region ② can be seen more clearly in Fig. 4.12, which shows an example of the static pressure measured at three locations along the length of the tube for flow condition B. The pressure trace labeled S4 was acquired with the fourth shock counter of the driven section, which is located approximately 7.6 m downstream of the primary diaphragm (shown schematically by the inset of Fig. 4.12). At this fixed location, the pressure of the test gas in state ② initially has a value of ∼123 kPa (averaged over a small window after the arrival of the primary shock wave) and increases by 8% by the end of the slug. The trace labeled S5 corresponds to the static pressure measured by the first shock counter of the expansion section, which is located approximately 2 m downstream of the secondary diaphragm. At this fixed location, the trace shows that there is no pressure increase during the flow of the shocked expansion gas in state ⑳. However, there is an approximate 20%

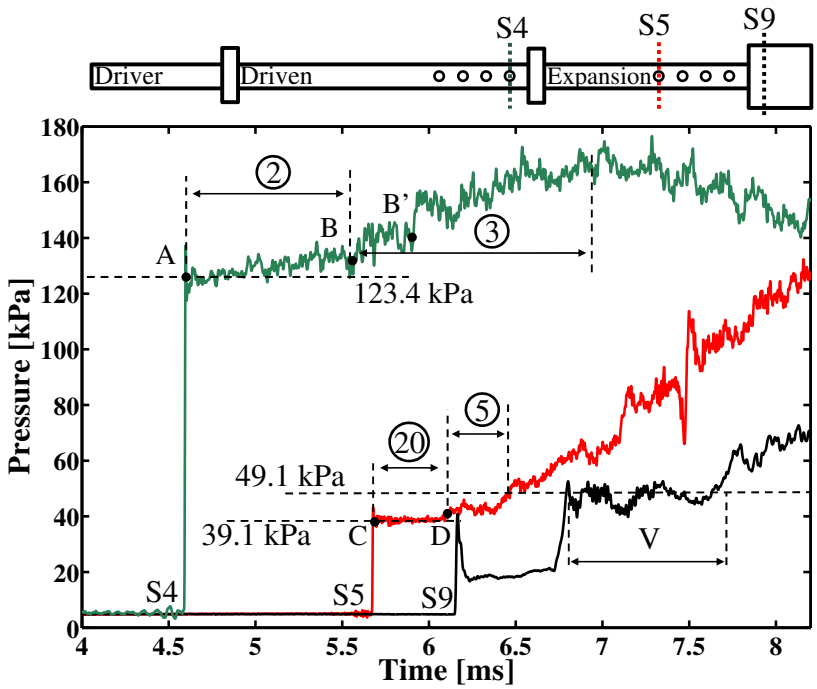

Figure 4.12: Static pressure measured at three locations along the expansion tube. Data refers to flow condition B.

increase in pressure over the test gas slug in state ⑤ before the second expansion tail arrives at this location. Finally, the trace labeled S9 was acquired in the test section approximately 3.1 m downstream of the secondary diaphragm using the same assembly described previously in Fig. 4.10. At this location, the test gas pressure varies by approximately ±7% of its average value of 49.1 kPa over the slug of fluid in state ⑤.

The points labeled A through D on the pressure traces of Fig. 4.12 indicate the arrival of either a compression wave or contact surface. The corresponding points are labeled in the computed x-t diagram of flow condition B, shown in Fig. 4.13. The x-t diagram was computed using the known fill pressures and experimentally measured shock speeds as inputs to a solver which computes the various state properties. The thermodynamic states are then used to compute the wave trajectories using the method of characteristics and unsteady shock wave theory [114]. The trajectories of the contact surfaces are corrected to incorporate the effects of viscosity through the

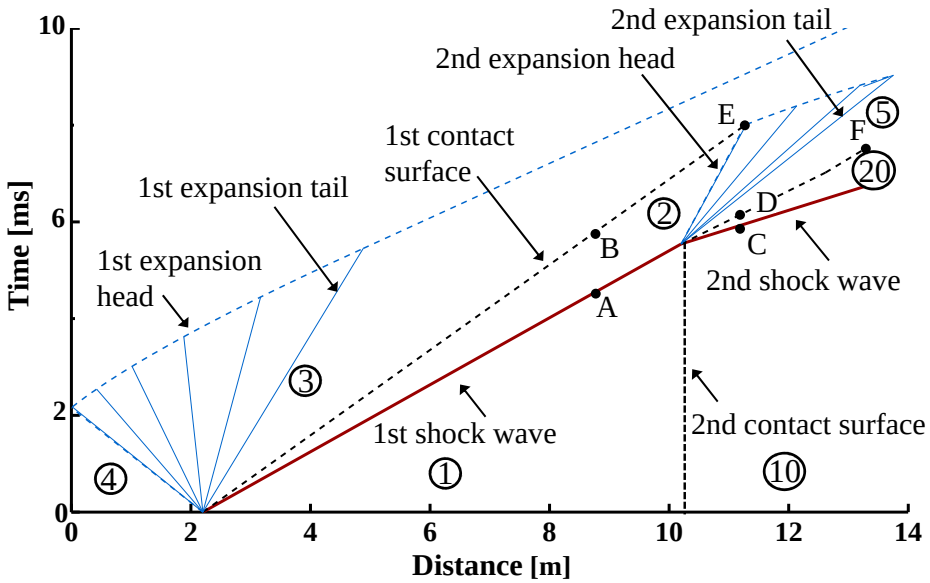

Figure 4.13: Computed spacetime diagram of the wave trajectories during the operation of MHExT for flow condition B.

Condition	A	B	C
Experimental [μs]	950	920	5540
Mirels [μs]	880	940	5450
Inviscid [μs]	1280	1120	5650

Table 4.3: Comparison of the generated test time for three flow conditions.

work of Mirels [133, 134]. The trends of the pressure traces were found to agree well with the computed times of arrival of the shocks and contact surfaces. For example, point A indicates the arrival of the primary shock and hence a step-change in pressure. Point B indicates the arrival of the first contact surface, which is followed by a gradual increase in pressure from the gas in state ③.

The point labeled B' in Fig. 4.12 indicates the computed time of arrival of the first contact surface based on inviscid considerations. For this condition, the inviscid calculation underestimates the speed of the contact surface by approximately 30%. A comparison of the nominal slug lengths of gas in states ② and ⑳ is shown in Fig. 4.14.

The results obtained using three methods are shown for both conditions A (solid) and B (dash). The time of arrival between the shock and contact surface is normalized by the corresponding nominal inviscid gas speed. The experimentally measured values are an average over three shots, and were extracted from eight shock counters along the tube's length. The arrival of the contact surface is delineated by a distinct rise and periodic fluctuation in pressure as can be seen in the S4 trace of Fig. 4.12. The results reveal how the inviscid calculations systematically underestimate the speed of the contact surface, which in reality accelerates. On the other hand, the solution using the model of Mirels [133, 134] is in good agreement with the experimentally measured values. The remaining discrepancies may be due to a combination of the uncertainty in the measurement technique as well as the fact that the viscous correction was based on the assumption that the boundary layer was fully turbulent in states ② and ⑳, whereas theory for a transitional boundary layer may be more appropriate for these conditions.

The formation of the boundary layer acts as an aerodynamic sink that absorbs mass from the core flow. In order to conserve mass, the contact surface accelerates reducing its distance from the shock wave. This is observed to have a significant consequence on the test time since the reflection of the secondary expansion head off of the first contact surface (point E in Fig. 4.13) is usually the process that limits the test time. Effectively, the presence of boundary layer growth in states ② and ⑳ causes points E and F in Fig. 4.13 to occur earlier. In turn, the accelerating first and second contact surfaces have a competing effect to reduce and increase the test time, respectively. Generally, the effect induced by the acceleration of the first contact surface outweighs the effect induced by the acceleration of the second. This results in an overall reduction in the available test time as compared to the inviscid solution. This is shown in Table 4.3, where a comparison of the test times for all three conditions is presented by comparing them through three methods.

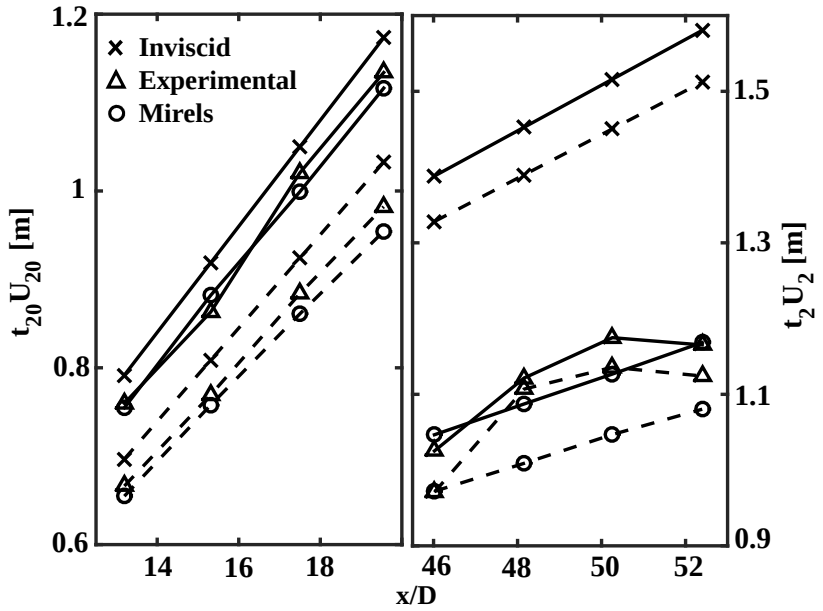

Figure 4.14: Comparison of state 20 (left) and state 2 (right) nominal slug lengths using three methods (Inviscid, Experimental, and Mirels) for conditions A (solid) and B (dash).

The solution based on Mirels's work is obtained by treating the expansion tube as two separate shock tubes. In short, the computed test time is obtained by solving for the corrected locations of points E and F in Fig 4.13. This formulation neglects any effect that the secondary expansion wave has on the boundary layer. Therefore, since the results of this analysis show a satisfactory agreement between the test time obtained experimentally and with Mirels's solution, we infer that the effects of the secondary expansion wave on the trajectory of the waves may be minimal.

4.4.2 Summary of Average Bulk Flow Conditions

A summary of the initial and resulting test gas bulk flow properties for each of the three selected test conditions is given in Table 4.4. The indicated uncertainties are based on a total of 15 runs for each condition where the only exception is the measured Mach number, which was analyzed over a fewer number of runs. The final aerothermal bulk properties of the test gas are a function of the measured shock speeds (primary and secondary) and the initial fill conditions (composition, pressure,

and temperature). Properties labeled as "semi-theoretical" were computed based on these parameters using the expansion tube solver. On the other hand, properties labeled as "measured" were acquired directly through the use of fast-response pressure sensors. Finally, the method of characteristics and unsteady shock wave theory are used to compute the theoretical test time using knowledge of the initial fill parameters and lengths of each of the three sections.

The indicated uncertainties (presented as percentages of the corresponding mean value) are defined based on the standard deviation between runs. Thus, they represent a shot-to-shot variation and not spatial and/or temporal uncertainty in the measurement method used since their contribution to the overall uncertainty budget was found to be inconsequential. For "measured" aerothermal properties (Mach number and static pressure) in region ⑤ of Fig. 4.13, the reported uncertainties are based on the temporal average and root-mean-square values computed over the useful test time.

The static pressure measured through the tube wall corresponds to a combined temporal average over the four shock counters in the expansion section. The average is over a period of time just after the passage of the secondary shock until a time in which the flow remains unaffected by the effects of boundary layer growth. An example of this is shown in region ⑳ of Fig. 4.12. This is an indirect measure of the test gas pressure under ideal inviscid conditions, because it relies on the validity of the assumption of continuity in pressure imposed by the necessary kinematic constraints between regions ⑳ and ⑤. The static pressure measured in the test section is a temporal average of the test gas in region ⑤ over the useful test time indicated by region V in Fig. 4.12. The static pressure measured in the test section of region ⑤ is always greater than the what is measured at the tube wall as a result of boundary layer growth. Nevertheless, the "semi-theoretical" value of static pressure agrees very well with the pressure measured at the tube wall just after the passage of the shock

Condition	A	B	C
Initial Setup			
Composition [Driver Driven Expansion]	[He Air He]	[He Air He]	[Air Ar He]
Driver Fill Pressure [kPa]	1896	1724	586
Driven Fill Pressure [torr]	74.3	45.4	82.8
Expansion Fill Pressure [torr]	148.2	36.6	50.2
Test Gas Properties			
Nominal Flight Mach Number	6	8	NA
Primary Shock Speed [m/s]*	1351 ± 0.5%	1442 ± 0.6%	696 ± 0.3%
Secondary Shock Speed [m/s]*	2160 ± 0.2%	2585 ± 0.5%	1562 ± 0.3%
Mach Number*	2.07 ± 0.6%	2.75 ± 0.9%	1.73 ± 3.3%
Mach Number‡	2.05 ± 0.5%	2.76 ± 0.6%	1.76 ± 0.6%
Static Pressure (Test Section) [kPa]*	122.4 ± 0.9%	49.1 ± 0.9%	25.6 ± 0.5%
Static Pressure (Tube Wall) ⑳ [kPa]*	107.6 ± 0.4%	39.1 ± 0.8%	18.3 ± 0.6%
Static Pressure [kPa]‡	106.1 ± 0.4%	38.0 ± 0.9%	18.0 ± 0.7%
Test Time (Total) [μs]*	950 ± 5.0%	920 ± 8.8%	5540 ± 1.8%
Test Time (Useful) [μs]*	550 ± 7.9%	690 ± 19%	4570 ± 13%
Test Time (Mirels) [μs]$^\diamond$	880	940	5450
Stagnation Enthalpy [MJ/kg]‡	1.92 ± 0.3%	2.37 ± 0.6%	0.44 ± 0.7%
Static Temperature [K]‡	980 ± 0.5%	910 ± 0.7%	420 ± 0.3%
Velocity [m/s]‡	1259 ± 0.3%	1637 ± 0.7%	673 ± 0.7%
Reynolds Number‡	8×10^7	1×10^8	7×10^5
Secondary Diaphragm Accel. [m/s^2]‡	4×10^8	3×10^8	7×10^7

Table 4.4: Summary of the MHExT performance based on a statistical analysis of the shot-to-shot variability. Aerothermodynamic properties pertain to the test gas (region 5) unless otherwise noted. *Measured quantity; ‡ Semi-theoretical quantity; $^\diamond$Theoretical quantity.

waves. This shows that the expansion tube solver is able to accurately compute the gas pressure when viscous effects are neglected.

The measured property "total test time" in Table 4.4 refers to the time between the arrival of the test gas (III) and the arrival of any of the rarefaction waves (VI) labeled in Fig. 4.10. This is the ideal length of the test time if the contact surface were truly discontinuous and if viscous effects were negligible. On the other hand, the measured property "useful test time" refers to region V and corresponds to the region of the flow in which the pitot trace remains to within ±5% of its average value.

There are a number of conclusions that can be drawn from the information pro-

vided in Table 4.4. First, the shot-to-shot variability in the measured shock speeds is only a fraction of a percent. This is a result of repeatable initial filling of each section with the desired composition and pressure before each run; the close control over the initiation of the run; and the clean rupturing of the diaphragms which minimizes flow disturbances. The consequences of the shot-to-shot variability in the measured shock speeds on the final bulk test gas properties are shown by the properties labeled "semi-theoretical" because their values depend on the measured shock speeds. Secondly, the measured properties such as Mach number compare well with their corresponding semi-theoretical properties. Although the measured values of pressure used to infer the test gas Mach number in region V are greater than the ideal inviscid values, the Mach number during V compares well with the semi-theoretical calculation.

4.4.3 Time-History of Flow Mach Number from Schlieren Imaging

To visually evaluate the temporal evolution of the flow, a standard Z-type schlieren system was set up to acquire kHz-rate schlieren images of the generated flow field as it developed over a 20° wedge. Static pressure measurements downstream of the oblique shock were simultaneously acquired through a recessed-mounted fast-response piezoelectric pressure transducer instrumented inside the wedge. The captured images were reduced by removing dark noise and normalizing by the mean illumination field with no flow.

An example of two processed images extracted from the schlieren movie at different instances during the evolution of the flow are shown in Fig. 4.15. The pair of images, which pertain to flow condition B, are overlaid by a schematic of the wedge including the position of an internally mounted static pressure sensor. The first image in Fig. 4.15(a) shows the flow field during the passage of the contact surface (IV). The supersonic flow is just beginning to flow over the wedge and form a shock wave.

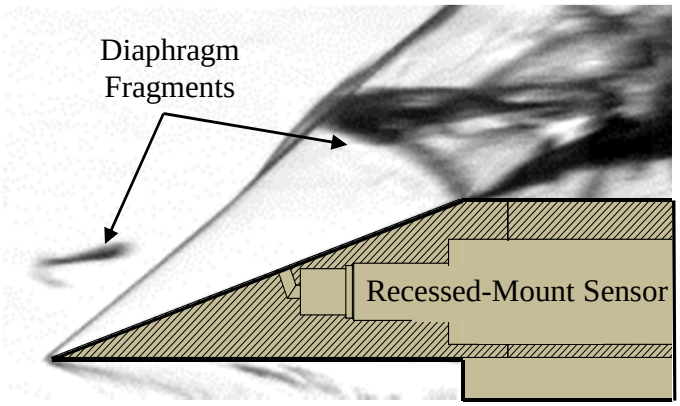

(a)

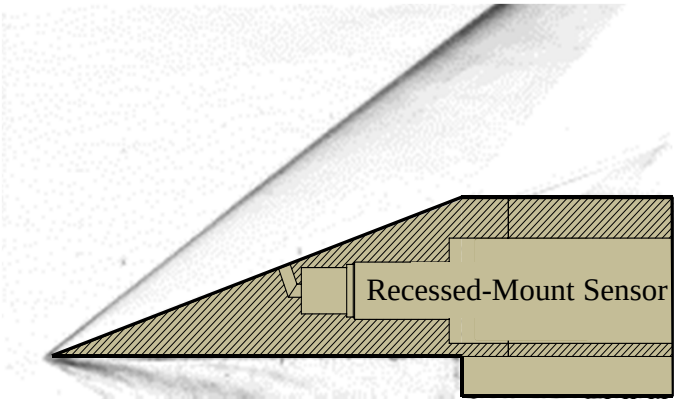

(b)

Figure 4.15: Instantaneous snapshots of the flow structure around a 20° wedge during (a) passage of the contact surface (IV) and (b) useful test time (V). Data refers to flow condition B.

Some diaphragm debris are also visible in this particular case. The second image in Fig. 4.15(b) shows the flow field as the supersonic test gas flows over the wedge during the useful test time (V).

From each schlieren image composing the movie for a run, a spatially averaged Mach number of the flow upstream of the oblique shock was computed by measuring the wave angle and using the solution for oblique shock waves (for constant γ) [114]. A value of γ equal to the average between the values across the oblique shock was used. Fig.4.16 shows a time-history of the inferred flow Mach number upstream of the oblique shock (M_5) for flow condition B. The vertical and horizontal error bars correspond to uncertainties in measuring the oblique shock angle and temporally correlating the images to the pressure trace, respectively. The results show a region of uniform test gas flow where the standard deviation of the Mach number during the useful test time (V) is 0.7% of the mean value. On average, the measured oblique shock angle during the useful test time was 38.9 degrees which corresponds to a value of $M_5 = 2.76$. The uncertainty in measuring the wave angle translates to $\pm 1.5\%$ of M_5. This measured value of M_5 agrees well with the computed semi-theoretical value as well as the Mach number inferred from the simultaneously measured pitot-static pressure measurements.

Fig. 4.17 shows the corresponding time-history of the static pressure measured on the surface of the wedge downstream of the oblique shock (flow condition B); labels identify the main phases of the flow evolution described previously. The measured time-average static pressure on the surface of the wedge during the useful test time was 165 kPa which corresponds to a pre-shocked static pressure of 50 kPa. This value is 2% larger than the measured value using the pitot-static probe assembly. The same method was used to infer the test gas Mach number for flow condition A which was found to be 1.96. This value is 4.3% less than the computed semi-theoretical value of 2.05. The measured time-averaged static pressure during the useful test time was

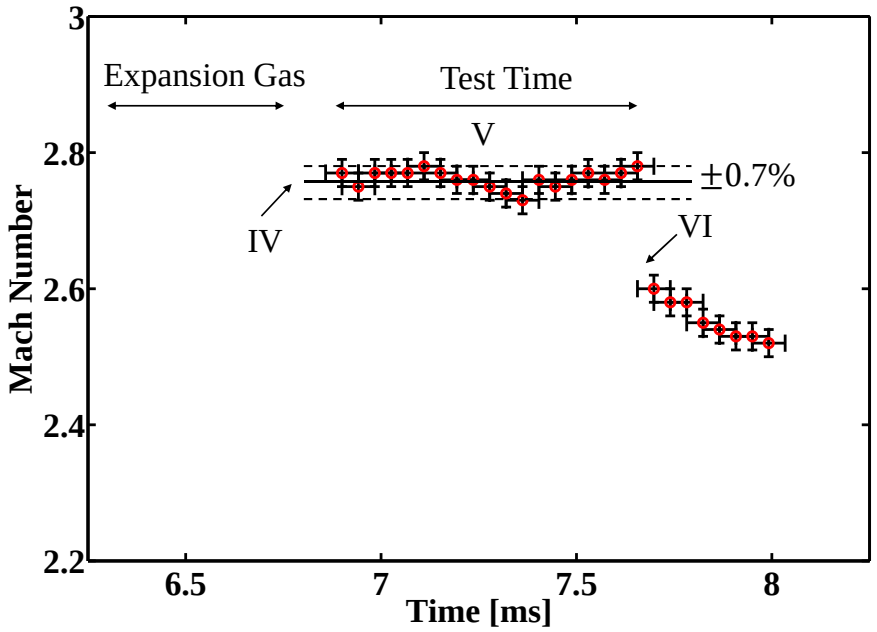

Figure 4.16: Inferred gas Mach number based on measured oblique shock angle. Data pertains to Condition B.

317 kPa, which corresponds to a pre-shock static pressure of 118 kPa. This value is 3.5% lower than the measured value using the pitot-static probe assembly. This method was not used to measure the test gas Mach number for condition C because the lower test gas Mach number results in a detached oblique shock wave. Based on the limited cases considered here, it appears that this approach might tend to consistently underestimate the measured value of flow Mach number compared to the pitot-static assembly.

The experimental methods used in this study to indirectly measure or infer test gas properties have also been used in other facilities. Strand et al. [136] took measurements of flow properties in expansion tube flows, such as flow temperature and speed, using both direct and indirect methods similar to those used here. They found good agreement between the two methods, thus demonstrating that the type of measurements used in this study are capable of accurately capturing the bulk properties of the generated flows.

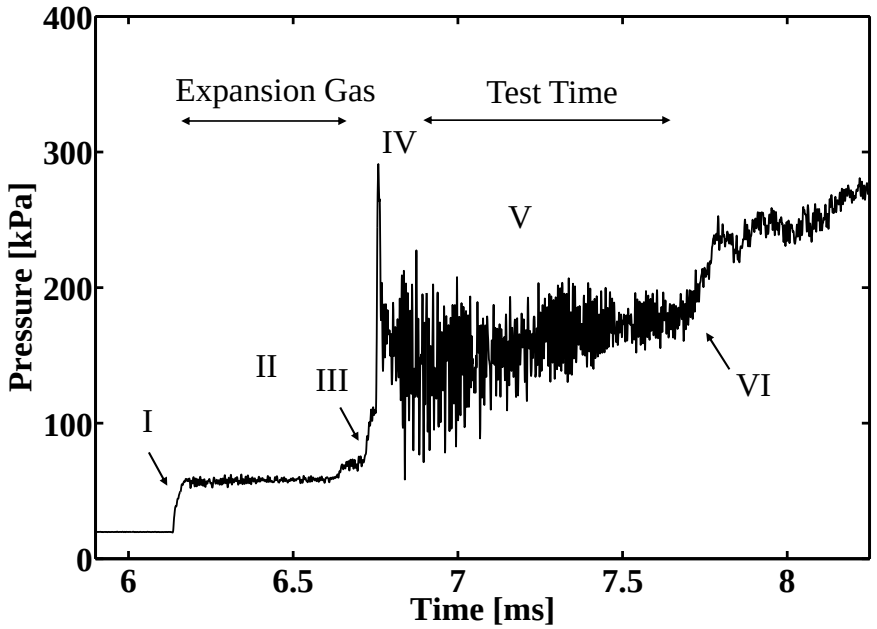

Figure 4.17: Static pressure measured on wedge surface. Data pertains to Condition B.

4.4.4 Spatial Uniformity of Flow

Since the test gas travels several tube diameters before it reaches the test section, the growth of the boundary layer has a significant effect on the radial uniformity of the flow properties and the size of the core flow. Therefore, it is important to evaluate the effective core size of the flow and how test gas properties vary along the radial direction of the flow during the useful test time. The radial distribution of properties were obtained by using a pitot rake assembly fixed in the test section approximately 3 mm from tube exit plane to ensure that the sensors were always within the test gas core flow.

For each experimental run, pitot pressure measurements were temporally averaged over the useful test time to construct radial profiles of mean quantities. Typical time-history measurements taken simultaneously at four radial locations across the diameter of the tube for Condition A is shown in Fig. 4.18(a). P_a is the mean static pressure over the useful test time and has a value of 122.4 kPa. The roman numerals correspond to the description outlined in the previous section. The pitot

measurements taken at positions $r/R = 0$, and ± 0.4 are shown to lie within the core flow. These three traces have the same average value over the test time, and they also qualitatively have the same temporal evolution, including the small time-scale variations of pitot pressure observed during the evolution. More specifically, the cross-correlation coefficients computed from the pitot pressure traces within the core flow have a value very close to unity. These observations indicate that the core flow has some degree of radial homogeneity and that whatever feature causes the small time-scale variations is fairly planar. On the other hand, the pitot probe located at $r/R = 0.8$ exemplifies a trace of the pitot pressure at a point that is in the boundary layer of the flow. Within the boundary layer the value of the mean pitot pressure is lower than in the core (lower Mach number), the magnitude of the temporal fluctuations are larger, and the temporal evolution is poorly correlated to those measured within the core.

The radial profile of the temporally averaged pitot pressures for condition A is shown in Fig. 4.18(b). The x-axis of the figure is normalized by the inner radius of the tube, and the y-axis was normalized by an average measured static pressure value of $P_a = 122.4$ kPa (see Table 4.4). The error bars correspond to the temporal standard deviation measured over the useful test time. From these measurements we can now quantify the size of the useful core flow, which is defined as the region where the value of the pitot pressure is within an acceptable range about the mean value. For case A, the useful core flow was found to span 70% of the inner diameter of the tube. The standard deviation of the temporally averaged values (circular symbols) in the useful core region was found to be within $\pm 3.3\%$ of their mean value, which is equal to $7.0 P_a$. A similar procedure was followed for flow conditions B and C and the resulting mean radial profiles (during the useful test time) are shown in Fig. 4.19. The results show that for all three cases, the flow properties across the tube diameter remain to within $\pm 5\%$ of the mean value in the useful core flow, which spans approximately 2/3 of

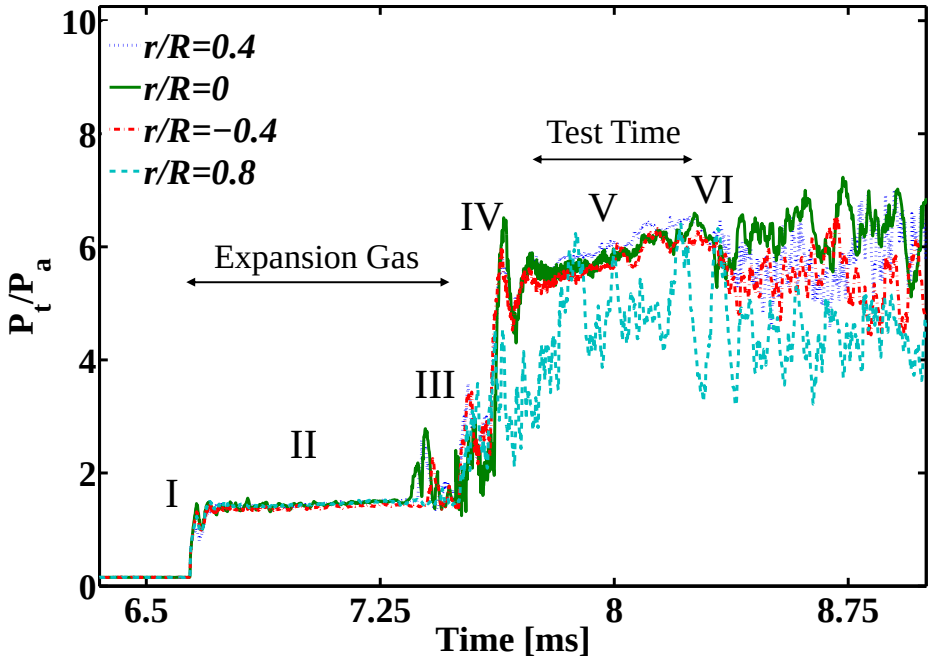

(a)

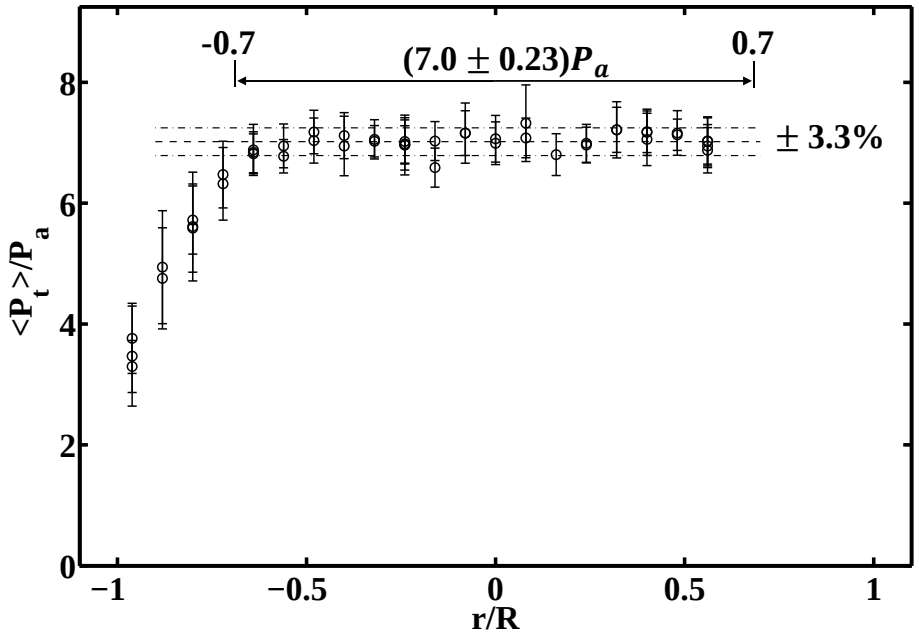

(b)

Figure 4.18: (a) Time-history of pitot pressure measurements at four radial locations. (b) Temporally averaged radial pitot profile. Data pertains to Condition A.

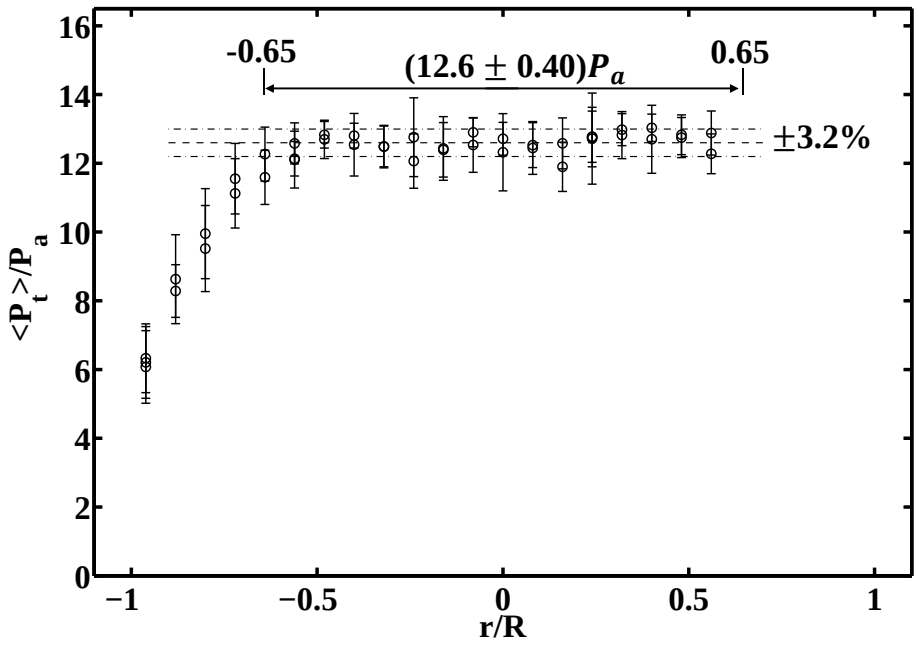

(a)

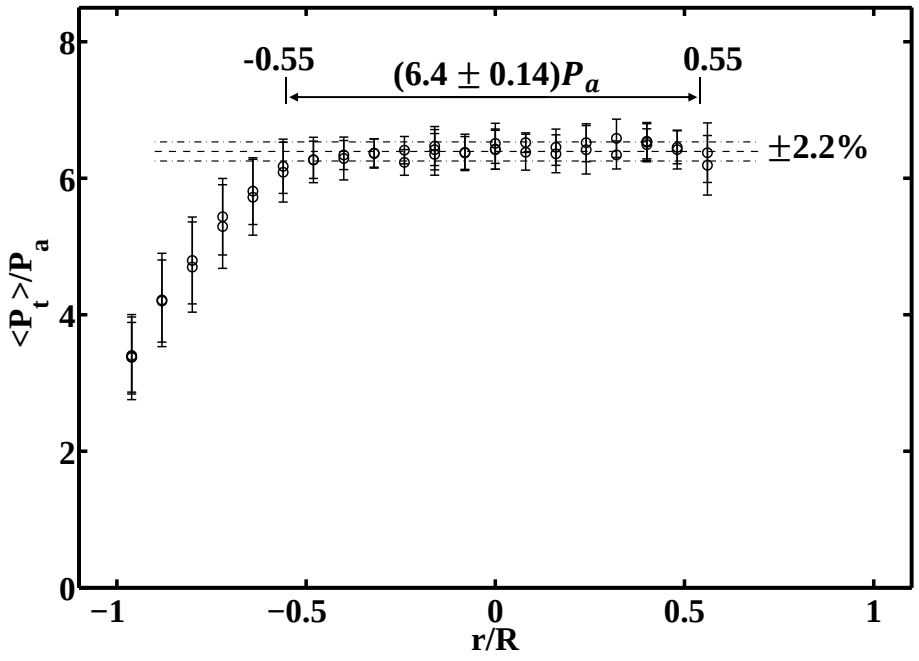

(b)

Figure 4.19: Temporally averaged radial pitot profiles for conditions (a) B and (b) C.

the tube diameter. There is however a small variation of the effective useful core size among the cases; the useful core size increases with increasing test gas pressure and was not found to correlate with Reynolds number.

4.4.5 Boundary Layer Properties

The acquired pitot profile data was used to further characterize the test gas boundary layer. The computed flow Reynolds number, based on the bulk freestream properties and tube diameter, for each condition is tabulated in Table 4.4 for reference. Based on the work of Ref. [138], the transitional Reynolds number depends on the ratio of the wall-to-freestream temperatures, Mach number of the flow relative to the wall, and the ratio of the shock speed and the freestream speed in the shock-fixed coordinates. The transition Reynolds number was found to range between values of 5×10^5 and 5×10^7, which encompasses the Reynolds number values of this study. Therefore, the test gas boundary layers in this study are assumed to be turbulent.

By assuming that the static pressure is constant along the radial direction, approximate radial distributions of the temperature $T(r)$ and flow speed $U(r)$ were computed from the measured pitot pressure assuming that temperature and flow speed are related by the Crocco-Busemann relation (assuming unity Prandtl number):

$$T(r) = T_w + (T_{aw} - T_w)\frac{U(r)}{U_5} - \frac{1}{2}\frac{(\gamma-1)}{\gamma}\frac{U(r)^2}{\mathcal{R}} \tag{4.8}$$

where the local speed is computed from the local Mach number $M(r)$ given from the measured pitot pressure using the Rayleigh pitot formula as:

$$U(r) = M(r)\sqrt{\gamma\mathcal{R}T(r)} \tag{4.9}$$

Here r is the radial distance from the centerline of the tube; T_w and T_{aw} are the wall and adiabatic wall temperatures respectively; and U_5 and $\mathcal{R}$ are the test gas freestream

speed and gas constant, respectively [114, 139]. Owing to the short duration of the experiments, the wall temperature was taken to be room temperature. In addition, the estimated radial profile of the flow speed was then fit to an approximation profile. Assuming that the boundary layers are turbulent, a $1/7^{th}$ power law approximation was used [139]:

$$\frac{U(r)}{U_5} = \begin{cases} 1, & r < R - \delta, \\ \left(\frac{R-r}{\delta}\right)^{1/7}, & r > R - \delta \end{cases} \tag{4.10}$$

where δ is the boundary layer thickness corresponding to $U/U_5 = 0.99$ and it was found by a least-squares fitting of the measured radial profile to Eqn. 4.10.

Fig. 4.20(a) shows the resulting normalized radial profile of flow speed as a function of distance from the wall for the three cases. The distances from the wall for each condition are normalized by the corresponding boundary layer thickness δ_i ($i = \mathrm{A}, \mathrm{B}, \text{and } \mathrm{C}$). The $1/7^{th}$ power law is also plotted and can be seen to describe the speed profiles quite well. The resulting average boundary layer thicknesses δ_i/R over the test time for conditions A, B, and C are 0.46, 0.43, and 0.51, respectively. The estimated thicknesses were not found to scale with the flow Reynolds number. The results of this procedure give a more conservative estimate of the useful core flow size as compared to the method defined in the previous section. Nevertheless, the two methods are in acceptable agreement.

This method is also used to evaluate the radial distribution of other quantities of interest defining the test gas properties. Fig. 4.20(b) shows the corresponding radial profiles of temperature for each of the cases. The temperature profile for condition A has a monotonic behavior from the freestream through the boundary layer. On the other hand, the boundary layer temperature for condition B increases past the freestream value because of the relatively larger freestream speed of the flow. The same non-monotonic behavior is observed for condition C, where this time the relatively lower specific heat of the Argon test gas allows the transfer of energy to

more readily increase the gas temperature within the boundary layer.

It is also of interest to gain insight regarding the temporal evolution of the boundary layer. The useful test time was divided into segments of duration Δt and the boundary layer thickness was extracted using the procedure described above from the average pitot pressure over the time segment. Δt was taken to to be 1/50 of the total useful test time. In this manner, the boundary layer thickness for each condition δ_i was computed as a function of time. The results are illustrated in Fig. 4.21, where $\hat{t}$ is the time elapsed from the start of the test time normalized by the total useful test time for each respective flow condition.

It is difficult to discern a boundary layer growth rate for condition A. This is a consequence of the relatively short test time which is approximately 1/9 of that of condition C. On the other hand, the results for conditions B and C reveal the behavior of the boundary layer as it grows over the test gas slug. It can also be seen that by the end of the test time, the flow for condition C has almost reached a state that is of a fully-developed pipe flow (i.e., $\delta_C \to R$).

4.4.6 Flow Disturbances

A potential inherent limitation of expansion tube facilities is the presence of flow disturbances, which are observed in the form of significant pressure fluctuations in the final test gas, and limit the range of accessible conditions to only those with an acceptably steady test flow. The work of Paull and Stalker [140] showed that disturbances could be sufficiently modeled as first-order lateral acoustic waves. They postulated that the flow disturbances originate in the driver gas as a result of the primary diaphragm rupturing process. They define two limits in which an expansion tube facility may be operated: the high-enthalpy and low-enthalpy condition limits. The former is defined as when the sound speed of the shocked test gas is greater than that of the expanded driver gas, $a_2/a_3 > 1$. Whereas the latter is when the facility is

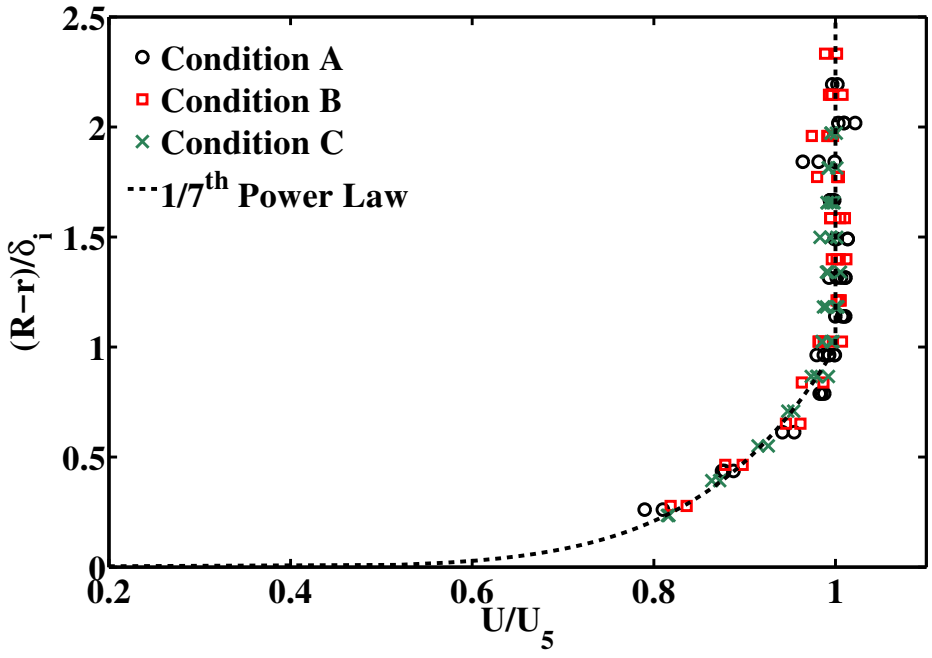

(a)

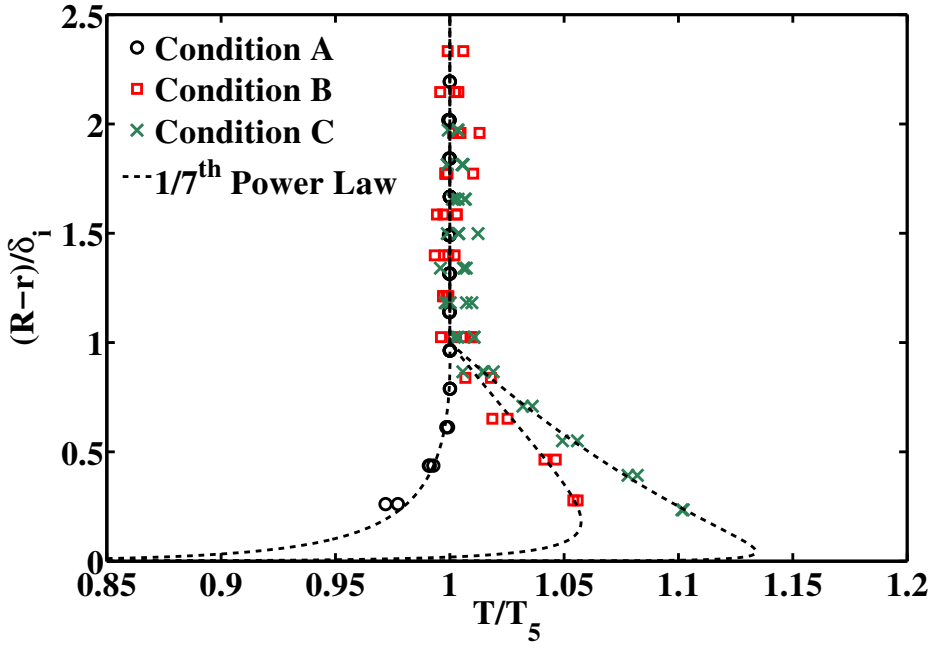

(b)

Figure 4.20: (a) Radial profiles of test gas speed compared to the $1/7^{th}$ power law approximation. (b) Radial profiles of test gas temperature.

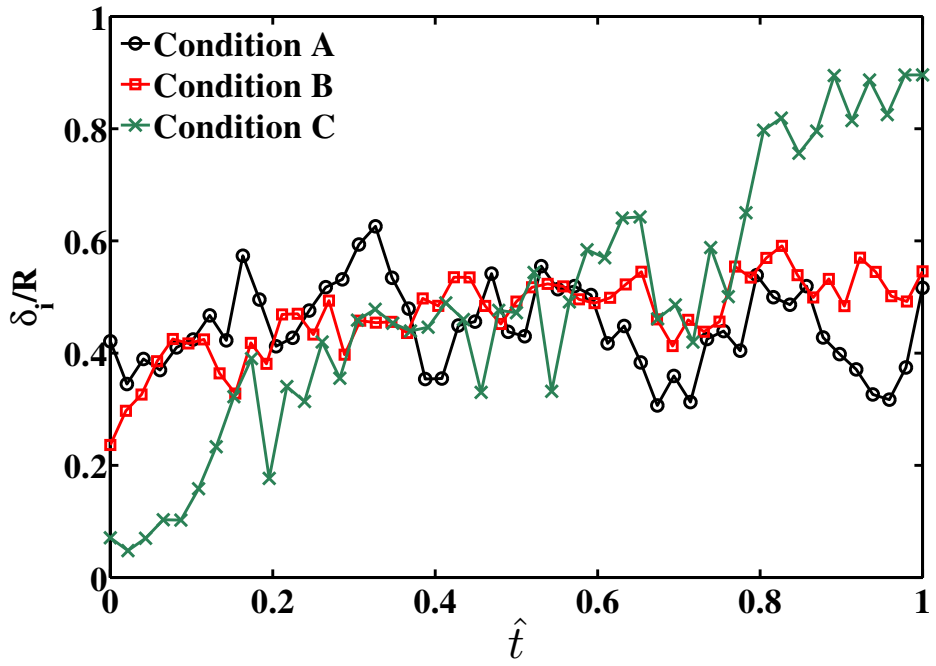

Figure 4.21: Boundary layer thickness as a function of time during the test gas flow.

operated such that $a_2/a_3 < 1$.

There are two effects that one should consider regarding flow disturbances due to lateral waves. The first one is the extent in which disturbances are transmitted across an interface. In the case of a high-enthalpy condition, noise transmission through the contact surface is attenuated by increasing the ratio of a_2/a_3. The degree this ratio must be greater than unity reduces as a_3 increases because the contact surface behaves as a low-frequency filter, where the extent of noise filtering/attenuation increases with the ratio a_2/a_3 and a_3.

The second effect is the focusing of the range of frequencies of noise transmitted into the test gas. Frequency focusing occurs as the test gas is processed by the secondary unsteady expansion wave. This results in a final test gas flow with a noticeable narrow bandwidth noise, which can cause the test gas flow to be of limited use. Frequency focusing is mostly a concern when operating in the low-enthalpy regime, since noise will have more readily been transmitted into the test gas upon rupturing the primary diaphragm. They will then focus to unacceptable levels after

being processed by the secondary expansion wave. In the laboratory reference frame, the dominant frequency in which noise is focused to across the secondary expansion wave is given by:

$$\nu = \frac{\lambda \left(a_2 + \frac{\gamma_2 - 1}{2} U_2\right)}{2\pi \left[1 - \left(\frac{\gamma_2 - 1}{2}\right)^2\right]^{1/2}} \tag{4.11}$$

where γ_2 and U_2 are the ratio of specific heats and flow speed in region ②, and λ is the set of permissible values given by the infinite number of solutions of $J_1(\lambda R) = 0$, except for $\lambda R = 0$; J_1 is the first-order Bessel function of the first kind and R is the inner radius of the tube.

For the flow conditions used in this study, the values of a_2/a_3 were 1.0, 1.1, and 1.9, for flow conditions A, B, and C, respectively. These three conditions lie within the high enthalpy regime of the expansion tube operating limits, using the definition described earlier. Therefore, one would expect a limited amount of noise transmitted into the test gas, and a negligible amount of focusing of the noise after being processed by the secondary expansion wave. The resulting focus frequencies (using Eq. 4.11) for conditions A, B, and C are 7.1, 7.3, and 5.6 kHz, respectively. Figure 4.22 shows a spectral decomposition of the test gas for all three conditions. Moreover, the magnitude of disturbances with frequencies greater than 20 kHz are less than a value of 0.1 for all cases, indicating that greater pressure fluctuations are confined within a band in the lower frequency range. Although the conclusions are limited by the achievable spectral resolution, the calculated focus frequencies are not clearly apparent for any of the cases. Rather than a distinct frequency being amplified, a band of frequencies with relatively larger amplitudes are observed. However, the magnitudes are not sufficient enough to cause disturbances which render the test gas to be of no use. This is because the sound speed ratio across the secondary expansion a_5/a_2, was never lower than a value of 0.78 for any of the three conditions, resulting in a weak focusing effect. This is a similar observation to the one made in Ref. [141].

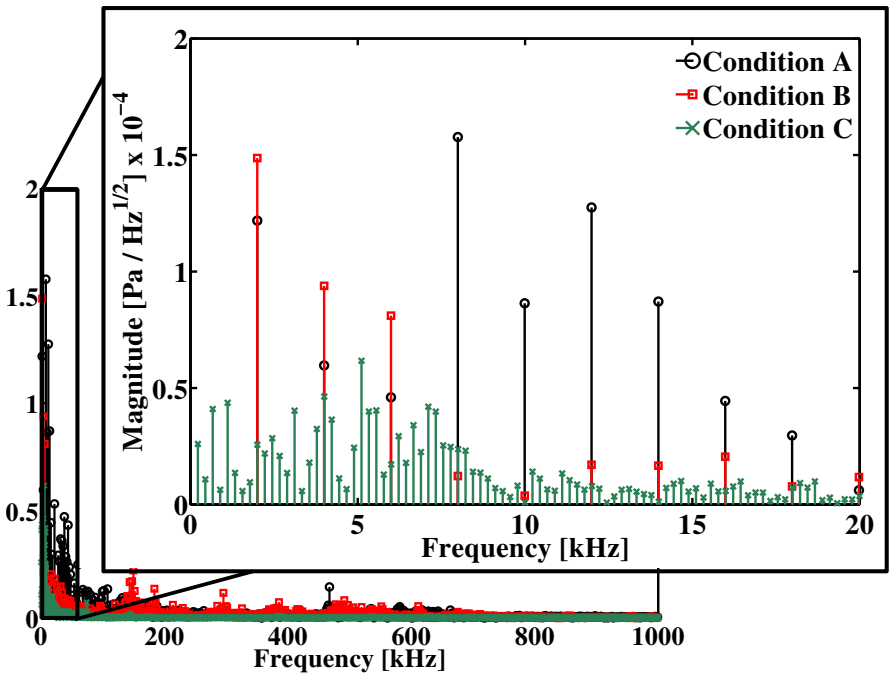

Figure 4.22: Spectral decomposition of test gas pitot pressure traces for three flow conditions.

4.5 Test Model Induced Interference Effects

The operation of an expansion tube relies on a series of unsteady shock and expansion waves to generate a high-enthalpy supersonic flow. This type of flow facility has several advantages over others in its ability to generate a wide range of high-enthalpy flow conditions. However, the range of accessible flow conditions is ultimately limited by a combination of undesired effects, such as flow disturbances, boundary layer growth, limited core flow size, and short test times. In addition to these undesired effects, this portion of the dissertation reports on observations of non-ideal operation of impulse facilities that result in undesired test gas properties. The interference effect investigated here results from the interaction of the initial unsteady flow with models located in the test section, and induces a significant increase in test gas pressure and temperature at the beginning of the test time. Thus, the experimental flow conditions are altered from what was desired. The test-model induced interference effect is postulated to be caused by the secondary shock wave diffracting around the test article,

generating a series of compression waves that coalesce into an upstream-propagating shock wave, which we refer to as a disturbance wave. In some respect, it is analogous to test model blockage effects in steady flow facilities [142, 143]. However, the effects studied here are different from other flow disturbances discussed in Sec. 4.4.6; they also differ from test gas composition contamination in expansion tubes [144] and reflected shock tunnels [145–147]. Lastly, the results of this study are not limited to expansion tubes, but rather apply to any impulse facility operating under relevant conditions.

Under certain operating conditions with test models mounted inside the test section, a strong distortion of the test gas pressure time history measured in the test section (e.g., on models) has been observed, which effectively reduces the test time and alters the aerothermodynamic flow properties from what was desired. Fig. 4.23 shows the static pressure measured in the test section for a typical case where this effect is observed. The static pressure was measured with a flush-mounted PCB piezoelectric transducer inserted in a flat plate with the leading edge protruding 2.1 cm into the expansion section. After the initial phase where the secondary shock (I) and shocked expansion gas arrive (II), there is a rapid increase in pressure at the end of the expansion gas flow, which results in what we here denote as the secondary overshoot. This is then followed by the test gas with an additional rapid increase in pressure (III) to a peak value approximately 2 times the design flow pressure, here denoted as the primary overshoot. Subsequently, the pressure decays to the nominal design value (IV) until the arrival of the test time termination wave.

A generalized space-time diagram summarizing the wave processes responsible for altering the test gas properties is shown in Fig. 4.24. The labeling of the states follows that of Trimpi [14]. After the secondary shock (W_2) arrives in the test section, a disturbance wave (W_U) processes the shocked expansion gas and interacts with the contact surface at a distance $\hat{x}$ from the secondary diaphragm. This results in

generating two new waves, a transmitted and a reflected wave. The transmitted wave processes a portion of the test gas and thus alters its aerothermdynamic properties which causes the primary overshoot in Fig. 4.23 and is denoted as (5c) in Fig. 4.24. Furthermore, the interaction reduces the speed of the contact surface which further limits the useful test time. The reflected wave, which processes the shocked expansion gas, is responsible for the secondary overshoot in Fig. 4.23 and is denoted as (20b) in Fig. 4.24.

This study investigates the mechanism for the onset of such flow disturbance using a combined experimental, computational and analytical approach. A series of experiments and computer simulations using ANSYS CFX was carried out to gain insight on the cause of the pressure overshoots and reach the conclusions summarized in Fig. 4.24. An analytical model describing the observed effects is formulated and is shown to be a useful tool in predicting the extent of test gas interference. Lastly, we provide a brief discussion on what is required to limit the undesired interference effects.

4.5.1 Experimental Methodology

A series of experiments was conducted to discern the cause of the pressure overshoot upon arrival of the test gas. The experiments were carried out with the Michigan Hypersonic Expansion Tube Facility [148] (MHExT), while an additional set of data was acquired in the expansion tube facility at Stanford University [149]. The only geometric difference between the two facilities relevant to this study is the inner radius of the tube R, which is 7 cm and 7.2 cm for the Stanford and Michigan facilities respectively.

Figure 4.25 provides a schematic drawing of the assembly that was fixed in the test section to measure the test gas pressure. It is composed of a flat plate with a sharp leading edge instrumented with flush-mounted PCB piezoelectric pressure

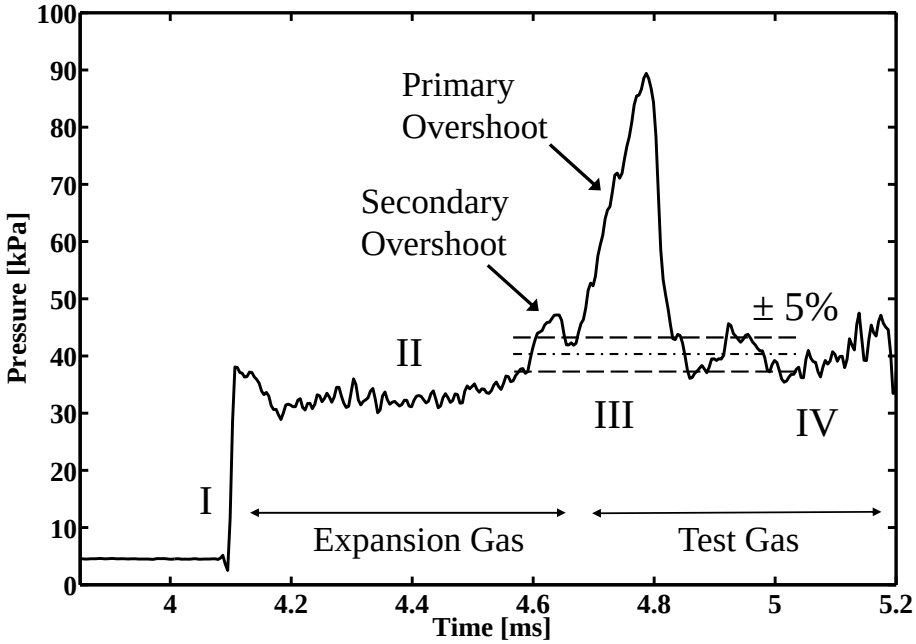

Figure 4.23: Static pressure measured on a flat plate mounted inside of the test section under non-ideal operation of an expansion tube facility. Condition pertains to Run 2 in Table 6.1.

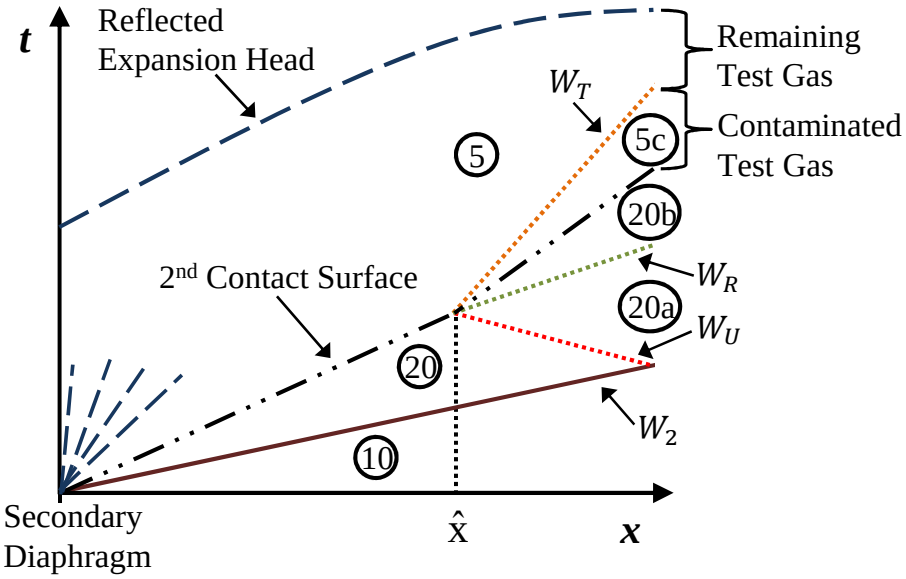

Figure 4.24: Generalized space-time diagram of the unsteady wave process responsible for changes in test gas properties. State labels after Trimpi [14].

transducers (Model 113B21). In the Stanford facility, the flat plate was instrumented with three transducers, while in the Michigan facility only one transducer was used. The position of the leading edge of the flat plate from the tube exit is given by Δ_{LE}; the resulting distance of each sensor from the tube exit is Δ_i ($i = 1, 2, 3$ for each of the three sensors). The origin is taken to be on the centerline at the exit plane of the tube. Both facilities used a geometrically similar configuration of the flat plate assembly. The span of the plate is 10.2 cm. Two flow conditions referred to as A and B in Table 6.1 were considered, and differed in M_{20} (flow Mach number of the shocked expansion gas) which was designed to be greater or less than unity, and M_{W_2} which is the Mach number of the secondary shock wave. Both conditions used air and helium as the test gas and expansion gas, respectively. They were run with the assembly configured either with the leading edge protruding ($\Delta_{LE} < 0$) or recessed ($\Delta_{LE} > 0$) from the expansion tube exit. The different cases are summarized in Table 6.1. Separate experiments simultaneously measuring pitot and static pressures were carried out to characterize the flow conditions, establish the temporal evolution of the flow properties, and determine the arrival of the secondary contact surface marking the start of the test time.

4.5.2 Numerical Methodology

The experimental results were modeled with a representative two-dimensional domain using the commercial software ANSYS CFX. Here we consider a two-dimensional representation of the problem to generate a qualitative approximation of the system of waves generated by the presence of a test model; thus providing us with an initial view of the controlling physical processes without any expectation of replicating our experimental observations with much fidelity. The two-dimensional calculations were not intended to fully describe the exact details of the experiments, and certainly do not capture the complexity of the actual (three-dimensional) problem. The flow was

modeled as inviscid since the phenomena of interest was not believed to be governed by viscous effects. In fact, because the magnitude of the observed interference effects on test gas conditions are so large and because wave propagation is considered to be at the root of the observed phenomenon, it was believed that the overall driving mechanism remains inertia-dominated with viscous effects having no effect on the onset of these disturbances but at most affecting their evolution over long times.

The inlet and outlet boundary conditions were supersonic, while all walls were imposed with a free slip boundary condition. A second order backward Euler transient scheme was used and the mesh was composed of cells with dimensions 3 mm $\times$ 3 mm. The solution used the NASA polynomials [150] to compute the thermodynamic properties of the gas assuming an equilibrium thermally perfect gas model. Solution convergence was determined by ensuring that: 1) the solution was grid independent; and 2) the RMS residual for the mass, momentum, and energy equations decreased by at least 3 orders of magnitude.

Figure 4.26 shows the domain that was modeled. It includes the test section, flat plate, and a portion of the expansion section. The domain was initialized with axial profiles for velocity, mass fraction, pressure and temperature and with uniform properties in the cross-sectional direction. For each of the two conditions, the initial values were pre-computed from experimentally measured shock speeds and initial fill pressures using an expansion tube solver similar to that of Trimpi [14] and includes equilibrium temperature-dependent properties. The pre-computed inlet boundary conditions were kept uniform across the inlet plane. Property changes across the secondary shock wave and contact surface were approximated with error function profiles with an initial thickness of 0.5 cm and 2 cm, respectively. The final solution and conclusions of this study were not found to be sensitive to the initial thickness of these features.

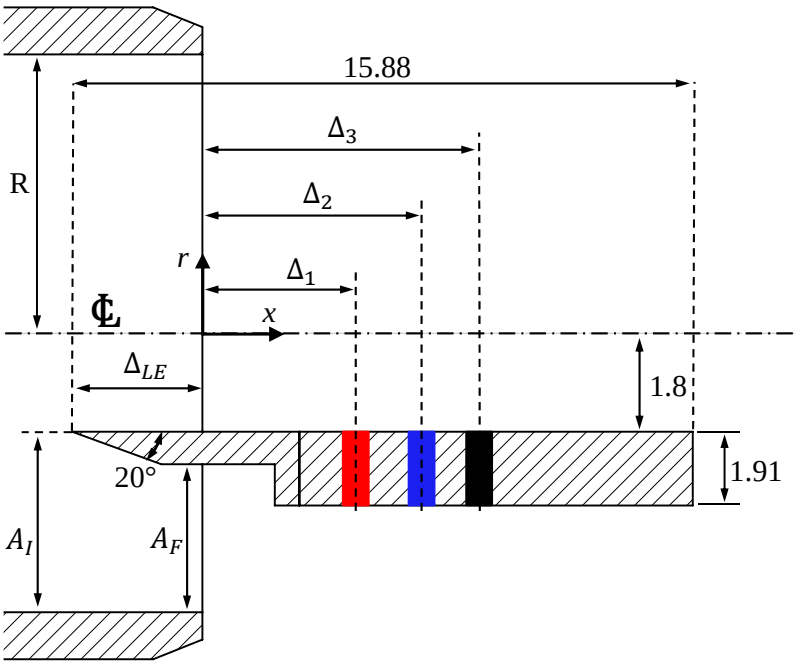

Figure 4.25: Fig. 3 Schematic of the experimental assembly in the protruding configuration. Dimensions are given in centimeters.

Run Number	Flow Condition	M_{W_2}	M_{20}	Δ_{LE}	Δ_i	R [cm]
1	A	2.6	0.95	0.06	1.01, 1.29, 1.56	7.0
2	A	2.6	0.95	-0.49	0.47, 0.74, 1.01	7.0
3	A	2.6	0.95	0.11	1.06	7.2
4	A	2.6	0.95	-0.46	0.49	7.2
5	B	3.5	1.1	0.11	1.06	7.2
6	B	3.5	1.1	-0.46	0.49	7.2

Table 4.5: Summary of the experimental and numerical test matrix. The subscript 20 refers to the shocked expansion gas [14]. The distances given by Δ_{LE} and Δ_i are normalized by the inner tube radius R.

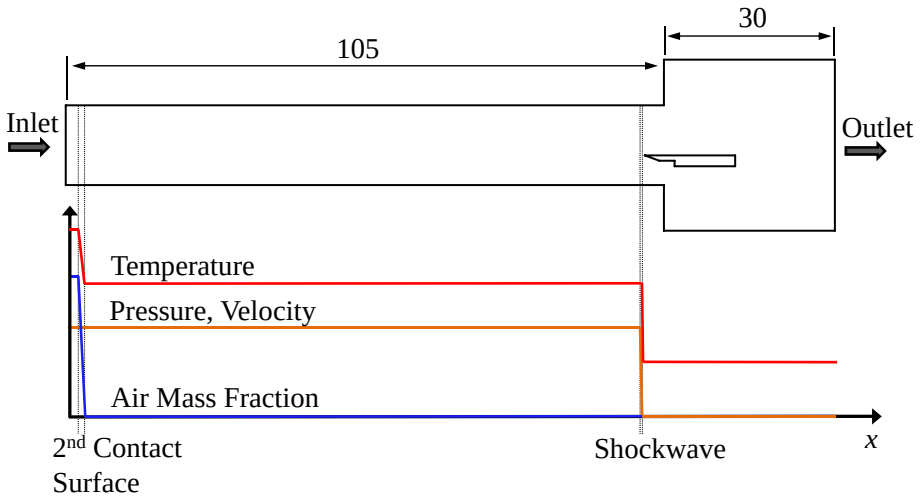

Figure 4.26: The two-dimensional CFX domain with a qualitative description of its initialization. All units are in cm.

4.5.3 Results

The measured surface pressure for Run 1 and 2 (case A) are provided in Figs. 4.27(a) and 4.27(b) (solid lines), respectively. The corresponding numerical solution is also shown for comparison (symbols). For both cases, the value of M_{20} is slightly less than unity (Table 6.1). The leading edge is recessed into the test section in Run 1 and protrudes into the expansion tube in Run 2. For each case, all three traces, which are the wall-static pressure measurements at three downstream positions from the leading edge of the flat plate, are observed to share a similar qualitative behavior. The arrival of the secondary shock wave results in the initial step-change in pressure (label I). After the shock wave sweeps past the model, the shocked expansion gas follows (label II). While in the expansion section, the flow in state (20) is nearly sonic with $p_{20} > p_{10}$; thus, as the expansion gas further expands into the test section, it behaves as an underexpanded near-sonic jet with a pressure ratio of about 10. The decreasing trend of the measured pressure at different points along the plate (compare curves for different sensor locations in region II) is consistent with the decrease in pressure in the barrel shock of an underexpanded sonic jet [107, 108].

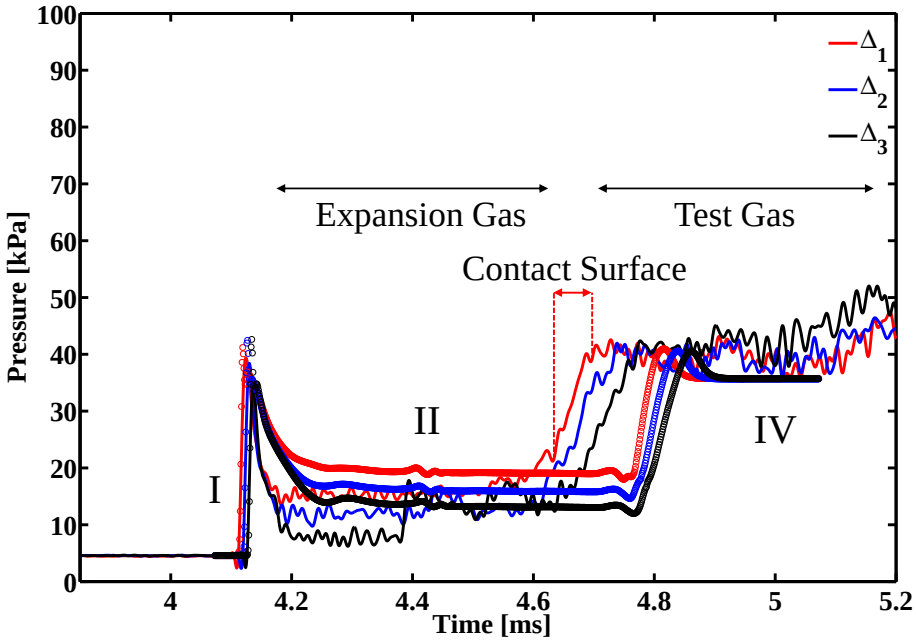

(a)

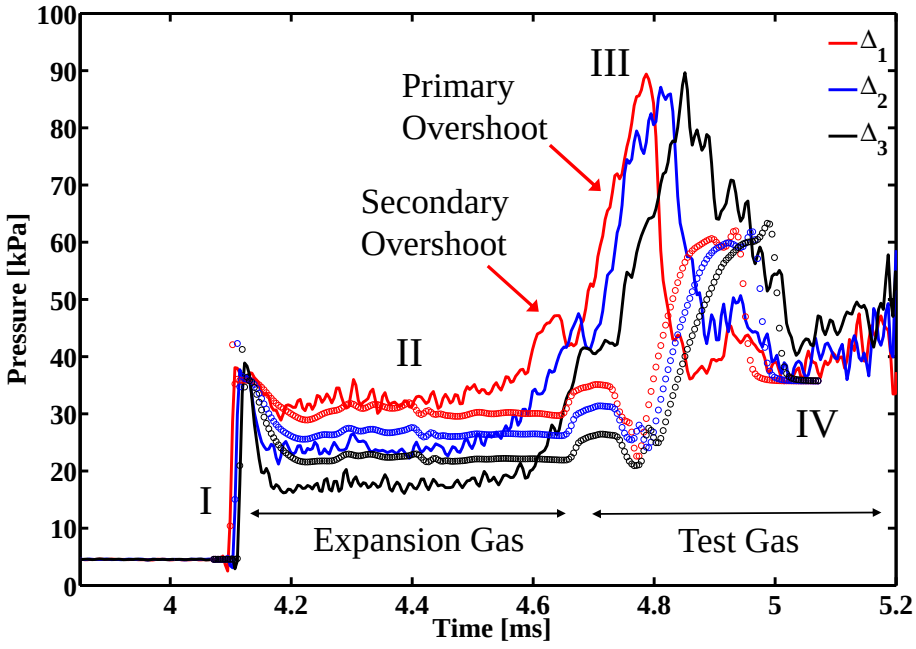

(b)

Figure 4.27: Comparison of experimental (solid) and computational (symbol) pressures for flow condition A. a) Recessed (Run 1) b) Protruding (Run 2)

The arrival of the secondary contact surface is at the end of region II. At this time, the measured pressure gradually increases, indicating an evolution in the flow. This is due to the combination of the finite thickness of the contact surface [135, 137], the inherent transient evolution associated with the change in flow structure from the barrel shock of the initial underexpanded near-sonic expansion gas to the final underexpanded supersonic test gas flow (IV), and the limited response time of the piezoelectric sensors. However, in the case of Fig. 4.27(b), where the leading edge of the plate protrudes into the expansion tube, there is a region of flow labeled as III which exhibits a pressure approximately twice that of the designed test gas pressure (i.e., at IV). For this particular case, the contaminated portion of the test gas (referred to as the primary overshoot) extends for approximately 50% of the total test time, rendering the flow condition of limited use. There is also a less pronounced increase in pressure just prior to the primary overshoot, which is referred to as the secondary overshoot, and takes place within the shocked expansion gas in state (20b). Finally, by comparison of the gas in region II, it is clear that the gas in region II of Fig. 4.27(b) is greater than that of Fig. 4.27(a) which is evidence that the expansion gas is further shock-processed in the protruding case.

To ascertain that the observed effects were not facility dependent, flow condition A was replicated in the MHExT facility. These measurements are Run 3 and 4, and are shown in Fig. 4.28. We observe the primary and secondary pressure overshoots in the second facility as well. The primary overshoot contaminates approximately 60% of the test gas. The results support our belief that the observed interference effect is independent of the expansion tube facility, but is related to test model interference during the onset of the shocked expansion gas flow. This hypothesis was further investigated through the numerical experiments.

Qualitatively, the numerical solutions (symbols in Figs. 4.27(a) and 4.27(b)) replicate the same behavior as was observed in the experiments. The quantitative differ-

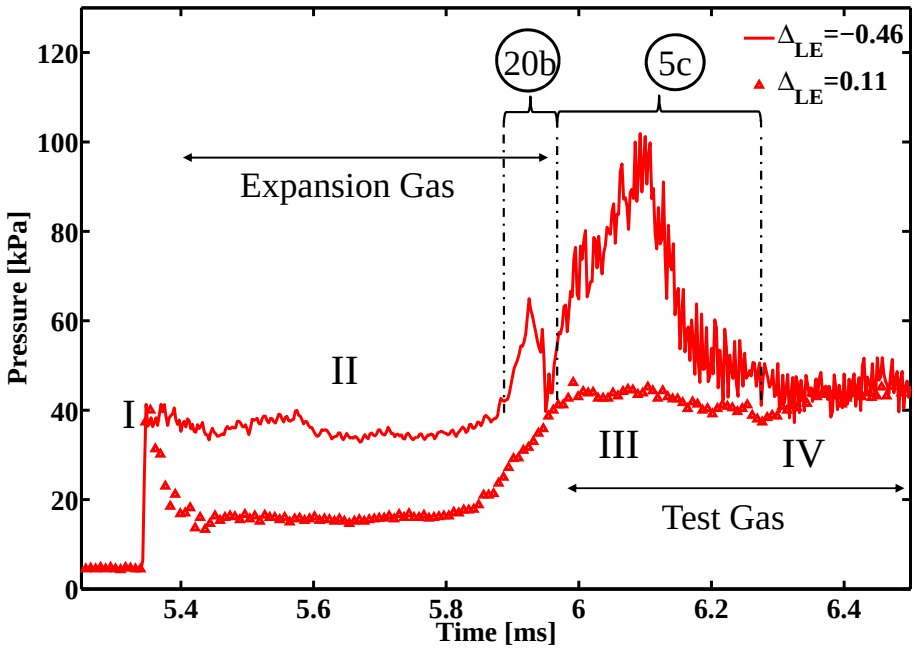

Figure 4.28: Experimentally measured pressures for the recessed (Run 3) and protruding (Run 4) configurations for flow condition A.

ences between the experimental and numerical solutions presented in Figs. 4.27(a) and 4.27(b) are due to a number of reasons. First, the difference in pressure in region II is believed to be a result of the simulations being two-dimensional, which will form a barrel shock structure that is not equivalent to that of a three-dimensional under-expanded jet of the same jet pressure ratio. This can be seen by comparing the work of Refs. [107, 108, 151] where two and three dimensional underexpanded jet structures were experimentally investigated over a wide range of pressure ratios. The two-dimensional jet yields a barrel shock structure with a Mach disk location that is further downstream of the exit plane as compared to a three dimensional jet, for the same pressure ratio. Therefore, a larger pressure in region II of the CFD simulations as compared to the experiments is to be expected. Secondly, there is a difference in the peak value of the pressure overshoot in the contaminated test gas. This may be attributed to the simulations being two dimensional and the actual area blockage by the test article in the test section not being adequately represented in

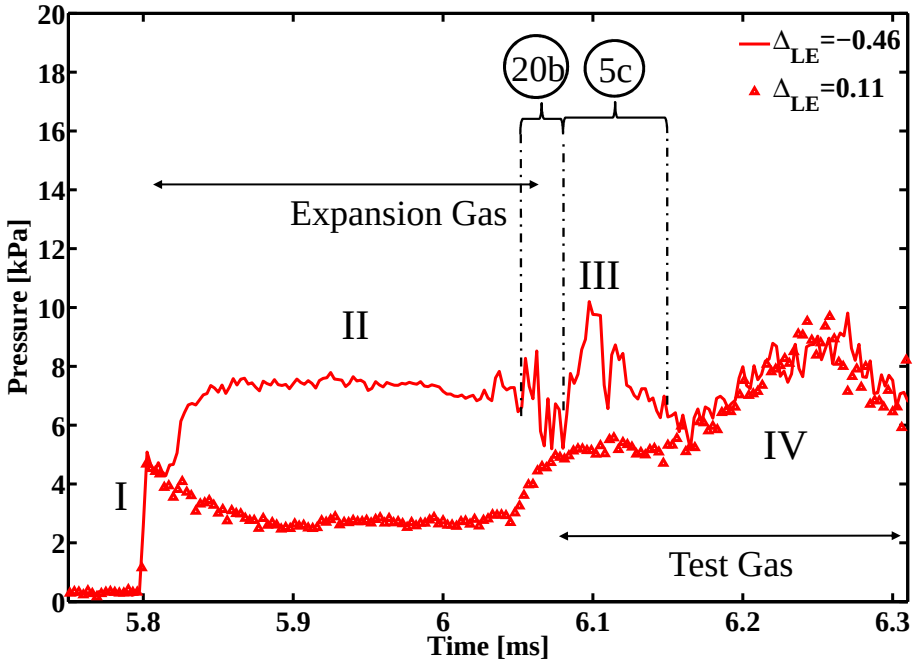

Figure 4.29: Experimentally measured pressures for the recessed (Run 5) and protruding (Run 6) configurations for flow condition B.

the simulations. For example, in the experiments the flat plate does not span the entire inner diameter of the tube. Moreover, the plate is fixed to the test section floor through a pair of struts, effectively increasing flow blockage. As a result, there are three-dimensional effects present in the experiments that are not accounted for in the simulations. Nevertheless, the simulations capture the same qualitative behavior as was obtained experimentally, providing indication of possible causes of the test gas interference effect.

The numerical and experimental results show that the adverse effects of test gas interference are avoided if the leading edge of the plate does not protrude into the expansion section. To further evaluate the nature of the disturbance, and specifically to ascertain its strength, a second flow condition (B) was designed such that a stronger secondary shock was generated and $M_{20} > 1$. In this case with the flow being supersonic, the upstream propagation of compression waves (relative to the flow) would be altered. The results of the protruding (Run 5) and recessed (Run 6) cases

for flow condition B are shown in Fig. 4.29. The results show that a portion of the test gas is still affected by the interference effect. Therefore, the disturbance wave must be supersonic relative to the flow in state ⑳. Unlike the case with $M_{20} < 1$, the pressure trace in region II for the protruding configuration is not the same as the corresponding one for the recessed configuration. The difference is postulated to be the result of flow compression by a steady detached shock that forms in front of the leading edge of the plate. Finally, based on the results of separate experiments using a pitot-static probe assembly, the measured change in pressure over the test time (IV) for condition B is an undesired characteristic inherent to the flow condition itself and not a result of the interference effect being discussed here.

The numerical solution was used to further explain the link between the observed interference and a possible underlying wave system. A series of pressure contours of the partial domain at relevant time steps for condition A is provided in Fig. 4.30. The variable t corresponds to the time elapsed from the arrival of the secondary shock wave at the leading edge of the flat plate. The plot beneath each contour represents the air mass ratio along the two-dimensional space, indicating the location of the contact surface. The air mass ratio is defined as the relative amount of air at any point in the domain and it is used to differentiate between fluid that originates from state ⑤ from fluid that originates from state ⑳. The series of contours show that the secondary shock separates around the test model. The portion of the shock propagating on top of the flat plate is observed to sweep past the model without generating any upstream propagating disturbances. On the other hand, the portion of the shock propagating beneath the plate diffracts around the leading edge of the test model as it continues through the contracted area [152]. The diffracted portion of the wave coalesces into a finite-strength shock wave at $t = 30$ μs. After an initial formation period ($t = 150$ μs) which originates underneath the test model, the disturbance wave grows to envelop the entire area of the tube and propagates at a speed W_U, in the shock reference

frame. As it propagates upstream, it processes the shocked expansion gas from state (20) to state (20a) until it reaches the contact surface at $t = 500$ μs. The wave is then partially reflected and transmitted through the contact surface at $t = 530$ μs. The reflected wave (moving at a speed W_R) is swept downstream, where it further processes the expansion gas from state (20a) to (20b). The portion of the expansion gas in state (20b) corresponds to the secondary overshoot. At the same time, the transmitted wave (propagating at a speed W_T) propagates through a portion of the test gas, processing it from state (5) to (5c), as it is swept downstream at $t = 670$ μs. The result is a slug of test gas convected into the test section with a significant portion having different aerothermodynamic properties than what was originally intended. The primary overshoot is the signature of this portion of the test gas.

4.5.4 Theoretical Modeling

A one-dimensional unsteady wave model of the unsteady process controlling the interaction was constructed to quantitatively predict the impact of the wave system on the final test gas conditions. Modeling of the test gas interference effect was done in two parts. The first portion describes the formation of the disturbance wave as a function of several test parameters while the second portion describes its interaction with the contact surface. The analysis and numerical results of this section are specific to helium as the expansion gas and high temperature air (γ_5=1.30) as the test gas, but they can be readily adapted for any test gas / expansion gas combination.

4.5.4.1 Formation of the Disturbance Wave

Based on the results of the CFX simulations, it was believed that the origin of the disturbance wave was a result of the interaction of the secondary shock wave with the test model. Specifically, it was found that the wave diffracts around the leading edge of the test model as a result of the area contraction it was propagating through [152].

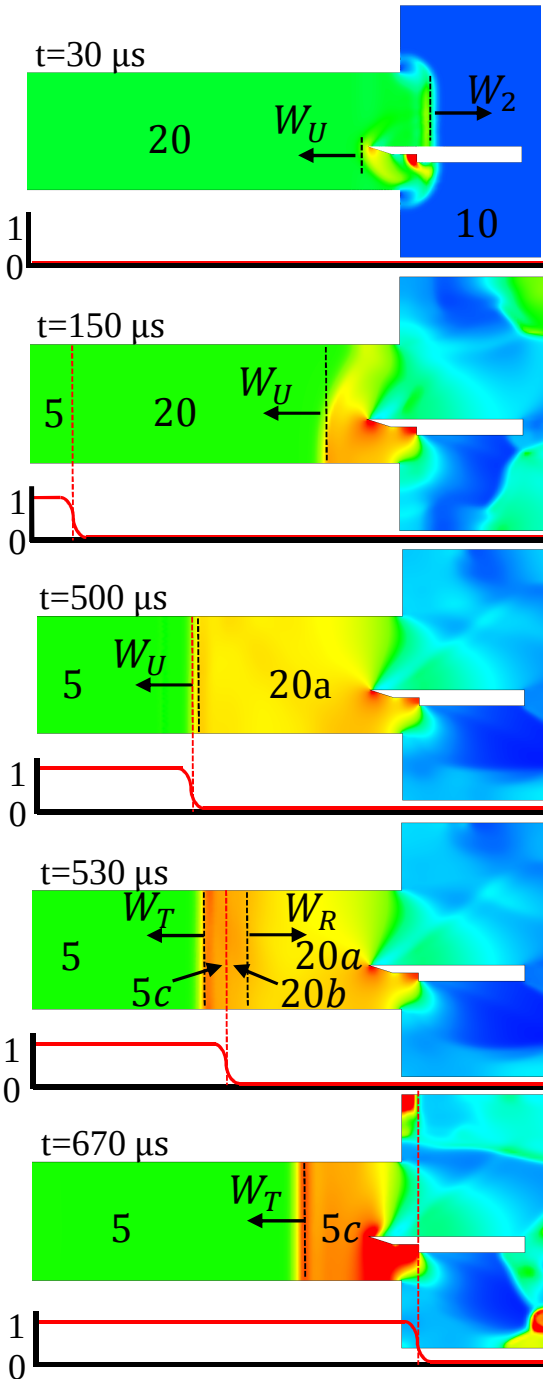

Figure 4.30: Pressure contours generated with CFX for Run 2 illustrating the wave processes leading to test gas contamination.

The diffraction process leads to a modified secondary shock wave as well as generates waves which coalesce into an upstream propagating disturbance.

There has been an abundance of work that studied the effects of shock-wave propagation through a channel of varying area. The majority of the studies were primarily aimed towards analyzing and optimizing a gradual change in area in order to optimally strengthen the incident shock wave in a shock tube without increasing energy requirements. In particular, the work of Chester [153], Chisnell [154], Whitham [155] studied the effects of a shock as it propagated through a monotonically varying area change. Using different methods, they individually obtained a similar relation for the strength of a shock wave as a function of the cross sectional area of the channel it was propagating through. Russel [156] and Bird [157] experimentally investigated the interaction of normal shock waves with symmetrical nozzles of varying geometry. They showed that the gain in shock strength depended on the rate of area change.

In this study, we are interested in capturing the change in shock strength of the secondary shock and the formation of additional (e.g., reflected) waves as it passes through a constriction. Since the the area change in which the secondary shock propagates through is not monotonically changing, we adopt the model outlined by Laporte [158]. A schematic of the one-dimensional model is shown in Fig. 4.31. The secondary shock propagates at a speed W_2 in a channel of initial cross-sectional area A_I through a contracted area of A_F. In our case, the areas correspond to the initial and final cross-sectional areas beneath the leading edge, as indicated in Fig. 4.25. Upon reaching the constriction, a new set of waves are generated which include a strengthened transmitted wave and a reflected wave propagating at speeds W_3, and W_U, respectively. This interaction forms a region of changing entropy and is shown as the gray region of gas convecting downstream. This region of varying entropy is formed as a result of being shocked by the transmitted wave of incrementally increasing strength as it propagates through the area contraction. As a result, the gas

in state (30) and (40) will have the same speed and pressure, but have different entropies, temperatures, and densities. The strengthened wave processes the expansion gas initially in state (10) to state (30), while the reflected wave processes the expansion gas from state (20) to (20a). Finally, we approximate the gas as being isentropically compressed from state (20a) to (40). This is valid as long as the angle of the contraction is sufficiently less than 90 ° and the flow in state (40) remains unchoked. The flow in state (40) chokes as a result of the combination of the secondary shock strength being sufficiently large and the area constriction being sufficiently small. In this case, the Mach number of the flow in state (40) is fixed to unity since an aerodynamic throat would be required to accelerate it to supersonic speeds.

The upstream propagating disturbance in the present study is the reflected wave in this model. Given the strength of the secondary shock (i.e., W_2), the strength of the upstream propagating disturbance is found using the solution of moving normal shocks and isentropic flow [114] by coupling the solution of the reflected (disturbance) wave with the solution of the strengthened transmitted wave and assuming isentropic compression across the constriction (from (20a) to (40)). This model closely follows the solution of Laporte [158] for a similar configuration. In the case the flow in region 40 reaches the sonic limit (choked), the model remains the same except for the additional condition that the Mach number in state (40) is unity.

This analysis was implemented for helium and is shown in Fig. 4.32. The strength of the disturbance wave strength given by P_{20a}/P_{20} is shown as a function of area ratio (A_I/A_F) for multiple secondary shock strengths (p_{20}/p_{10}). The strength of the upstream-propagating wave increases with increasing secondary shock strength and decreasing area-ratios. The Mach number of the wave is in the shock reference frame and is given by

$$M_{W_U} = \frac{U_{20} + W_{U_{lab}}}{a_{20}} \tag{4.12}$$

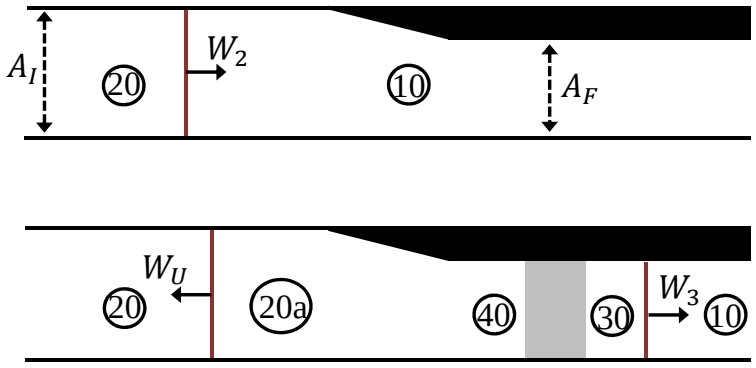

Figure 4.31: Schematic drawing of the resulting unsteady wave process generated by the interaction of a shock wave with a sudden contraction.

where $W_{U_{lab}}$ is the wave speed in the lab reference frame. In the limit $A_I/A_F \to 0$, the solution of a shock wave reflected by a wall is found (i.e., the reflected shock tube problem).

Based on this model, we conclude that any combination of secondary shock strength and area contraction will generate a disturbance wave of sufficient strength to propagate upstream. In other words, a condition cannot be designed such that U_{20} is sufficiently large to sweep the disturbance wave downstream. This is in agreement with the experimentally observed results of flow condition 2, where M_{20} was designed to be supersonic, yet the test gas interference effect was still observed.

4.5.4.2 Interaction of Disturbance Wave with the Contact Surface

Upon reaching the contact surface, which is modeled as a zero-thickness material discontinuity, the disturbance wave is partially reflected and transmitted into new waves as was shown in Fig. 4.30. The strength of the two new waves is determined by solving the propagation of a shock wave through a material discontinuity and imposing that the resulting states across the reflected and transmitted waves satisfy the conditions: $U_{5c} = U_{20b}$ and $P_{5c} = P_{20b}$ [114]. Finally, the portion of test gas that is contaminated by the transmitted wave is given by:

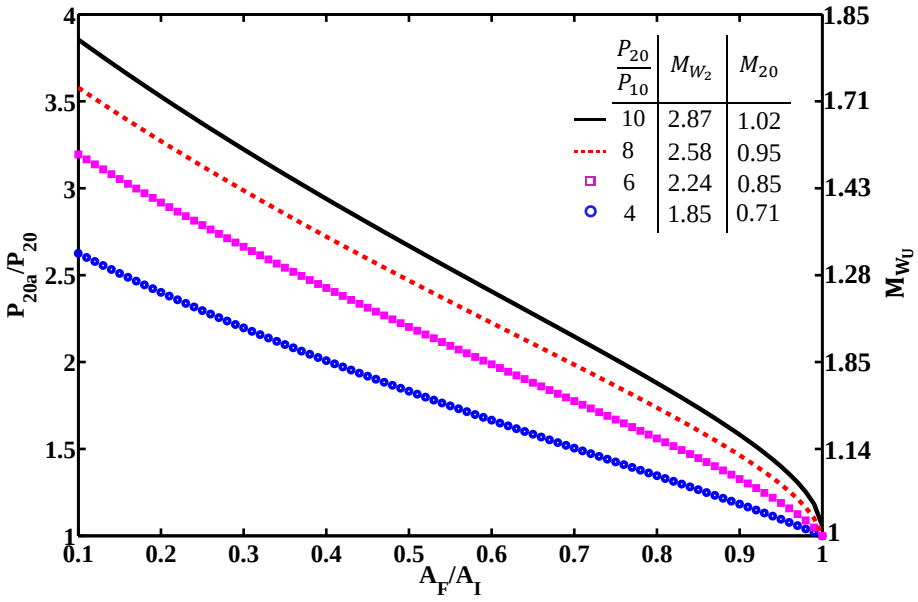

Figure 4.32: Upstream-propagating wave strength as a function of area ratio for constant secondary shock strengths. Results are specific to helium gas.

$$t_c = \frac{L_{10} - \hat{x}}{W_T} - \frac{L_{10} - \hat{x}}{U_{5c}} \tag{4.13}$$

where L_{10} is the length of the expansion section, and U_{5c} is the speed of the flow in region ⑤c. W_T is the speed of the transmitted wave and is given by:

$$W_T = U_5 - a_5 \left[\frac{\gamma_5 + 1}{2\gamma_5} \left(\frac{P_{5c}}{P_5} - 1 \right) + 1 \right]^{1/2} \tag{4.14}$$

The quantity $\hat{x}$ is the distance from the secondary diaphragm at which the contact surface and the upstream-propagating wave intersect and can be computed as:

$$\hat{x} = \frac{U_{20} L_{10}}{W_2} + U_{20} L_{10} \frac{W_2 - U_{20}}{W_2} \frac{1}{U_{20} + W_U} \tag{4.15}$$

W_2 is the secondary shock speed. By this analysis, we can infer that $U_{20b} < U_{20}$, thus the speed of the contact surface has decreased.

This portion of the model was solved and the results are shown in Fig. 4.33.

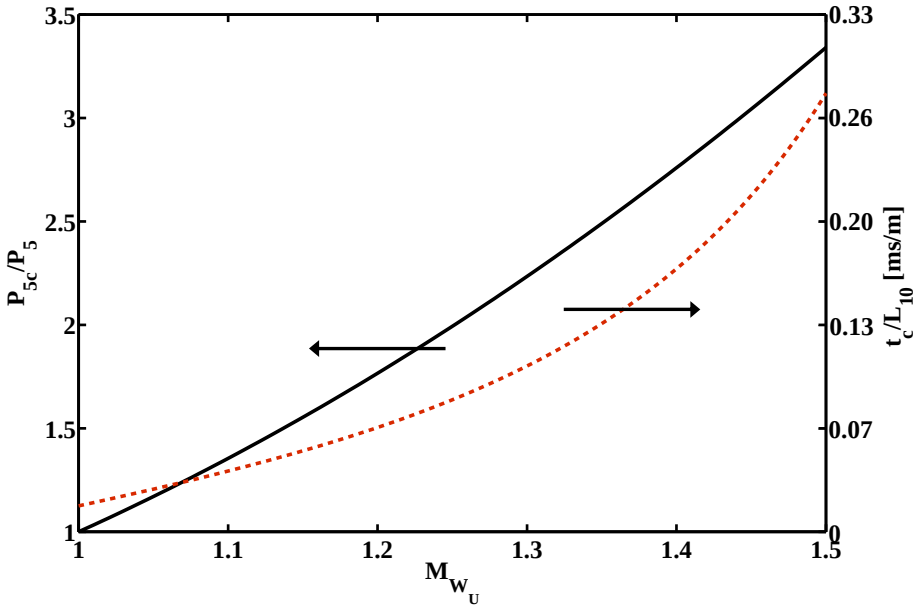

Figure 4.33: Peak contaiminated test gas pressure and contaminated test time as a function of upstream propagating wave strength. The peak pressure and contaminated test time are normalized by the nominal test gas pressure and expansion section length, respectively. This analysis is specific for helium expansion gas and air (γ=1.30) as the test gas.

The peak contaminated test gas pressure and contaminated test time are given as a function of the disturbance wave strength. The peak pressure is normalized by the nominal test gas pressure when no disturbances are present. The contaminated test time t_c is normalized by the expansion section length since it was found to scale linearly with expansion section length, for a given M_{W_U}.

The analysis shows that if the disturbance has the strength of a Mach wave ($M_{W_U} = 1$), it does not alter the test gas pressure. However, the wave is still moving relative to the flow if U_{20} is subsonic, and therefore will penetrate through the test gas. As the strength of the disturbance increases, it penetrates through the contact surface a greater extent and alters the test gas pressure in the process.

4.5.4.3 Analysis of Model

Based on the outlined analysis, the peak contaminated test gas pressure and time are dependent on several experimental parameters; this dependence can be conveniently summarized as:

$$(P_{5c}, t_c) = \tilde{F}\left(W_2, \frac{A_F}{A_I}, \gamma_{20}, \gamma_5, a_{20}, P_{20}, L_{10}\right) \tag{4.16}$$

The proposed model was used to predict the extent of the test gas interference effect for the two flow conditions studied experimentally. The results are summarized in Table 4.6, where the run number corresponds to that of Table 6.1. The results show that the model is capable of accurately predicting the extent of the interference effect reasonably well considering the approximations that were made. Discrepancies between the experiments and model may be a result of several factors. First, the formation process of the disturbance wave requires some finite amount of time until it is fully developed and propagates at a nominal speed of W_U. In fact, the disturbance wave is the result of a series of compression waves that coalesce with one another and originate from each incremental change in area. Second, it may also be important to consider that the disturbance wave grows in size from an initial cross sectional area of A_F to the entire area of the tube. This processes is not accounted for in the model. Third, the contact surface was modeled as a zero-thickness material discontinuity which is not the case experimentally. The finite thickness of the contact surface will cause the interaction with the upstream propagating wave to be more complex in nature, where a series of transmitted and reflected waves are generated and eventually coalesce. Fourth, we conjecture that the effects of the boundary layer in state ⑳ has a negligible effect on the upstream propagating disturbance wave, which may not be the case in state ⑤. This conclusion is drawn from the measured static pressure in the expansion section of the tube. An example of a pressure trace

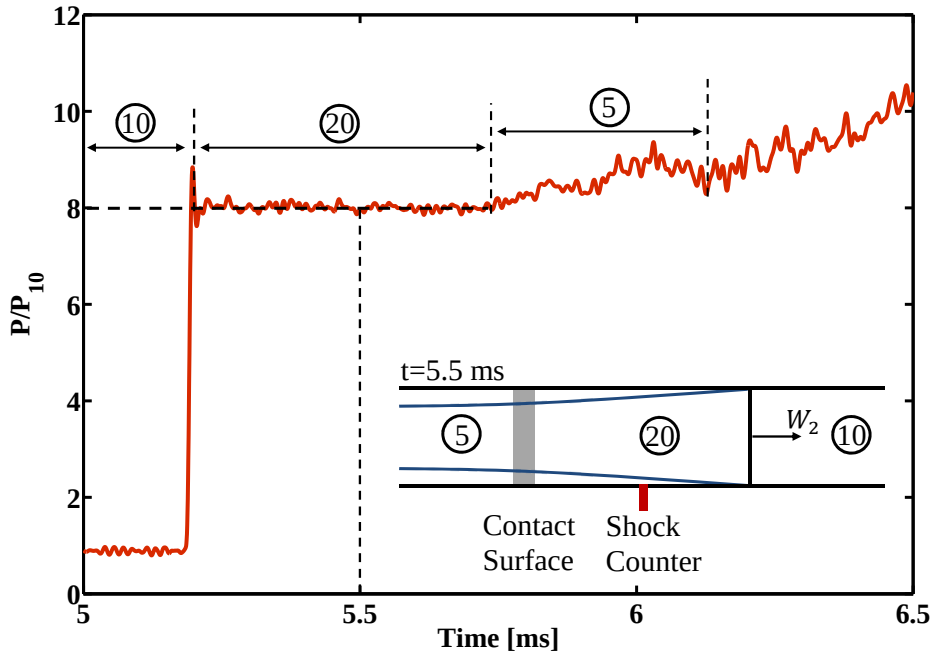

Figure 4.34: Static pressure trace for flow condition A acquired 2.82 m downstream of the secondary diaphragm.

acquired for flow condition A is given in Fig. 4.34, where the location of the sensor is shown schematically in the figure inset. After the arrival of the secondary shock, the measured pressure of the shocked expansion gas in state ⑳ is constant, which suggests that no significant boundary layer growth has occurred. On the other hand, the test gas in region ⑤ has traveled a significantly longer distance and has been processed by an expansion wave; thus the boundary layer had a significantly longer time to grow. In this case significant boundary layer growth can be inferred by the observed increase in static pressure measured at a fixed point. Therefore, we expect that it is only when the transmitted wave penetrates through the contact surface that the boundary layer has an effect on any of the additional waves. A similar trend of the behavior of the boundary layer was observed in flow condition B as well as in flows generated in Ref. [3, 148, 159]. Thus, in general we use this as an indication that boundary layer growth is negligible in state ⑳, but is present in state ⑤.

Run Number	$\frac{A_F}{A_I}$	$\frac{P_{5c}}{P_5}$		$\frac{t_c}{t_{total}}$	
		Exp.	Model	Exp.	Model
2	0.79	2.1	2.1	0.49	0.55
4	0.82	2.3	2.1	0.62	0.57
6	0.82	1.5	1.8	0.17	0.11

Table 4.6: Comparison of the experimental and modeling results. The peak contaminated test gas pressure is normalized by the nominal test gas pressure when no interference effect is present. The contaminated test time is normalized by the experimentally measured total test time.

4.5.5 Conclusions

The effects of test article induced interference on test gas properties in expansion tube flows was studied through a series of experiments, numerical simulations, and analytical considerations. This is a critical aspect to consider in expansion tube flows because of the limited size of the test gas core flow and test time in such facilities. Moreover, the results of this study are not limited to expansion tubes, but rather apply to any impulse facility operating under relevant conditions. The study shows that a system of compression waves is generated and coalesce into an upstream-propagating disturbance wave as a result of the initial interaction of the secondary shock with the test model which partially blocks the expansion tube cross-section. The disturbance wave has been shown to propagate upstream through the expansion gas and interact with the contact surface only to generate two new waves: a transmitted and a reflected wave. The transmitted wave partially penetrates the test gas, thus altering its aerothermodynamic properties. Furthermore, the speed of the contact surface is reduced.

Based on the present study, the interference effect can be accurately modeled to be a function of a several parameters which include the contraction area ratio and strength of the secondary shock wave. The effects of test gas interference are only suppressed if the test article is recessed into the test section. Based on the formulated

model, any test model which protrudes into the expansion section and causes an area contraction will generate and upstream-propagating disturbance. Furthermore, this disturbance will always be strong enough to propagate upstream. More specifically, a secondary shock wave that has sufficient strength to generate a supersonic flow in state ⑳ will always generate an upstream propagating disturbance, traveling at a speed W_U that is greater than U_{20}. A one-dimensional unsteady wave model was formulated to quantitatively predict the strength and temporal duration of the test gas interference and was found to accurately predict them for the range of flow conditions used in this study.

CHAPTER V

Detonation Tube Model with Heat and Momentum Losses

5.1 Introduction

In order to quantitatively evaluate the combustion effects that the post-detonation products have on the reacting supersonic system, it is essential to understand the properties of the exhausting gas as a function of time. In this chapter a model is developed to predict the properties of the post-detonation gas generated in the experiments. The detonation waves used in this study were generated in a 0.75 m long pipe that had a 4.8 mm inner diameter. The detonation wave speeds and pressure profiles were measured with a pair of fast-response piezoelectric sensors near the open end of the tube, in a manner outlined in Section 3.2.2. A typical example of an acquired pressure trace is shown in Fig. 5.1. The data reveals how the PD tube is partially choked during the filling process (prior to the arrival of the detonation) since the measured pressure inside the tube is approximately 1.6 times larger than the bulk test gas freestream pressure ($P_5 = P_\infty = 40$ kPa). The data exhibits a sharp increase in pressure upon passage of the detonation wave. The measured peak pressure is less than the predicted CJ-state value. This may be due to the large wave speeds being measured and the limited response time of the sensors, which are incapable

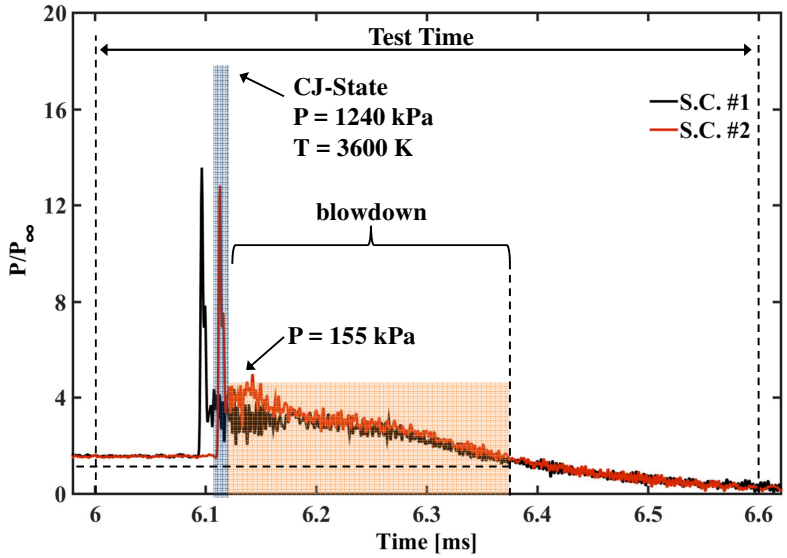

Figure 5.1: Pressure-time history of a H_2-O_2 detonation wave and consequent blowdown process acquired from two piezoelectric pressure sensors mounted in series near the open end of the tube. The data was acquired during an experimental run and the pressure is normalized by the nominal freestream test gas pressure.

of faithfully resolving the pressure gradients in the vicinity of the detonation wave itself. Upon passage of the detonation, the pressure decreases rapidly to a value of approximately $P/P_\infty = 4$. From then on, the pressure decays gradually as the Taylor wave and exhausting wave expand the post-detonation gas. The total blowdown process is approximately 300 μs in length, and is defined as the time between when the detonation reaches the open end of the tube until the pressure within the tube reaches the ambient value.

There are a number of striking aspects of the pressure profiles in Fig. 5.1. Since the pressure sensors are approximately 0.75 m away from the closed end, the region of gas within the Taylor wave should be large enough to exhibit a gradual decrease in pressure from the CJ-state value to the value obtained by expansion to state ③ conditions ($U_3 = 0$). If the arrival of the reflected wave is neglected, the time of arrival between the detonation wave and the tail of the taylor wave is approximately 200μs. Experimentally this is not observed, rather, there is a rapid decrease in pressure (end

of blue region in Fig. 5.1), to a value that is less than half of what is computed in state ③ of Fig. 2.13. Moreover, a back of the envelope calculation indicates that the time for the first C_- characteristic of the exhausting wave to propagate through the tube, reflect off the closed end, and return back to the open end is more than three times longer than the length of the blowdown period that is measured. These observations lead to the understanding that the PD was used to generate detonations within a non-ideal regime of operation.

There have been an abundance of research efforts that studied the theory of non-ideal detonation wave propagation. The experimental work of Ref. [160] was the first to correlate the effects of heat loss to the large gas velocity and pressure deficits observed behind detonation waves. This work confirmed the theoretical analysis of Refs. [161] and [162] which analyzed the influence of heat loss on the expanding post-detonation gas. The work of Ref. [163] found that the decrease in performance of a PD tube increased with longer tubes. This was attributed to the post-detonation gases residing for longer periods of time within the tube, and therefore being subject to the energy loss mechanisms for longer periods of time. The experimental work of Ref. [164] observed how decreasing tube diameters resulted in lower detonation velocity speeds as compared to the ideal CJ value.

Several difficulties arise when relying on the classical hydrodynamic theory of detonations [66, 68] to predict detonation velocities, structure, and post-detonation properties. The simplified CJ theory is incapable of predicting limits for stable detonation wave propagation, and rather provides predicted detonation wave parameters for any gas mixture that can react exothermically. Moreover, it is well accepted that detonation waves have a three-dimensional structure, due to the presence of transverse waves, which is not considered in the one-dimensonal ZND theory. Any transport effects that occur in the transverse (radial) direction that introduce strong interaction mechanisms that alter the detonation properties need to be accounted for. In reality,

momentum and heat losses to the walls have been shown to have significant effects on the detonation wave parameters and properties of the post-detonation gases that are expanding in the trailing Taylor wave.

5.2 Loss Mechanisms

The propagation of an ideal detonation can only be sustained when the energy release is rapid enough to counter the adverse effects of heat and momentum losses. The extent in which these non ideal effects alter the detonation wave properties arises from the competition between chemical reactions and several mechanisms that extract energy from the flow. Within the reaction zone, the energy released by chemical reactions accelerate the flow to sonic conditions (CJ-state) relative to the wave. On the other hand, heat and momentum losses act to remove energy and mass from the freestream, and in turn drive the flow away from sonic conditions. This in turn alters the structure of the detonation wave, by delaying and inhibiting heat release. These effects continue downstream of the sonic plane, altering the properties of the post-detonation gas.

The loss mechanisms being discussed are illustrated in Fig. 5.2. The figure represents the steady flow through a detonation wave with the coordinates fixed in the shock reference frame. The description follows the same structure as the ZND theory, except with the addition of a viscous and thermal boundary layer that develop at the leading shock wave [165]. Upstream of the shock the unburnt gas moves with a uniform velocity (U_1) that is equal to the detonation propagation velocity. The tube wall has a constant velocity that is also equal to the detonation propagation speed ($U_{wall} = U_1$). Inside the reaction zone, the flow speed is lower than it was upstream of the shock, and varies both axially and radially. Axially, the heat release accelerates the flow to sonic conditions at the CJ-plane. After the sonic plane, the flow is processed by the Taylor wave which brings it to rest. Radially, the presence of a

viscous boundary layer increases the flow speed to match the larger wall speed. Similarly, the temperature is varying both axially and radially. The heat release increases the post-shock temperatures in the axial direction to the CJ-state value at the sonic plane. After the sonic plane, these temperatures are reduced by the trailing Taylor wave. Radially, the large difference in the burnt gas temperature and wall temperature forms a thermal boundary layer that conducts heat from the flow to the wall. In this illustration, the momentum and thermal diffusivities of the gas are approximated to be equal (unity Prandtl number), and therefore the two boundary layers (thermal and viscous) coincide with one another. Moreover, the tube wall temperature is kept at a constant value assuming the material has a sufficiently high thermal conductivity.

Since there is no mechanism to support a radial pressure gradient, the freestream gas is cooled isobarically as it enters the boundary layer. Therefore, the gas entering the boundary layer not only accelerates to match the wall speed, but it will also increases in density. The end result is that the mass appears to be drawn from the freestream flow to the tube wall. In other words, the boundary layer acts like a subsonic diffuser, causing the streamlines in the reaction zone to diverge. This effect can be modeled as a negative displacement thickness δ^* growing behind the shock [165].

The growth of both boundary layers can have substantial effects on the detonation wave parameters as well as the properties of the post-detonation products. For example, gas that enters the thermal boundary layer that has not yet began reacting, will undergo a significant temperature reduction that will further delay or eliminate the reactions all together. In addition, the flow divergence (mass sink) effect of the viscous boundary layer will decrease the heat release rate within the reaction zone. These effects become more significant as the ratio of the mass entering the boundary layers to the mass remaining in the freestream increases. There are two methods to alter this ratio. The first is to reduce the tube diameter which will cause the boundary

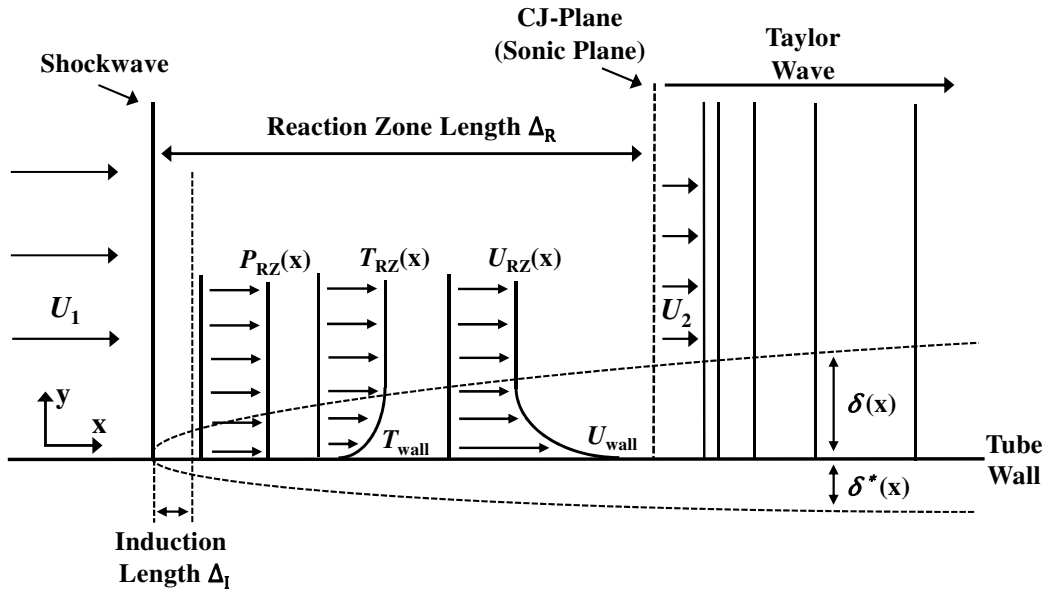

Figure 5.2: Depiction of flow through a detonation wave with the coordinates fixed in the shock reference frame.

layers to envelope a larger portion of the flow, and in turn reduce the relative amount of gas remaining in the freestream. The second method is to decrease the initial pressure which will enhance the growth of the boundary layer. Moreover, decreasing the pressure will have an inhibiting effect on the chemical reaction rates, causing ignition and heat release to be delayed.

The rate at which energy is extracted from the freestream flow causes the detonation to operate in various regimes, as is illustrated in Fig. 5.3. For sufficiently large tube diameters and initial pressures, ideal detonation wave propagation is observed. The adverse effects of the energy transfer mechanisms are not sufficient to overtake the sufficiently fast chemical reaction rates. This implies that the structure of the detonation is sufficiently one-dimensional and can be described sufficiently by the ZND theory discussed in Section 2.3. Moreover, the properties of the trailing post-detonation gases can be sufficiently described by isentropic expansion through the trailing Taylor wave, as was described in Section 2.3.2.

As the tube diameter or initial pressure is decreased, the heat release rate within the reaction zone decreases. For small reductions in heat release rate, the propagation

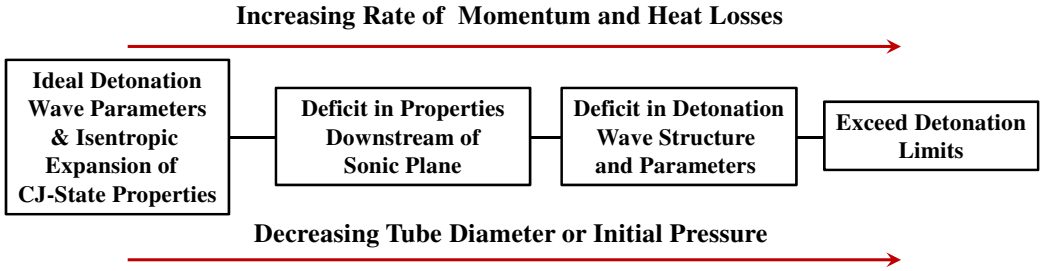

Figure 5.3: Various regimes of detonation tube operation that result from increased momentum and heat losses to the tube walls.

speed and detonation parameters are unaffected since the reaction zone length is very small. In other words, there is very little time (distance) for the energy transfer mechanisms to extract sufficient energy within the limited length of the reaction zone. However, the properties of the post-detonation products downstream of the CJ-plane can still be altered significantly since their lengths are typically several orders of magnitude greater than the reaction zone length [162, 166, 167]. As the tube diameter or initial pressure are further decreased, the heat release rate within the reaction zone can be sufficient to alter the detonation parameters and propagation speed. In this case, a sufficiently large amount of energy release is delayed past the sonic plane, and therefore cannot propagate upstream and contribute to supporting the detonation wave [168, 169]. As a consequence, the properties of the post-detonation products are significantly altered as well. Lastly, if the tube diameter or pressure are sufficiently small, the detonation limits will be exceeded [170]. In this regime, the amount of energy release within the reaction zone is not sufficient to sustain the propagation of the detonation wave.

5.3 Description of Numerical Model

A one-dimensional model was constructed to understand the effects of momentum and heat losses on the experimentally generated detonation waves. The formulation of the one-dimensional model follows that of Refs. [171, 172] and is based on a

multi-entropic formulation of the method of characteristics. Appendix D provides the derivation of the characteristic equations and entropy equations from basic principles. The capitalized variables represent non-dimensionalized quantities, in a manner outlined in Appendix D. The non-dimensionalized compatibility equations of the model are given by,

$$\frac{\mathrm{D}_{\pm}}{\mathrm{D}\tau}\left(\frac{2}{\gamma-1}A \pm U\right) = \frac{\mathrm{D}_{\pm}S}{\mathrm{D}\tau} + \frac{\gamma-1}{A}\frac{\mathrm{D}S}{\mathrm{D}\tau} \pm \Psi \tag{5.1}$$

where the Reimann variables along the $C_{\pm}$ characteristics are

$$C_{+} : P = \frac{2}{\gamma-1}A + U \tag{5.2}$$

$$C_{-} : Q = \frac{2}{\gamma-1}A - U \tag{5.3}$$

respectively. The flow field solution is sought along a family of three characteristic lines in $\xi - \tau$ space. The trajectory of the first two represent the propagation paths of acoustic disturbances, while the third is the pathline of a fluid element, and are given by

$$C_{+} : \ \frac{\mathrm{d}\xi}{\mathrm{d}\tau} = U + A \tag{5.4}$$

$$C_{-} : \ \frac{\mathrm{d}\xi}{\mathrm{d}\tau} = U - A \tag{5.5}$$

$$C_{0} : \ \frac{\mathrm{d}\xi}{\mathrm{d}\tau} = U \tag{5.6}$$

Finally, for the case of a detonation propagating through a round tube, the rate of change of entropy along a particle pathline caused by momentum and convective heat

losses is given by

$$\frac{\mathrm{D}S}{\mathrm{D}\tau} = -\frac{2C_f U\beta}{A^2(\gamma-1)}\left[A^2-(\gamma-1)U^2-A_w^2\right] \tag{5.7}$$

This formulation describes and treats the transport of momentum and heat losses due to the wall as a set of source terms and therefore neglects any complex or time-transient gradients of momentum and temperature. The variable β is the ratio between the length and diameter of the tube ($\beta = L/d$). Since there are three dependent variables (A, U, and S), the characteristic equations given by 5.1, and the entropy equation given by 5.7 are sufficient to complete the system of equations. These three governing governing equations determine the change in properties A, U, (through the Reimann variables P and Q) and S along the characteristic directions. The governing equations as well as the slopes of the characteristics lines are integrated numerically by a first-order finite difference scheme along the length of the tube ($0 < \xi < 1$).

Figure 5.4 illustrates the solution method in $\xi - \tau$ space for various parts of the flow, including interior points, the closed end boundary, and the open end boundary. Points 1 and 2 are two points at which all flow properties are known. Point 3 lies at the intersection of the C_+ characteristic through point 1 and the C_- characteristics through point 2. The characteristic lines are approximated to be straight line segments that connect two successive grid points. The particle path line C_0 through point 3 intersects line 1-2 at point 4. By knowing the solution at points 1 and 2, a discretized set of ten equations is used to find the solutions at points 3 and 4. The $C_\pm$ compatibility equations (Eqns. 5.1) reduce to

$$P = \frac{2}{\gamma-1}(A_3-A_1)+(U_3-U_1) = A_{13}(S_3-S_1) - \frac{2C_f U_{13}\beta}{A_{13}}\left[A_{13}^2-\left(\frac{\gamma-1}{2}\right)U_{13}^2-A_w^2+U_{13}A_{13}\right](\tau_3-\tau_1) \tag{5.8}$$

$$Q = \frac{2}{\gamma - 1}(A_3 - A_2) + (U_3 - U_2) = A_{23}(S_3 - S_2) - \frac{2C_f U_{23}\beta}{A_{23}} \left[A_{23}^2 - \left(\frac{\gamma - 1}{2} \right) U_{23}^2 - A_w^2 - U_{23} A_{23} \right] (\tau_3 - \tau_2) \quad (5.9)$$

The value of the friction coefficient C_f is a fixed parameter in the present model. For turbulent flows, it is only a function of the surface conditions of the tube. Using thin platinum film gauges, the heat flux measurements of Refs. [160, 173] showed that a good value of the friction coefficient is

$$C_f = 0.006 \quad (5.10)$$

The entropy equation (Eqn. 5.7) reduces to

$$S_3 - S_4 = \frac{-2C_f U_{34}\beta}{(\gamma - 1)A_{34}^2} \left[A_{34}^2 - \left(\frac{\gamma - 1}{2} \right) U_{34}^2 - A_w^2 \right] (\tau_3 - \tau_4) \quad (5.11)$$

the family of characteristic equations (Eqns. 5.4, 5.5, and 5.6) reduce to

$$\frac{\xi_3 - \xi_1}{\tau_3 - \tau_1} = U_{13} + A_{13} \quad (5.12)$$

$$\frac{\xi_3 - \xi_2}{\tau_3 - \tau_2} = U_{23} - A_{23} \quad (5.13)$$

$$\frac{\xi_3 - \xi_4}{\tau_3 - \tau_4} = U_{34} \quad (5.14)$$

and the interpolation relations for point 4 are

$$\frac{\tau_4 - \tau_1}{\tau_2 - \tau_1} = \frac{\xi_4 - \xi_1}{\xi_2 - \xi_1} \quad (5.15)$$

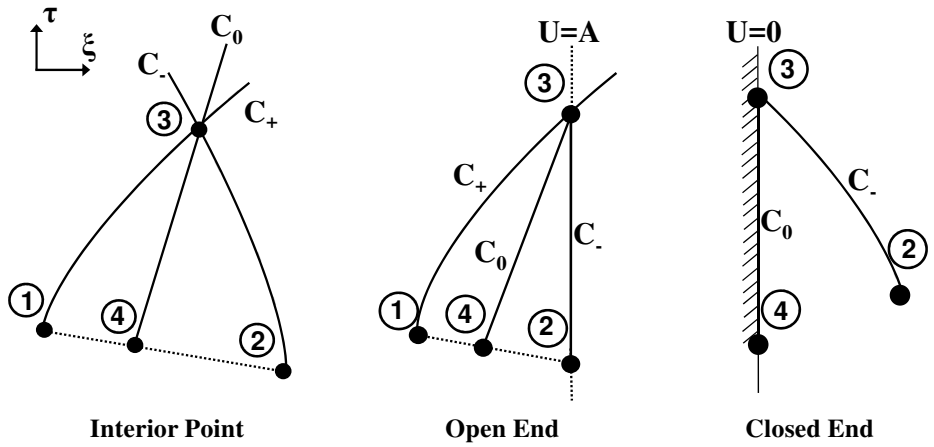

Figure 5.4: Construction of characteristic grid for interior and boundary points.

$$\frac{S_4 - S_1}{S_2 - S_1} = \frac{\xi_4 - \xi_1}{\xi_2 - \xi_1} \tag{5.16}$$

$$\frac{A_4 - A_1}{A_2 - A_1} = \frac{\xi_4 - \xi_1}{\xi_2 - \xi_1} \tag{5.17}$$

$$\frac{U_4 - U_1}{U_2 - U_1} = \frac{\xi_4 - \xi_1}{\xi_2 - \xi_1} \tag{5.18}$$

Double subscripts denote an average value between the specified points (e.g., $A_{23} = 1/2(A_2 + A_3)$). The set of equations need to be placed in a suitable form depending on where in the domain (interior or boundary point) the solution is being sought.

For the case of an interior point, the solution at point 3 is sought for A_3, U_3, S_3, ξ_3, and τ_3 and lies between the solution at points 1 and 2, which are already known. Point 3 is located at the intersection of the C_+ and C_- characteristics passing through points 1 and 2, respectively. Point 4, which needs to be found as part of the solution, lies at the intersection of a straight line between points 1 and 2, and the C_0 characteristic (particle path) passing through point 3. The solution at point 4 is found by a linear interpolation between points 1 and 2.

Perhaps the most critical aspect of the solution is to properly apply the correct

boundary condition at the open end of the tube. Along the open end of the tube, the flow exhausting condition is approximated as sonic outflow. In reality, it is a complex transient and three-dimensional process. However, several studies [174] have shown that as long as the pressure near the exit is sufficiently large, the exit condition can be reduced to a one-dimensional sonic boundary condition. Therefore, along the exit plane ($\xi = 1$) the solution is imposed to satisfy the condition $U = A$. At the closed end of the tube ($\xi = 0$), the gas is imposed to always be at rest, and the equations are set up to satisfy the conditions $U = 0$ and $S = S_0$. In this case S_0 is a reference entropy taken to be the CJ-state value, however, since relative changes in entropy are of interest, the absolute value is inconsequential to the solution. The computations are initialized with an isentropic solution at an early time along the first C_- characteristic at the closed end of the tube. The leading C_+ characteristic propagates into a uniform region of gas with CJ-state properties at the CJ speed.

Finally, in order to compute the pressure field from the obtained solution, the energy equation and ideal gas law are combined and integrated along a particle path to obtain

$$\frac{P}{P_{CJ}} = A^{2\gamma/(\gamma-1)} e^{\gamma(S_{CJ}-S)} \tag{5.19}$$

where the reference state was taken to be the CJ-state for convenience.

5.4 Results of the Model

The intersection points of the net of characteristics are used to compute the flow properties within the domain ($0 \leq \xi \leq 1$), through the method of characteristics. An example of three computed wave-diagrams is shown in Fig. 5.5. As a reference, the diagram on the left (Fig. 5.5(a)) was computed for the case where the flow past the detonation wave was isentropic and no energy loss takes place. In this

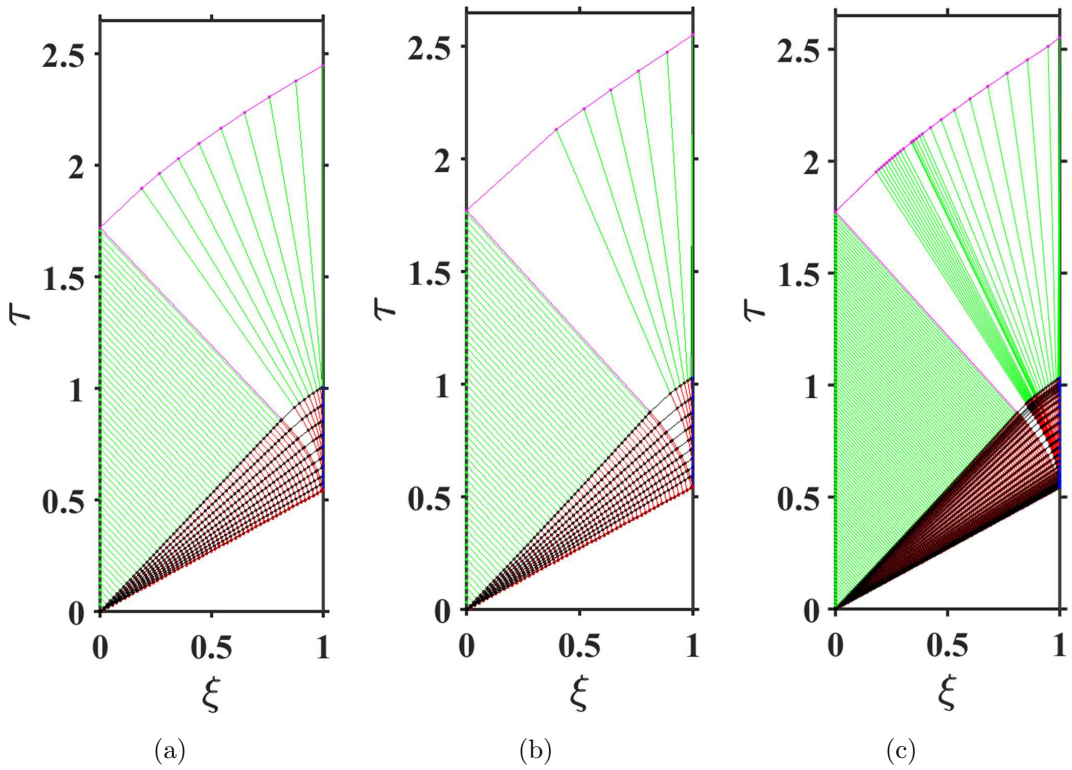

Figure 5.5: Computed space-time diagrams for a stoichiometric H_2-O_2 detonation wave propagating through a tube with an open end. (a) Isentropic expansion of CJ-state gas (coarse grid). (b) Expansion of CJ-state gas with kinetic energy loss ($\beta = 50$) due to friction and heat transfer to the walls (coarse grid). (c) Expansion of CJ-state gas with kinetic energy loss due ($\beta = 50$) to friction and heat transfer to the walls (refined grid).

case, the Reimann variables (Eqns. 5.2 and 5.2) are constant along their respective characteristic lines. The terms on the right hand side of Eqn. 5.1 are zero. Therefore, all of the characteristic lines within the simple regions are straight lines, with constant slopes. This diagram was computed with a relatively coarse net of characteristics to reveal the behavior of individual lines.

When wall loss mechanisms such as convective heat transfer and wall shear stress are included in the post-detonation flow, the wave trajectories are altered. An example of this is given by Fig. 5.5(b) where a value of $\beta = 50$ was used. This choice of β was used for two reasons; it is a practical value for typical pulsed detonation tubes, and it is similar to the value of the pulsed detonation tubes used to experimentally

measure the value of $C_f = 0.006$ [160, 173]. In this case, the Reimann variables vary along the characteristic lines, and therefore do not maintain a constant slope even within the simple regions. The loss of energy causes the flow temperature and speed to decrease, and is observed by the increasing slopes of the C_+ characteristic of the Taylor wave for example. Moreover, these effects cause a strong expansion to occur immediately behind the detonation wave, leaving an increasingly large space between the detonation and following C_+ characteristic. In order to resolve the flow features within the vicinity of the detonation, a refinement technique is implemented where new C_+ lines are introduced near the detonation. The same process is also used in the tail region of the Taylor wave. An example of the net of characteristics that were computed with the refinement scheme is shown in Fig. 5.5(c). Lastly, since the sound speed and flow speed are decreased, the wave propagation speeds are decreased and the blowdown period is observed to increase. This observation is based on the delayed arrival of the waves at the open end of the tube, when compared to the isentropic case.

Figure 5.6 shows the computed pressure and temperature contours of the flow field for the isentropic case. The computations were carried out for only a portion of the blowdown period, and therefore, the contours do not describe the entire exhausting process. As is expected, the temperature and pressure initially decrease across the Taylor wave, and more so after being processed by the exhausting wave. The values of pressure can reach as low as $P/P_{CJ} = 0.38$ and $P/P_{CJ} = 0.13$ within the simple and complex regions, respectively. Similarly, the values of temperature can reach as low as $T/T_{CJ} = 0.89$ and $T/T_{CJ} = 0.79$ within the simple and complex regions, respectively.

Figure 5.7 provides a quantitative comparison between the isentropic and non-isentropic flow fields. The non-isentropic flow fields were computed with a value of $\beta = 50$. The plots represent the percentage differences in pressure (5.7(a)), temperature

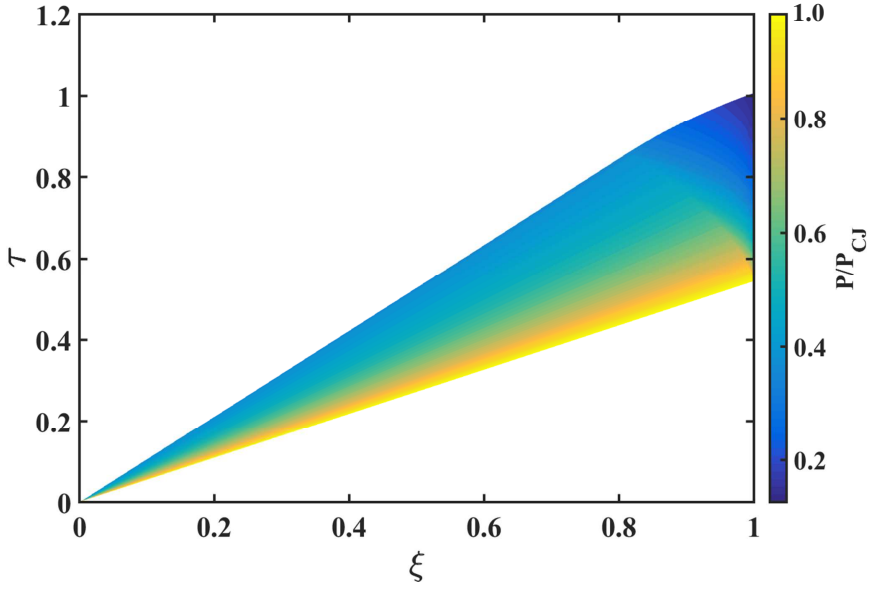

(a)

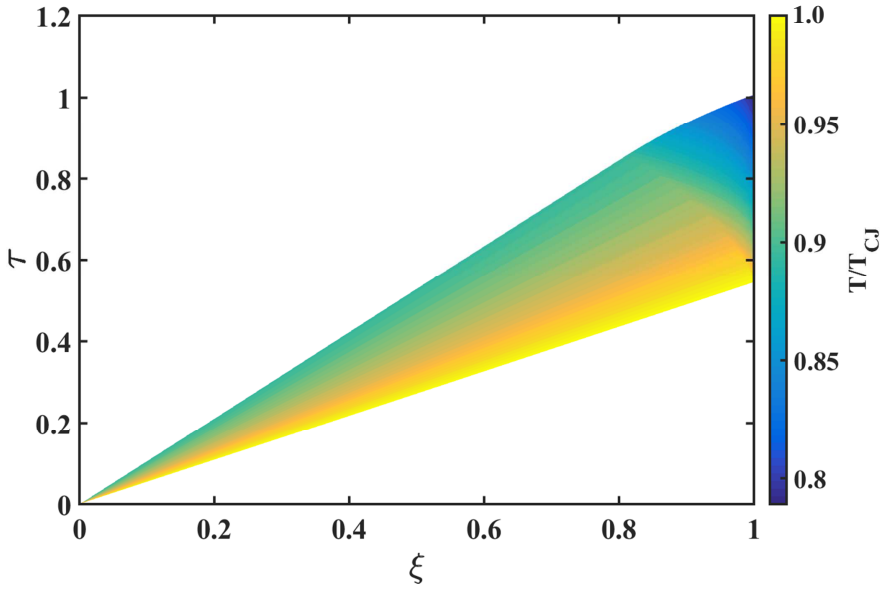

(b)

Figure 5.6: Computed (a) pressure and (b) temperature contours of a stoichiometric H_2-O_2 detonation wave propagating through a tube with an open end. Contours correspond to the case of an isentropic expansion of the CJ-state gas, neglecting all energy loss mechanisms.

(5.7(b)), and entropy (5.7(c)), between the two cases. The largest differences occur within regions of the flow that are moving fastest, and where the particles have been subject to the energy loss mechanisms the longest. For example, particles originating from a location near the closed end of the tube will experience minimal energy losses because they are in motion for a very short period of time. In other words, the time of arrival between the detonation wave and tail of the Taylor wave is small. Since the convective heat transfer and friction losses only take place when the fluid is in motion, there is a minimal effect near the closed end of the tube. The largest differences occur near the open end of the tube, where a fluid element is never stagnated and is expanded to sonic speeds by the exhausting wave.

The value of the product $C_f\beta$ is an important parameter in the current model. In fact, the solution of the flow field is unique to a given value of $C_f\beta$. This can be seen by inspection of the governing equations, where the nondimensional product $(C_f\beta)$ is observed to solely determine the extent the solution deviates from the self-similar isentropic case. In the current study, C_f was always kept constant, and therefore the value of β was the controlling free parameter.

The length scale ratio (β) determines the magnitude of the energy loss mechanisms and the time duration the flow is subject to them. Increasing the value of β increases the transport of momentum and heat to the walls, and causes a greater deviation from the isentropic solution. Smaller diameter tubes will increase the wall shear force (Eqn. D.35) and the heat transfer rate (Eqn. D.31). Moreover, longer tubes subject the flow to the energy loss mechanisms for extended periods of time, and therefore result in larger deficits in the post-detonation gas properties.

The energy losses to the wall can have a significant impact on the properties of the gas exhausting from a detonation tube. Figure 5.8 shows the computed exit pressure (Fig. 5.8(a)) and temperature (Fig. 5.8(b)) of several cases with varying values of β. The black curves correspond to the case of isentropic expansion of

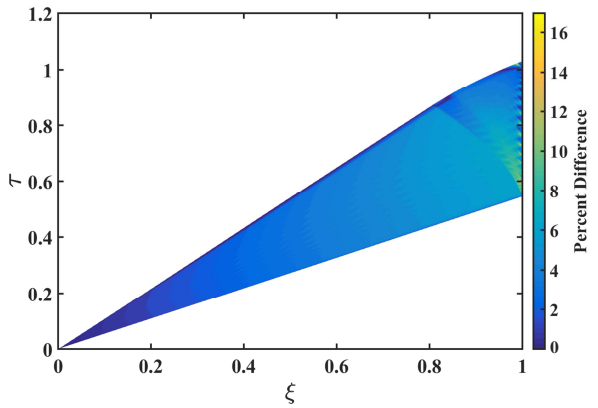

(a)

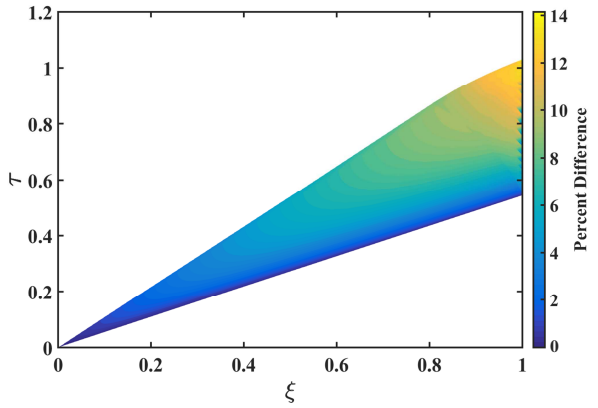

(b)

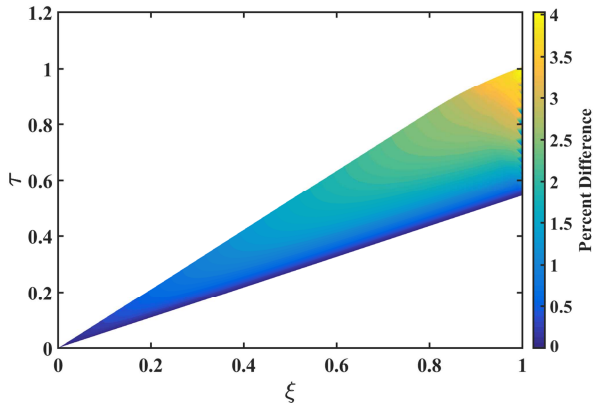

(c)

Figure 5.7: A comparison of the flow field properties between an isentropic flow following the detonation, and the case with heat and momentum losses with a value of $\beta = 50$. The color contours represent the percentage difference in the distribution of (a) pressure, (b) temperature, and (c) entropy. The contours were computed for a stoichiometric H_2-O_2 detonation wave propagating through a tube with an open end.

the post-detonation gases, while the other curves correspond to increasing values of $C_f\beta$. All of the computations correspond only to the time when the detonation first arrives at the closed end, until the time when the tail of the exhausting wave clears the open end. The results show that the pressure asymptotes to nearly the same value with increasing β, however, the rate at which the pressure decreases within the vicinity of the detonation increases. This is attributed to the increased expansion that occurs immediately downstream of the detonation wave. As β is increased, the rate of temperature decay is observed to increase. Moreover, the gas temperatures are cooled to lower values, significantly reducing the available thermal energy of the gas over the exhausting process. Based on these observations, we can therefore expect the effects of the energy losses on the flow properties exhausting from the PD to have a significant effect as the variable β is increased.

5.5 Discussion of Model Assumptions and Implications

The formulation of the model is inherently only capable of capturing the effects of the loss mechanisms downstream of the sonic plane, and does not consider losses occurring within the reaction zone or how those losses couple with the flow past the sonic plane. The one-dimensional model treats the energy transfer processes as a set of source terms, simplifying the numerous and complex nature of transverse energy transport mechanisms. Before evaluating the accuracy of the model in predicting the experimentally measured pressure along the tube, we consider several physical time-scale arguments to provide a means of identifying the physical phenomena that may or may not be captured. The physical description of the loss mechanisms provided by Fig. 5.2, relies on the formation of viscous and thermal boundary layers to transfer energy from the freestream flow to the walls. If the diameter of the tube is of the same order as a physical scale in the axial direction, such as the reaction zone length, gas properties in the freestream can be altered by an additional mechanism. Since the flow

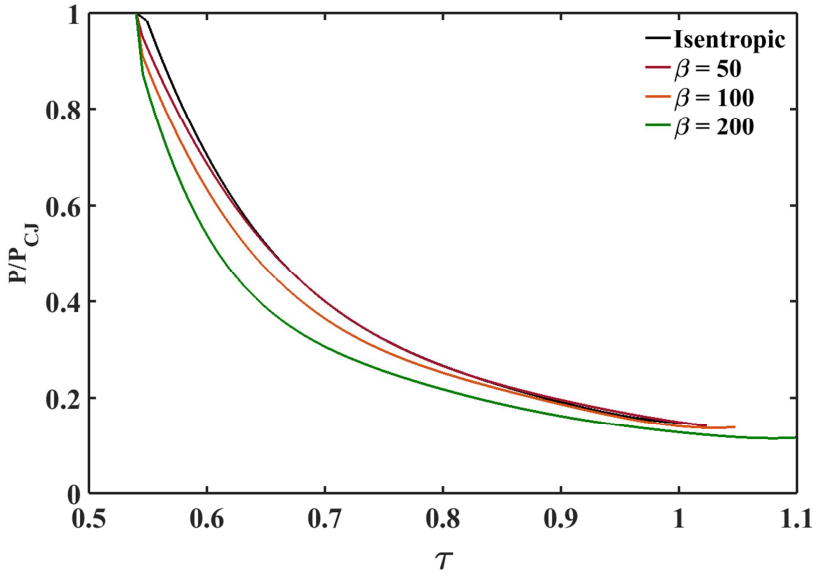

(a)

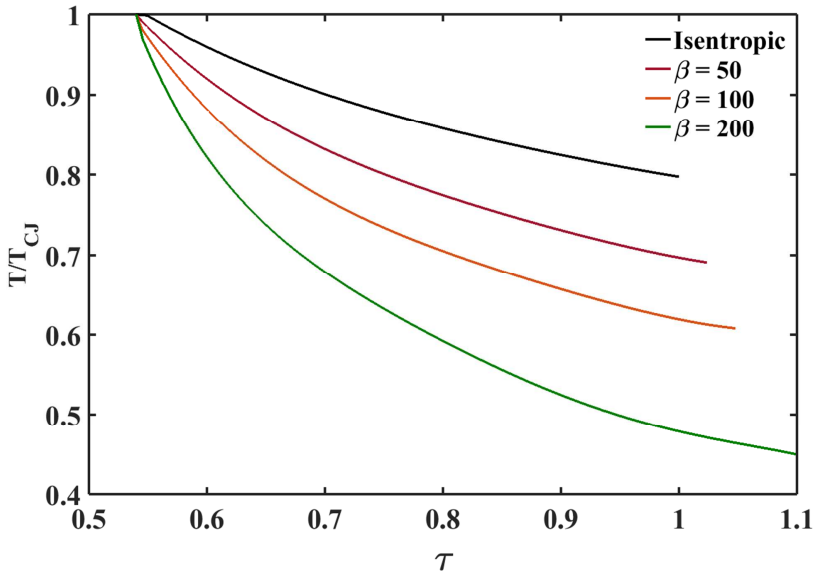

(b)

Figure 5.8: Computed (a) pressure and (b) temperature profiles at the exit ($\xi = 0.99$) of the detonation tube. The curves correspond to the isentropic case as well as cases with increasing values of $\beta = L/d$.

is subsonic, the properties of the freestream flow can be altered by the loss of energy at the walls through transverse propagating waves. These transverse waves further complicate the detonation wave model and invalidate the approximation of a one-dimensional structure. If the time scale of the transverse waves to propagate between the freestream and the tube wall is less than the chemical time scale, significant effects on the detonation wave structure can be observed. Moreover, this mechanism will persist past the sonic plane altering the post-detonation gas properties.

Since the characteristic velocity scales in the radial and axial directions within the vicinity of the detonation are approximately equal to the acoustic speed of the burned gas, it is a comparison of the relative length scales that determines how large of a role this effect has. This length scale ratio will be referred to as

$$\sigma = \frac{d}{\Delta_R} \tag{5.20}$$

Typically, detonation tubes are operated and studied within the regime where the chemical time scales are much shorter than the transverse (radial) expansion time scales ($\sigma >> 1$). Therefore this loss mechanism is not observed to affect the detonation parameters (such as propagation speed) since the losses at the tube wall are communicated over relatively long distances downstream of the sonic plane. However, they have still been observed to have a significant effect on the trailing post-detonation products within the Taylor wave. In the present study the diameter of the PD tube (4.8 mm) is of the same order of the reaction zone length ($\sim$1 mm). Therefore it is expected that this loss mechanism will have a significant effect on both the detonation structure and properties of the trailing burnt gas.

The value of C_f used in this study was obtained strictly from heat-flux measurements and disregarded friction effects [160, 173]. Moreover, the measurements were obtained with tube diameters on the order of centimeters with hydrogen as the fuel. Therefore, the values of σ were much greater than one. The numerical simulations of Ref.

[166], which used this value of C_f and were intended to model the post-detonation gas properties only, were capable of accurately predicting experimentally measured pressure profiles by only considering heat transfer effects and neglecting momentum losses. Therefore, it is believed that losses due to the viscous boundary layer may have an insignificant impact on the gas past the sonic plane within the range of parameters that were considered. However, this is only true because of the regime of PD operation that was under investigation, where the tube diameter was at least an order of magnitude larger than the reaction zone length.

In the present study, the same value of the friction coefficient is used for heat transfer as well as momentum losses. This in it of itself is an approximation since the measured values of the friction coefficient were only based on heat flux measurements and are not intended to capture momentum loss effects. Moreover, since the work of Refs. [160, 173] used a detonator tube with a value of σ much greater than one, the heat transfer rates and subsequently inferred value of C_f, are assumed to be lower than what are realized in the experiments of the present study.

The present model does not consider flow processes occurring within the reaction zone itself. Sufficient losses can occur within this region that can alter the detonation structure and properties, without having a significant effect on the detonation propagation speed. These losses are not captured with this model. Lastly, when the flow is brought to sonic conditions at the CJ-plane, there will be a number of competing effects that determine the subsequent flow properties downstream of the sonic plane. The effects of friction (fanno flow) and diverging of the freestream flow to the walls act to drive the flow to supersonic speeds. Meanwhile, the overall effects of cooling the freestream (rayleigh flow) and the trailing Taylor wave act to drive the flow to subsonic speeds. This complex interaction may may persist for sufficiently long times to have a substantial effect on the thermodynamic properties of the burnt gas within the vicinity of the CJ-plane.

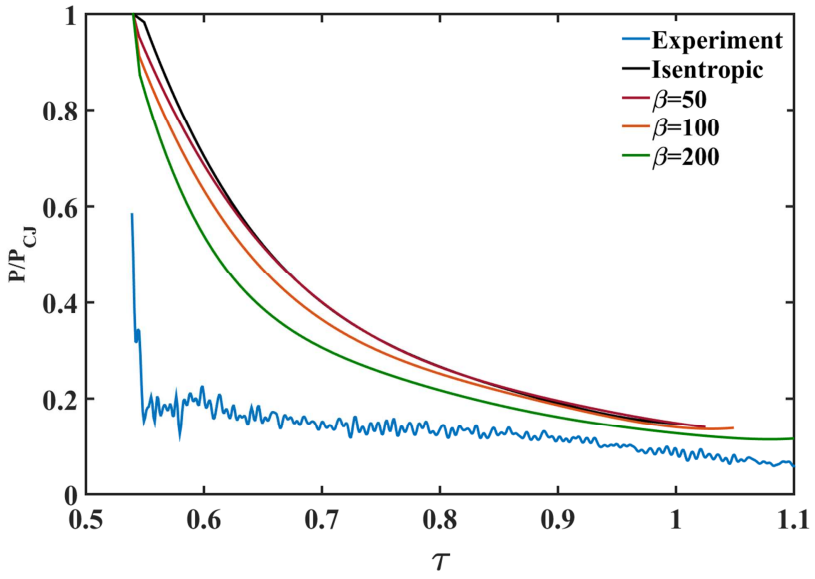

Figure 5.9: Comparison of a typical experimentally acquired pressure trace near the open end of the tube and the computed pressure profiles for several values of β. All results are for a stoichiometric H_2-O_2 detonation wave with $P_1 = 0.5$ atm and $T_1 = 300$ K.

Figure 5.9 compares calculated and experimentally measured pressure traces of a stoichiometric H_2-O_2 detonation wave with $P_1 = 0.5$ atm and $T_1 = 300$ K. The measurement was taken using the same PD device described in Section 3.2.2, at a location of $\xi = 0.95$. The value of β is approximately 160 for the experimental PD device that was used in this study. The results show that the current model is incapable of faithfully capturing the properties of the post-detonation gas. This is especially the case within the vicinity of the detonation wave, where a sharp decrease in pressure occurs over several microseconds, when in the ideal case it is predicted to take place over several hundreds of microseconds.

It is important to note that the calculated pressure traces correspond to only a portion of the blowdown period, and refer to the time between the arrival of the denotation wave and when the tail of the exhausting wave has cleared the open end. Therefore, the total blowdown period is several times longer than the period of time that is shown (see Fig. 5.5). On the other hand, the experimentally acquired trace

corresponds to the total blowdown period, defined as the time between the arrival of the detonation wave, and when the measured pressure reaches ambient conditions. Therefore, if the detonation tube was being operated under [near] ideal conditions, the experimental pressure trace would be ~ 4 times longer than the computed profiles.

The detonations that were experimentally generated were measured to propagate nominally at the CJ-speed, however, immediately downstream of the detonation wave, a considerable deficit in pressure was measured. Based on several experimental and numerical studies [169, 170, 175] the detonator tube was being operated well within the detonation limits. This is attributed to the fast chemical time scales of H_2-O_2 chemistry, which are capable of sustaining the detonation with such a small diameter. The large discrepancy between the numerical and experimental results implies that significant losses are occurring within the reaction zone itself. This however would mean that the detonation wave parameters, such as propagation speed, would be effected. However, no velocity deficits, outside of the spread shown in Fig. 3.8(a), were measured experimentally. There may be several ways to reconcile this inconsistency:

1. There may very well be a detonation velocity deficit that was not resolved experimentally. The resolution of the detonation speed measurements is accurate to within approximately ± 25 m/s. A deficit in the propagation velocity would invalidate the use of the present model because it assumes that there are little to no losses occurring within the reaction zone, and that the properties at the CJ-plane are indeed what is computed with the classical hydrodynamic theory of detonations [66, 68].

2. There may be energy losses occurring within the reaction zone that are insufficient to altering the detonation parameters, but are substantial enough to alter the post-detonation gas properties.

3. A combination of several other mechanisms, such as conductive heat transfer,

water condensation, and chemical recombination at the walls, could have a significant impact on the flow[176, 177].

4. The use of a skin friction coefficient of $C_f = 0.006$ to describe both the heat transfer and momentum losses may be inadequate for several reasons. First, it invokes the assumption of the Reynolds analogy, which may not be the case in such turbulent regimes of operation. Secondly, the value of C_f that was used is based on experimental heat-flux measurements with pulsed detonators that were an order of magnitude larger in diameter than the one used in this study. Therefore, it may not be a representative coefficient in the current regime of operation.

5. The one-dimensional model treats the momentum and convective heat losses as source terms and does not consider the effects that the initial pressure has on the subsequent detonation. For example, the initial pressure will have implications on chemical reaction rates within the reaction zone, as well as the growth rates of the viscous and thermal boundary layers. In reality, maintaining a value of β and varying the initial mixture pressure should have a significant effect on the detonation wave parameters and properties. However, this is not the case with the present model.

CHAPTER VI

Experimental Observations and Analyses

6.1 Introduction

Several experimental campaigns were undertaken to understand the fluid mechanic and chemical effects that a detonation wave and subsequent products had on a reacting transverse jet in supersonic crossflow. The PD was staged downstream of the JISCF, and was capable of providing a short-duration, high temperature and momentum, radical-rich plume of gas to the wake of the primary jet. In this study, high-speed schlieren and OH^* chemiluminescence imaging are used to study the temporal evolution of the interaction of the PD with the primary jet. OH^* imaging was used as a proxy of the global heat release distribution. Furthermore, planar laser-induced fluorescence (PLIF) of OH was used to mark the distribution of OH throughout the flow field and to infer the instantaneous, local structure of the reaction zones and post-combustion regions as the interaction of the PD with the primary jet evolves in time. Several mechanisms of interaction are believed to take place throughout the flow field that lead to an overall enhancement in combustion. The fluid mechanic and chemical effects are, to a first order, decoupled by varying the primary jet injectant between hydrogen and helium.

In the following sections, experimental observations of the structure of the isolated PD issuing into the crossflow and the effects of the PD on the structure and com-

bustion characteristics of the JISCF system are made. Variations in the primary jet momentum flux ratio provide an understanding of the coupling between the primary jet and PD. All images are presented with a time-stamp to indicate when they were taken relative to the time when the detonation wave cleared the PD exit port. The image axes are normalized by the diameter of the primary jet (d = 2mm), which is located at $x/d = 0$. The images provided in this chapter represent only a subset of the total acquired data, and are intended to summarize numerous observations in a concise and condensed manner. The descriptions and analysis that are made throughout the study are based on carefully repeated experimental runs under nominally identical conditions. To better quantify a number of morphological properties, a statistical investigation was carried with the collected data. However, because of the short test times generated by the expansion tube facility and the inherently turbulent, unsteady, and three-dimensional nature of the phenomena being studied, a thorough statistical analysis of the combustion properties was not possible.

6.2 Experimental Methodology

The high-enthalpy supersonic crossflow was generated with the Michigan Hypersonic Expansion Tube Facility (MHExT) [148, 159]. A single crossflow condition with air as the composition was used throughout all of the experiments. The effective bulk flow properties were inferred from a series of calibration experiments prior to undertaking the combustion studies. The calibration experiments relied on measurement techniques similar to those discussed in Chapter IV. An example of simultaneously acquired pitot and static pressures in the test section is shown in Fig. 6.1(b). The nominal freestream properties used in the present study were representative of combustor entry conditions for Mach 7 flight: $M_\infty = 2.35$, $P_\infty = 40$ kPa, $T_\infty = 1330$ K, and $U_\infty = 1660$ m/s. The useful test time was measured to be approximately 600 μs. Quantification of the shot-to-shot variation of the test gas thermodynamic properties

was performed statistically from the measured primary and secondary shock speeds. The range of shot-to-shot variability was approximately 1.1%, 2%, and 1.5% of the bulk values of the freestream Mach number, pressure, and temperature, respectively. Figure 6.1(a) is an image of the test model mounted inside of the MHExT test section.

Throughout the series of experiments, the only parameter that was varied was the momentum flux ratio J_{j} of the primary jet. The values of J_{j} were chosen to span a number of flame stabilization regimes [3]. Lower values of J_{j} confine the primary jet penetration height to the order of the boundary layer thickness ($\sim$ 1 mm), while larger values result in more prominent shock structures and deeper penetration into the freestream. A summary of the test parameters for the various cases are presented in Table 6.1. The momentum flux ratio J_{j} was varied between values of 0, 0.5, 2.5, and 5.0 by varying the jet stagnation (plenum pressure) as outlined in Table 6.1.

In this study, the PD blowdown process is separated into two components, each with its characteristic value of momentum flux ratio (refer to Fig. 5.1). The first component, which is experimentally observed to impact the flow field for approximately 20 μs, is associated with the transmitted wave itself. The momentum flux ratio over this period of time is denoted by J_{CJ} , and is approximated and evaluated in terms of the detonation wave Mach number and pressure rise for a lean ($\Phi = 0.85$) H_2-O_2 detonation (determined from the CEA equilibrium code [110]). The expected temperature and pressure ratios across the transmitted detonation wave are approximately 12 and 18, respectively. The pressure traces in Fig. 5.1 do not capture this pressure rise, and the reasons are believed to be due to the large convective wave speeds, steep property gradients within the vicinity of the detonation wave, and the limited response time of the sensors.

The second component of the blowdown process, which is approximately 250 μs long, is associated with the high-temperature, radical rich detonation products that are expanded out of the detonator tube. The momentum flux ratio during this period,

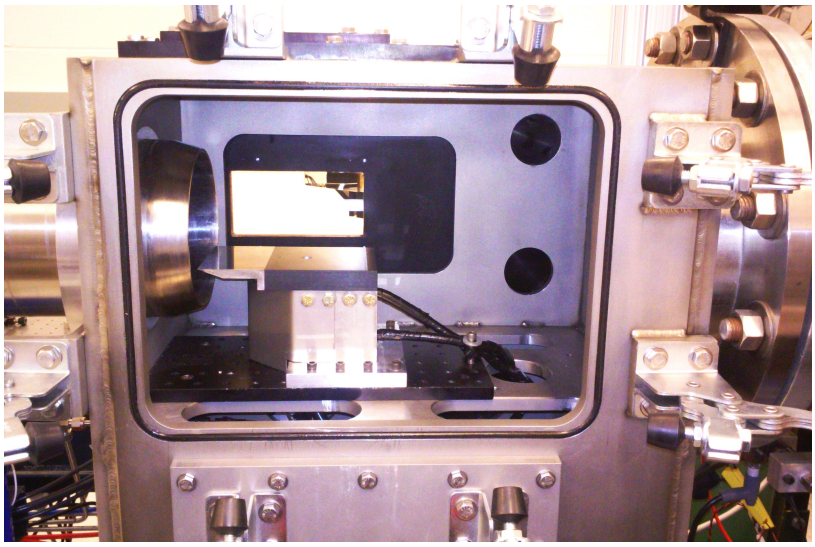

(a)

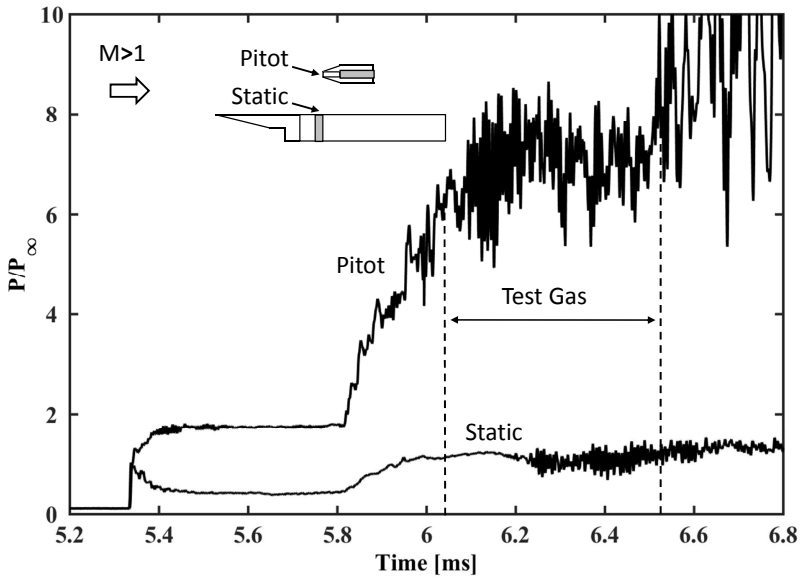

(b)

Figure 6.1: (a) Image of staged JISCF-PD test model mounted inside of the MHExT test section. (b) Simultaneously acquired pitot and static pressure measurements of the high-enthalpy flow condition used for the series of combustion experiments.

denoted by J_{bd}, is defined by the measured pressure near the open end of the tube, and assuming that the gas is expanded to sonic conditions ($M = 1$) at the exit. A summary of the PD momentum flux ratios is given in Table 6.1. The value of J_{bd} decreases during the blowdown process since the exit pressure decreases, therefore, the tabulated values are the initial values soon after the passage of the detonation wave ($P = 155$ kPa). The temperature of the exhausting gas over the blowdown process is difficult to determine, and is not simply given by an isentropic expansion from the CJ state gas. This is because of the non-isentropic processes of momentum and heat loss that occur within the PD tube. Since the model described in Chapter V is incapable of fully replicating the experimentally measured PD pressure profile, the complete thermodynamic state of the exhausting post-detonation gas was not determined. However, since the PD will be shown to exhaust OH radicals throughout the entire blowdown process, it is inferred that the gas exit temperature is always greater than 2000 K. This can be seen by inspection of Fig. 6.2 which shows the equilibrium species concentration of a stoichiometric H_2-O_2 mixture at a constant pressure of 0.5 atm and as a function of temperature. The mole fraction of all species correspond to the left axis, while that of H_2O corresponds to the right axis. At this pressure, which is the nominal freestream value, the equilibrium composition will contain radicals such as OH as long as the temperature of the reactants is above 2000 K.

As was discussed in Section 2.2.2, the interaction between the primary jet and cross flow significantly alters the pressure field in the near-jet region [2, 43]. The pressure modification is complex and varies in a nonuniform manner around the injector. A low pressure wake is formed downstream of the primary jet where its size and magnitude depends on J_{j} . For larger values of J_{j}, the wake pressure decreases and encompasses larger regions of the flow. Since the exit of the PD tube can reside within the low pressure wake, the tabulated values of J_{CJ} and J_{bd} reflect the subsequent

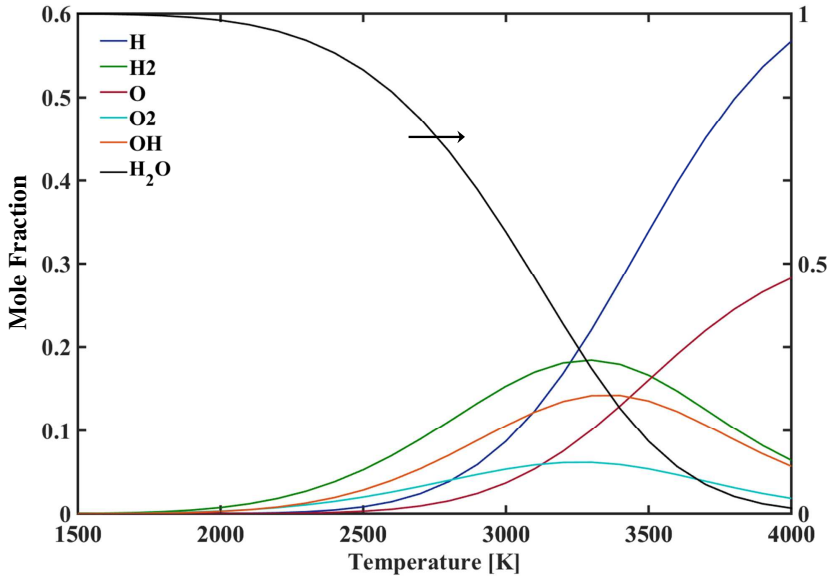

Figure 6.2: Equilibrium species composition of a stoichiometric H_2-O_2 mixture as a function of temperature and at a constant pressure of 0.5 atm. All profiles correspond to the left axis except for H_2O.

increased expansion of the exhausting detonation wave and products. In other words, the variation in the values of J_{CJ} and J_{bd} between cases is a consequence of their dependence on J_{j} which was the only parameter that was independently varied during this study. Lastly, it is important to note that cases C and D have equivalent values of J_{CJ} and J_{bd} because the size of the low pressure wake downstream of the primary jet does not extend to the PD exit port as it does in other cases.

Case	$J_{\mathbf{j}}$ [–]	$\dot{m}_{\mathbf{j}}$ [g/s]	$P_{\mathbf{0j}}$ [kPa]	$J_{\mathbf{CJ}}$ [–]	$J_{\mathbf{bd}}$ [–]
A	5.0	3.9	2030	250	1.2
B	2.7	2.1	1095	170	0.8
C	0.5	0.4	200	125	0.6
D	0	0	0	125	0.6

Table 6.1: Test matrix summarizing several parameters of the primary jet and pulsed detonation tube. Quantities with the subscript j refer to the primary jet, while the subscripts CJ and bd refer to the pulsed detonation. The mass flow rates are specific to hydrogen as the injectant composition.

6.3 Flow Structures

The shock and fluid structures of the flow fields were visualized with the schlieren technique. An example of a set of images that were acquired at a frame rate of 63 kHz and with an exposure time of 310 ns, are presented in Fig. 6.3. The images from the first row to the last provide a time-series of the impact of the PD blowdown process on the flow field. The first, second, and third columns correspond to cases A, C, and D, respectively. A number of images are labeled to highlight pertinent flow features and their evolution. Point A indicates the location of either a bow shock (cases A and C) or a Mach wave (case D). The formation of these waves is a consequence of flow blockage and therefore, their strength depends on J_{j}. Larger values of the primary jet momentum flux ratio lead to stronger shocks that subsequently have a greater impact on the flow field as well as combustion characteristics. The Mach wave identified in case D is believed to originate from the presence of the PD port which was 4.8 mm in diameter. Point B indicates the location of the intersection of the generated wave with the top of the image. This provides, to first order, a measure of the global strength of the three-dimensional wave system. For example, during the blowdown process the strength of the waves are increased, leading to greater shock-heating as well as pressure losses. Moreover, the interaction of the strengthened waves with the incoming boundary layer may lead to separation or larger recirculation regions upstream of the primary jet. Due to the poor resolution of the imaging system, the formation of a separation shock and subsequent recirculation region upstream of the primary jet cannot be clearly identified. However, they will be shown to exist indirectly using other imaging techniques in the following sections.

When the detonation wave reaches the open end of the tube, a shock wave is transmitted and diffracts into the flow field. The strength of the transmitted wave, which is (ideally) initially the von Neumann spike, decays as the flow trailing it expands radially. Point C indicates the location of the transmitted shock wave for the

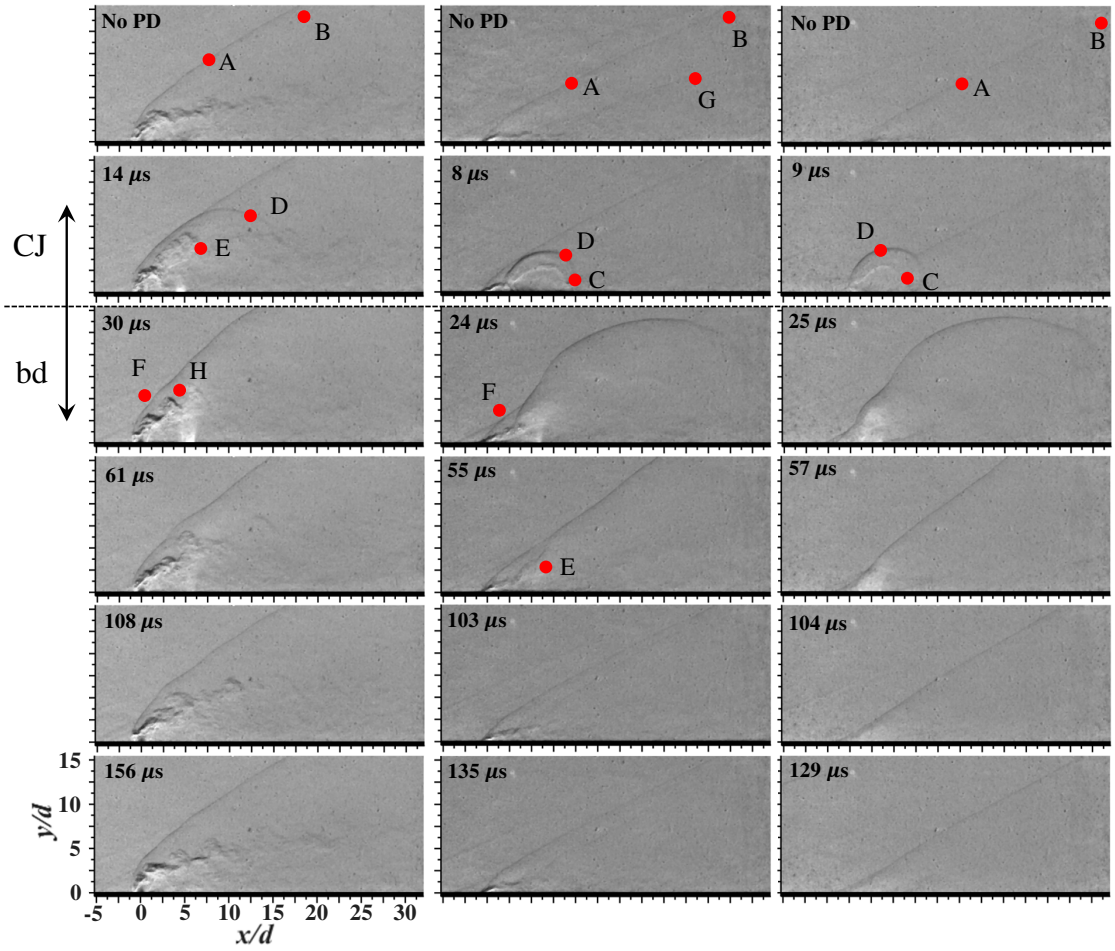

Figure 6.3: Schlieren pseudo-time-series of the blowdown process for case A (1st column), case C (2nd column), and case D (3rd column). All images were acquired with a 310 ns exposure. The labels are described in the text.

cases where it is captured. It is observed as a light curved wave feature that emanates into the flow, and provides a delineation of the original JISCF system and the post-detonation products. The transmitted wave and trailing post-detonation products act as additional flow blockage that alter the flow speed and pressure distribution within their vicinity. Therefore, a second bow shock which is indicated by point D is formed around the transmitted wave to adjust the incoming flow properties. The unsteady formation and propagation of the second bow shock is a consequence of the modified flow field. It is observed to propagate radially into the flow until it merges with the initial shock system given by point A (cases A and C).

The initial expansion of the PD products into the flow takes place in the form of a high-momentum flux ratio underexpanded jet. Upon reaching the barrel shock structure of the PD, the primary jet fluid is expanded around the fluidic body of the exhausting post-detonation gases [27]. This leads to a significant alteration of the primary jet trajectory, causing it to penetrate deeper into the crossflow as is indicated by points labeled E. As was discussed in Section 2.2.4, the interaction of the crossflow, staged primary jet, and PD create a complex flow field that depends on several parameters such as the spacing and distribution of momentum flux ratios and mass flow rates between the primary jet and PD. For case A, it is believed that the region between the primary jet and PD remains subsonic during the majority of the blowdown period since only one (combined) bow shock is observed upstream of the primary jet, labeled F. On the other hand, case C reveals a more complex flow in the region between the primary jet and PD at the location labeled F. In this case, the bow shock formed by the primary jet intersects a second bow shock formed just upstream of the PD. This intersection occurs at approximately $x/d = y/d = 3.75$. This implies that the flow in the region between the primary jet and PD recovers to supersonic speeds, and the presence of the PD flow blockage requires that a second bow shock be formed to adjust the incoming flow properties. However, the region

between the primary jet and PD where $y/d < 2$ is believed to be subsonic since the bow shock that forms around the PD does not extend to the floor, but terminates at the location of intersection with the primary jet boundary. Therefore, for sufficiently large values of J_{j} (case A and B which is not shown), the entire region between the primary jet and PD is subsonic. Whereas for low values of J_{j} (case C), the subsonic flow between the primary jet and PD is confined to regions near the floor. Regions further from the floor are initially processed by a weak portion of the primary jet bow shock and recover to supersonic speeds before being processed once again by the bow shock formed by the PD exhaust.

Point G indicates the formation of a weak shock that emanates from the shear layer of the primary jet and crossflow boundary. The presence of eddies along the shear layer intrude into the incoming flow sufficiently to form relatively weak waves. Lastly, the interaction of the post-detonation gases and primary jet cause eddies that form at the upstream primary jet-crossflow boundary to grow larger. This can be seen by the point labeled H. This is postulated to be caused by an amplification of the Kelvin-Helmholtz instability, which may in turn lead to increased near-field mixing of the primary jet fluid as was observed in Refs. [26, 27]. The impact that the detonation tube has on the flow field is observed to decrease with time as the PD momentum flux ratio decreases from the tabulated J_{bd} value to zero (Table 6.1). By comparing the first and last rows, the shock wave systems recover to their undisturbed JISCF steady-states after approximately 1/2 of the blowdown period. Therefore, significant hydrodynamic effects of the PD on the flow field are only observed to take place during the first half the blowdown period. During the remainder of the blowdown period, the influence of the PD on the flow field is believed to be confined and limited to the boundary layer. This is a consequence of the non-ideal operation of the detonation tube used in this study, where a significant portion of the post-detonation gas kinetic energy is dissipated by interaction with the tube walls.

6.4 Heat Release Distribution

The global characteristics of the combustion system were investigated with OH* chemiluminescence imaging of chemically excited hydroxical radicals, as they decay from the $A^2\Sigma^+$ excited electronic state to the $X^2\Pi$ ground state through spontaneous radiative emission. The collected fluorescence is used as an approximate indicator of heat release. The technique provides a temporally and line-of-sight integrated visualization of the characteristics of the evolving combustion processes. The images were acquired at a frame rate of 41 kHz and with an exposure of 24.4 μs. The frame rate was chosen to provide sufficient insight regarding the temporal evolution of the combustion processes, and therefore segment the blowdown process into approximately 10 frames. While the long exposure time did not provide instantaneous images of the combustion processes, it minimized the amount of emitted light that was not collected between frames, which was an important pre-requisite in using the data for any subsequent heat release analysis. In addition, the images were acquired and post-processed in the same manner between all cases. Since the intensity of the collected radiation varied significantly between cases with and without the PD, the presented images were normalized differently to provide a meaningful visual analysis of the combustion processes. The difference in intensity scale can be determined by comparing the scaling of the color maps between separate figures.

6.4.1 Jet in Supersonic Crossflow

Figure 6.4 is an example of acquired OH* images of the reacting jet in supersonic crossflow. The first, second, and third rows correspond to cases A, B, and C, respectively with no PD present. The first column represents the temporally integrated signal over a 24.4 μs period (1 frame), which corresponds to approximately twice the characteristic large-scale convective time scale of the system. This was determined by comparing a characteristic length scale, taken to be the maximum observed jet

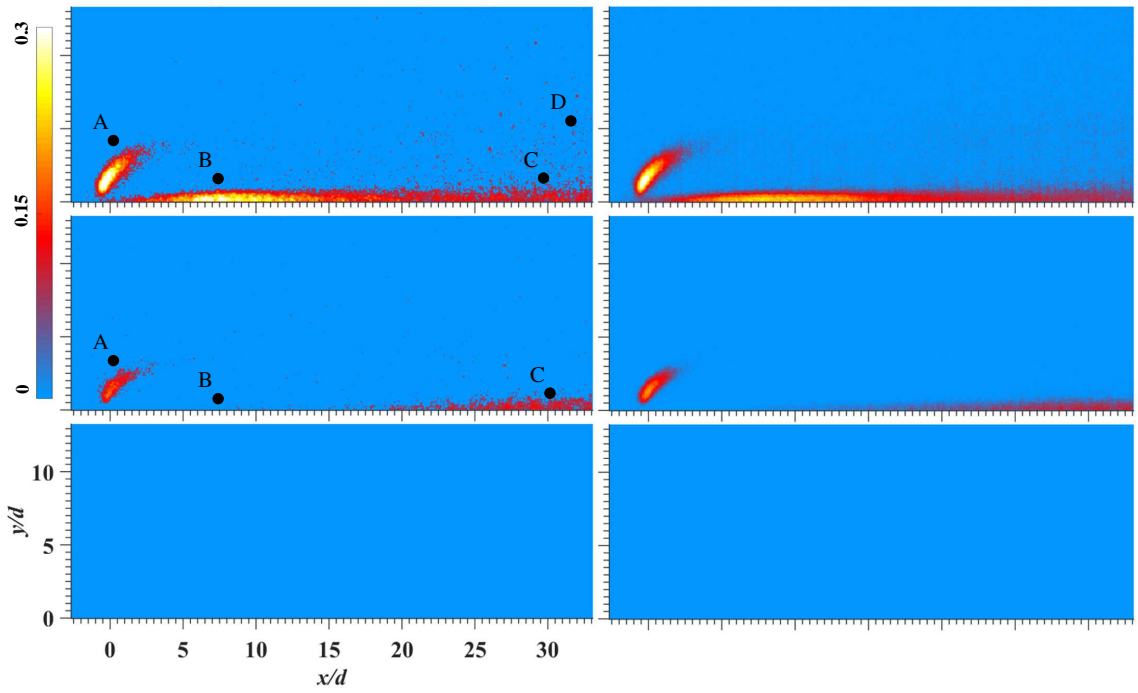

Figure 6.4: Line-of-sight integrated OH* chemiluminescence images of the global flame structure of the isolated primary transverse jet of case A (1st row), case B (2nd row), and case C (3rd row). The images of the left column are single frames with a 24.4 μs exposure. The images on the right column are an average of 10 frames, each with a 24.4 μs exposure. The labels are described in the text.

penetration, to a characteristic velocity, taken to be the mean between the freestream ($U_\infty = 1660$m/s) and jet exit velocity ($U_\mathrm{j} = 1200$ m/s). The frames were acquired well after the arrival of the test gas flow such that the flow was fully established (Section 4.3.3). The second column is the average signal collected over a period of time that is equivalent to the blowdown process (10 frames) which is equivalent to more than 20 times the characteristic large-scale convective time scale. The similarity between the first and second columns indicates that the combustion processes maintain a steady nature with respect to the time scale associated with the exposure time.

Analysis of the images reveals the indirect dependence of the combustion characteristics of the system on J_j . For low values of J_j reactions are not observed to take place within the field of view (case C). The fuel penetration is nearly the same as the boundary layer thickness, confining the fuel-air mixing to small regions near the

floor. The effects of compressibility have a negligible influence on ignition and flame stabilization. Therefore initiation of reactions relies on sufficiently long residence times of the fuel and air, considering the long ignition delay times of the relatively low temperature mixture. The contrast in heat release distribution between cases A and B indicates differences in the rate of evolution of processes that control ignition and heat release. As the value of J_{j} is increased, the flame stabilization location is observed to move upstream. In general, this is attributed to increased effects of compressibility which provide greater shock-heating and the formation of recirculation regions that serve to stabilize the flame [3]. Point A marks the presence of reactions occurring upstream of the primary jet boundary. Shock heating is sufficient to locally autoignite the fuel-air mixture and therefore, reactions are more intense for larger values of J_{j} . A drastic difference between cases A and B is observed near the wall in the leeward side of the primary jet (point B). For case A, near-wall burning is observed to increase from the location of injector to approximately $x/d = 7.5$, where intense emission takes place. On the other hand, no emission is detected within this region for case B. Instead, near-wall burning begins to stabilize at approximately $x/d = 15$. The contrast between these two cases is attributed to a competition between the effects of rapid flow expansion around the jet and chemical reaction rates. The flow expansion causes decreased temperatures and pressures while simultaneously increasing flame straining. These effects are sufficient to inhibit reaction rates immediately downstream of the jet for case B. However, as the flow is recompressed further downstream, chemical reactions progress favorably and the flame is stabilized. For case A, the initial flow expansion around the primary jet quenches reactions in a small region immediately downstream of the injector. However, unlike case B, a recirculation region upstream of the primary jet exists which promotes chemical reactions. With this additional mechanism, chemical reaction rates are ultimately sufficient to overcome the adverse effects of the flow expansion since intense burning is observed

immediately downstream of the small quenched region. The increased reaction rates are attributed to increased shock heating, as well as the supply of intermediates from the upstream recirculation zone. Near wall burning occurs in the far-field as the local mixtures have enough time to react (point C). However, heat release within the freestream wake of the jet is only observed within the field of view for case A (point D).

6.4.2 Staged Jet and Pulsed Detonation

The exhausting post-detonation products have a significant impact on the global heat release distribution of the flow field. Fig. 6.5 shows a pseudo-time-series of the blowdown process for cases A, C, and D (left to right). The high-temperature and radical-rich post-detonation gas is observed to penetrate deep into the cross flow as it first leaves the detonator tube (point A). The emission intensity is always greatest within the vicinity of the PD exit port, however, substantial heat release is observed throughout the entire flow field. At early times during the blowdown process, the outline of a swept barrel shock structure is identified. The barrel shock is terminated by a Mach disk which is identified by an intense burning region that is triangular in shape (point B). As the flow is expanded through the barrel shock, chemical reactions are quenched which is observed by an absence of radiative emission. Subsequently, the post-detonation gas is abruptly compressed through the terminating Mach disk, causing the local temperature to increase and chemical reactions to reinitiate. The location of the Mach disk is at the base of the triangular region which can be identified by the radiative emission from newly formed electronically excited hydroxyl radicals.

The region upstream of and surrounding the barrel shock is observed as a region of intense OH^* emission (point C) and is believed to be a consequence of two reasons. First, the expanding post-detonation gases can leave the barrel shock structure through the side boundary where they are compressed by an incident shock. Second,

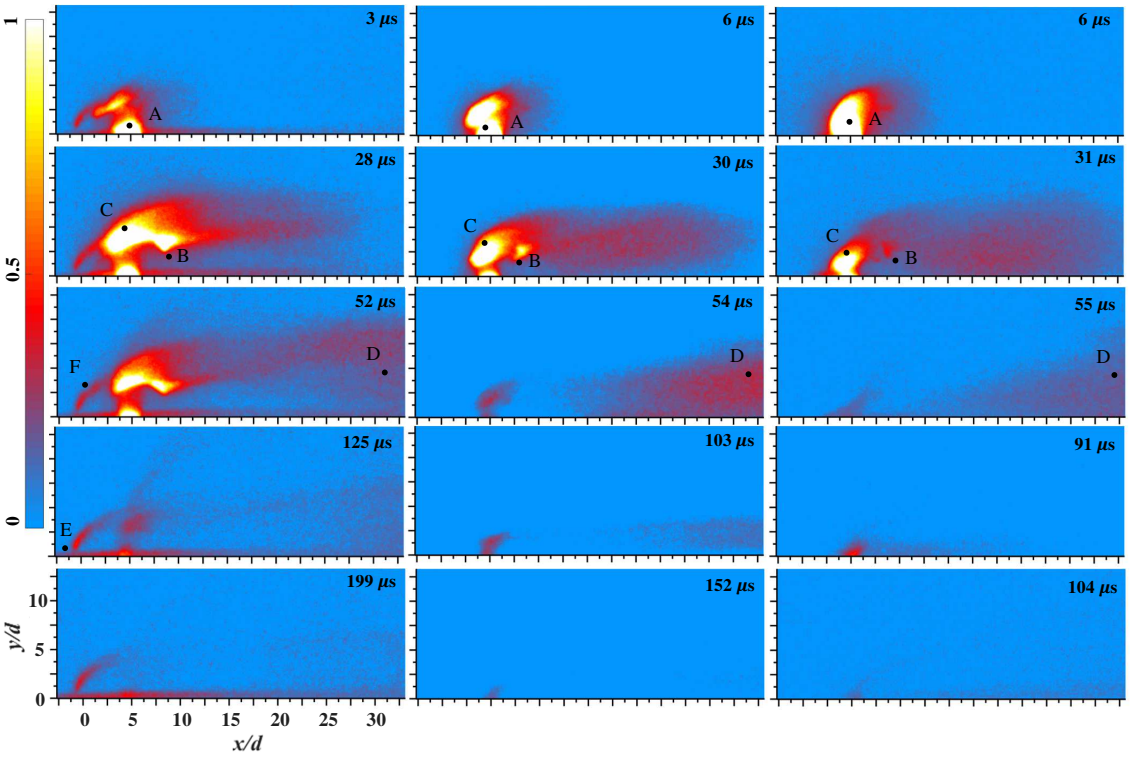

Figure 6.5: Line-of-sight integrated OH* chemiluminescence pseudo-time series of the global flame structure for case A (1st column), case C (2nd column), and case D (3rd column). All images were acquired with a 24.4 μs exposure. The labels are described in the text.

the high-temperature post-detonation gases are believed to cause the primary jet to auto-ignite within microseconds of mixing through a Damköhler number effect. An analysis on the ignition delay and flammability limit enhancement that the PD products provide to a reacting system is given in Chapter VII. Furthermore, the high temperature PD products are believed to augment ignition by pre-heating the fuel and is observed as increased heat release in the wake of the jet-PD system (point D). Finally, the high-momentum flux PD exhaust increases near wall burning even upstream of the primary jet (point E). The post-detonation gases are believed to transport upstream through the subsonic region between the primary jet and PD, as well as boundary layer. This enhances the flame stabilization characteristics of the upstream recirculation region that exists at sufficiently large values of J_{j} .

The distributions of OH^* chemiluminescence shown in Fig. 6.5 are used as a proxy for the global heat release. Therefore the streamwise distribution of the heat release $q(x/d)$ was obtained by integrating the signal along each column of an image. An example of a resulting series of profiles is given for case A in Fig. 6.6. Each curve represents the streamwise distribution of heat release temporally averaged over the exposure time (24.4 μs). The curves are labeled with increasing numbers to identify which frame they correspond to in time. The curve labeled 1, corresponds to the frame acquired just prior to the arrival of the detonation wave, and therefore represents the heat release distribution of the first (top-left) image in Fig 6.4. In this case, $q(x/d)$ first peaks near the location of the primary jet injector (point F), where it subsequently decreases to a non-zero value immediately downstream of the injector. In the far-field ($x/d > 25$) the heat release is observed to increase slightly and is attributed to the increased reactions in the wake of the primary jet (point D).

The remaining curves 2 - 9 represent the heat release during different times of the blowdown process. For example, the curves labeled 2 and 3 correspond to the first two images of Fig. 6.5 (case A). The peak signal is located at the PD exit port and

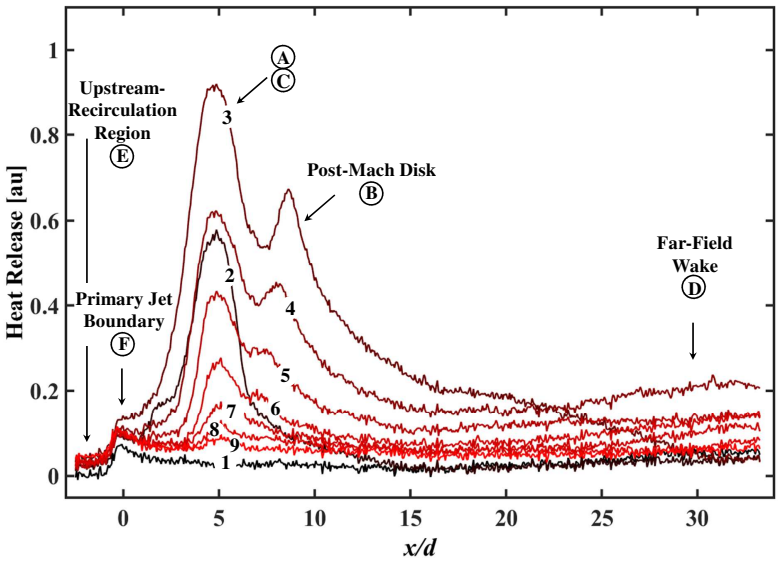

Figure 6.6: Temporal evolution of the streamwise heat release distribution during the blowdown process for case A. Each curve corresponds to a vertical integration (along each column) of the signal acquired over a 24.4 μs exposure. The labeling of the curves corresponds to the frame number from the series they were acquired. The alphabetic labels are described in the text and pertain to the same labels of Fig. 6.5.

corresponds to a number of phenomena such as, the emission of the reacting post-detonation gas as it first exits the PD (point A), reactions of the post-detonation gases as they are compressed through the barrel shock boundary (point C) and enhanced reactivity of the impinging primary jet fluid (point C). The second largest peak occurs just downstream of the PD exit, and corresponds to the intense emission from reactions that are reinitiated after being compressed by the Mach disk (point B). Interestingly, the heat release is increased along the entire streamwise direction, including the upstream recirculation region (point E) of the primary jet. The post-detonation gases are believed to transport upstream through the boundary layer as well as the subsonic region between the primary jet and PD.

6.4.2.1 Coupling Between Jet and PD

Varying the primary jet momentum flux ratio provides a means of identifying several coupling effects that take place between the primary jet and PD exhaust. First, although the blowdown period defined by the pressure traces in Fig. 5.1 has been established to extend to approximately 250 μs, the emission from the short-lived OH^* species exhausting from the PD port ceases as early as 100 μs for case D. OH^* emission is observed to exhaust from the PD for longer portions of the blowdown period as J_j is increased. For example, detection of OH^* persists to approximately 250 μs, 220 μs, and 150 μs for cases A, B, and C respectively. Therefore, it is concluded that the post-detonation gases terminate their chemical reactions as they leave the PD, however, increasing J_j extends chemical reactions by subjecting the gases to greater expansions that tend to freeze the chemical processes.

Second, the size and intensity of the region of OH^* emission surrounding the barrel shock (point C) of the PD exhaust increases with increasing J_j . This is believed to be a consequence of a combination of chemical and fluid mechanic effects. First, increasing J_j also increases the mass flow rate of the primary jet, and hence may lead to increased reactivity of the primary jet within the vicinity of the PD. This is considered a chemical effect that will lead to greater heat release and would be recognized by larger and more intense regions of OH^* emission. Second, increasing J_j causes the low pressure wake of the primary jet to increase in magnitude and size. The consequence of this is considered a fluid mechanic effect because the modification of the pressure field increases the expansion of the post-detonation products at the exit. This in turn leads to effectively larger momentum flux ratios of the PD exhaust (as is outlined in Table 6.1) that increase penetration into the crossflow as well as compression through the barrel shock (point C) and Mach disk (point B).

Increasing J_j enhances both the fluid mechanic and chemical processes that lead to larger and more intense regions of heat release. From these results alone, it is

impossible to determine the independent role that the described mechanisms have on the flow field as J_j is varied. For example, it may very well be that the increased size and intensity of regions of OH^* emission surrounding the barrel shock are dominated by fluid mechanic effects, and that there is a negligible contribution from increased reactivity of the primary jet fluid. In order to distinguish between the fluid mechanic and chemical processes, and determine the extent of impact that each has on the flow as J_j is varied, the cases outlined in Table 6.1 were carried out with helium as the primary jet injectant composition. By using an inert gas with a similar molecular weight to hydrogen, a number of relevant fluid mechanic and flow processes are maintained. Specifically, this implies that properties of mixing rates, flow field pressure distribution, shock wave systems, recirculation regions, and jet/PD penetration do not vary significantly between cases of helium and hydrogen primary jet inectant. This first-order approximation is valid since several studies have shown that such properties primarily depend on the primary jet momentum flux ratio J_j, while the influence of flow parameters such as the primary jet density, exit speed, and Reynolds number can be regarded as having a high-order influence that do not alter the global features of the JISCF system [178, 179].

Helium is known to be an ineffective quencher of electronically excited OH in the $A^2\Sigma^+$ state [180, 181], where radiative decay is the primary decay process of OH in a bath of helium gas. On the other hand, collisions with hydrogen induces significant nonradiative decay processes. This is attributed to the relatively large quenching cross section of hydrogen reported in Ref. [182]. Since OH in the $A^2\Sigma^+$ state is more readily quenched by hydrogen, the collected emission for cases with hydrogen primary jet injectant will yield a smaller signal, under the assumption that temperatures remain low enough for combustion to not occur. If larger amounts of emission from OH^* is collected with hydrogen as the primary jet injectant, this implies that increased chemical reactions (combustion) are producing sufficient OH^*

to compensate for the increased quenching. Therefore, the following analysis will provide a conservative estimate of the contribution of increased reactivity of the primary jet (chemical processes) on the observed differences in size and magnitude of OH^* emission surrounding the barrel shock structure of the PD exhaust. Lastly, helium is known to be a less efficient third-body collisional partner than hydrogen since it is typically modeled with a Chaperon efficiency of 1.0 while hydrogen has a value of 2.0 or greater, depending on the kinetic mechanism [183]. This further supports that the current analysis will provide a conservative estimate of combustion enhancement by using helium to decouple chemistry from hydrodynamic effects.

A qualitative comparison between cases A, B, and C (bottom to top) with helium (left column) and hydrogen (right column) as the primary jet injectant compositions is given by Fig. 6.7. The OH^* emission during an early time of the blowdown process is presented for all cases. Furthermore, the time of acquisition for a given case and varying primary jet injectant are nearly identical and at most differ by approximately 1 μs, to provide a consistent comparison. For the cases with helium injectant (left), the size and penetration of regions of OH^* emission increase with increasing J_j . To first order, this is primarily due to an increased expansion of the PD exhaust which is observed to form a larger barrel shock structure, and greater compression across the Mach disk and shock along the boundary of the barrel structure. Similar observations are made for the cases of hydrogen injectant (right). However, in addition to the enhancement of OH^* emission attributed to greater expansion of the PD exhaust, increased chemical reactions are observed to contribute significantly for cases with larger J_j . This observation is inferred by comparison of the relative increase in OH^* emission (for helium and hydrogen injectants) between two cases with equivalent J_j .

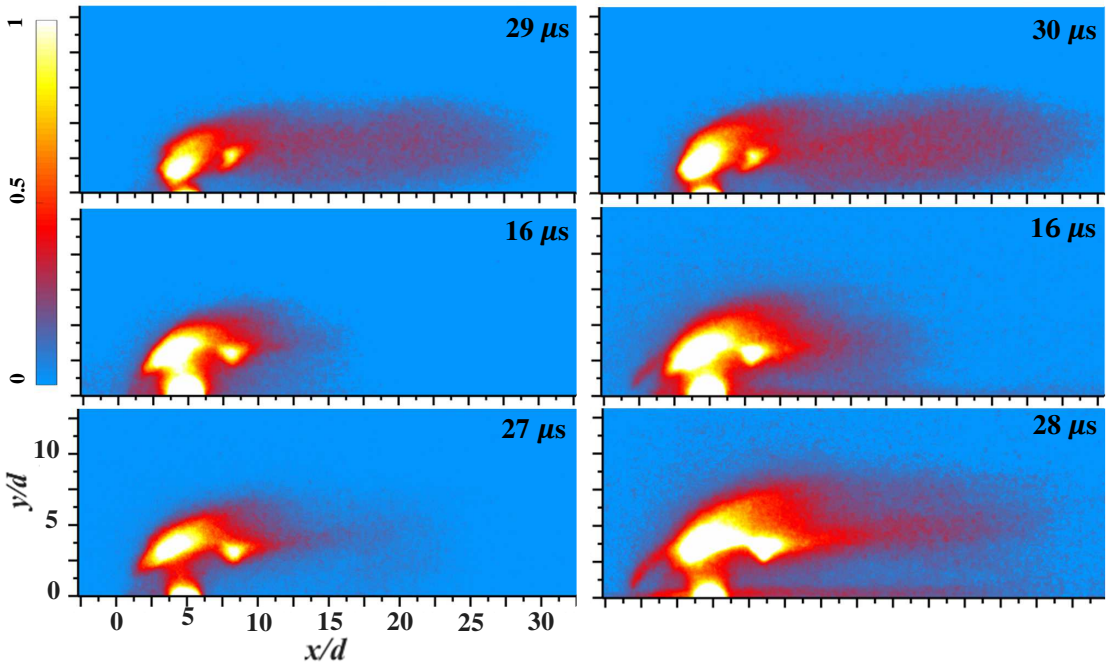

Figure 6.7: Line-of-sight integrated OH* chemiluminescence images of the global flame structure for case A (3rd row), case B (2nd row), and case C (1st row). The first and second columns correspond to helium and hydrogen primary jet injectant, respectively. All images were acquired over a 24.4 μs exposure.

6.4.2.2 Heat Release Enhancement

While the images in Figs. 6.4, 6.5, and 6.6 provide a realization of the global heat release characteristics of the system, they do not provide insight to the heat release that is solely due to combustion enhancement of the primary jet. Instead, the heat release distribution provided by those images is due to three sources: (1) the primary jet reacting with the freestream air (Fig. 6.4); (2) the ongoing chemical reactions of the post-detonation gas as it exhausts from the detonation tube (left column of Fig. 6.7); and (3) the enhanced reactivity of the jet in crossflow system due to the presence of the high-temperature post-detonation products. To first order, the contribution from each component can be obtained by taking the difference between different cases (isolated primary jet, staged jet-PD with hydrogen injectant, staged jet-PD with helium injectant) with equivalent values of J_{j} . For example, the contribution of OH^* emission that is due to the combined effects of the reacting primary jet (1) and combustion enhancement of the primary jet (3) is given by

$$q_1 = q\big|_{staged,\ \mathrm{H_2}} - q\big|_{staged,\ \mathrm{He}} \tag{6.1}$$

where the terms on the right hand side are temporally integrated signals over one PD cycle, which is taken to be the blowdown period for convenience (250 μs). The evaluation at *"staged"*, refers to cases with the staged jet-PD configuration. Similarly, the contribution of OH^* emission that is solely due to combustion enhancement of the primary jet (3) is given by

$$q_2 = q_1 - q\big|_{No\ PD,\ \mathrm{H_2}} \tag{6.2}$$

where the evaluation at *"No PD"*, refers to cases with the primary jet alone. The spatial distribution of heat release $q(x/d)$ integrated over one PD cycle for several cases is provided in Fig. 6.8. With the exception of case D, the solid curves are

evaluated using the expression given by Eqn. 6.1. To first order, they represent the heat release attributed to the reacting primary jet as well as the combustion enhancement of the primary jet due to the presence of the post-detonation products. The cases given by the dashed curves represent cases A, B, and C, but without the presence of the PD. Therefore, the arithmetic difference of curves with the same color is equivalent to the expression given by Eqn. 6.2, and represents the contribution of heat release solely due to the combustion enhancement of the reacting JISCF system. The results reveal the significant impact that the post-detonation products have in modifying the reaction progress of the JISCF system. The PD is observed to increase the net heat released along the entire streamwise direction for all cases, and particularly in the vicinity of the PD exit port. This implies that the mechanisms governing the combustion enhancement are sufficient to promote ignition and heat release within very short flow residence times. The enhanced heat release of case C is particularly interesting since no heat release is detected within the field of view without the PD (dashed blue curve). The post-detonation products are observed to increase heat release starting immediately at the location of the PD exit and continuously downstream of the jet-PD system.

For the cases with the isolated primary jet (dashed curves), a recirculation region upstream of the primary jet only exists for case A, since OH^* emission is not observed at $x/d < 0$ for cases B and C. With the presence of the PD (solid curves) the high-momentum flux post-detonation gas is observed to enhance heat release within the recirculation zone upstream of the primary jet of case A. Moreover, the size of the recirculation region is increased since the region of OH^* emission extends further upstream and past the field of view before it decays to zero. These results also imply that the additional flow blockage of the PD exhaust is not sufficient to separate the upstream boundary layer for cases B and C.

To summarize the overall enhancement in heat release that the post-detonation

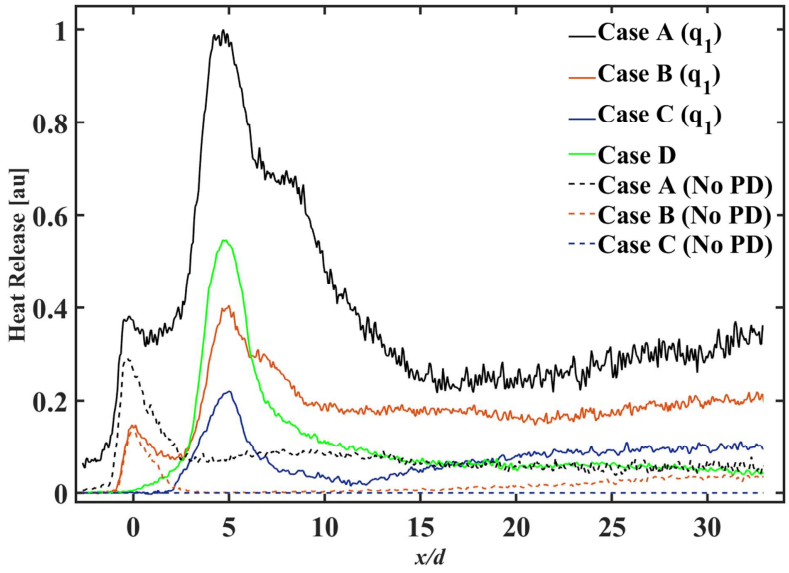

Figure 6.8: Streamwise heat release distribution. Each curve corresponds to a vertical integration (along each column) of the signal integrated over 10 frames, each with a 24.4 μs long exposure.

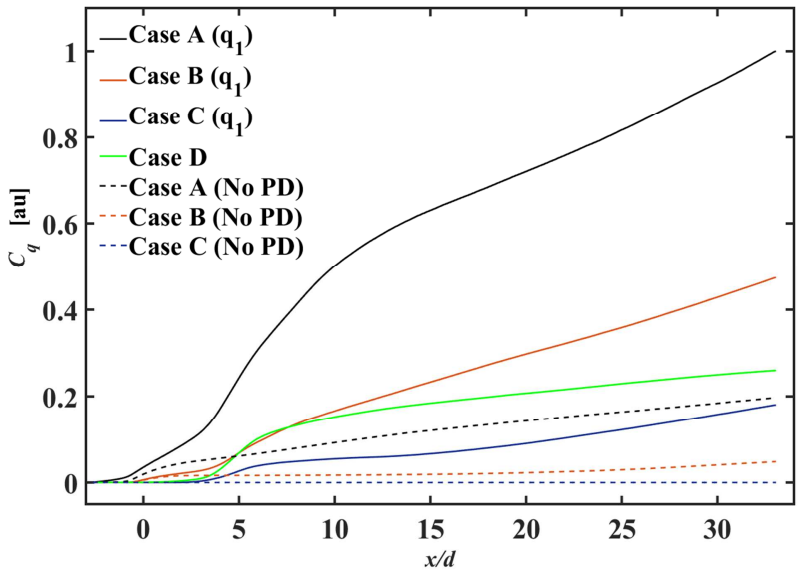

Figure 6.9: Cumulative sum $C_q(x/d)$ of the streamwise heat release distribution.

products provide to the reacting JISCF system in a condensed manner, a cumulative summation of the streamwise heat release distribution is performed for each case presented in Fig. 6.8. The cumulative distributions of heat release $C_q(x/d)$ are shown in Fig. 6.9. For all cases with the presence of the PD, the slopes of the curves are greatest in the vicinity of the PD port, indicating the location of the most rapid heat release. On the other hand, the cases of the isolated primary jet reveal that after the initial heat release within the vicinity of the injector, the majority of energy is released in the far-field.

From these curves, the total heat released for each case was extracted, and is given by the final value of C_q in the far-field of each curve. This calculation was repeated for a number of experimental data sets, and the results are summarized in Fig. 6.10. The presented values of C_q correspond to the total integrated heat release within the field of view and over one PD cycle. The values of heat release given by the circle symbols were computed using Eqn. 6.1, where the contribution of heat release solely due to the presence of ongoing chemical reaction of the post-detonation products was removed. Therefore, the circle symbols represent the total heat release attributed to the reacting JISCF and the combustion enhancement of the JISCF system. On the other hand, the diamond symbols correspond to the total heat release attributed to the reacting JISCF alone.

The results reaffirm the conclusions obtained by visual inspection of Fig. 6.8, in that the post-detonation products enhance the reactivity of the JISCF system. Significantly greater amounts of heat are released for all cases. However, it is important to consider that the total heat released by a reacting system will depend on the heat of reaction of the mixture and the amount of reactants present. Therefore, by normalizing the data of each case by the respective mass flow rate of the primary jet, a comparison of the heat released unbiased by the amount of reactants is obtained. The heat release per unit mass of hydrogen injected through the primary jet is given

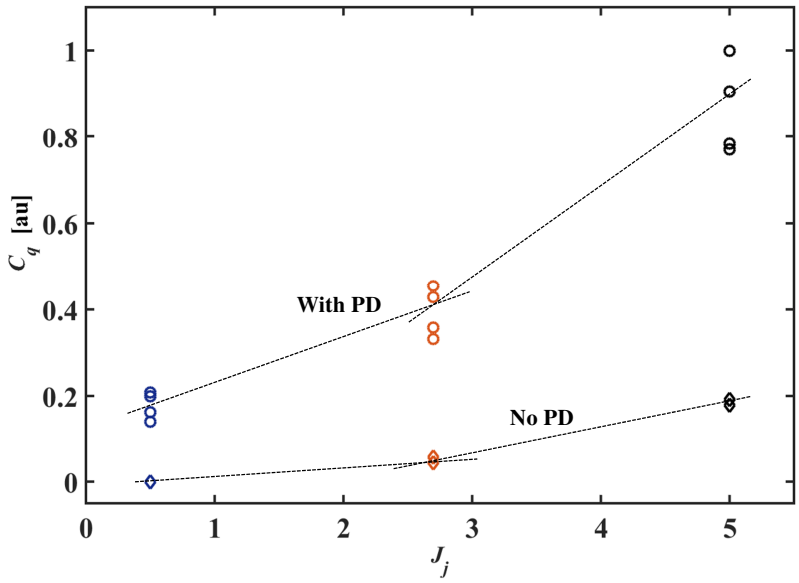

Figure 6.10: Total heat release integrated over one PD cycle or blowdown period (250 μs).

by Fig. 6.11. The results reveal a similar trend for the cases of the isolated primary jet, where a nearly linear increase in heat release is observed with J_{j} for the range of conditions considered. However in the case where the PD is used, the greatest heat release per unit mass of primary jet injectant occurs at the lowest value of J_{j} (case C), and does not vary significantly between cases A and B. The results imply that for the range of conditions considered in this study, the rate of combustion enhancement increases inversely with primary jet momentum flux ratio J_{j}.

The causes of this trend are believed to stem from the complex flow processes that govern the interaction and mixing of the primary jet fluid and PD exhaust. For example, since the penetration of the primary jet is limited to the boundary layer thickness for case C, there is more time over one PD cycle (blowdown period) for the primary jet fluid to mix and react with the post-detonation products. Larger values of J_{j} limit the most significant interactions between the primary jet and PD exhaust to the early portions of the blowdown period. This is because a significant portion of the primary jet fluid will not interact and mix with the post-detonation gases

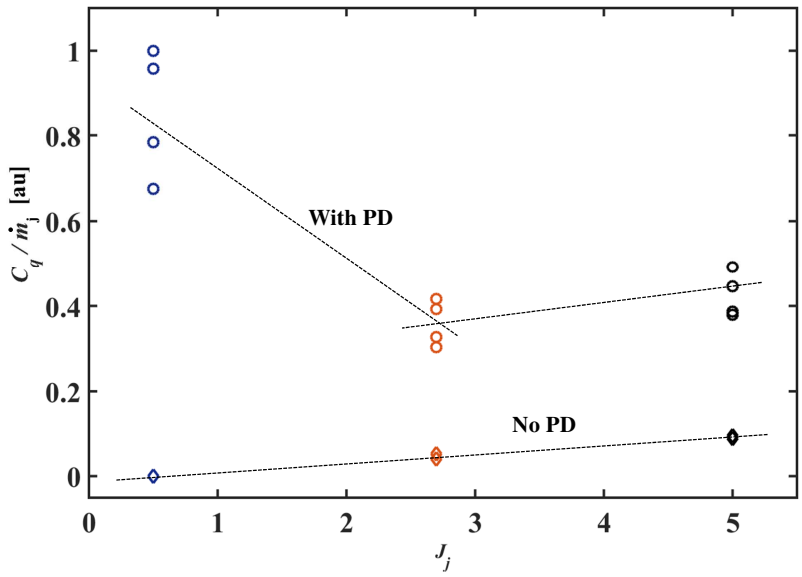

Figure 6.11: Total heat release per unit mass of primary jet injectant integrated over one PD cycle or blowdown period (250 μs).

after the momentum flux of the PD has decreased and the PD exhaust penetration is reduced to the boundary layer thickness. Based on the schlieren images of Fig. 6.3 and OH* images of Fig. 6.5, this occurs for nearly half of the blowdown period. These results imply that the effectiveness of the use of a pulsed detonation device to enhance the combustion characteristics of a supersonic system are sensitive to the specific way it is used and configured. Moreover, lower primary injectant mass flow rates will lead to locally higher initial mixture temperatures between the crossflow air, hydrogen fuel, and post-detonation gas. On the other hand, larger values of $\dot{m}_j$ will decrease the local initial mixture temperatures. Since reaction rates have an exponential dependence on temperature, this can significantly affect the combustion progress of the system. A system level analysis to determine the optimal value of $\dot{m}_j$ would depend on the specific pulsed detonation tube that is used. The relative mass flow rates of the primary jet and PD, as well as their temperatures, would need to be considered. This analysis is provided in Chapter VII.

6.5 Reaction Zone Structure

Images of the instantaneous reaction zone and distribution of OH within the flow field were obtained using OH Planar Laser Induced Fluorescence (PLIF). The measurements were obtained by the collection of spontaneously emitted radiation from OH radicals populated in the $A^2\Sigma^+$ excited electronic state through laser induced stimulated absorption from the $X^2\Pi$ ground state. The images were acquired over several imaging planes including the centerline streamwise plane, and four cross-sectional planes. The locations of the four cross-sectional planes were judiciously chosen to better understand several phenomena that were observed with the OH centerline plane as well as other imaging techniques. A series of single-shot images at different time delays from the firing of the detonation tube were acquired to construct a pseudo-time-series of the evolving three-dimensional regions of OH. Since the intensity of the collected radiation varied significantly between cases with and without the PD, the presented images were normalized differently to provide a meaningful visual analysis of the combustion features. The difference in intensity scale can be determined by comparing the scaling of the color maps between separate figures.

In the following section, a brief discussion on the combustion characteristics of an isolated transverse jet in supersonic crossflow is provided to give an understanding of the base flow field. This is then followed by an analysis of how the PD products are observed to alter a number of combustion features. Throughout the analysis, it is important to keep in mind that since the post-detonation products contain OH radicals, the acquired PLIF images do not explicitly mark the instantaneous reaction zones of the flow field. Rather, they mark reaction zones as well as regions of the flow that maintain sufficiently high temperatures where OH is chemically stable including OH originating from the PD.

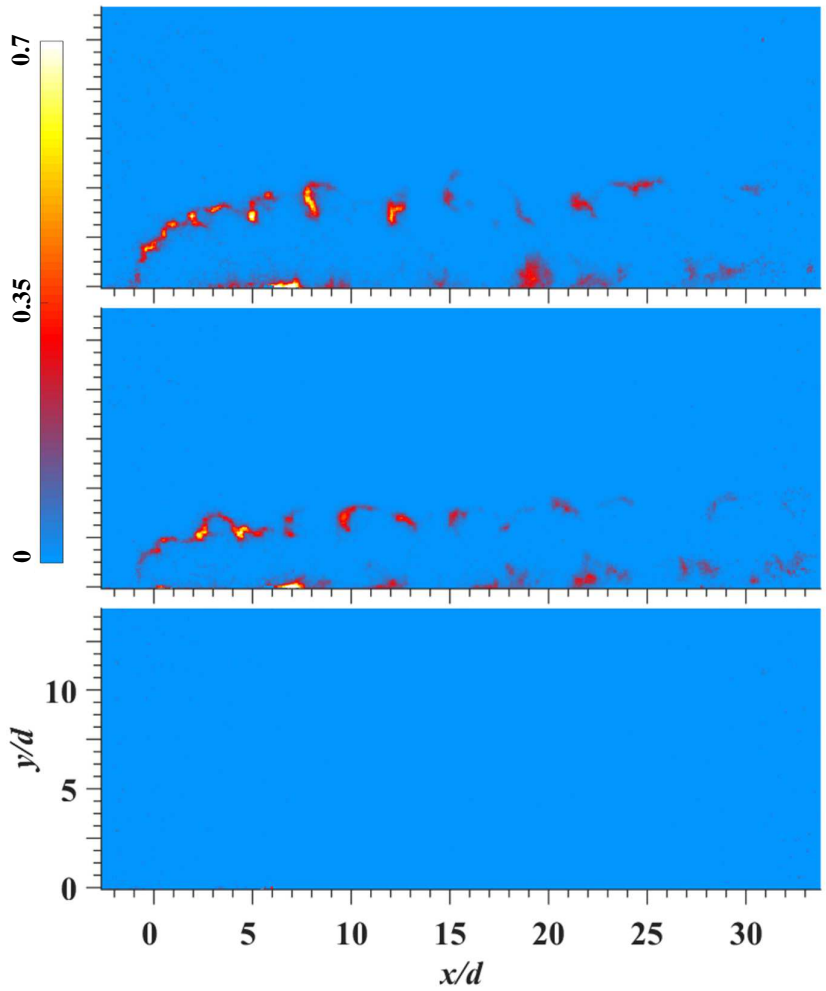

Figure 6.12: Center-plane OH PLIF images of the isolated transverse primary jet of case A (1st row), case B (2nd row), and case C (3rd row).

6.5.1 Jet in Supersonic Crossflow

OH PLIF images along the center plane of the isolated primary jet for cases A, B, and C are shown in Fig. 6.12. Reactions are only observed to occur within the field of view for sufficiently large values of J_j , and therefore are not observed for case C. This is attributed to the negligible effects of compressibility that are present in the low J_j regime. The instantaneous features of the reacting flow field are similar between cases A and B, with the exception of an intermittently reacting upstream recirculation region that is only observed in case A.

Immediately upstream of the injector, a nearly vertical reaction zone exists along

the jet-freestream interface that is anchored at the injector. Reactions are observed to occur intermittently along the shear layer, extending to the windward side of the jet. Stabilization of reactions along the shear layer are believed to be due to shock heating as well as the supply of radicals from the upstream recirculation region for sufficiently large values of J_j (case A). The reaction zones are observed as corrugated and thin layers that resemble the description of laminar diffusion flames. Their shapes appear to resemble the periphery of large-scale vortical structures that exist along the shear layer. The unstable and intermittent nature of the reactions along the shear layer are believed to be due to flame straining. On the other hand, reactions are observed to take place in relatively broad zones near the floor. This suggests that reactions near the floor take place through premixed or partially premixed modes of combustion.

6.5.2 Staged Jet and Pulsed Detonation

A pseudo-time series compiled from single-shot images of the blowdown process for cases A, C, and D (left to right) is provided in Fig. 6.13. A few images are labeled to highlight pertinent flow features and draw attention to their evolution in time. The high temperature post-detonation products initially enter the flow field in a disruptive manner as they penetrate into the wake of the JISCF system. The signal immediately outside of the PD exit port (point A) is always larger than other parts of the flow. Since the signal intensity is primarily dependent on the concentration of OH and temperature, which affects quenching rates and the boltzmann population distribution, the images alone are not sufficient to provide the cause for the increased signal. However, it can be inferred that the larger signal in the vicinity of the PD exit port is due to the larger concentration of OH, since a relatively low vibrational quantum number ($Q_1(N'' = 7)$ line) was used for the electronic transition. By using a simple two-level model of OH fluorescence via excitation of the vibrational quantum number $N'' = 7$, the LIF signal can be determined as a function of temperature, for a

fixed pressure and gas mixture composition. The results of the simulation are provided in Fig. 6.14, and indicate an monotonic inverse relationship between the LIF signal and temperature for majority of the simulated range. Under the assumption that the largest flow field temperatures are within the immediate vicinity of the PD exit, the results show that the LIF signal near the PD exit would be lower. However since this is not the case, the consistently larger LIF signal near the PD exit is attributed to the relatively larger concentration of OH radicals. The rapidly diminishing signal in regions further from the PD exit, is due to a combination of displacement of OH outside of the imaging plane as well as quenching and chemical reactions with OH. This will be discussed in more detail in the subsequent sections. Moreover, the variation in flow field pressure is assumed to be inconsequential on the acquired LIF signal (see Eqn. 3.4) in the quenching dominated regime ($Q_{21} >> A_{21}$) and when the laser line width is spectrally broad enough to overlap the entire absorption feature.

The reacting shear layer is labeled by point B. For case D, the post-detonation products provide a continuous supply of OH that clearly and continuously identify the interface with the freestream throughout the entire blowdown process. This implies that the temperatures along the shear layer and within the core of the exhaust are maintained above approximately 2000 K (see Fig. 6.2). The presence of the post-detonation products are observed to alter the nature of the reacting shear layer for large values of J_{j} such as that of case A and B (not shown). Instead of an intermittently reacting shear layer, shown in the cases of the isolated primary jets of Fig. 6.12, reactions are observed to occur continuously. Combustion is believed to occur in a more stable manner as the post-detonation gases provide several mechanisms to enhance the extinction strain rates of the non-premixed interface. The mechanisms, which will be discussed in more detail in Chapter VII, are due to thermal (fuel pre-heating) and kinetic (modification of kinetic mechanism by the addition of radicals) effects which collectively enhance several combustion properties of the reacting

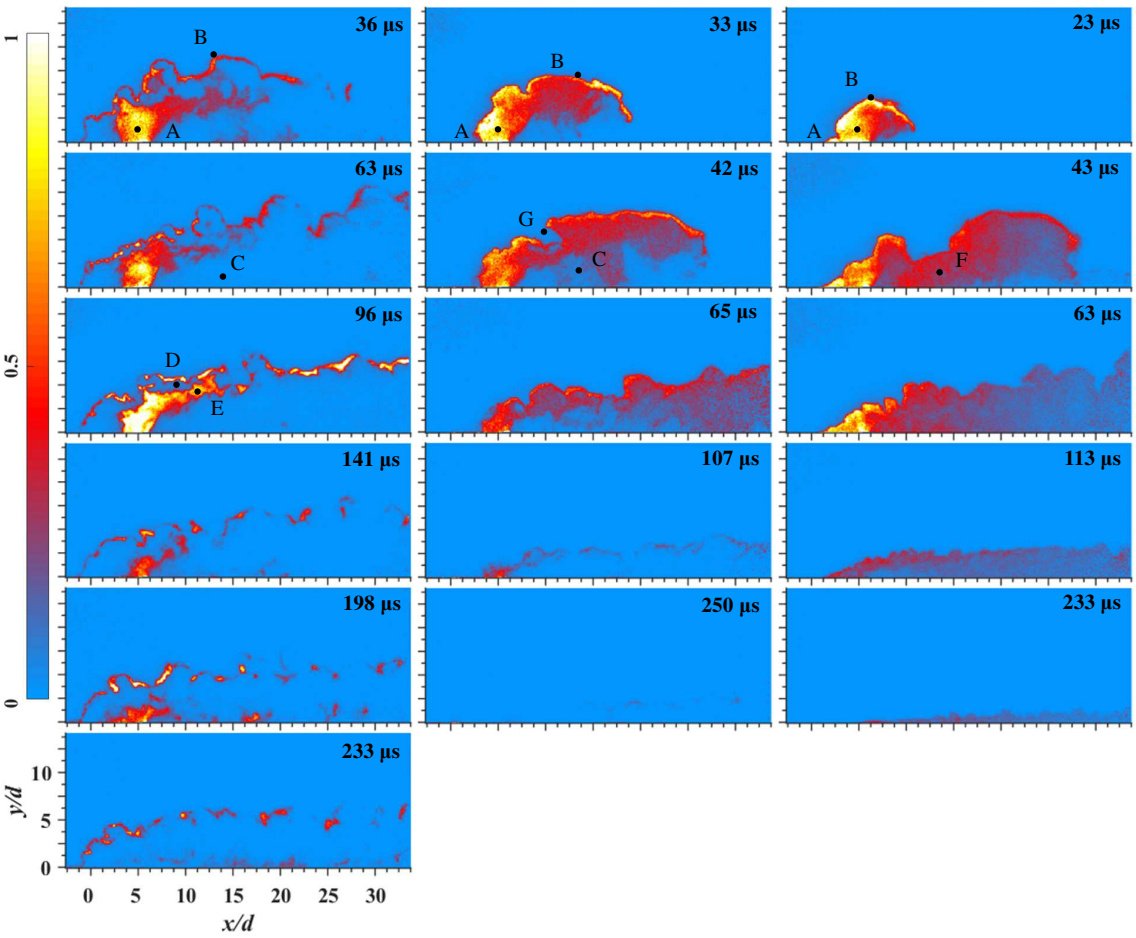

Figure 6.13: Center-plane OH PLIF pseudo-time-series of the blowdown process for case A (1st column), case C (2nd column), and case D (3rd column). The labels are described in the text.

system.

The reacting shear layer of case C is more similar to that of case D since the penetration of the primary jet is several times smaller than that of the PD exhaust. The shear layer is believed to be primarily composed of OH originating from the PD, since the majority of the cold primary jet fluid expands around and not over the PD exhaust. This is indicated by the point labeled C, where an absence of signal is attributed to the low temperature primary jet fluid quenching the OH radicals through the following reactions

$$OH + H_2 \longrightarrow H + H_2O \tag{6.3}$$

$$H + OH + M \longrightarrow H_2O + M \tag{6.4}$$

By comparison of point C of case C and point F of case D, the effects of the expansion of the primary jet fluid around and into the wake of the PD can be identified. These images qualitatively support studies of staged jet injection [4], which reveal how primary jet fluid expands around and into the low pressure wake of a secondary jet (PD in our study) and subsequently mixes. Interestingly, the regions with absence of OH in the wake of the PD exhaust penetrate deep into the flow. Since these regions are observed to extend to as much as $y/d = 5$, and since the penetration of the isolated primary jet shear layer at most reaches $y/d = 2$ in the very far field (based on schlieren data), it is believed that the interaction of the primary jet fluid with the vortices formed in the wake of the PD exhaust cause the primary jet fluid to be lifted away from the floor. This observation is in support with those made in Ref. [27]. Similarly, the same interaction causes the wake of the staged jet-PD system in case A to be absent of OH. Moreover, a thin region where no OH is detected delineates the structure of the initial exhaust that exits the PD (point A) and the reacting shear

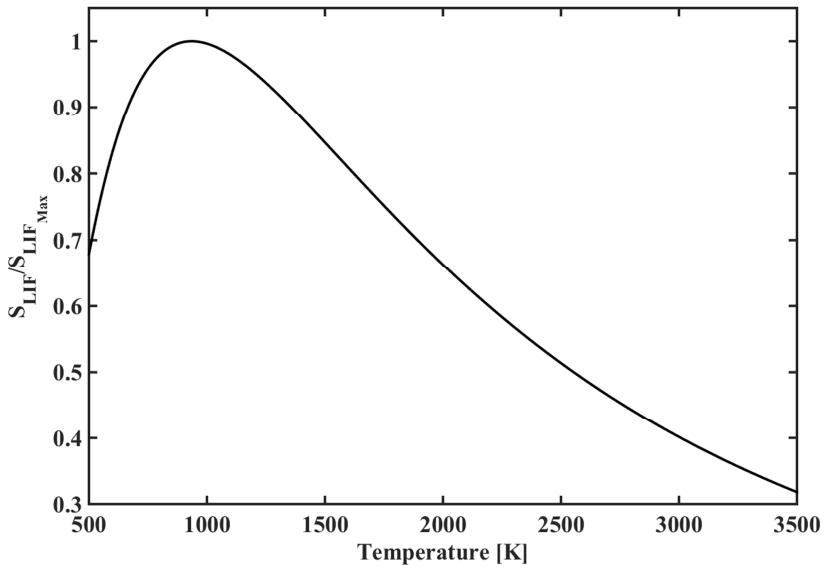

Figure 6.14: Simulated laser induced fluorescence intensity of OH after excitation of the $N'' = 7$ vibrational quantum number of the $X^2\Pi$ ground state. The results are given as a function of temperature, for a fixed pressure and composition.

layer (point B), and is given by point D. In this case, because J_j is sufficiently large, the primary jet fluid is observed to be carried over and around the PD exhaust. This forms a cold and fuel rich region that surrounds the exhausting post-detonation gases and therefore quenches a portion of the OH radicals before they reach the shear layer.

The regions of the PD exhaust which maintain sufficiently large temperatures to support the OH radicals are observed to extend downstream and towards the shear layer (point E). This may be an additional means of increasing combustion stability along the shear layer, as the high temperature radicals are delivered to the primary jet- freestream interface. Finally, point G reveals how the initial interaction between the primary and and PD causes a portion of the shear layer to be locally quenched as primary jet fluid is carried over the PD exhaust.

Comparison of cases A (1st column) and D (3rd column) also provide insight to the mixing characteristics of the staged configuration. The structure of OH originating from the PD and extending towards the shear layer (point E), never extends past

x/d =15. OH that is detected in the wake of the staged jet-PD past this axial streamwise location is not believed to originate from the PD, but rather marks existence of new reactions. Therefore, it is believed that the vast majority of reactants emanating from the PD the PD are sufficiently mixed with the JISCF system approximately 10 primary jet diameters downstream of the PD (x/d =15), during the entire blowdown process.

The exhaust of the PD products are observed to act as a fluidic body that the primary jet fluid is forced over and around. This increases the overall penetration of the reacting shear layer to values that are approximately twice as large as those of the isolated primary jet cases (Fig. 6.13). As the blowdown evolves in time, the momentum flux of the pulsed detonation tube decays. This reduces the fluid mechanic influences of the PD on the JISCF system, and the shear layer penetration decays back down to steady state conditions when no PD is present. The decay of the PD momentum flux and penetration limits its impact on the shear layer, as less high-temperature radicals survive the transport process between the exit of the PD tube and the shear layer. However, even towards the end of the blowdown period, the post-detonation gases are still believed to have temperatures greater than 2000 K, which then pre-heat the fuel and augment the ignition and heat release processes that occur farther downstream.

From the limited available data set, an attempt was made to quantify the stability of combustion along the shear layer in order to understand the nature of the recovery process over the blowdown period. The intermittancy of reactions along the shear layer was quantified by evaluating the ratio of the sum of regions along the shear layer (in the streamwise direction), starting from the location of the PD exit ($x/d = 4.8$), where reactions were extinct to the approximate distance convected by the PD exhaust (in the streamwise direction) using the bulk freestream speed. The intermittancy I is defined as

$$I = \frac{\sum L(x)_{extinct}}{U_{\infty} t} \tag{6.5}$$

where t refers to the time elapsed since the detonation first exits the PD. When the value of the denominator exceeds the field of view, then a constant value of 60 mm was used, which represents the distance between the PD exit port and the furthest location in the streamwise direction that was imaged. This analysis was carried out for case A only since there was not enough data for case B, and the reacting shear layer of cases C and D were not of the jet-freestream interface, but rather of the boundary between the PD exhaust and the freestream. The results are shown in Fig. 6.15. The results reveal a nearly linear trend which the shear layer undergoes throughout the blowdown process. Initially, the large mass flow rate and momentum flux of the PD exhaust is sufficient to reach the shear layer and stabilize reactions by increasing local temperatures and supplying combustion intermediates. As time elapses, the temperature, mass flow rate, and penetration of the PD exhaust decays which decreases its influence in stabilizing combustion along the shear layer. Interestingly, although the penetration of the PD exhaust is much less than the primary jet during the second half of the blowdown period, it is still observed to increase combustion stability along the shear layer. This is believed to be attributed to the effects of pre-heating the primary jet fuel before it subsequently reaches the shear layer to react.

6.5.2.1 Cross-Sectional Planes

The explanations of the observations are further supported with imaging of the OH distribution through cross-sectional planes. The four planes were chosen to be located at x/d = 2.5, 4.8, 10, and 30. They were judiciously chosen to provide more information on phenomena that was observed or inferred from the previous imaging configurations. Images taken at $x/d = 2.5$ reveal the combustion phenomena

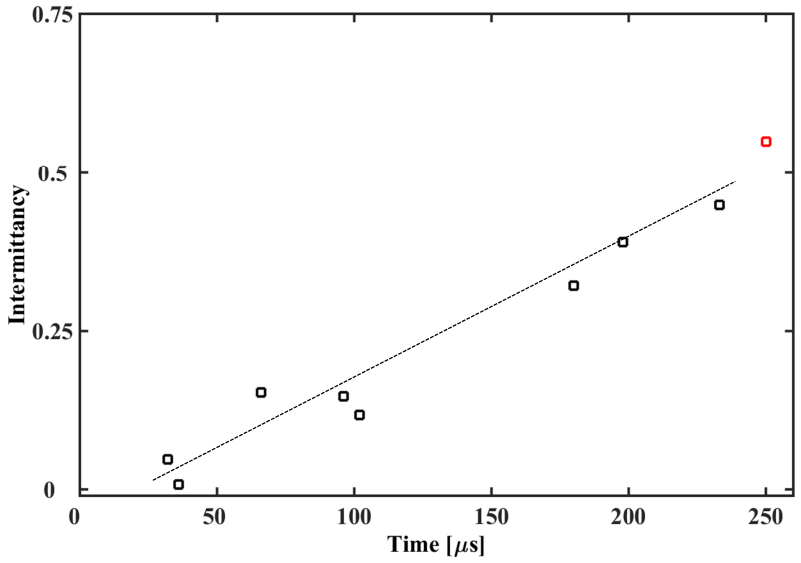

Figure 6.15: Intermittency of reactions along the shear layer of the staged PD-JISCF system over the blowdown period. Data pertains to case A.

occurring within the subsonic recirculation region between the primary jet and PD. The images provide insight of any upstream-propagating phenomena that originate from the PD that potentially enhance the combustion properties of the JISCF system. Images acquired at $x/d = 4.8$ provide information about the interaction of the primary jet with the PD at the location of largest temperatures and momentum flux. Based on the centerplane OH PLIF images and other imaging techniques, some of the most prominent fluid mechanic and chemical interactions occur in this region. The plane located at $x/d = 10$ was chosen because it was located near the end of the initial structure of post-detonation products that exhaust from the PD (point E in Fig. 6.13). It provides insight of the OH structures originating from the PD, before they completely react and are quenched further downstream in the wake. Lastly, images were acquired far enough downstream at $x/d = 30$ to provide sufficient time scales for any combustion enhancement mechanisms to develop and affect the characteristics and nature of the reacting JISCF system. A series of images are presented in Fig. 6.16 where the top to bottom rows represent images for the isolated primary jet case A,

case D, and case A, respectively. The time delay in acquiring images from one column to the next is equivalent to the large-scale flow convective time scale. Therefore, the images from left to right effectively track a slug of post-detonation gas (as it convects downstream) that was initially exhausted at a time of $t = 15$ μs. Labels A - F pertain to the same flow features that were previously discussed in Fig. 6.13.

The first row of images reveal the spatial evolution of the instantaneous reaction zone for the isolated primary jet (case A). The shear layer (point B) is composed of individual thin flamelets that collectively mark the periphery of the jet-freestream interface. The presence of local extinctions as well as the contrast in the overall structure between images is indicative of the highly turbulent nature of the flow. Further downstream, the jet boundary is observed to grow radially, as well as penetrate further into the crossflow. The most intense and stable burning is observed near the floor (point Z). These broad regions of OH extend on either side of the jet core boundary and are believed to be a signature of the horseshoe vortex system. The broad reactions zones are reminiscent of partially premixed or premixed modes of combustion. The stable burning within these regions is believed to be due to entrainment of air from the crossflow boundary layer (by the horseshoe vortex) which subsequently mixes with the fuel [42]. The flow residence times within these regions are greater than others in the flow field because of the circumferential component of velocity of the vortex that resides within the boundary layer. Farther downstream ($x/d = 30$), the reactions occurring within the horseshoe vortex system spread in the z/d direction, and are believed to play a larger role in providing stability to reactions occurring along the shear layer.

The second row of images reveals the spatial evolution of a slug of post-detonation products that were emitted at a time of 15 μs after the transmission of the detonation wave into the flow field. Both the shear layer (point B) and the core (point F) of the PD exhaust are composed of a continuous distribution of OH. The temper-

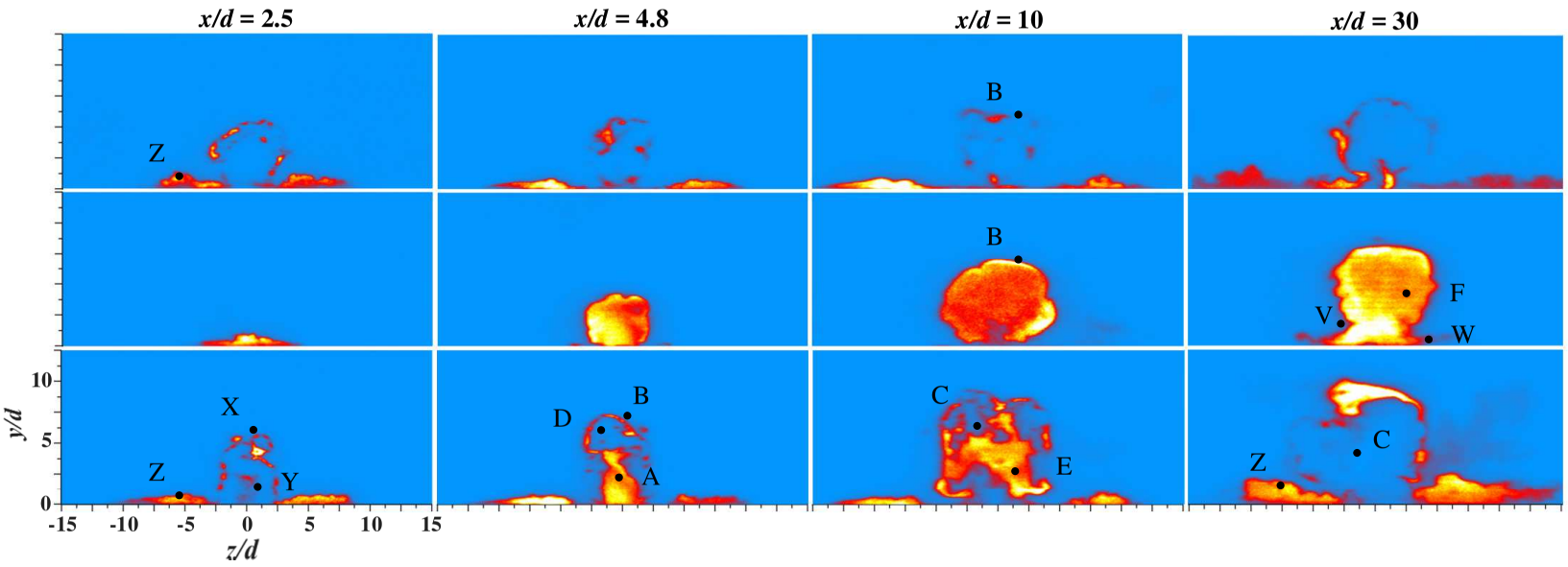

Figure 6.16: Cross-sectional OH PLIF images for the isolated primary jet case A (1st row), case D (2nd row), and case A (3rd row). Each column corresponds to a different imaging plane, where the time delay of image acquisition between columns is equivalent to the large-scale convective time scales of the flow.

atures within these regions are sufficiently large to sustain the OH that originates from the detonator tube. The exhaust is observed to expand radially as it convects downstream. Furthermore, the high-momentum flux exhaust is observed to convect upstream ($x/d = 2.5$) along the wall. During this early stage of the blowdown process, it is believed that vortical structures such as the CVP are forming as they convect in space. This is observed by the nascent state of the vortices near the floor which only take the form of prominent features (point W) after the slug of gas reaches $x/d = 30$. The formation of these vortices are a signature of the increasing influence of the streamwise CVP. As the strength of the CVP increase, more freestream air is drawn around the core, between the wall and the plume, and upward into the core of the exhaust. Evidence of this effects is given by the pinched (point V) shape of the PD exhaust- freestream boundary. In order to fill the void of gas that is being entrained from the floor up into the core, a second pair of vortices form near the floor (point W), which rotate in the opposite direction and entrain freestream air back down to the floor.

The final row of images show several flow processes that drastically affect the combustion features of the JISCF system. The high-momentum flux PD exhaust is observed to convect upstream residing within the core of the subsonic region (point Y). Since this is a relatively cold and fuel rich region of the flow, significant reactions are not expected to take place. However, the presence of OH in this region indicates that the local temperatures are sufficient to sustain radicals. Therefore, the upstream propagating PD exhaust that remains within the core of the primary jet is believed to be mainly pre-heating the fuel. However, post-detonation products that do not recombine as they propagate upstream are believed to help augment reactions as well. The combined effect of fuel pre-heating and supply of chain carries are believed to lead to the increased number of flamelets along the shear layer (point X). At the location of the PD exit ($x/d = 4.8$), a strong interaction between the primary jet

and PD exhaust is observed. The shear layer is observed to be carried deeper into the crossflow as it moves around the core of the PD exhaust (points A). A relatively cold and fuel rich region (point D) exists between the high-temperature PD exhaust (point A) and the reacting shear layer (point B).

Farther downstream ($x/d = 10$) the cold primary jet fluid is observed to quench the OH radicals by forming pockets within the core of the PD exhaust. The most preferred chemical pathways under these conditions are shown in Fig. 6.17. The net reaction rates ($k_f - k_b$) are shown for several pathways that are active under the cold fuel-rich conditions that exist in these parts of the flow. They were computed through a perfectly stirred reactor simulation with a mixture composed of 90 % hydrogen and 10 % post-detonation products (evaluated as the chemical equilibrium composition of the CJ state). The initial mixture temperatures were varied to simulate the effect of a varying degree of fuel pre-heating, while the pressure was fixed to 0.5 atm. The results show how the OH radicals primarily recombine to form water. In doing so, they release heat to the surrounding mixture and therefore have a thermal effect on the system by further pre-heating the fuel. The conclusions from this analysis do not change by varying the initial mixture composition, or the thermodynamic state in which the equilibrium composition of the PD products are evaluated. A more in depth analysis of the kinetic and thermal mechanisms that the post-detonation products provide the JISCF system is provided in Chapter VII. Farther downstream ($x/d = 30$), the OH radicals originating from the post-detonation products have either fully recombined within the core of the primary jet-PD or reached the shear layer. Therefore, OH signal from this plane is representative of the instantaneous reaction zone of the system.

By comparison of the 1st and 3rd rows (Fig. 6.16), the presence of the PD exhaust is observed to increase the area of the jet-freestream interface boundary. This happens as the primary jet fluid is pushed radially outward around the post-

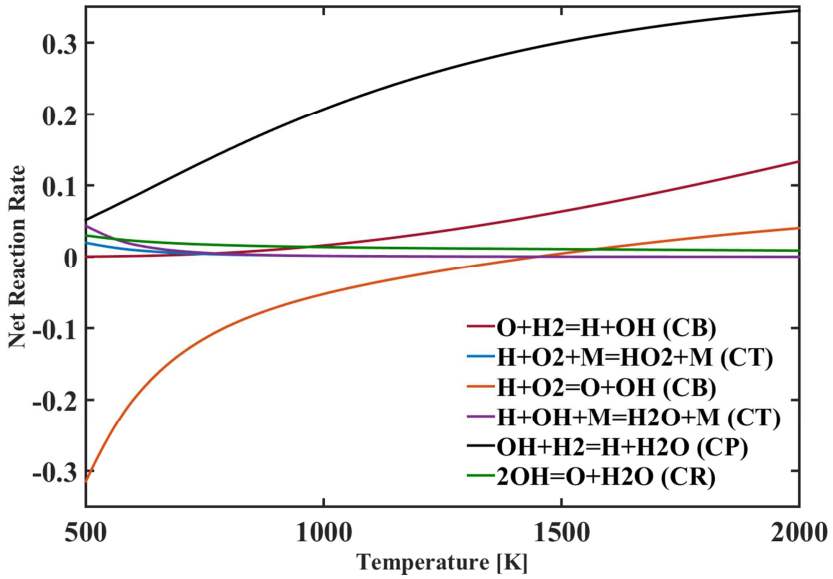

Figure 6.17: Calculated net reaction rates of several dominant reaction pathways for a mixture composed of 90 % hydrogen and 10 % post-detonation products. The composition of the post-detonation products is equivalent to the CJ-state chemical equilibrium composition generated from a stoichiometric H_2-O_2 detonation wave.

detonation gases. The interaction increases the contact area between the fuel and oxidizer streams, potentially leading to an enhancement in reactivity along the shear layer. Moreover, the post-detonation products are observed to increase the stability of combustion along the shear layer as fewer extinction events are identified. Finally, an interesting observation is made by comparing the instantaneous reaction zones near the floor within the plane at $x/d = 30$, between case A (3rd row) and the isolated primary jet case A (1st row). In the case of the isolated primary jet, the reactions are confined to the wall and extend along the floor (in the z/d direction) past the field of view. Combustion along these regions is controlled by the mixing induced by the horseshoe vortices. With the presence of the PD exhaust, the lateral (z/d) spread of the reactions decreases and are fully captured within the field of view. Moreover, they are observed to protrude deeper into the crossflow, forming a more compact region of reactions. This may be attributed to an enhanced vorticity of the horseshoe vortex system which more rapidly mixes the primary jet fluid with the crossflow boundary

layer and post-detonation products, and leads to more confined regions of reactions. This is a similar effect to decreasing the flame length of a non-premixed flame by increasing levels of turbulence and mixing rates.

6.5.2.2 Statistical Analysis

The descriptions and analysis that are made throughout the study are based on carefully repeated experimental runs under nominally identical conditions. Because of the short test times generated by the expansion tube facility and the inherently turbulent, unsteady, and three-dimensional nature of the phenomena being studied, a thorough statistical analysis of the combustion properties was not attempted. Rather experimental runs of each condition and time delay of PD firing were repeated to ensure that the observed trends and combustion characteristics were repeatable and accurate realizations of the combustion and flow processes. In addition to this, an attempt to quantify the probability for reactions to occur with and without the PD was made. The analysis was carried out for the imaging plane at the streamwise location $x/d = 30$, since it was sufficiently far downstream such that any OH originating from the PD tube was fully recombined, and therefore all of the existing OH within the streamwise location was attributed to the formation of OH through combustion of the primary jet fuel. Therefore, a direct comparison of the probability and nature of the OH structures occurring this plane with and without the use of a PD would indicate any combustion enhancement the post-detonation products provide to the JISCF system.

A series of OH PLIF images were acquired along the $x/d = 30$ cross-sectional plane, at $t = 80$ μs ± 8 μs, and therefore correspond to post-detonation gases emitted from the PD at approximately 50 μs ± 8 μs from the time the detonation wave is first transmitted into the flow. A total of 8 and 5 images were acquired for case A and the isolated primary jet case A, respectively. After the typical post-processing procedure,

each image was subsequently binarized using a different threshold value for each case. Then an average of the binarized images was taken to generate a reaction probability map for each case. The results are shown in Fig. 6.18, where the top and bottom rows correspond to case A and the isolated primary jet case A, respectively. The choice of the threshold value for each case was chosen based on the level of background signal, and did not alter the conclusions of this analysis.

The color contours of Fig. 6.18 essentially represent a probability for reactions to occur at $t = 80$ μs and along $x/d = 30$. The images are not statistically converged, however, they provide a qualitative comparison of the nature and frequency of the reaction zone structures. The maps reaffirm the observation that near-wall burning is far more stable than burning along the shear layer for both cases. However based on this analysis, the post-detonation products not only increase stability of reactions along the shear layer, but they also cause them to take place over broader regions along the interface. This can be seen by the difference in thickness of the reaction layers between the two cases. The cause for this may be due to several reasons. First, by pre-heating the primary jet fuel, the PD products augment ignition and reactions for a wider range of local mixture compositions. Second, the presence of intermediate species such as OH, in limited concentrations, has been shown to increase flammability limits. Therefore, the regions within the flow which are capable of reacting (being within the flammability limits) are increased, leading to broader reaction zones along the shear layer. Lastly, the presence of the PD exhaust may enhance mixing along the jet-freestream interface by altering local transport properties. It is important to keep in mind that the presence of the PD causes the shear layer to fluctuate, and therefore the broadened reaction zone thickness observed over the limited number of averaged images is also a manifestation of the unsteady nature of the shear layer between experimental runs.

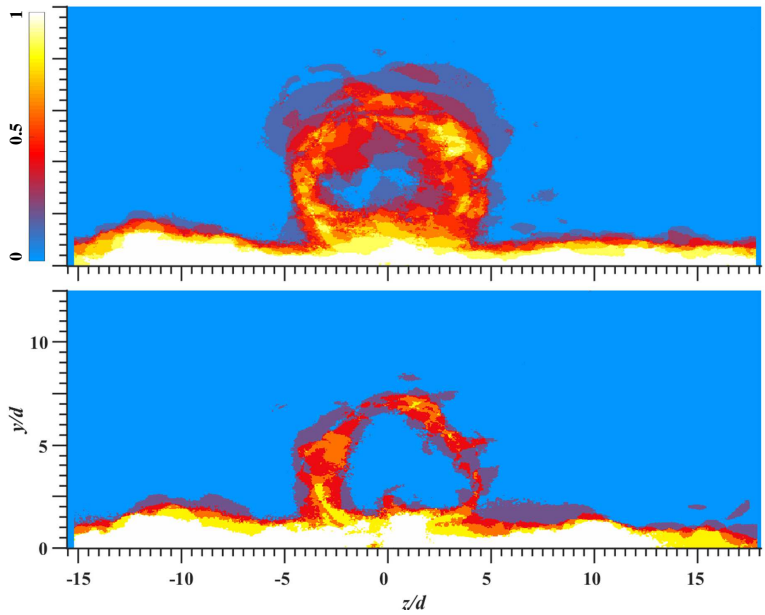

Figure 6.18: Reaction probability maps for case A (top), and the isolated primary jet case A (bottom). All images were taken at $x/d = 30$ and correspond to the flow field at $t = 80\mu$s ± 8 μs.

6.6 Conclusions

The effects of issuing a high-momentum flux detonation wave and subsequent post-detonation products into the wake of a reacting JISCF were studied experimentally. A number of observations are made regarding the strong and coupled interaction by varying the primary jet momentum flux ratio J_j and composition between hydrogen and helium. The former provided a means of understanding the processes which couple the primary jet and PD, while the latter provided a first-order means of decoupling the hydrdynamic and chemical influences of the PD exhaust on the flow field.

The staged configuration was observed to significantly modify the flow field pressure distribution. An upstream recirculation region of the isolated primary jet cases was only observed when $J_j = 5.0$. The presence of the PD exhaust increased heat release within this region when $J_j = 5.0$ and is believed to stem from two processes. First, the presence of the PD exhaust increased the crossflow blockage thereby increasing the upstream bow shock strength which subsequently forms a larger upstream re-

circulation region for chemical reactions to take place. Secondly, the region between the primary jet and PD is believed to be subsonic since no formation of shock waves was observed from schlieren images, therefore providing a means for PD products to propagate upstream. This was observed to occur by acquisition of cross-sectional OH PLIF images in this region, which revealed the presence of OH near the floor inferred to originate from the PD. The subsonic region between the primary jet and PD provides a means of enhancing mixing of the two streams, thereby pre-heating the fuel, and augmenting ignition. This also occurs in the low pressure wake of the PD which further entrains primary jet fluid and freestream air, into the high-temperature and radical rich exhaust.

Along the shear layer, reactions occurred in a more stable manner. Fuel pre-heating and the addition of radicals increases the local reaction rates, and therefore increases the extinction strain rate. The heat release analysis revealed a significant increase in the net heat release distribution. From the observed trends, autoignition is believed to be the dominant mode of flame stabilization with the presence of the PD products. The analysis also reveals how the extent of combustion enhancement attainable with a PD device depends on the specific orientation of the device within the combustor. A greater total heat release per unit mass of primary jet injector fluid was observed for case C ($J_{\mathrm{j}} = 0.5$) as compared to case A ($J_{\mathrm{j}} = 2.7$) or B ($J_{\mathrm{j}} = 5.0$). This is believed to be due to the greater time in which the JISCF and PD exhaust interact. Moreover, the lower mass flow rates of case C lead to higher JISCF-PD mixture temperatures, and therefore more readily augment ignition.

CHAPTER VII

Theoretical Analysis of Combustion Enhancement

7.1 Introduction

The preceding chapters have served as a foundation for the experimental analysis of chapter VI. The post-detonation products issuing into the wake of a reacting JISCF system resulted in a net increase in total heat release within the field of view, implying that a greater number of reactions were being initiated. The acceleration of the reaction progress is largely due to increased reaction rates of the natural oxidation chemistry. However, the addition of intermediates into the reacting JISCF system provides additional kinetic enhancement mechanisms that alter the naturally prescribed chemistry, further enhancing the reaction progress of the system. A better understanding of the extent of impact of the combined and isolated thermal and kinetic mechanisms will help explain the observed stabilization of reactions along the shear layer, as well as the large increase in net heat release observed within the vicinity of the PD exit port. Furthermore, the implications and effects of OH radicals originating from the PD that recombine in the wake region of the primary jet-PD system requires further analysis.

To this end, a series of studies were carried out to better understand the experimentally observed phenomena as well as evaluate the practicality of using a pulsed detonation device to enhance combustion in supersonic flows. The following analysis

identifies and describes several mechanisms that lead to the experimentally observed enhancement in combustion. Furthermore, the sensitivity of these mechanisms to several experimental parameters is analyzed to provide an understanding of the strengths and limitations of the combustion enhancement technique in practical applications.

7.2 Detonation Tube Exhaust Properties

The work of chapter V revealed the effects of non-ideal detonation tube operation. It was shown that as the parameter $\beta = L/d$ was increased, heat transfer rates and momentum losses to the tube walls significantly alter the thermodynamic properties of the post-detonation gas trailing the detonation wave. Specifically, the non-isentropic processes have been shown to significantly alter the temperature of the post-detonation gas, which will be shown to have a large impact on the effectiveness of the PD products in enhancing combustion.

7.2.1 Effect of Varying the Parameter β

The exit properties of several detonation tubes operated with a stoichiometric H_2-O_2 mixture and where $T_1 = 300$ K and $P_1 = 0.5$ atm were computed using the model described in chapter V. In all four cases, the skin friction coefficient was kept constant ($C_f = 0.006$) as well as the inner tube diameter (1 cm), while the tube length was changed to vary β. After the solution along the net of characteristics were computed, the properties were extracted along $\xi = 0.99$ by using a two-dimensional interpolation scheme. Several relevant exit properties of the isentropic (black solid) and $\beta = 50$ (red dash), $\beta = 100$ (orange dash-dot), $\beta = 200$ (green dot) cases are shown in Fig. 7.1. The exit properties are plotted as a function of time (τ) and include pressure, temperature, momentum flux ratio, and mass flow rate. The final two plots showing the parameters q_{chem} and q_{sens}, will be explained and described in a later section.

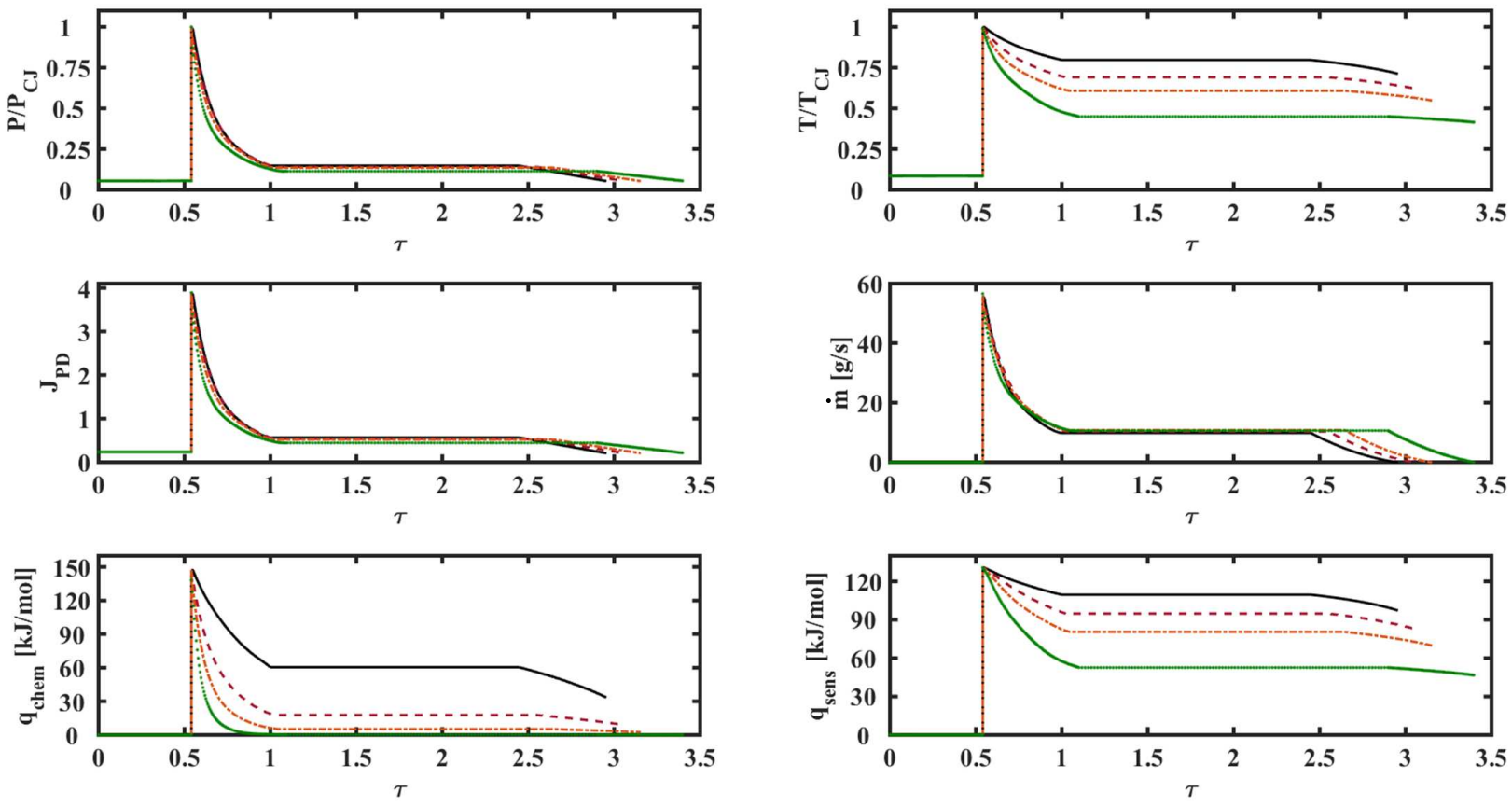

Figure 7.1: Computed temporal evolution of several properties near the detonation tube exit plane ($\xi = 0.99$). The properties are specific to a stoichiometric H_2-O_2 detonation with $P_1 = 0.5$ atm and $T_1 = 300$ K. Each curve represents a different case; isentropic (solid black), $\beta = 50$ (red dash), $\beta = 100$ (orange dot-dashed), and $\beta = 200$ (green dot). All cases were computed with a 1 cm tube and $C_f = 0.006$.

It is important to note that the numerical model was used to only compute properties in the $\xi - \tau$ domain just after the initiation of the detonation at the closed end until the arrival of the Taylor wave tail at the open end. For the exit properties shown in Fig. 7.1, this corresponds to a time up to approximately $\tau \approx 1$, and pertains to the time in which the properties begin the plateaued region of the profiles. The properties past this point in time are only approximate values. More specifically, the values of the properties within the plateaued portions of the profiles are taken to be equivalent to the solution of the last time step at $\xi = 0.99$. They are held constant until the arrival of the head of the exhausting wave which has reflected off of the closed end. In reality, this portion of the profile should not be constant, but rather, have a decreasing pressure and temperature for all cases except for the isentropic case. This is because unlike in the isentropic case, the Reimann variables along the C_- characteristics are not constant, and therefore propagate into a nonuniform region of gas in state ③ (Fig. 2.13). These waves (C_- characteristics) subsequently reflect off of the closed end wall, and propagate to the open end, further altering the exit properties after the arrival of the Taylor wave tail. After the plateaued regions, the pressure and flow speed profiles are approximated as linear decays to ambient conditions over a period of $\tau = 0.5$. The remaining properties are approximated using isentropic relations. The assumptions and simplifications used to compute the latter portions of the blowdown process do not change any of the conclusions of this work and were introduced to simplify a portion of the calculations.

The choice of 1 cm diameter tube for all cases was motivated by several reasons. First, it provides a mass flow rate of post-detonation products that is sufficient to condition the mass flow rate of a hypothetical primary jet in crossflow, which is typically on the order of a few grams per second. Second, the size of a 1 cm tube is sufficiently small to provide a compact design in practical applications. Third, the tube diameter is sufficiently large to provide a means of generating and sustaining

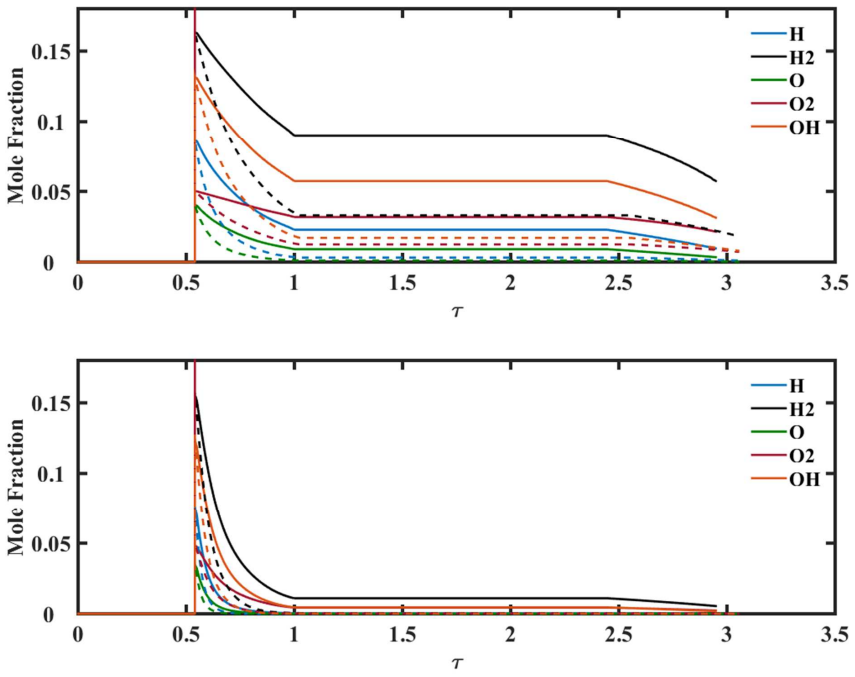

Figure 7.2: Computed temporal evolution of chemical equilibrium composition near the detonation tube exit plane ($\xi = 0.99$). The compositions are specific to a stoichiometric H_2-O_2 detonation with $P_1 = 0.5$ atm and $T_1 = 300$ K. All cases were computed with a 1 cm tube and $C_f = 0.006$. Each curve represents a different case; isentropic (top plot - solid curves), $\beta = 50$ (top plot - dashed curves), $\beta = 100$ (bottom plot - solid curves), and $\beta = 200$ (bottom plot - dashed curves).

ideal stoichiometric H_2-O_2 detonation wave propagation. The length of the tube, and hence value of β, should then control the deviation of the post-detonation gas properties from the case of ideal isentropic expansion. The results of Fig. 7.1 reveal how the parameters such as the mass flow rate, momentum flux ratio, and pressure are fairly insensitive to the parameter β. The effect of increasing β slightly decreases the value to which the values decay, and also increases the rate in which the properties decay during the time $0.54 < \tau < 0.8$. The latter is due to the increasingly rapid expansion of the post-detonation gases immediately downstream of the CJ-plane.

The results of Fig. 7.1 also show that the post-detonation gas exit temperature is very sensitive to the value of β, and hence length of the detonation tube. The effect of increasing β significantly decreases the value to which the temperatures decay, and

also increases the rate in which they decay during the time $0.54 < \tau < 0.8$. Because of the exponential dependence of reaction rates on temperature, this can severely limit the thermal effect that the post-detonation gases have on the reacting system. Furthermore, the results also have implications on the potential kinetic mechanisms that enhance combustion. This can be readily seen by assuming that the post-detonation gases issuing from the tube are in chemical equilibrium and computing the composition using a chemical equilibrium code such as CEA [109, 110] during the blowdown process. The resulting species compositions in mole fraction as a function of the blowdown period are given in Fig. 7.2. The top plot corresponds to the isentropic (solid) and $\beta = 50$ (dash) cases, while the bottom plot corresponds to the $\beta = 100$ (solid) and $\beta = 200$ (dash) cases. The concentrations of H_2O_2 and HO_2 were always less than 1/100 of a percent, and were therefore omitted for clarity. Therefore the mole fraction of H_2O (not shown), is approximately the remaining fraction of the mixture composition ($X_{H_2O} = 1 - \sum X_i$ where the subscript i refers to the species shown in Fig. 7.2).

The large difference in thermodynamic state of the exhausting products (between different cases of β), has a substantial effect on the exhausting species composition during the blowdown period. In the isentropic case, the temperatures remain sufficiently high to sustain a considerable concentration of intermediate species throughout the entire blowdown period. While radicals also exist throughout the blowdown process of the $\beta = 50$ case, they are reduced by more than 50% of the isentropic case. The reduction is even more severe for larger values of β shown in the lower plot. Based on the results of this model, only H_2O is exhausted from the detonation tube when $\tau > 0.7$ for the case where $\beta = 200$. Moreover, the rate of decay of the radical concentrations increases exponentially with increasing β, as a result of the larger rate of expansion immediately after the CJ-plane, and the exponential dependence of equilibrium composition on temperature.

7.2.2 Effect of Varying the Tube Wall Temperature

In practical applications, a detonation tube that is used to augment combustion in a supersonic reacting system would be operated at a repetition rate that is sufficient to condition the combustor flow field in a quasi-steady manner. This implies that the period between pulses should be at least of the same order as the particle residence time through the combustor. The large repetition rates and post-detonation temperatures will subject the tube walls to large heat transfer loads [184] and will require active cooling. Controlled heating of the detonator tube walls may be advantageous in practical operation as it reduces the gradients within the thermal boundary layer and hence heat transfer rate to the walls. This in turn may reduce the extent in which the trailing post-detonation gas properties deviate from the ideal isentropic expansion case.

In some ways, increasing the tube wall temperature has a similar effect as decreasing the parameter β. The effect of increasing the tube wall temperature on the exit pressure and temperature of the post-detonation gas is shown in Figs. 7.3 and 7.4. The computations were carried out for a fixed value of $\beta = 50$, and the effects of momentum losses were still considered in an equivalent manner for all cases. The profiles, which pertain to a portion of the blowdown period, reveal how increasing the wall temperature drives the solution closer to the isentropic case, where no heat is conducted between the gas and tube walls. Furthermore, based on the present formulation the results show how heat transfer losses dominate momentum losses. This is inferred by how the profiles converge to the isentropic solution with increasing wall temperature. In fact, in the limit that the wall temperature equals the CJ-state temperature (not shown), the temperature profile is nearly identical to that of the isentropic case. The rate of convergence to the isentropic solution occurs in a non-linear manner. In other words, only a marginal recovery towards the isentropic solution is obtained by increasing the wall temperature by 66% ($T_w = 500$ K) or 233%

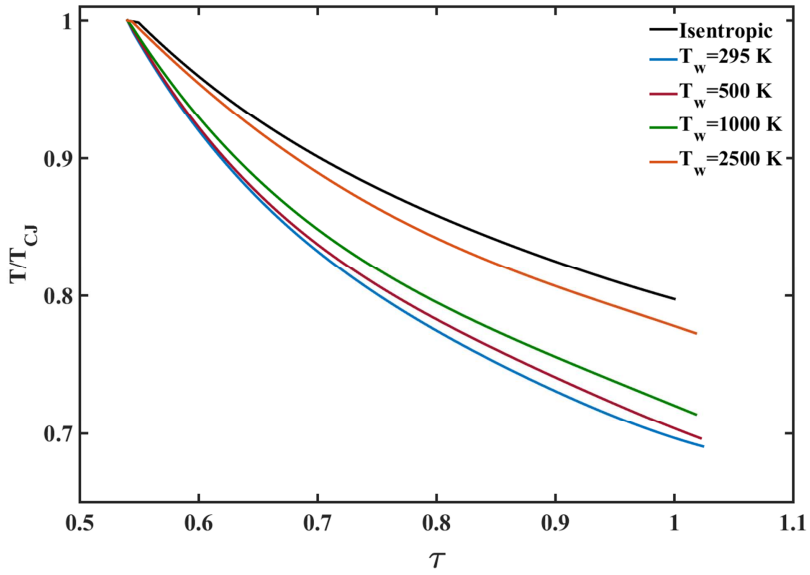

Figure 7.3: Computed temporal evolution of the gas temperature near the detonation tube exit plane ($\xi = 0.99$), for various tube wall temperatures (T_w). The computations are specific to a stoichiometric H_2-O_2 detonation with $P_1 = 0.5$ atm and $T_1 = 300$ K. All cases were computed with a 1 cm tube, $C_f = 0.006$, and $\beta = 50$.

($T_w = 1000$ K). This nonlinear behavior is controlled by the third term inside of the brackets of Eqn. 5.11, which only has a significant impact on the relation as the wall temperature approaches the CJ-state temperature ($T_w \longrightarrow T_{CJ}$).

In practical applications, the temperatures of structural components such as the tube walls need to be actively cooled. Based on the current analysis, maintaining elevated tube wall temperatures to practical levels (taken to be 1000 K) can only marginally improve the performance of the detonation tube. Furthermore, the presented results assume that there is negligible heat conduction between the tube walls and initial gas that fills the detonation tube. In other words, the initial stoichiometric H_2-O_2 gas mixture temperature is $T_1 = 300$ K. In reality, the initial temperature of the gas mixture will be closer to tube wall temperature, which can significantly alter the detonation parameters and post-detonation gas properties. To understand the effects of increasing the initial mixture temperature on the performance of the PD, the ZND profiles of several detonation waves were computed with Cantera [71], using

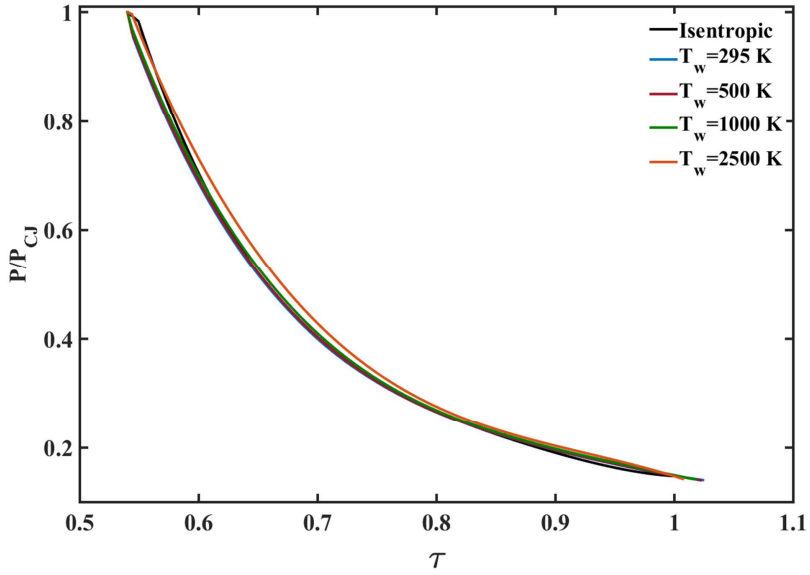

Figure 7.4: Computed temporal evolution of the gas pressure near the detonation tube exit plane ($\xi = 0.99$), for various tube wall temperatures (T_w). The computations are specific to a stoichiometric H_2-O_2 detonation with $P_1 = 0.5$ atm and $T_1 = 300$ K. All cases were computed with a 1 cm tube, $C_f = 0.006$, and $\beta = 50$.

the GRI 3.0 mechanism [72]. The profiles are shown in Fig. 7.5, and correspond to the resulting wave structures of stoichiometric H_2-O_2 detonations where $P_1 = 0.5$ atm and $T_1 = 300$ K (solid), 500 K (dash), and 1000 K (dashed-dot).

The detonation wave structure and properties differ drastically as the initial mixture temperature is varied. While the temperatures at the CJ-plane (not shown) are within 4% of one another, the difference in pressures is as large as 80%. The primary cause for this lies in the significant change in detonation wave Mach number. The detonation propagation speeds of the $T_1 = 500$ K and $T_1 = 1000$ K cases are approximately 4% and 7% less than the $T_1 = 300$ K case, respectively. This implies that the strength of the expansion process within the reaction zone that drives the shock forward is decreasing with increasing T_1, but not sufficiently to resolve the vastly different profiles. However, since the speed of sound of the initial gas mixture increases by $\sqrt{T_1}$, the detonation Mach number decreases. The subsequent jump conditions across the leading shock decrease, leading to lower pressures in the von Neumann

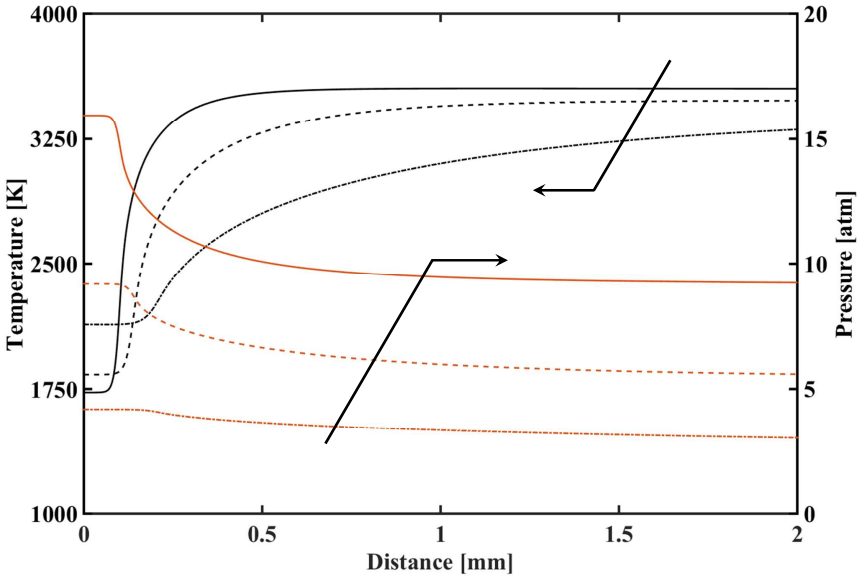

Figure 7.5: Calculated ZND profiles for stoichiometric H_2-O_2 detonations initially at $P_1 = 0.5$ atm and $T_1 = 300$ K (solid), $T_1 = 500$ K (dash), and $T_1 = 1000$ K (dashed-dot). The leading shock is located at $x = 0$.

state, which further decrease after expansion through the reaction zone. Although the temperatures in the von Neumann state are higher with increasing T_1, the impact of the significantly lower pressures cause an overall reduction in the binary reaction rates. This is observed as an increase in both the induction zone length as well as the reaction zone length. Since increasing the initial mixture temperature decreases the leading shock strength, the potential advantages offered by the pressure-gain combustion process of the detonation wave are squandered. In the context of using a PD for supersonic combustion enhancement applications, the pulsed detonation device will exhibit lower exhaust temperatures and momentum flux ratios. Generally, this will lead to a decrease in the extent of impact (both through fluid mechanic and chemical processes), the detonation device has in enhancing the mixing and combustion properties of the supersonic reacting system.

7.2.3 Exhausting Species Composition During Blowdown Process

To analyze the impact of the post-detonation gas on the reacting flow field, and determine the underlying mechanisms that lead to enhanced combustion, knowledge of the time-varying species composition exhausting from the PD is required. While the profiles provided in Fig. 7.2 reveal the time varying equilibrium species composition at the exit plane of the PD, they may not be representative of the final species composition that is being issued into the JISCF flow field. Since the detonation tube exit pressure is greater than four times the ambient pressure when $0.54 < \tau < 0.8$, the PD exhausts into the flow as a highly underexpanded sonic jet [15, 185]. Therefore, before the post-detonation products reach the JICF system, they are first expanded through a barrel shock that is subsequently terminated by a Mach disk that recompresses the flow.

A schematic of the barrel shock structure is given in Fig. 7.6. The variation in temperature and pressure along the centerline axial coordinate is also given qualitatively. Both pressure and temperature decrease as the gas is accelerated from the exit plane Ⓔ to a location just upstream of the Mach disk ①. The gas is then compressed as it is processed by the Mach disk, increasing the temperature and pressure ②. The gas temperature nearly recovers to the value at the exit, while the pressure in state ② is less than the exit pressure and of the ambient pressure surrounding the barrel shock. Downstream of location ② the gas is further compressed to the ambient pressure by a series of weaker oblique shocks (not shown). The location of the Mach disk (y/d), and therefore its strength, is a characteristic of the underexpanded jet and has been found to primarily correlate with the the jet exit to ambient pressure ratio [107, 108]. The empirical relation was previously discussed and is given by Eqn. 3.2.

The flow upstream of the Mach disk of a high-pressure ratio jet, has been commonly calculated by the method of characteristics (MOC) [186–188]. For the purposes of this study, the self-similar solution of the Mach number profile along the centerline

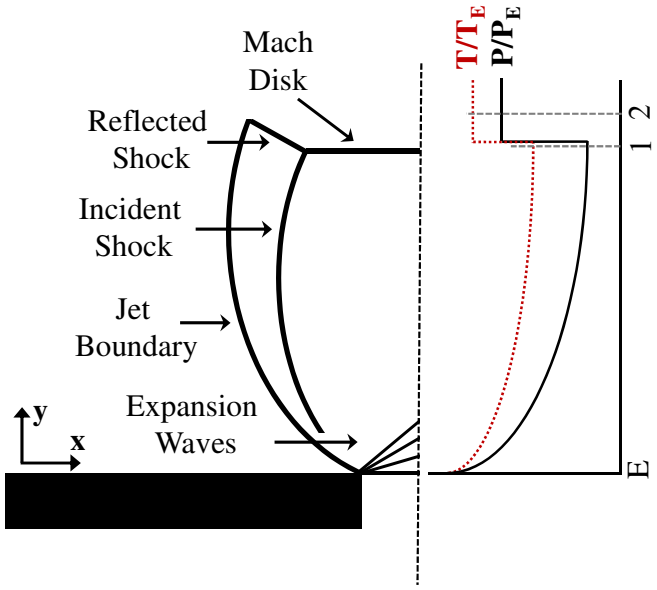

Figure 7.6: Schematic of a highly underexpanded ($P_j/P_a > 4$) sonic jet, revealing several relevant flow structures and a qualitative description of the thermodynamic properties along the centerline.

axial coordinate was extracted from Ref. [15] and is shown in Fig. 7.7. By assuming the post-detonation products behave as a calorically perfect gas within this region of the flow, the axial variation of flow velocity, temperature, and pressure can then be obtained by using isentropic relations [114]. The empirical relations given by Refs. [107, 108], are used to determine the location of the Mach disk. By knowing the local Mach number just upstream of the Mach disk (location ①), the jump conditions across it are determined using normal shock relations for a calorically perfect gas [114]. Subsequently, the spatial coordinate (y/d) along the axial direction is converted to a flow time, such that a finite rate calculation of the post-detonation gas as it is expanded through the barrel shock structure and terminating Mach disk can be performed. Based on this simplified model, the finite rate calculation of a slug of post-detonation gas traversing the barrel shock corresponds to a specific point in time during the blowdown period. This is because the location and strength of the Mach disk depend on the jet pressure ratio, which is varying in time.

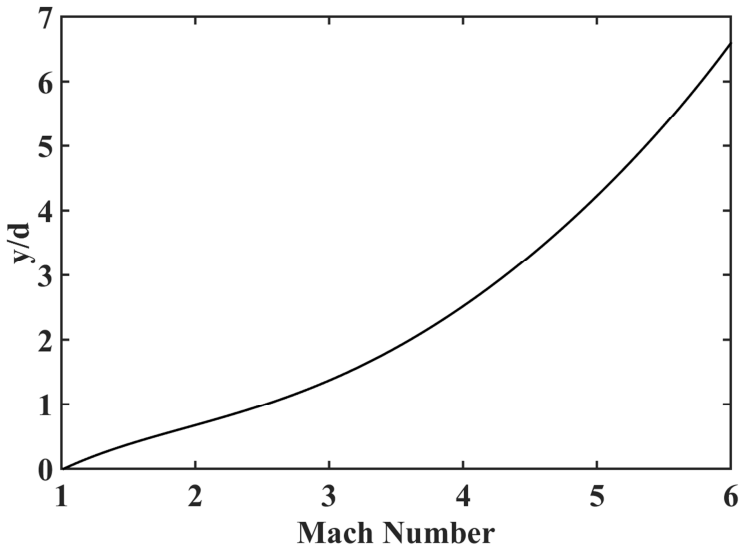

Figure 7.7: Computed Mach number profile along the centerline of a highly under-expanded sonic jet, taken from Ref. [15].

The finite rate calculations were carried out for three times during the blowdown period, $\tau = 0.54$, 0.8, and 1.5. The percent deviation from frozen chemistry of the species compositions across the barrel shock and Mach disk is shown in Fig. 7.8. The gas is observed to react as it exits the PD exit port and traverses the barrel shock structure. The simultaneous decrease in temperature and pressure have competing effects on the local composition. Lower temperatures drive the composition towards fully recombining to form water, while lower pressures result in dissociation of water and a stable presence of intermediate species. The combined effect results in limiting the amount of deviation from frozen chemistry, as well as causing the variation in composition to occur gradually. Upon being processed by the Mach disk, the species composition changes rapidly, as the combined effect of the increased temperature and pressure drives the composition towards a larger concentration of intermediate species. The results also reveal how the species composition just downstream of the Mach disk is within $\pm 10\%$ of the frozen chemistry composition at the conditions located at the exit plane of the PD, for all cases. Therefore to a first order, the post-detonation gas composition entering the JISCF system can be approximated as

being equivalent to the chemical equilibrium composition at the exit of the pulsed detonation tube. To this end, the species composition profiles given by Fig. 7.2 were used in the remainder of the analysis as sufficiently accurate representations of the detonation tube exhaust species composition throughout the blowdown process.

7.3 Sensible and Chemical Heating

The elevated temperature of the post-detonation gas can significantly alter the distribution of local mixture temperatures within the JISCF system. Mixing of the PD products with the primary jet fuel and freestream air increases the local initial mixture temperatures, and subsequently has an exponential effect on the reaction rates. This leads to a more rapid generation of chain carriers to augment and sustain stable chemical reactions. Therefore, several macroscopic combustion properties are enhanced, such as the extinction strain rate, flammability limits, flame speed, heat release rate, and ignition delay.

The thermal impact of the post-detonation products on the reacting JISCF system stems from a combination of sensible and chemical heating. This can be seen by considering the contributions to the total enthalpy of any species, as the sum of the energy associated with the chemical bonds and the energy associated with the temperature (i.e. internal energy). The former is referred to as the enthalpy of formation, and is defined as the heat evolved when 1 mole of a substance is formed from its elements in their respective standard state (usually $T_{ref} = 298$ and $P_{ref} = 1$ bar). The latter is referred to as the sensible enthalpy and is a measure of the thermal energy of a substance. The enthalpy of a species i and with a temperature T can therefore be expressed as,

$$h_{0,i}(T) = h_{f,i}(T_{ref}) + h_{s,i}(T - T_{ref}) \tag{7.1}$$

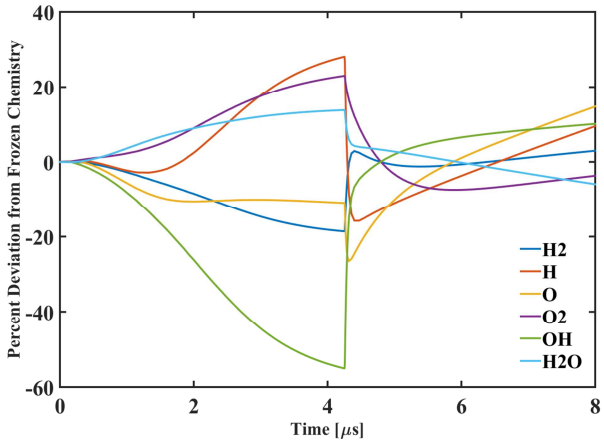

(a)

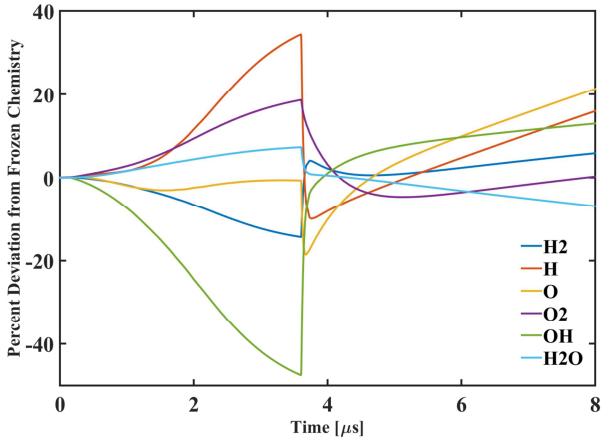

(b)

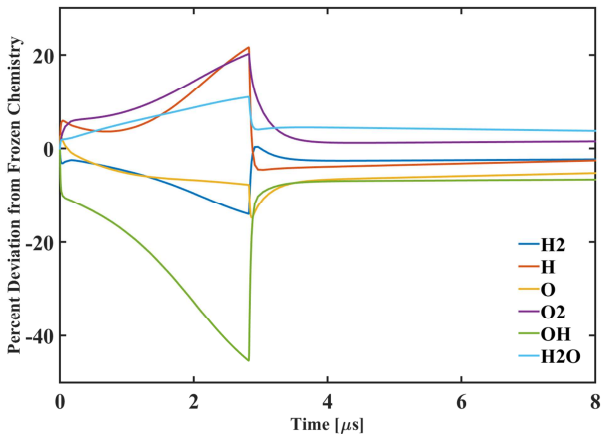

(c)

Figure 7.8: Finite-rate calculations of the species composition profiles along the centerline of a sonic underexpanded jet generated by the exhaust of a stoichiometric H_2-O_2 detonation with $P_1 = 0.5$ atm and $T_1 = 300$ K. The figures represent the species composition profiles along the barrel shock structure at different times during the blowdown period; (a) $\tau = 0.54$ (b) $\tau = 0.8$ (c) $\tau = 1.5$

The sensible portion of heating arises from the adiabatic and isobaric mixing of inert gases with different initial temperatures. The final mixture temperature is found by an energy balance between the sum of the sensible enthalpies of the gases in their initial unmixed state and the sensible enthalpy of the final mixture. The energy balance implies that the initial mixture species are chemically frozen throughout the mixing process. The expression is given by the following,

$$h_{s,mix} = \sum_i X_i h_{s,i} \tag{7.2}$$

or more specifically,

$$\int_{298}^{T_{mix}} C_{p_{mix}}(T)\ dT = \sum_i X_i \int_{298}^{T_i} C_{p_i}(T)\ dT \tag{7.3}$$

where X_i refers to the mole fraction of species i, and mix refers to the final mixture.

The second mechanism in which the post-detonation products thermally impact the reacting system is by chemical heating. This is caused by the formation of water through the recombination of radicals, as they are cooled by mixing with the JISCF system. The amount of energy that is released through this process and in turn heats the JISCF system can be determined by first considering the heat of reaction. The heat of reaction is defined as the difference in the enthalpy of formations of the products and reactants of a given reaction. This is expressed as follows,

$$H_r = \sum_p X_p h_{f,p} - \sum_r X_r h_{f,r} \tag{7.4}$$

where the subscripts p and r denote products and reactants. Typically, elements such as H_2, O_2, and N_2, which are in their standard ideal gaseous state ($T_{ref} = 298$ K and $P_{ref} = 1$ bar), are assigned an enthalpy of formation value of zero. For example, the heat of reaction of a stoichiometric H_2-O_2 mixture is simply equivalent to the enthalpy

of formation of H_2O. By definition, in order for the heat of reaction of any chemical reaction to be completely released, the reactants (H_2 and O_2) must completely react to form products (H_2O). If after the chemical reaction has taken place, intermediate species or reactants remain and do not form stable products, the total potential heat of reaction of the system is not released. For example, by inspection of Fig. 6.2, if the final temperature of a hypothetical reaction were to be less than 2000 K, all reactants are converted to H_2O, and therefore, the total heat of reaction is released and is equivalent to the heat of formation of H_2O. However, if the final temperature of a hypothetical reaction is greater than 2000 K, a portion of the final equilibrium composition will be composed of intermediate species and reactants. In this case, the heat or energy released from the reaction is solely due to the portion which was converted to water. The remaining available energy is stored in the chemical bonds of the reactants and intermediate species. The remaining available energy, which can only be released if the reactants and intermediate species completely react to form water (i.e. cooled down), is given by

$$h_{chem} = h_{f,\mathrm{H_2O}} - \sum_{p} h_{f,p} \tag{7.5}$$

7.3.1 Model Describing the Available Sensible and Chemical Heating

In consideration of these two mechanisms, a model outlined in Fig. 7.9 was used to evaluate the thermal impact of the post-detonation products on the reacting JISCF system. The zero-dimensional model inherently neglects the unsteady, and three-dimensional mixing and combustion phenomena that govern the extent of impact that the post-detonation products have on the flow field. The complex nature of the combustion system is reduced to a perfectly stirred reactor analysis, in which only state properties are sought. However, the model provides insight to trends and properties of limiting scenarios within the flow field. This in turn provides an

understanding of the strengths and limitations of the technique and therefore helps to establish guidelines to extract the full potential of the post-detonation products in augmenting combustion.

Chemical reactions with the JISCF system are not considered, and therefore the composition of the JISCF system is treated as chemically frozen throughout the entire process. The model includes five free parameters (given in red), which include the freestream temperature (T_{fs}), JISCF system equivalence ratio (Φ), the length to diameter ratio of the detonator tube (β), the time within the blowdown process (τ), and the amount of post-detonation products added to the system (α). The model begins by considering the isobaric and adiabatic mixing process of the primary hydrogen jet and freestream air, which comprise the JISCF system. The temperature of the hydrogen is taken to be 300 K, while the temperature of the air (T_{fs}) is a free parameter. The second free parameter is the equivalence ratio (Φ) of the hydrogen-air mixture. For a given value of Φ, the JISCF mixture temperature is found through a balance of the sensible enthalpies.

The composition and properties of the post-detonation products are computed by a subsequent expansion of the CJ-state gas that is generated by the ideal propagation of a detonation wave through a stoichiometric H_2-O_2 mixture with an initial temperature and pressure of 300 K and 0.5 atm, respectively. The unsteady expansion process is an additional free parameter that is computed through the model described in Chapter V. In addition to an isentropic expansion process, the trailing post-detonation gas is modeled with varying levels of heat transfer and momentum losses to the tube walls, therefore altering the time varying exhaust properties and composition of the detonation tube, as is shown in Figs. 7.2. After defining the extent of interaction and losses between the post-detonation gas and tube walls through the parameter β, a fraction α of post-detonation products, taken at a time τ during the blowdown period, are mixed with the JISCF system through an isobaric process.

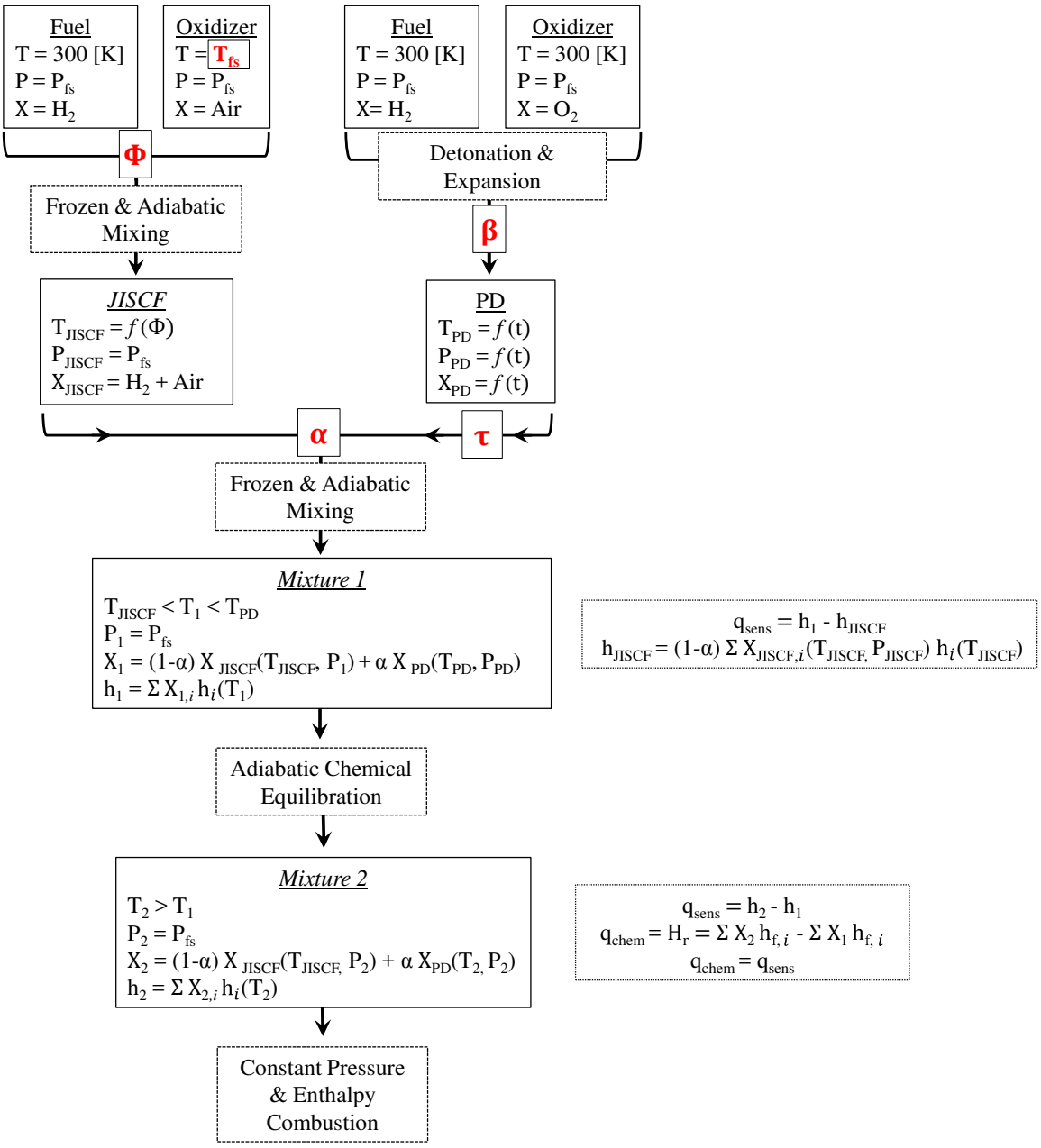

Figure 7.9: Diagram of model used to compute the thermodynamic properties of the JISCF-PD system. The solid boxes represent various states, while the dashed boxes represent processes. The free parameters are given in red and are described in the text. The freestream pressure P_{fs} was always taken to be 0.5 atm.

The thermal effects of mixing the post-detonation products with the JISCF system are broken into two parts: (1) sensible and (2) chemical heating components. The extent of sensible heating is determined by allowing an adiabatic mixing process of the chemically frozen post-detonation products to take place with the JISCF system. Since both mixtures are chemically frozen, only a balance between the sensible enthalpies is treated. In essence, this is equivalent to the process of mixing two streams of inert gases with specific heats and molecular weights that are equivalent to those of the JISCF and PD. Through this process, the amount of energy that is added to the JISCF system is given by

$$q_{sens} = h_{s,1} - h_{s,JISCF} \tag{7.6}$$

and is solely due to the sensible contribution of heating. The system is now composed of non-equilibrium JISCF and PD compositions with a thermodynamic state labeled *Mixture 1*. Next, the contribution of heating due to the chemical portion of enthalpy is considered. This is computed by only allowing the post-detonation gas in state *Mixture 1*, to reach chemical equilibrium through an adiabatic and non-isobaric process. Through this process, the mixture reaches a state labeled *Mixture 2*, where $T_2 > T_1$ and $P_2 = P_1 = P_{fs}$, since the energy released through chemical equilibration is put back into the system as sensible energy. The thermodynamic properties of the final state *Mixture 2* are found by equating the sensible enthalpy of the mixture in state *Mixture 2*, with the energy released by the formation of H_2O. Specifically, this is computed by iteratively solving the following expression for T_2 using a chemical equilibrium solver,

$$h_{s,2} - h_{s,1} = \sum_i X_{2,i}\ h_{f,i} - \sum_i X_{1,i}\ h_{f,i} \tag{7.7}$$

Therefore, the amount of energy added to the JISCF system by chemical heating of

the post-detonation products is given by

$$q_{chem} = \sum_i X_{2,i}\ h_{f,i} - \sum_i X_{1,i}\ h_{f,i} \tag{7.8}$$

which is the more general form of Eqn. 7.5, that does not assume that the composition in state *Mixture 2* is all H_2O.

7.3.2 Quantification of Thermal Heating Effects

The thermal impact analysis starts by considering several cases of detonation tube operation with varying values of the parameter β. In order to gain a sense of the total heating potential of the post-detonation products, the value of α is chosen to be one, and the value for τ is varied to encompass the entire blowdown period. Setting $\alpha = 1$, is equivalent to determining the total amount of heat or energy the PD can provide. In this case, the values of q_{sens} and q_{chem} are independent of any parameters defining the JISCF system, and therefore quantify the potential of the PD device irrespective of the properties of the reacting system it is issuing into.

The results are summarized in the bottom row of plots of Fig. 7.1. Like the other plots within the figure, the solid black, dashed red, dashed-dot orange, and dotted green curves correspond to isentropic, $\beta = 50$, 100, and 200 cases, respectively. The results show how during very early portions of the blowdown period, both forms of heating provide the largest amounts of energy and are also of the same order of magnitude. The peak sensible heating is directly correlated and attributed with the largest temperatures of the PD exhaust. Similarly, the peak chemical heating is observed to occur over the largest exhaust temperatures, however in this case there is an increased sensitivity to variations in temperature, as well as an additional dependence on pressure. This is because of the highly-non linear dependence of the chemical reaction rates and equilibrium constants on temperature and pressure. While the amount of sensible heating decreases by 15% (isentropic) and 25% ($\beta = 50$)

over most of the blowdown period, the chemical heating is observed to decrease by nearly 60% (isentropic) and 88% ($\beta = 50$). The large variation is of course reflected in the equilibrium chemical composition profiles of the PD exhaust (Fig. 7.2), since the chemical heating depends on the availability of intermediate species. Similarly, since increasing the value of β has a significant effect on the PD exhaust temperature profile, large variations in sensible and chemical heating are observed between various cases of β. This implies that practical detonation tube designs for scramjet applications may not be capable of providing the full-potential enhancement of the isentropic case.

Throughout this analysis, the equivalence ratio of the detonation mixture was fixed to the stoichiometric value. It is of interest to explore the expected non-linear effects of varying the equivalence ratio on the chemical and sensible heating mechanisms, in order to understand what can be potentially gained or lost. To this end, the CJ-state properties of detonations propagating through mixtures with $T_1 = 300$ K, $P_1 = 0.5$ atm, and $\Phi = 0.5$, 0.75, 1.0, 1.25, and 1.5 were computed. The CJ state properties were then isentropically expanded to ambient pressure (P=0.5 atm), to simulate the effect of an ideal blowdown process. The results are shown in Fig. 7.10, where the red and black curves correspond to sensible and chemical heating, respectively, and curves with different symbols correspond to different values of Φ. Essentially, each curve is analogous to the isentropic curves of Fig. 7.1, except in this case, the expansion (along each curve from right to left) is not subject to the specific time-dependent variation of the blowdown process.

The results reveal how insensitive the sensible component of heating is with respect to equivalence ratio. This is because of the weak dependence that the detonation wave parameters and CJ-state properties have on equivalence ratio within this range, as was shown in Figs. 3.9. Moreover, as is expected, the peak heating is obtained along the curve that corresponds to $\Phi = 1$. On the other hand, the chemical portion of heating is observed to be very sensitive to the mixture equivalence ratio. The

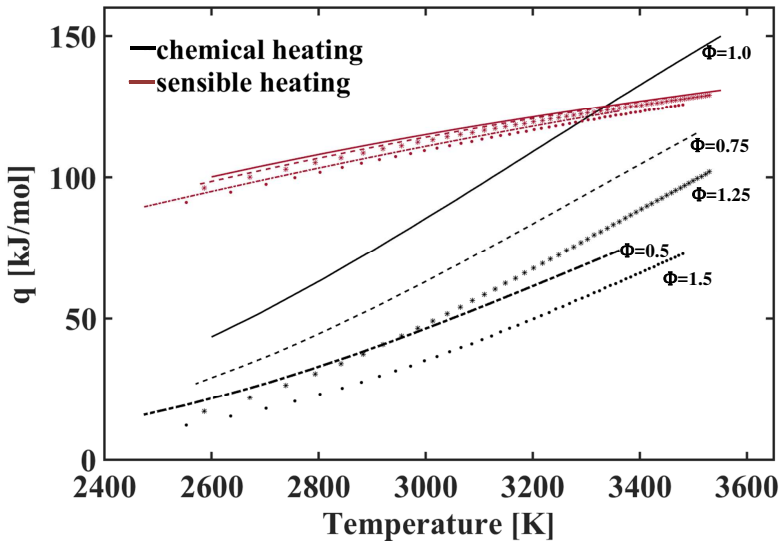

Figure 7.10: The total amount of sensibe and chemical heating that is provided by the post-detonation products of a H_2-O_2 detonation with $P_1 = 0.5$ atm and $T_1 = 300$ K. Each curve corresponds to a different initial mixture equivalence ratio. Along each curve, the properties are isentropically expanded from the CJ-state (initial values on the right) to ambient pressure (final values on the left), therefore representing the variation of thermal heating during the blowdown process of a detonation tube.

greatest amount of chemical heating is obtained with an equivalence ratio of one, and is decreased with richer and leaner mixtures. Interestingly, as Φ is varied, the extent of chemical heating behaves asymmetrically about $\Phi = 1$. This is seen be comparing the $Phi = 0.5$ curve to the $\Phi = 1.5$ curve, and similarly by comparing the $\Phi = 0.75$ curve to the $\Phi = 1.25$ curve. Leaner mixtures provide greater amounts of chemical heating than corresponding rich mixtures that deviate equally from stoichiometry. The variation of the CJ-state thermodynamic properties between these cases alone is not sufficient to explain the large differences in chemical heating. In other words, the differences in CJ-state temperatures and pressures are responsible for no more than a 2% difference in the equilibrium concentration of H_2O between lean and rich mixtures with an equal deviation from stoichiometry. The cause for the large differences in chemical heating is primarily due to the difference in initial mixture compositions and the subsequent chemical kinetic processes that determine the

final equilibrium composition. At these elevated temperatures, lean mixtures contain greater concentrations of atomic oxygen and smaller concentrations of atomic hydrogen, as compared to rich mixtures. Since the enthalpy of formation of atomic oxygen is nearly 14% greater than that of atomic hydrogen, more chemical energy is stored and can be released with leaner mixtures. Since the stoichiometric mixture generated the greatest amount of sensible and chemical heating, it was kept fixed throughout the remainder of the analyses in this study.

While an evaluation of the integrated heating potential of the PD products over a single cycle (blowdown period) may be useful in some instances, the approach is incapable of providing insight to the temporal evolution of the heating mechanisms. This is due to the fact that the mass flow rate of the PD tube changes by an order of magnitude during the blowdown process. To this end, the following expression was used to determine the contribution of heating associated at various times of the blowdown process,

$$\psi_k = \frac{\int_0^{\tau<\tau_{bd}} \dot{m}\ q_k\ d\tau}{\int_0^{\tau_{bd}} \dot{m}\ q_k\ d\tau} \tag{7.9}$$

where the subscript k denotes either the sensible or chemical form of heating. The integral of the denominator is evaluated over one blowdown period τ_{bd}. The variable ψ_k is the relative temporal variation of heating. The variations of ψ for different values of β and for both the sensible and chemical forms of heating are shown in Figs. 7.11 and 7.12, respectively. The results reveal how ψ_{sens} is fairly insensitive to the parameter β. Although the total amount of heat released between cases is different, the results imply that regardless of the degree of non-ideal operation of the PD tube (β), approximately 70% of the total sensible heating occurs within the first 15% of the blowdown period (approximately $0.54 < \tau < 1$). On the other hand, ψ_{chem} is observed to have a more significant dependence on the parameter β. Larger values of β confine greater portions of the heat release within smaller and earlier portions

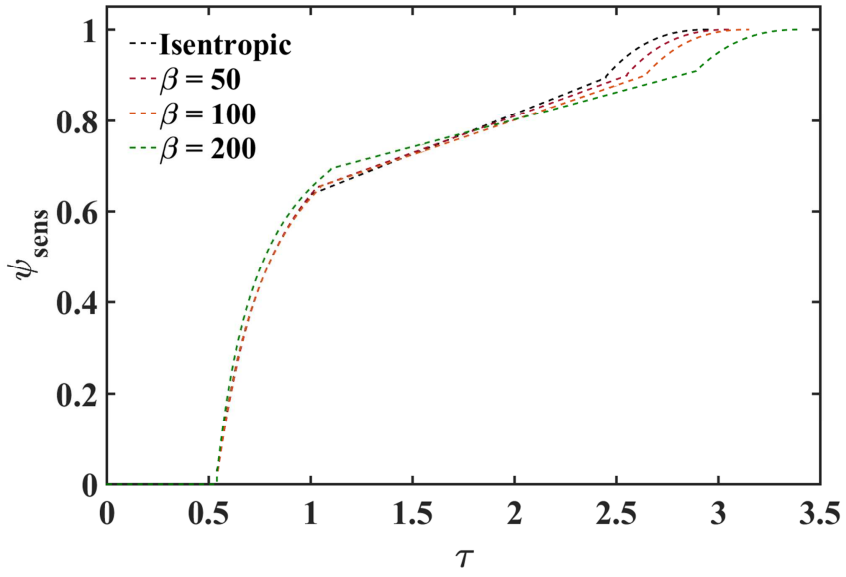

Figure 7.11: The fractional sensible heat release over a single PD cycle (blowdown period). Each curve corresponds to varying degrees of non-ideal detonation tube operation.

of the blowdown period. For example, while in the isentropic case approximately 75% of the chemical heat release occurs within $0.54 < \tau < 1$, nearly all of the heat is released within $0.54 < \tau < 0.8$ for the $\beta = 200$ case. This is a manifestation of the rapid decrease in radical concentrations that occur due to the increasingly rapid expansion of the post-detonation (with increasing β) gas immediately downstream of the CJ-plane.

The combined results of Figs. 7.11 and 7.12 imply that over 70% of the total heat is release (sensible plus chemical) occurs within the first 15% of the blowdown period, regardless of the value of β. Therefore, the post-detonation products are expected to have a greater impact on the reacting flow field within the first 15% than the remaining portion of the blowdown combined. Fig. 7.13 provides an understanding of how ψ_k varies relative to the total heat released with the isentropic case. The dashed and solid lines correspond to the sensible and chemical forms of heating, respectively. The curves were evaluated with the following expression,

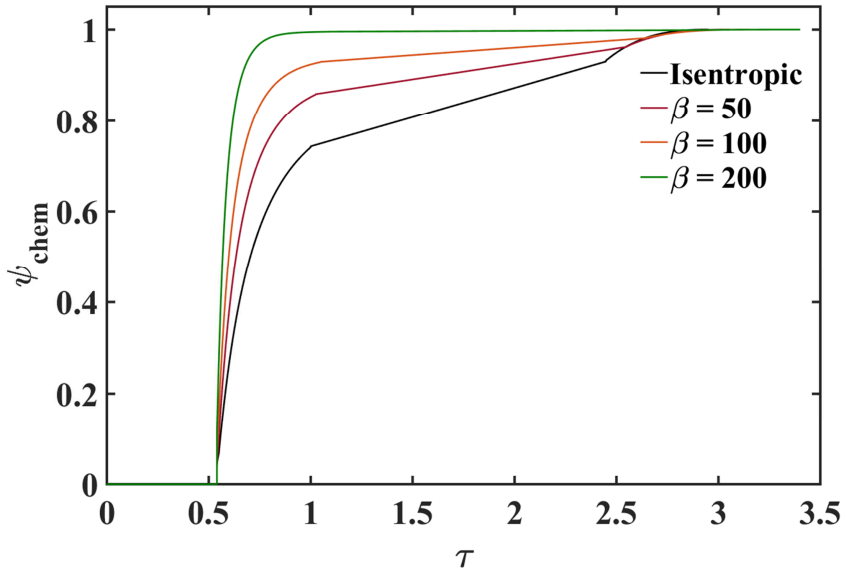

Figure 7.12: The fractional chemical heat release over a single PD cycle (blowdown period). Each curve corresponds to varying degrees of non-ideal detonation tube operation.

$$\frac{\psi_k}{\psi_{Isentropic}} = \frac{\int_0^{\tau<\tau_{bd}} \dot{m}\ q_k\ d\tau}{\int_0^{\tau_{bd}} \dot{m}\ \left(q_{chem} + q_{sens}\right)_{Isentropic}\ d\tau} \tag{7.10}$$

The value along each curve represents the corresponding integrated heat release contribution with respect to the total heat released (sensible and chemical) through the blowdown period of the isentropic case. For example, the nonlinear decrease in the total heat released (with increasing β) is evident by comparison of the final values of each curve with the corresponding (dashed or solid) black curves. Moreover, the contribution of heat release from sensible heating is always greater than the chemical, and the difference in contribution between the two increases with β.

Although the analysis thus far has been limited to the thermal impact of the post-detonation products, from the results obtained so far it is clear how detonation tube designs used for scramjet applications should be limited to $\beta \leq 50$. Larger values result in smaller heat release budgets. Since chemical reaction rates have an exponential dependence on temperature, the effectiveness of the post-detonation

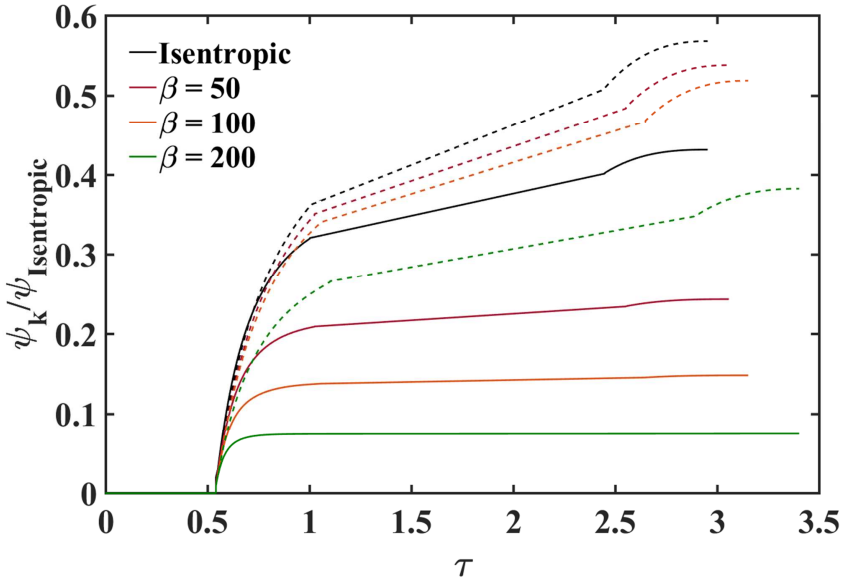

Figure 7.13: The fractional sensible (dashed) and chemical (solid) heat release with respect to the isentropic case, over a single PD cycle (blowdown period). Different color curves correspond to varying degrees of non-ideal detonation tube operation.

products in enhancing reactivity of a system will be very sensitive to the parameter β. Furthermore, it will be shown how the availability of radicals has a larger role in enhancing combustion than just releasing heat. By providing the reacting supersonic flow field with a requisite amount of radicals, the chemical kinetic processes of the system are altered, significantly impacting several macroscopic combustion properties.

7.3.3 Impact on Mixture Temperatures

In the previous section, the heating ability of the post-detonation products were analyzed in a general manner that was not specific to any parameters of a reacting system. The purpose of this section is to demonstrate the impact of the post-detonation products on the initial mixture temperature distribution of a non-premixed system over a range of flow conditions relevant to supersonic combustion. In reality, the analysis is not specific to any fuel-injection scheme, such as a JISCF, since it reduces the flow field and mixing streams into a zero-dimensional model. The final state of gas

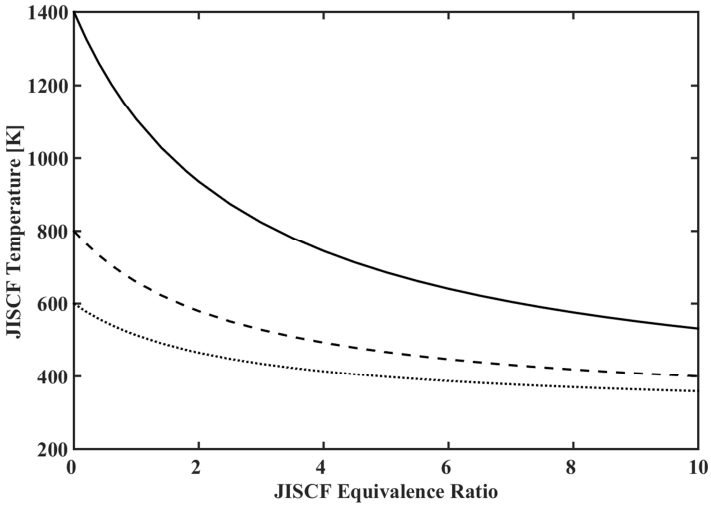

Figure 7.14: Temperature variations of several H_2-Air mixtures, where $T_{H_2} = 300$ and $T_{fs} = 600$ K (dot), 800 K (dash), and 1400 K (solid). Mixing is taken to be an adiabatic, isobaric, and chemically frozen processes.

labeled as *Mixture 2* in Fig. 7.9 represents the state of a local mixture of gas in the reacting system that has been chemically frozen and pre-heated by mixing with post-detonation products. The step following this state is where constant pressure and enthalpy combustion of the JISCF-PD system takes place, and where macroscopic combustion properties such as the flammability limits, flame speed, heat release rate, and ignition delay can be evaluated.

Figure 7.14 illustrates the temperature variation of chemically frozen mixtures of hydrogen and air, as is given by the *JISCF* state of Fig. 7.14. The global pressure of the JSICF system is taken to be 0.5 atm, which is a representative value for a large range of hypothetical flight envelopes. Mixing occurs through an isobaric process, while the initial temperature of the hydrogen gas was fixed at 300 K, and the temperature of air (T_{fs}) was varied between 600 K (dot), 800 K (dash), and 1400 K (solid). The temperatures were chosen to simulate a range of combustor entry conditions of a hypothetical vehicle. Two low temperatures are specifically chosen to understand the impact of the PD products within the context of cold-start conditions. The equivalence ratio was varied between $0 < \Phi < 10$ to determine the effects over a

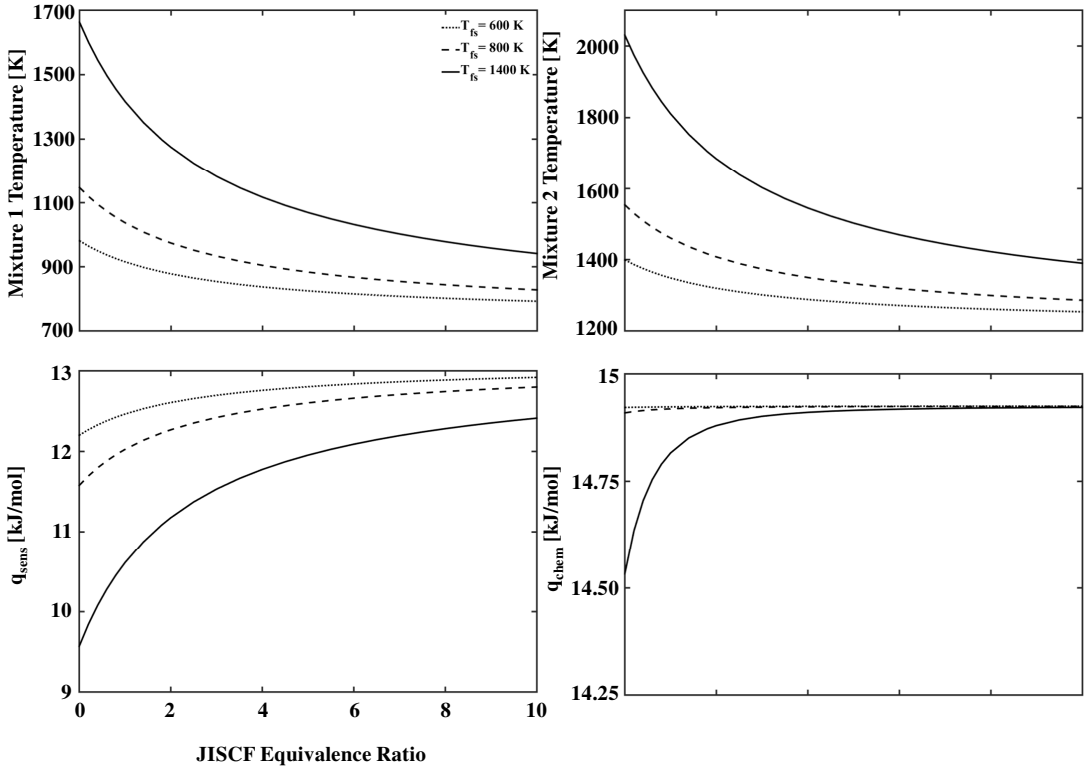

Figure 7.15: Various properties computed with the model outlined in Fig. 7.9 for $T_{fs} = 600$ K (dot), 800 K (dashed), and 1400 K (solid), $\alpha = 0.10$ (10% PD composition), and $\tau = 0.54$ (CJ-state properties). All curves correspond to ideal detonation tube operation, where CJ-state properties are isentropically expanded, and no energy losses to the walls occur.

wide range of regions within the non-premixed reacting flow field. The temperature profiles start with their respective freestream air temperature values when $\Phi = 0$, and asymptote to the temperature of the hydrogen fuel (300 K) with richer mixtures. The low air temperature cases ($T_{fs} = 600$ and 800 K) are always well below the hydrogen-air explosion limits, while the high temperature case ($T_{fs} = 1400$ K), is only within the explosion limit for a narrow range of Φ.

Figure 7.15 shows the temperature variation for the *Mixture 1* and *Mixture 2* states, when 10% of the mixture composition ($\alpha = 0.1$) is composed of post-detonation products taken at a time $\tau = 0.54$ of the blowdown period. This choice of τ is representative of the CJ-state gas, and therefore its properties are independent of the

choice of β (see Fig. 7.1). By comparison of the temperature profiles in Figs. 7.14 and 7.15, it is very clear how by only having 10% of the composition be composed of PD products, a significant gain in the mixture temperatures is obtained. This is attributed to the large CJ-state temperature, which is several time larger than the freestream air temperature of any of the cases. After the sensible and chemical forms of energy have been transferred to the JISCF system (state *Mixture 2*), the mixture temperatures of all cases are well above the explosion limits for the entire range of Φ considered.

Figure 7.15 also illustrates the variation of q_{sens} and q_{chem} that heat the JISCF system from state *JISCF* to *Mixture 1* and state *Mixture 1* to *Mixture 2*, respectively. The largest amounts of sensible and chemical heating occur for richer mixtures that have the lowest initial temperatures. In fact, the values of q_{sens} and q_{chem} asymptote (seen most clearly by inspection of the $T_1 = 600$ K curve) to 10% of the value given by the plots in Fig. 7.1, at a time of $\tau = 0.54$. This is because 10% of the mixture was chosen to be composed of post-detonation products (i.e. $\alpha = 0.1$). As the initial mixture temperature of the JISCF system approaches 298 K (zero sensible energy), the complete energy supplied by the post-detonation products is exploited. As the initial mixture temperature of the JISCF system increases (leaner mixtures), less energy from the post-detonation products can be used, as can be seen by inspection of the energy balance in Eqns. 7.6 and 7.8.

The decrease in q_{chem} that is observed in leaner mixtures (seen most clearly by inspection of the $T_1 = 1400$ K curve), is a consequence of the large final equilibrium temperatures of state *Mixture 2*. In this state, the equilibrium composition contains intermediate species and is not fully composed of H_2O. Therefore the mixture possesses energy in the form of chemical bonds that has not yet been released. The remaining intermediates can either react to release heat after they are transported to colder parts of the flow field, or they can remain within the local mixture, providing

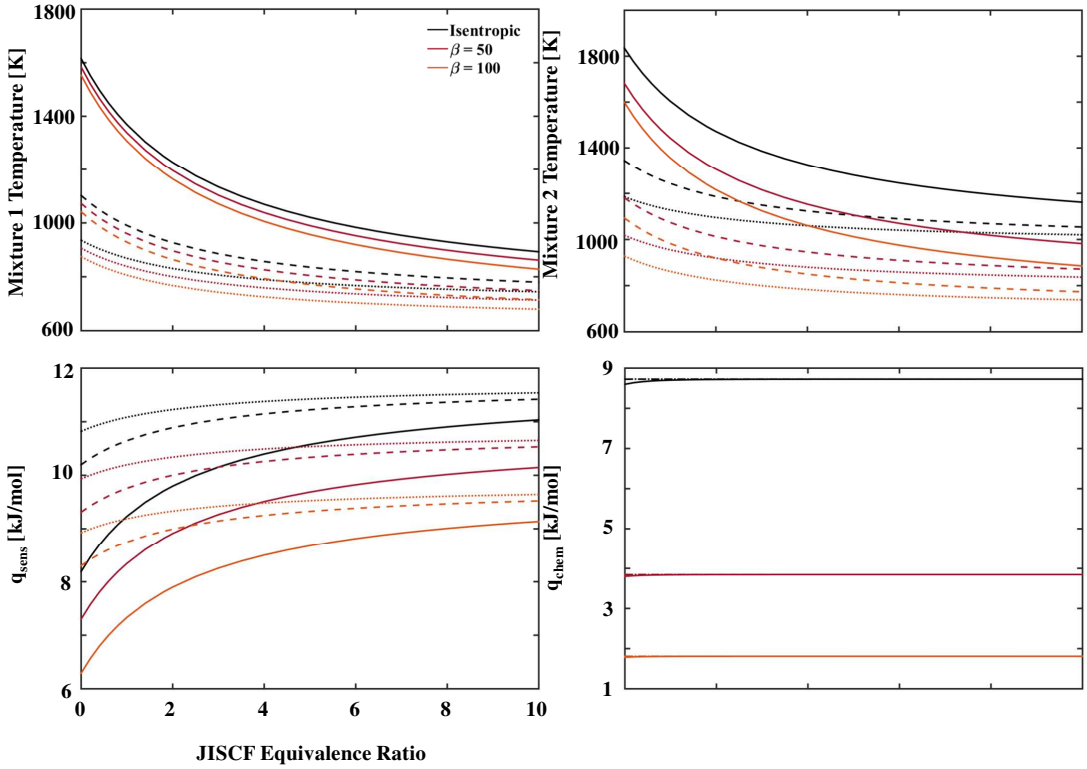

Figure 7.16: Various properties computed with the model outlined in Fig. 7.9 for T_{fs} = 600 K (dot), 800 K (dashed), and 1400 K (solid), $\alpha = 0.10$ (10% PD composition), and $\tau = 0.8$. Different colored curves correspond to different values of β.

additional interaction mechanisms that accelerate the chemical kinetic processes. The latter possibility will be discussed in more detail in the next section.

As the blowdown process progresses, the PD exhaust temperature decreases and contains smaller concentrations of radicals. In order to analyze how the thermal effects change at later times in the blowdown period, the same calculations were carried out with $\tau = 0.8$ and 1.5. The results are illustrated in Figs. 7.16 and 7.17, respectively. The black, red, and orange curves correspond to the isentropic, $\beta = 50$, and $\beta = 100$ cases respectively, while the solid, dash, and dotted curves correspond to $T_{fs} = 600$ K, 800 K, and 1400 K, respectively. Under ideal detonation tube operation (isentropic curves), the PD exhaust is capable of preheating the JISCF system above 900 K (state *Mixture 2*) throughout most of the blowdown process, and with only

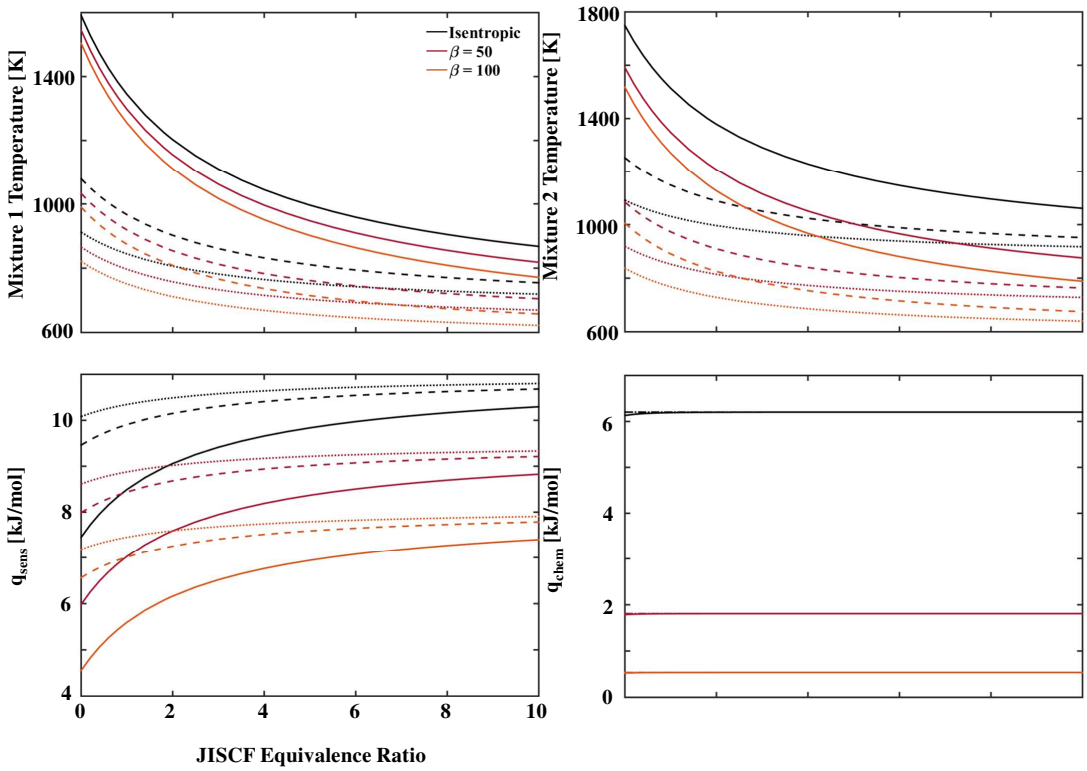

Figure 7.17: Various properties computed with the model outlined in Fig. 7.9 for T_{fs} = 600 K (dot), 800 K (dashed), and 1400 K (solid), $\alpha = 0.10$ (10% PD composition), and $\tau = 1.5$. Different colored curves correspond to different values of β.

10% of the composition being composed of PD products. However, as the value of β is increased to practical values, this is no longer the case. The $\beta = 100$ (orange curves) case reveals how non-idealities in the operation of the detonation tube can cause the extent of thermal impact of the PD products to suffer. In order to compensate for the reduced thermal impact, larger concentrations of the post-detonation products are required. In the case of $\beta = 50$ (red curves), the PD exhaust is capable of heating the JISCF system to over 800 K over most of the range of conditions that was considered.

Preheating the fuel and/or oxidizer of a non-premixed system is known to enhance the extinction strain rate. This concept is typically shown by an S-curve, which describes the hysteric behavior of ignition and extinction of a combustion system. When the Damköhler number is sufficiently high, or equivalently the strain rate is

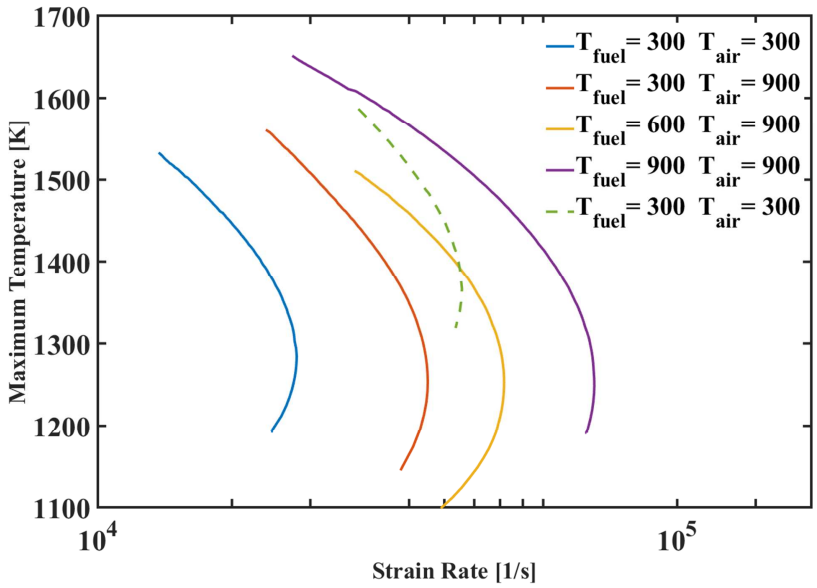

Figure 7.18: Maximum reaction temperatures of non-premixed H_2-Air flames subject to increasing strain rates. The different curves represent different initial fuel-air conditions. The solid and dashed curves correspond to pressures of 0.5 and 1 atm, respectively.

sufficiently small, a stable state of combustion exists. As the strain rate is increased, by decreasing the flow residence time for example, the maximum reaction temperature decreases as larger amounts of heat are transported outside of the flame. As the strain rate is further increased, a state is reached where the chemical reaction rates are not sufficiently fast to release energy within the reaction zone. This state is referred to as extinction, and it occurs when the heat loss from the flame exceeds what is required to sustain steady burning. Increasing the local Damköhler number reduces the susceptibility of the flame to extinction. This can be achieved by increasing the flow residence time or by increasing the reaction rates.

Figure 7.18 shows how increasing the initial temperatures of the fuel or oxidizer increases the tolerance of the flame to larger strain rates. The OH PLIF images shown in Chapter VI reveal how reactions along the shear layer of JISCF system were more stable with the presence of the post-detonation products. This effect is attributed to the pre-heating of the fuel, as well as the supply of radicals to the shear layer, which

increase local reaction rates and therefore augment and sustain stable reactions.

7.4 Oxidation Chemistry

The mechanisms of combustion enhancement by the addition of intermediate species of combustion is not limited to thermal heating. As was discussed in Section 2.4, the presence of radicals in requisite form, can significantly alter the natural kinetic mechanism of the reacting system. A significant modification to the naturally prescribed kinetics of the reacting system is attained if requisite concentrations of post-detonation products are delivered to locally non-premixed or partially premixed reaction zones or premixed regions of the flow. However, the prerequisite of having sufficiently high temperatures to sustain the branching and propagation of radicals is required. If the local mixture composition of a flow contains a sufficient concentration of post-detonation products, the temperatures will remain sufficiently elevated to sustain chain branching and propagation pathways. It is only when the local mixture temperatures are low (fuel rich regions), or when the local concentration of radicals is low, that chain termination reactions become the preferred pathways as was shown in Fig. 6.17.

Experimentally, early portions of the blowdown period generated a large flow rate of post-detonation products. A fraction of the PD exhaust is believed to survive transport to the reaction zones along the shear layer. This is observed in the OH PLIF images and is indicated by point E in Fig. 6.13. During early times of the blowdown process, the mass flow rate and temperature of the PD exhaust are sufficiently high relative to the primary jet, that even upon mixing, the temperatures will be sufficiently high to sustain the existence of radicals. This can be seen from the results of Fig. 7.15, which shows the mixture temperatures for a conservative value of $\alpha = 10$. When this occurs, the oxidation chemistry is believed to be enhanced as reaction rates are increased. The chemical kinetic processes are modified, as the avail-

ability of intermediates provide multiple chain branching and propagation pathways to accelerate the progress of the reactions.

To demonstrate how the PD products modify the kinetic mechanism of a H_2-O_2 reacting system, several simulations were carried out with a perfectly stirred reactor model. The reactor had an initial pressure of 0.5 atm and was comprised of a stoichiometric H_2-O_2 mixture. Four cases were chosen to span the second explosion limit of hydrogen-oxygen reactions, where the initial temperature $T_i = 600$ K (case 1 and 3) and $T_i = 1000$ K (case 2 and 4). The compositions of cases 3 and 4 are comprised of 5% post-detonation products from the CJ-state of a stoichiometric H_2-O_2 detonation where $T_1 = 300$ K and $P_1 = 0.5$ atm. Before mixing the products with the stoichiometric H_2-O_2 mixture, they were chemically frozen and isentropically expanded to the same thermodynamic state as the mixture they were being put into. This effectively eliminates the effects of sensible heating, and permits only chemical heating and kinetic mechanisms to come into effect. This effectively serves as a conserved evaluation of the impact of the post-detonation products on the reacting system.

The temporal evolution of temperature during the ignition process of each case is shown in Fig. 7.19. Of course, case 1 does not ignite as the thermodynamic state is well below the explosion limits, and is only shown for completeness. Under these conditions, the reaction rate of the primary chain termination reaction (Eqn. 7.12) exceeds that of the dominant chain branching reaction (Eqn. 7.11). The opposite occurs for case 2, where after an induction period that is on the order of hundreds of microseconds, the mixture autoignites. During the induction period, the reaction rates of chain initiation and branching pathways are sufficiently high to support and build a radical pool that eventually leads to explosion. The oxidation chemistry in this is referred to as "undisturbed", since it progresses and accelerates without any modification (i.e. addition of radicals from an external source).

The induction period of case 4 is significantly reduced compared to case 2, and

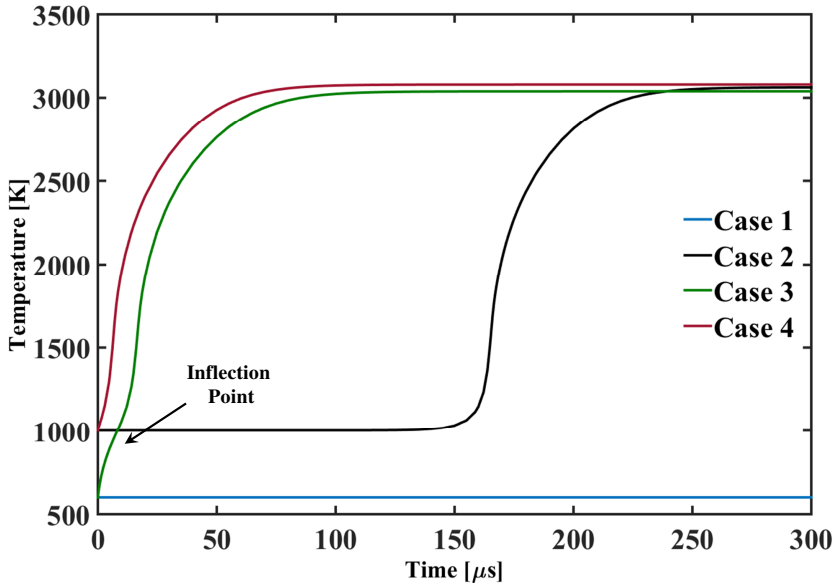

Figure 7.19: Temporal evolution of temperature during the ignition process of a constant pressure (0.5 atm) perfectly stirred reactor. The cases are comprised of a stoichiometric H_2-O_2 mixture, where T_i = 600 K (case 1), T_i = 1000 K (case 2), T_i = 600 K (case 3), and T_i = 1000 K (case 4). The compositions of cases 3 and 4 are comprised of 5% post-detonation products from the CJ-state of a stoichiometric H_2-O_2 detonation with T_1 = 300 K and P_1 = 0.5 atm.

is on the order of several microseconds. In addition to the chemical heating mechanism that enhances the reaction rates, the addition of radicals reduces the reliance on endothermic chain initiation reactions to begin radical production and achieve explosion. At elevated temperatures, the presence of radicals increases the reaction rates of chain branching and exothermic chain propagation reactions, allowing them to have a more significant role in the oxidation chemistry early on. In case 3, the contribution of the thermal and kinetic mechanisms in augmenting ignition are even more evident. The initially low mixture temperatures are not sufficient to support and sustain the propagation of radicals. Rather, chain termination pathways which form water are preferred, releasing chemical energy into the sensible form and elevating the mixture temperature. The mixture temperature increase during the first 20 μs is attributed to this effect. After the crossover temperature is reached, an inflection point is observed in the temperature profile, and is believed to coincide with the turning point. At this time, the radical pool is sufficiently high to carry the reaction forward. The remaining radicals not only continue to heat the mixture, but also provide additional reaction pathways to accelerate the ignition process.

$$\text{ChainBranching}: \ \mathrm{H + O_2 \longrightarrow OH + O} \tag{7.11}$$

$$\text{ChainTermination}: \ \mathrm{H + O_2 + M \longrightarrow HO_2 + H} \tag{7.12}$$

A more direct way of realizing the enhanced oxidation chemistry that takes place with the addition of combustion intermediates, is by determining the sensitivity of the ignition process to each reaction pathway. The response of the system is evaluated after being perturbed near the ignition point. Specifically, the response is taken to be the rate of change of the concentration of OH radicals, since they exhibit a strong sensitivity to the reaction progress. The system is perturbed through the

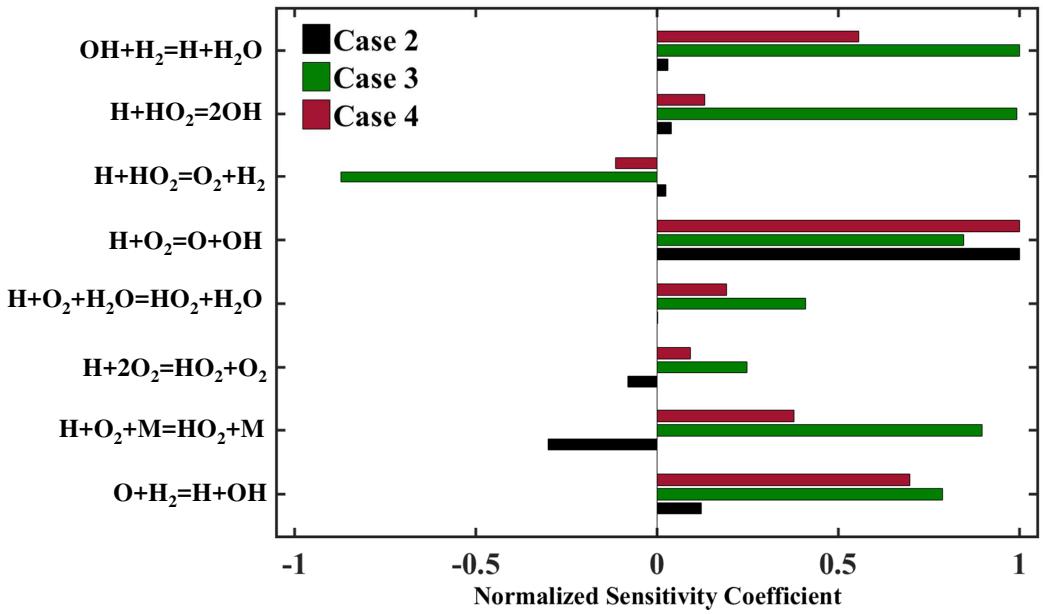

Figure 7.20: Normalized sensitivity coefficients for ignition for Cases 2, 3, and 4.

pre-exponential factor, A, of the reaction constant k_f (see Eqn. 2.20). Therefore, the sensitivity coefficient η_{ij}, to the rate of change of species concentration X_j, by perturbation of the pre-exponential factor A_i, of reaction i, is given by

$$\eta_{ij}(t) = \frac{\partial X_j}{\max(X_j)} \Big/ \frac{\partial A_i}{A_i} \tag{7.13}$$

The expression can be evaluated over the entire chemical reaction. However, in order to determine the sensitivity of the system on ignition, the expression is evaluated near the turning point of the system. This is taken to be during the solution time step just before a rapid rise in OH radicals occurs. The sensitivity coefficients are subsequently normalized by the largest absolute sensitivity coefficient among all reactions. The results for several dominant pathways are shown in Fig. 7.20.

A positive value for the sensitivity coefficient indicates that ignition is promoted by the acceleration of the corresponding reaction, while a negative value indicates the opposite. The results reveal how the sensitivity of the ignition process is vastly different with (case 3 and 4) and without (case 2) the addition of the post-detonation

products. As is expected, through undisturbed oxidation chemistry (case 2), the ignition process is primarily controlled by the chain branching pathway given by Eqn. 7.11. In essence, the reaction progress is constrained by primarily relying on a single reaction pathway. This has two effects on the ability of a system to ignite. First, if the accumulation of radicals mainly relies on a single pathway, then the rate in which radical explosion is achieved is limited. If a greater number of branching pathways are available (by increasing their reaction rates), radical explosion can be achieved sooner, and the induction period decreases. Second, the location of the second explosion limit is governed by the the competition between reactions 7.12 and 7.11, which essentially determines the flammability limits of the mixture. The addition of intermediate species of combustion causes the second explosion limit to be governed by the competition of the chain termination reaction (Eqn. 7.12) with *multiple* chain branching reactions. This will cause chain branching and progression of the reaction to be favorable over a wider range of conditions, increasing the flammability limits. It is clear from the results of Fig. 7.20 that the sensitivity coefficients of cases 3 and 4 exhibit large positive values for a number of chain branching and propagation pathways. Interestingly, ignition for cases 3 and 4 is favored with reactions that generate HO_2, while the opposite is true for the case of undisturbed oxidation (case 2).

7.5 Ignition Delay and Reaction Time

The combination of thermal and kinetic mechanisms have been shown to enhance the reactivity of a combustion system. The increased reaction rates reduce chemical time scales, which augments ignition and flame stabilization. This includes reactions that occur through autoignition, as well as through premixed, and non-premixed modes of combustion. In order to determine the impact of the PD products on the autoignition controlled reactions, a simplified perfectly stirred reactor analysis is used. In all cases, a constant pressure combustion process is simulated over a range of

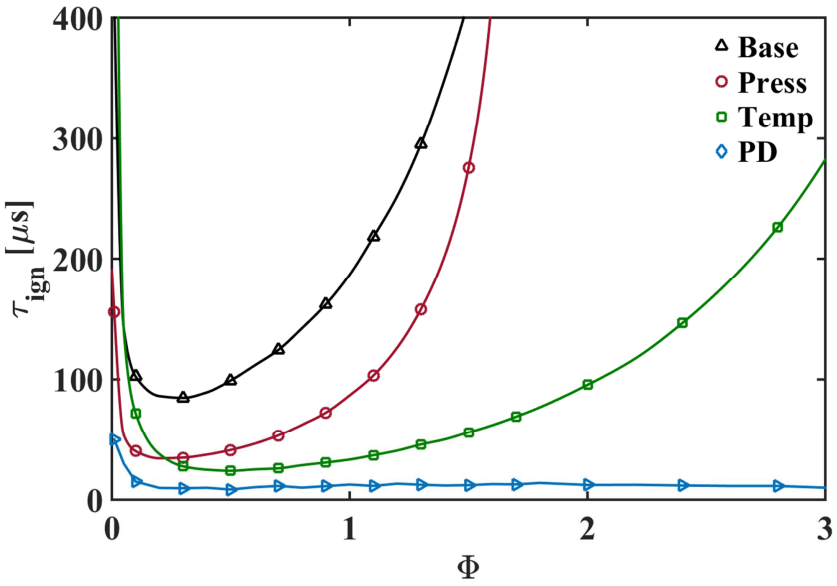

Figure 7.21: Ignition delay time as a function of the equivalence ratio Φ for isobaric and adiabatic mixing of hydrogen (T= 300 K), air (T= 1330 K), and post-detonation products. Description of cases is given in the text.

equivalence ratios. The *Base* case conditions are representative of the experimental condition used in this study. That is, freestream air at 1330 K and hydrogen fuel at 300 K, are chemically frozen and isobarically mixed (0.4 atm) to generate a range of mixtures with different equivalence ratios Φ. Similar to the the previous analyses of this research, the temperature of the unburned hydrogen-air mixture varies with equivalence ratio Φ. The *Press* and *Temp* cases are identical to the *Base* case except that the pressure is 1 atm and the air temperature is 1830 K, respectively. Lastly, the *PD* case is identical to the *Base* case except that the composition is comprised of 5% post-detonation products. The composition was evaluated at the CJ-state of a stoichiometric H_2-O_2 detonation where $T_1 = 300$ K and $P_1 = 0.5$ atm. Before mixing the products with the stoichiometric H_2-O_2 mixture, they were chemically frozen and isentropically expanded to the same thermodynamic state as the mixture they were being put into. This effectively eliminates the effects of sensible heating, and permits only chemical heating and kinetic mechanisms to come into effect.

The computed ignition delay times are provided in Fig. 7.21, which were defined as the time required for the temperature to reach 5% of the total temperature change ($\tau_{ign} = 0.05(T_{final} - T_{initial})$). The *Base* case is observed to exhibit only a narrow range of mixtures which are ignitable within a practical amount of time for supersonic combustion applications. An exponential increase in ignition delay occurs for mixtures where $1.1 < \Phi < 0.1$. This is caused by a combined influence of temperature and composition on the chemical time scales. The results suggest that the autoignition controlled reactions are highly sensitive to and limited by the mixing processes. Moreover, the location of minimum ignition delay occurs at $\Phi = 0.25$, and not near stoichiometric conditions. This stems from the non-isothermal mixing process which causes leaner mixtures to have higher temperatures than stoichiometric mixtures. Therefore, a competition between the influence of temperature and composition on chemistry exists, and the overall effect yields shorter ignition delay times for lean mixtures.

The effect of increasing pressure reduces the ignition delay nearly equally across the range of mixtures considered. Since ignition in this regime is governed by two-body reactions, ignition delay will have a linear dependence on pressure (see Eqns. 4.4). This effect is captured in the results, since the percent reduction in ignition delay (at a given Φ), is equal to the percent increase in pressure. On the other hand, the effect of increasing temperature has a non-linear effect on ignition delay. Since reaction rates have an exponential dependence on temperature, the ignition delays are significantly reduced. This causes a significantly larger range of rich mixtures (Φ) to be ignitable within a practical period of time.

The effect of adding post-detonation products has an even larger effect on the ignition delay. As was mentioned earlier, only chemical heating and chemical kinetic effects are at play. With these two mechanisms alone, the ignition delay is reduced to a few microseconds over the entire range of mixtures that were considered. This

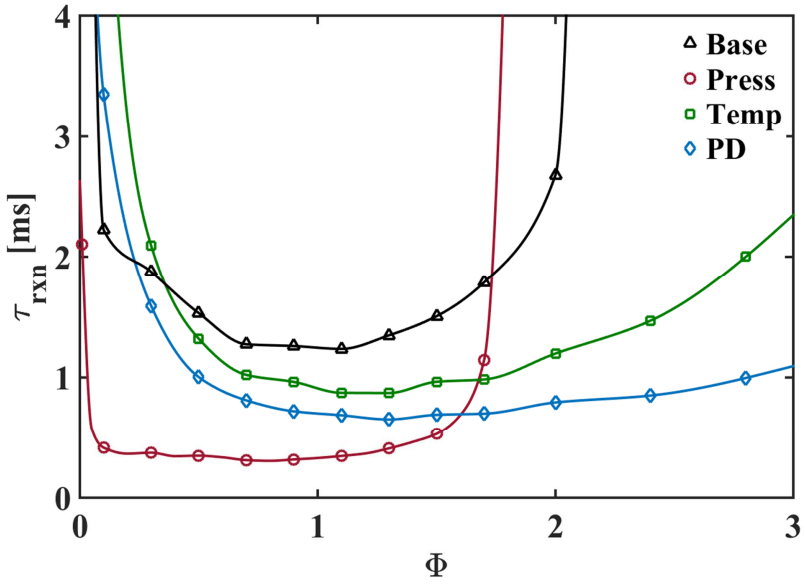

Figure 7.22: Reaction time as a function of the equivalence ratio Φ for isobaric and adiabatic mixing of hydrogen (T= 300 K), air (T= 1330 K), and post-detonation products. Description of cases is given in the text.

implies that the presence of the post-detonation products may cause the dominant reaction stabilization mechanism to be autoignition controlled. Moreover, the dependence of the reacting system on the mixing processes and time scales is alleviated since very lean and rich mixtures react within several microseconds. The local mixture composition and temperature no longer has to be brought to and subsequently maintained within a narrow range of values for ignition to take place.

In order for a reaction to progress to completion (complete release of chemical energy), the reactants and chain carriers need to be maintained within a certain range of conditions so that they are not quenched. However, because of the large and rapid changes in thermodynamic properties present in supersonic flow fields, this can be a challenging task. Shorter reaction times increase the probability of achieving complete fuel-oxidation once ignition has taken place. They may permit combustors to be designed with shorter lengths, as complete chemical heat release can occur within shorter fluid residence times.

The reaction time for each case is provided in Fig. 7.22, and is defined as the length of time required for the temperature to reach 95% of the total temperature change ($\tau_{rxn} = 0.95(T_{final} - T_{initial})$). The results show how the *Base* and *Press* cases exhibit strong exponential behaviors, depending significantly on the temperature. However, the effect of increasing pressure reduces the reaction time by an order of magnitude for $0.1 < \Phi < 1.5$. Providing the reacting system with post-detonation products reduces the reaction time by approximately a factor of 2 for $0.5 < \Phi < 2$, and by even more for larger values of Φ.

7.6 Conclusions

This chapter provided a theoretical analysis of the extent of impact of the post-detonation gas on a reacting system. The thermal and kinetic enhancement mechanisms were to a first order decoupled and evaluated using zero-dimensional models. The results of the simplified model are then used to explain the experimental observations of the reacting flow field. The addition of the post-detonation products into the wake of the JISCF is believed to increase the reaction rates and thereby increasing the local Damköhler number. Initiation of reactions is achieved over significantly shorter induction periods, and over significantly larger ranges of flow composition and properties (pressure and temperature).

While the combined thermal and kinetic mechanisms are believed to enhance several combustion properties of the premixed and non-premixed regions of the flow, they are predominantly believed to lead to enhancing autoignition controlled reactions. The post-detonation products effectively reduce the dependence of the reacting system (JISCF) on mixing processes. This is supported by the OH^* chemiluminescence images which show that the greatest amount of heat release occurs in the direct vicinity of the PD exit port, immediately after interaction with the primary jet fluid. This observation is in agreement with the perfectly stirred reactor analysis, which

revealed how relatively rich mixtures ($\Phi = 3$) can be autoignited within several microseconds.

Furthermore, the analysis of this chapter shows how non-ideal detonation tube operation leads to significant losses in the potential of the thermal and kinetic mechanisms. The exhaust temperature of the detonation tube was very sensitive to the parameter β. However, the results show that by keeping detonation tube designs with $\beta < 50$, a significant portion of the enhancement potential of the ideal isentropic case can be retained. Varying the tube wall temperature within practical limits only marginally helps to subdue the momentum and heat losses that are incurred by the post-detonation gas interaction with the wall. Lastly, regardless of the design of the detonation tube (β), the study shows how over 70% of the total heat release during a single PD cycle occurs within the first 15% of the blowdown period. This is due to the fact that both the exit temperature and mass flow rate are the greatest during the CJ-state, and decrease exponentially in time.

CHAPTER VIII

A Unified Model

8.1 Summary of Unified Model

This chapter is designed to combine the theoretical, experimental, and analytical results of this dissertation, along with conclusions from the literature, to provide a condensed and cohesive description of what occurs when a pulsed detonation is issued into the wake of a transverse reacting jet in supersonic crossflow.

Since the fluid residence time in supersonic combustion devices is short, ignition typically cannot be achieved by solely relying on diffusion and heat conduction alone. The work of this dissertation explores a new technique of combustion augmentation and is examined within the context of a supersonic combustion environment. Specifically, a linear detonation device is used to generate and deliver high-temperature combustion intermediates to the wake of a reacting jet in supersonic crossflow (JISCF) system. A strong and coupled interaction is observed between the crossflow, primary jet, and high-momentum flux PD exhaust. A series of experiments and analytical models were used to identify and understand the extent of impact of the post-detonation products on the JISCF system. The observed enhancement of several combustion properties of the JISCF system were shown to stem from a number of hydrodynamic and chemical mechanisms.

The experimental work provides a semi-quantitative and qualitative analysis of the

combustion enhancement effects observed through a series of experiments utilizing a number of diagnostics techniques. Experimentally, the properties of the blowdown period which was comprised of the post-detonation gas exhausting from the detonation tube, was shown to be sub-ideal. Although the speed of the generated detonation waves agree well with the value of a lean ($\Phi = 0.85$) Chapman-Jouguet H_2-O_2 detonation wave, a large deficit in the trailing post-detonation gas pressure was measured. The pressure gradient in the expansion region downstream of the CJ plane was far greater than that predicted by isentropic (ideal) relations. A one-dimensional model was constructed to account for the energy losses that result from the flow interaction with the walls. The formulation treats the convective heat transfer and momentum transfer from the flow to the tube walls as a set of source terms. Although the model was shown to accurately predict the exhaust properties of detonation tubes with a β parameter value ≤ 50, it was incapable of capturing the severity of the losses incurred by the detonator tube used in this study which had a β parameter greater than 150. Nevertheless, although the detonation wave used in this study was generated through a lean ($\Phi = 0.85$) mixture, and the trailing post-detonation gas incurred severe deficits in pressure and temperature, it still had a substantial effect on the combustion properties of the JISCF system that it exhausted into.

The augmentation of ignition and combustion afforded by the post-detonation products are due to a synergy of hydrodynamic, thermal, and kinetic effects, owing to a nonlinear behavior of induction time versus gas temperature and initial radical concentration. The consequences are of critical significance under non-premixed compressible flow environments. The underlying processes and mechanisms are illustrated graphically in Fig. 8.1. The impact on chemistry is derived from the combined contribution of radical addition and thermal influence. The direct thermal influence corresponds to the adiabatic mixing of the high-temperature post-detonation products with the relatively colder JISCF system. The thermal energy of the JISCF is

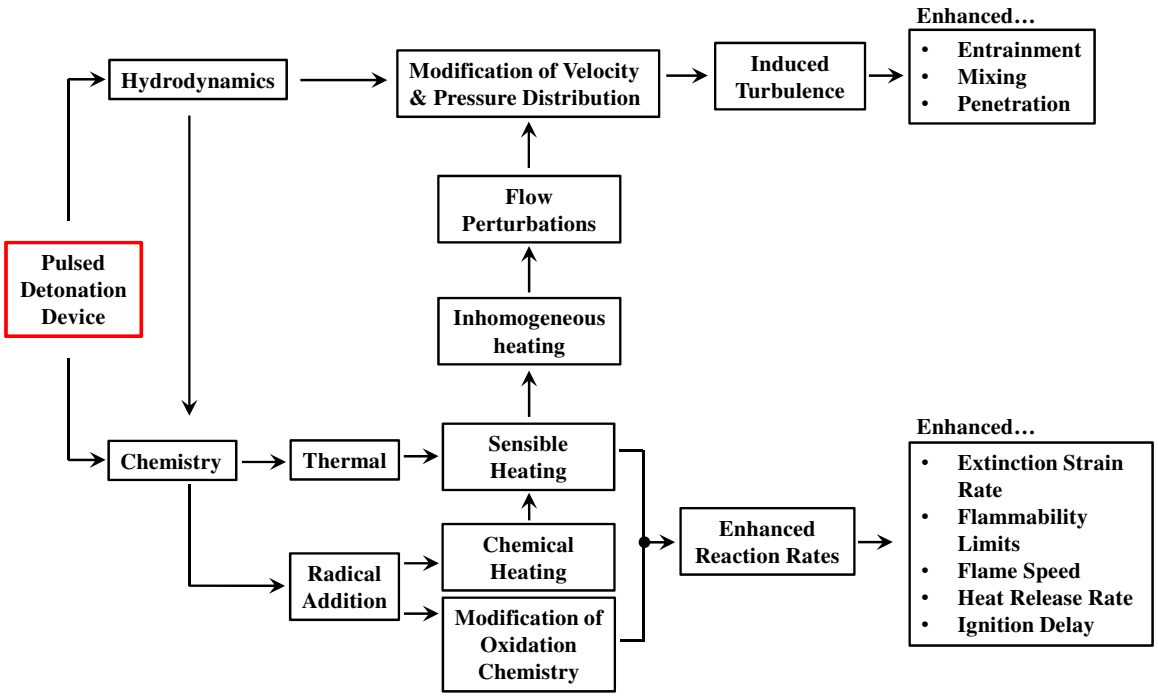

Figure 8.1: A roadmap of processes illustrating the independent and coupled hydrodynamic and chemical effects that the post-detonation products have on a reacting flow field.

increased, and therefore is observed as an increase in sensible energy. On other hand, the addition of high-temperature combustion intermediates into the reacting system results in two different interaction pathways. Under all conditions, chemical heat release occurs as molecular bonds of radicals are destroyed and reformed to generate water. The heat release raises the thermal energy of the local JISCF-PD mixture and therefore provides an additional contribution to the sensible energy of the system.

When the local mixture temperatures are sufficiently high to sustain chain propagation and branching pathways, the addition of radicals modifies the oxidation chemistry of the reacting system. The sufficiently large temperatures and initial concentration of radicals increases the reaction rates of multiple chain branching and propagation pathways, thereby providing a means for the system to bypass endothermic chain initiation pathways to build up a radical pool. Ignition sensitivity is significantly reduced as the reaction progress is no longer bottle-necked by any single

reaction pathway. Rather, numerous pathways are available to accelerate the process of accumulating radicals which eventually leads to explosion. This causes the rate of the overall reaction to increase and leads to a faster fuel-oxidation process. Moreover, the boundaries of the explosion limits are extended as ignition is favored over a larger range of conditions. The kinetic mechanism is altered by providing the system with numerous branching pathways to compete with chain termination pathways. Both the thermal and kinetic mechanisms have a non-linear effect on the reaction rates of individual elementary pathways. Ultimately, these manifest themselves as an enhancement of a number of macroscopic combustion properties relevant to both premixed and non-premixed systems.

The exhausting detonation wave and subsequent post-detonation products have a number of hydrodynamic effects on the flow field, some of which are shown in Fig. 8.2. The hydrodynamic effects can either lead to an influence of several fluid mechanic processes or affect chemical processes. The additional flow blockage provided by the PD exhaust increases shock heating across the bow shock that wraps around the primary jet. This of course has a direct thermal effect on reaction rates. Moreover, the increased shock strength has been shown to increase the impact of the recirculation regions within the flow field, which enhance the influence that the radical addition has on any subsequent combustion processes. For example, the OH^* images reveal how the staged configuration leads to larger amounts of heat release in the recirculation region upstream of the primary jet, which is known to play a role in stabilizing reactions near the floor and along the shear layer. Moreover, the presence of the PD exhaust forms additional recirculation regions upstream and downstream of the exit. These regions promote mixing of intermediates with entrained freestream air and primary jet fluid and are denoted as red in Fig. 8.2, which is a plan-view schematic of the system under consideration. The schematic is a depiction of the flow field within the boundary layer, at an early time during the blowdown process, and in the case where

the primary jet momentum flux ratio $J_j \geq 5$. The red regions indicate recirculation zones while the vectors represent the direction of the flow. The blue and green regions represent the low pressure wakes of the primary jet and PD, respectively.

Staged jets in crossflow have been studied extensively in the past. The existence of a secondary jet (a PD in our case) can have a substantial influence on the flow field velocity and pressure distribution. In fact, a coupling between the two jets exists, where the extent of impact depends on the separation distance and the distribution of momentum flux ratios and mass flow rates. Previous studies have shown that the dominant mixing mechanism, believed to be large-scale vortex driven mixing in the near-field, occurs within approximately 10 primary jet diameters downstream of the staged jets [4]. The PD exhaust is transmitted into the flow field through the low-pressure wake of the primary jet (green region of Fig. 8.2). The low pressure wake increases the effective pressure differential of the PD exhaust, and therefore increases the extent of expansion or the effective momentum flux ratio. The PD exhaust penetrates farther into the crossflow, and has a more prominent impact on the vortex driven mixing processes, as it helps to more rapidly break up large coherent vortical structures and accelerate the progress of the turbulence cascade process.

During early times of the transient blowdown process, the large momentum PD exhaust acts as a fluidic body which modifies the trajectory of the primary jet fluid. The primary jet fluid that was initially expanded into the low-pressure wake (green region) is further expanded around the PD exit and into the low pressure wake of the PD exhaust (blue region). Entrainment and subsequent mixing of the primary jet fluid and high-temperature post-detonation gases is observed (from OH PLIF images) to occur within this region. This is indicated by the arrows entering the blue region. Furthermore, the entrainment is believed to generate the streamwise vortices that dominate the near-field mixing of the primary jet injectant. The mixing studies of Ref. [26, 27], have shown this region to consist of entrainment of the primary jet fluid

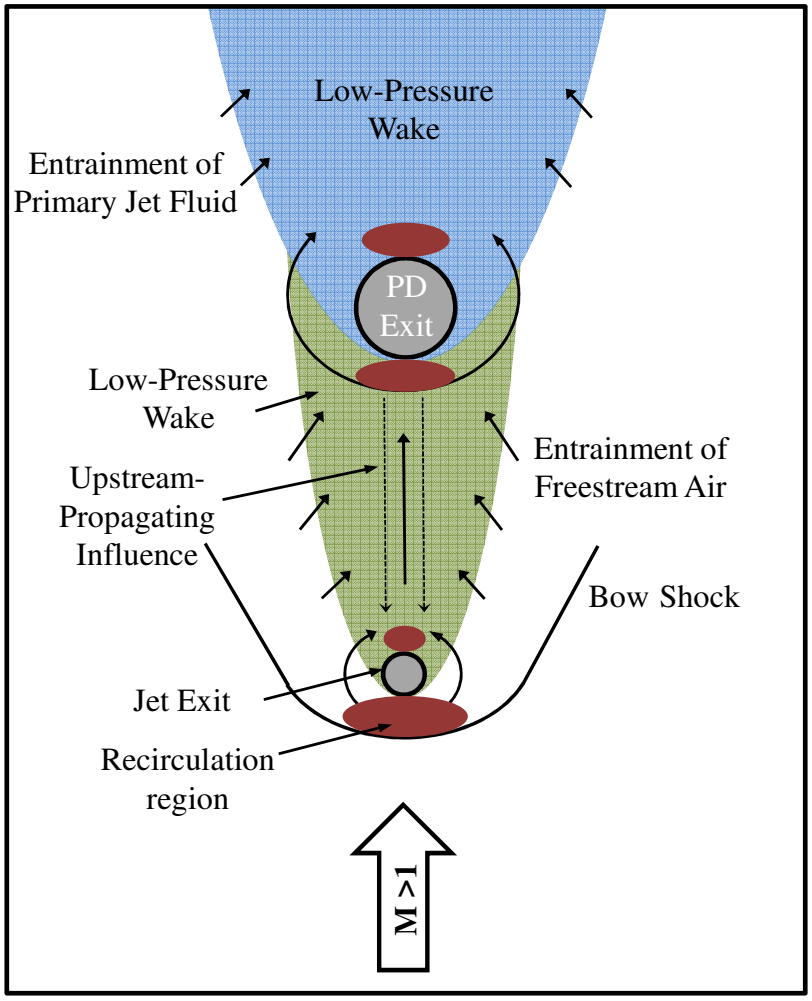

Figure 8.2: Plan-view schematic of the staged JISCF and PD configuration. The image is specific to early times during the blowdown process, corresponds to a plane within the boundary layer, and where the primary jet momentum flux ratio $J_j \geq 5$. Red regions indicate recirculation zones, while the arrows represent the direction of the flow.

into the large CVPs of the PD exhaust.

Under certain conditions, the secondary jet (PD) has been shown to have a strong upstream influence, significantly enhancing mixing of the primary jet fluid within the subsonic region between them (green region). The work of Ref. [4] showed how the rate of decay of the primary jet concentration was more than twice as large with a staged jet configuration as compared to a single jet, providing evidence of the upstream influence. The studies of this work have shown the existence of OH near the floor within this relatively fuel-rich subsonic region between the jets, that does not exist in the isolated JISCF cases. The OH in these low temperature regions are not believed to be markers of reaction zones, but rather markers of post-detonation products that travel upstream through the subsonic region and boundary layer, which is in support of previous findings. Finally, turbulence is believed to be induced through the modification of the flow field pressure and velocity distribution, whether by direct hydrodynamic processes (modification or formation of shocks and recirculation regions) or by inhomogeneous heating of the flow. For example, the formation of shocks can lead to the formation of large-scale vortices which eventually undergo a break-down process that leads to the enhancement of turbulence and mixing.

Figure 8.3 is a schematic along the center-plane of the flow-field during an early time of the blowdown process, and corresponds with a case where the primary jet momentum flux ratio $J_j \geq 2.7$. The primary jet and post-detonation gas expand into the flow as a series of underexpanded jets, generating barrel shock structures that are deformed by the hydrodynamic forces resulting from the interaction with the incoming crossflow. The flow blockage of the staged configuration induces a single three-dimensional bow shock that wraps around the primary jet ①. The strength of the bow shock is determined by the combined flow blockage, and therefore changes over the blowdown period. The bow shock increases the wall pressure upstream of the primary jet, and when J_j is large, the bow shock strength is sufficient to cause

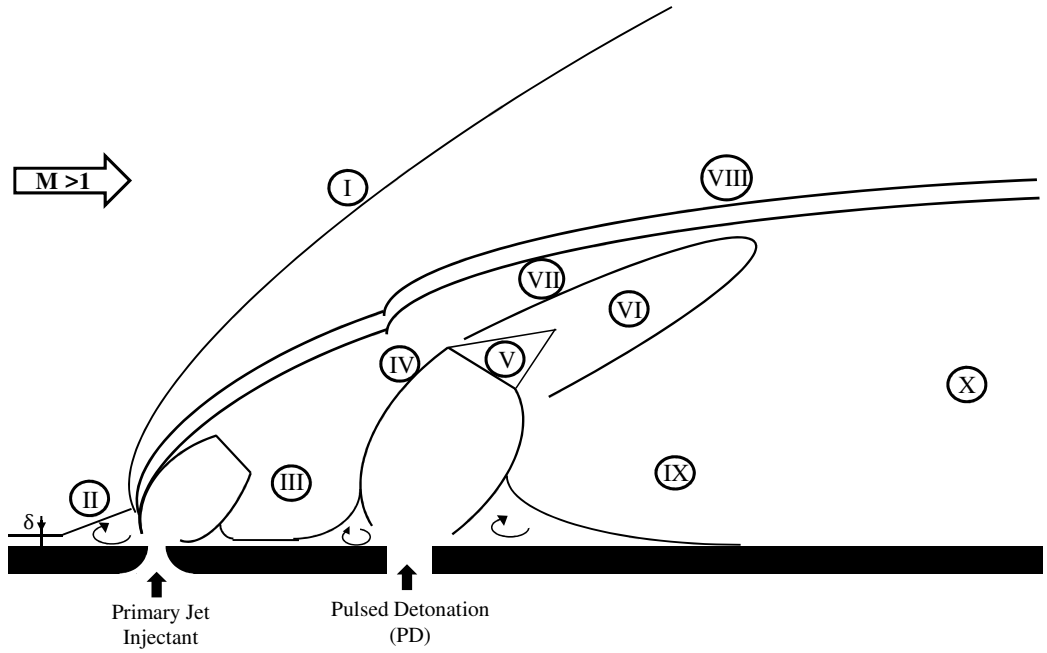

Figure 8.3: Centerline streamwise schematic of the staged JISCF and PD configuration. The image is specific to early times during the blowdown process and where the primary jet momentum flux ratio $J_j \geq 2.7$. The labels are described in the text.

the incoming boundary layer to separate. This forms a recirculation region upsream of the primary jet, which serves as a flame stabilization mechanism (II). The presence of the barrel shock structure of the primary jet is similar to a bluff body in crossflow, forming a second recirculation region immediately downstream as the flow expands around it. A similar pair of recirculation regions are believed to form around the barrel shock structure of the PD exhaust.

When J_j is large, the region between the primary jet and PD is subsonic since only a single bow shock is observed in the flow field (III). In the case where $J_j = 0.5$, this region was observed to be partially supersonic (away from the floor) and subsonic (closer to the wall), since a second bowshock was observed to stabilize just upstream of the PD exhaust. When J_j is large (greater than 2.7), the strength of the incident bow shock is sufficiently large to cause the flow to require longer distances to recover to back to freestream (supersonic) conditions. This does not occur within the $4.8d$ (9.6 mm) space between the two staged jets, which is in agreement with the surface

pressure measurement data of Ref. [2] (for large values of J_j). The subsonic region is believed to play an important role in enhancing the mixing and combustion properties of the primary jet by providing a means for the PD exhaust to exhibit an upstream influence. Combustion is believed to be augmented as the primary jet fluid is mixed and pre-heated sooner within this region.

The OH^* chemiluminescence images reveal how the greatest amount of net heat release occurs immediately upstream of the barrel shock structure of the PD exhaust (IV). This region corresponds to the primary jet and PD interface, and is believed to be a region where significant and rapid autoignition of the primary jet fuel occurs. Before reaching the interface, the CVPs of the primary jet are in a state of development and leads to the most significant amounts of entrainment of freestream air [37], before they subsequently mix with the high-temperature radical rich PD exhaust. The combined thermal and kinetic mechanisms are shown to be capable of igniting a wide range of mixture compositions (Φ) within microseconds. In most cases, supersonic combustion phenomena are mixing-limited process since the chemical time scales are usually much smaller than the transport time scales. The presence of the post-detonation products enhances the autoignition process by decreasing ignition delays over a significantly broader range of Φ, effectively alleviating the dependence of the reacting JISCF system on the naturally low mixing rates.

Chemical reactions within the post-detonation products are re-initiated as they expand through the barrel shock and are subsequently compressed through either the terminating Mach disk (V) or the incident shock along the boundary (IV). The resulting chemical equilibrium composition downstream of the Mach disk was shown to be nearly equal to the composition at the exit plane of the PD device. The high-temperature and flow rate of the PD exhaust sustains the presence of the radicals along a narrow core past the Mach disk (VI). The region extends out diagonally, reaching the shear layer in some instances early in the blowdown process. Post combustion

products emanating from the PD device (VI) are not observed past x/d =15, meaning they are rapidly mixed with the JISCF system within a short distance. The region between the core (VI) and the reacting shear (VIII) is believed to be where the primary jet fluid is pre-heated as it mixes with post-detonation gas. The absence of OH LIF signal in this region (VII) indicates that the post-detonation products are quenched. A perfectly stirred reactor analysis shows that when the PD products are mixed with colder mixtures over a large range of Φ, most of the preferred pathways are exothermic chain termination reactions that recombine the radicals to form water.

The reaction zones along the shear layer are observed as corrugated and thin layers that resemble the description of laminar diffusion flames (VIII). The effect of pre-heating the primary jet fuel before it reacts along the shear is apparent throughout the blowdown process. The increased reaction rates due to both thermal and kinetic enhancement increase the local Damköhler number. The OH PLIF images reveal how reactions occur in a more stable manner by the reduction of local extinction events due to increased extinction strain rates. Furthermore, the cross-sectional OH PLIF images reveal how the post-detonation products (on average) broaden the region along the shear layer where reactions occur. The broader reaction zone thickness is believed to be due to an enhancement in flammability limits. Regions along the shear layer which would be too rich or lean for ignition without the influence of the PD, are autoignited with the presence of the high-temperature PD products. Lastly, the primary jet fluid is pushed around the PD exhaust, increasing the shear layer penetration as well as the cross-sectional surface area of the shear layer. The latter leads to a larger interface where fuel-air mixing can occur and chemical reactions can follow.

The primary jet fluid rapidly expands around the PD exit port and into the wake of the PD exhaust where they subsequently mix (IX). Similar to region (VII), this region exhibits a lack of OH signal from LIF measurements since the post-detonation

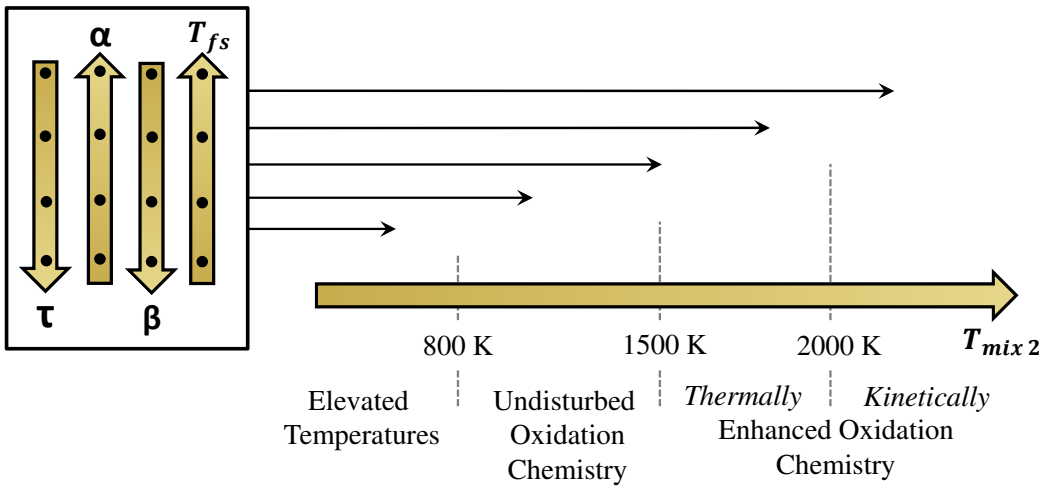

Figure 8.4: Qualitative illustration of how the combination of several parameters lead to different regimes of combustion enhancement.

products are recombined to form water as they mix with colder fuel. However, farther downstream (X) the OH* chemiluminescence images reveal a net increase in heat release. This is a consequence of the near-field mixing that augments autoignition and heat release events within the wake.

Figure 8.4 qualitatively illustrates the model discussed in Section 7.3 and shows how the combination of several parameters can lead to different regimes of combustion enhancement. The parameters τ, α, β, and T_{fs} correspond to the non-dimensionalized time during the blowdown period, the fraction of PD products in a fuel-air mixture, the extent of energy loss of the post-detonation gas occurring within the detonation tube, and the freestream temperature, respectively. The points along each vertical arrow represent different magnitudes of each corresponding parameter.

Different combinations of the variables given within the box will result in different values of mixture temperature ($T_{mix\ 2}$). The value of $T_{mix\ 2}$ is sufficient to determine the regime of combustion enhancement. The crossover temperature is taken to be the delineator between the Elevated Temperatures and Undisturbed Oxidation Chemistry regimes. The delineation between the Undisturbed Oxidation Chemistry and Thermally Enhanced Oxidation Chemistry regimes is given by $T_{mix\ 2} = 1500$ K,

since this is typically the largest freestream combustor entry temperature one would encounter; therefore, any increase in mixture temperature due to the presence of the PD can be considered a thermally enhanced condition. Finally, the delineation between the Thermally and Kinetically Enhanced Oxidation Chemistry regimes is given by $T_{mix\ 2} = 2000$ K for H_2-O_2 combustion, since radicals are stable above this temperature and hence can modify the oxidation process.

The regimes of combustion enhancement that occur throughout a PD cycle vary with time as well as spatial location in the flow field. Of course the illustration given in Fig. 8.4 only serves to show the direction of contribution of each parameter, and by no means captures the coupling between parameters and the individual weight they each hold in contributing to the outcome of an actual process.

CHAPTER IX

Summary and Recommendations

9.1 Conclusions

9.1.1 Development and Characterization of MHExT

A 14 m long expansion tube facility (MHExT) capable of generating a wide range of aerothermal properties representative of supersonic combustor entry conditions was successfully developed. The facility was theoretically shown to be capable of replicating the energy requirements representative of flight Mach numbers ranging between 4 and 11, with air as the test gas. A portion of this dissertation provides the necessary detailed assessment of the facility through a combined experimental, computational, and analytical analysis. The major conclusions of the study are as follows:

1. The shot-to-shot variability in the measured primary and secondary shock speeds amounts to only a fraction of a percent. The effective bulk-averaged test gas properties, estimated using a zero-dimensional expansion tube model based on real gas properties, vary by at most a few percent of their respective mean values.

2. The test gas flow was found to be spatially uniform (radial direction) outside of the boundary layer. The freestream core flow consumes approximately 2/3 of

the inner pipe diameter for all flow conditions. The boundary layer thickness of the test gas was not found to scale with the Reynolds number.

3. As a result of boundary layer growth, the competing effects of acceleration of the primary and secondary contact surfaces lead to an overall reduction of the available test time when compared to inviscid calculations by as much as 35%. In other words, the reduction in test time due to the acceleration of the primary contact surface outweighs the extension of the test time due to the acceleration of the secondary contact surface. Furthermore, the influence of the secondary expansion wave process on the wave trajectories was found to be negligible.

4. Boundary layer growth is observed to compress the test gas, causing the average measured static pressure over the test time to exceed what was predicted with inviscid calculations by as much as 38%. The test gas pressure always exhibited an increasing trend along the test gas slug. Interestingly, the test gas Mach number which was inferred by simultaneous pitot-static pressure measurements and schlieren imaging of an oblique shock angle agreed well with the inviscid predictions, and remained nearly constant throughout the test time. This is believed to be a consequence of the secondary expansion wave processing a non-uniform gas, in a manner that causes the axial variations in total and static pressure to nearly offset one another, keeping the test gas Mach number nearly constant.

5. An unsteady wave interaction with a test model that protrudes into the expansion section leads to a significant alteration of the intended test gas aerothermal properties, through the formation and upstream propagation of a finite-strength disturbance wave (shockwave). The only way to avoid these consequences is by recessing test models away from the exit plane of the expansion tube. The formulated model and experiments show how the interaction always generates a

disturbance wave that is sufficiently strong to propagate upstream, even if the shocked expansion gas flow (state (20)) is supersonic.

9.1.2 Modeling of Detonation Tube and Combustion Augmentation

A series of models were formulated and used to better understand the blowdown properties of a pulsed detonation tube device. The models provided insight to the strengths and limitations of using a PD as an active technique for combustion augmentation in supersonic flows. The first model describes the properties of an unsteady flow through a constant area channel with heat and momentum transfer to the walls, based on the method of characteristics. The model is used to compute the post-detonation gas properties along the tube for various length to diameter ratios (β). The second is a zero-dimensional model that is used to quantify the heating potential of PD devices. Finally, a perfectly stirred reactor model and opposed flow diffusion flame model were used to understand the thermal and kinetic enhancement mechanisms of the PD products on a reacting system. The major conclusions of the study are as follows:

1. The interaction of the post-detonation gas with the tube walls of the PD device resulted in significant heat and momentum losses. Even conservative yet practical detonation devices with $\beta = 50$ (length to diameter ratio) lead to more rapid expansion of the gas. In this case, the exhaust temperatures are approximately 15% less than that of an isentropic process (no heat or momentum losses) and the concentration of intermediate species of combustion is also reduced by approximately 50%. This is shown to significantly hinder the thermal and kinetic enhancement potentials of combustion augmentation.

2. Heating the detonation tube walls has a weak influence on suppressing heat transfer from the post-detonation products. This is because of the non-linear

dependence of the heat transfer rate on the tube wall temperature, as indicated by the third term inside of the brackets of Eqn. 5.11. Moreover, pre-heating the initial PD tube mixture before being processed by the detonation has adverse effects on the post-detonation products, reducing both their temperature and pressure.

3. Nearly 70% of the total heat release (chemical and sensible) occurs within the first 15% of the blowdown period, regardless of the value of β. Therefore, the early portion of the PD exhaust has the greatest impact on the combustion properties of the reacting system it is issuing into.

4. The addition of PD products to a non-premixed system is observed to enhance extinction strain rates and therefore stabilize reactions along fuel-air interfaces. The dominant mode of combustion augmentation occurs through enhancing the autoingnition properties of a reacting system. Ignition delay times are shown to be reduced to several microseconds for a large range of mixture compositions (Φ). Moreover, the heat release rate and flammability limits are observed to enhance significantly. In practice, this effectively alleviates the dependence of the reacting system (JISCF) on the low mixing rates of supersonic flows, by augmenting ignition and heat release over a wider range of mixture equivalence ratios.

5. The presence of the post-detonation products in a fuel-air mixture enhances several macroscopic combustion properties by enhancing reaction rates. This is achieved through a thermal impact, as well as modification of the radical pool concentration. The addition of radicals further enhances the oxidation chemistry, leading to accelerated ignition and heat release. The greater concentration of radicals near the turning point significantly reduces the ignition sensitivity to any single chain branching pathway.

9.1.3 Experimental Analysis of Combustion Augmentation

An active technique of combustion augmentation in supersonic flows was explored. More specifically, a pulsed H_2-O_2 detonation device was used to generate and deliver a high-temperature radical-rich exhaust through a high-momentum flux jet, to enhance the combustion characteristics of a JISCF system. The PD was staged downstream of a primary jet, resulting in strong hydrodynamic and chemical influences that enhanced the reactivity of the JISCF. Three imaging techniques including schlieren imaging, chemiluminescence imaging, and OH PLIF imaging, were used to understand the complex three-dimensional and transient interaction. The experiments provided insight to a number of hydrodynamic and chemical processes that govern the observed combustion enhancement. The major conclusions of the study are as follows:

1. The primary jet momentum flux ratio J_j was found to be an important parameter that controlled a number of chemical and hydrodynamic processes, by altering the flow field pressure distribution. For example, increasing J_j increased both the primary jet and PD exhaust penetration. When $J_j \geq 2.7$, the region between the primary jet and PD was entirely subsonic and only a single bow shock upstream of the primary jet was observed. On the other hand when $J_j = 0.5$, the region between the primary jet and PD was more complex, exhibiting regions of both supersonic and subsonic flow. Larger values of J_j enhanced the upstream influence of the PD by generated a larger low pressure wake/region between the primary jet and PD. For example, the amount of heat release within the region between the primary jet and PD increased with J_j . When $J_j = 5.0$, the upstream influence extended even farther upstream, and was observed to enhance the heat release in the upstream recirculation region of the primary jet.

2. Although the experimentally observed blowdown process was measured to be approximately 150 μs, the hydrodynamic effects of the PD on the flow field were only observed during the first half of the blowdown period based on the schlieren data. After approximately 150 μs, the penetration of the primary jet fluid and strength of the leading bowshock were approximately the same as in the case of the isolated JISCF. This implies that the momentum flux and mass flow rate of the PD device is significantly less during the second half of the blowdown process, and therefore does not provide the same mixing, entrainment, and penetration enhancement of the primary jet. Therefore, the combustion enhancement observed in the second half of the blowdown process relies, to first order, on the natural flow dynamics to entrain and mix the PD products with the JISCF system.

3. Issuing the post-detonation products into the wake of the JISCF system enhanced the stability of non-premixed mode of combustion along the shear layer. When $J_{\mathrm{j}} \geq 2.7$, reactions along the shear layer were stabilized. For the case of $J_{\mathrm{j}} = 5.0$, the stability of reactions decreased in a linear manner over the blowdown period. However, they extended throughout the entire blowdown process, even though the PD exhaust penetration was not sufficient to reach the shear layer during the second half of the blowdown process. This implied that primary jet fuel was being pre-heated near the floor where it was subsequently entrained to the shear layer, effectively increasing the local Damköhler number along the fuel-air interface.

4. There are two mechanisms which are believed to be the most important to augmenting ignition and heat release of the JISCF system. First, the most substantial heat release enhancement was observed in the vicinity of the PD exit. This is a result of the direct interaction of the primary jet fluid as it

impinged onto the barrel shock structure of the PD exhaust. Auto-ignition and heat release are believed to happen rapidly within this region. Second, the expansion of primary jet fluid into the wake of the PD is believed to rapidly mix the high-temperature radical-rich exhaust with the JISCF system. The rapid expansion is known to form a pair of CVP, which dominate the near-field mixing. The radicals originating from the PD are observed to be fully mixed within 10 primary jet diameters downstream of the PD.

5. For the conditions considered and with the specific staged configuration used in the present study, the net heat release per unit mass of primary jet injectant over one PD cycle was observed to decrease with larger values of J_{j} . This is believed to be due to the lower mass flow rates of the low J_{j} case, which lead to higher mixture temperatures, and a greater enhancement of reaction rates. Moreover, the lower J_{j} case leads to lower primary jet penetration into the freestream and therefore an increased contact area and interaction time (during the blowodwn process) with the post-detonation products. This leads to the understanding that the effectiveness of the PD device is sensitive to the details of how it is configured in an actual system.

6. Pulsed detonation devices will not provide the mixing and penetration benefits that pulsed jets have over steady jets when issued transverse to a supersonic crossflow. This is because the ratio of the PD exit velocity (taken to be equivalent to the gas sound speed) and crossflow speed will never exceed a value of two for a range of hypothetical supersonic combustor conditions. Generating vortex rings with superior penetration and mixing characteristics compared to the elongated structure of a steady jet is only possible when the velocity ratio exceeds a value of two. Therefore the penetration and mixing characteristics of the post-detonation products issuing into the crossflow will closely resemble

those of steady jets in crossflow, but with time-varying exit properties (momentum flux ratio, temperature, pressure, etc.). Experimentally, the center-plane OH PLIF images of the isolated PD issuing into the crossflow confirm this, since the structure and penetration of the post-detonation gas closely resembles the elongated structure of a steady jet with a time-varying (decaying) momentum flux ratio.

9.2 Future Work

9.2.1 Practical Considerations

The following is a list of practical considerations one may consider in future studies:

1. The dimensions of the detonation tube should be chosen to minimize heat and momentum losses and to harness the full potentials provided by the high-temperature and pressure exhaust. Therefore one should consider designing PD devices where $\beta < 50$. Furthermore, the dimensions need to be chosen based on the specific application. If the device is to be used to condition a supersonic flow field in a quasi-steady manner, then the pulse frequency of the PD should be several hundreds to thousands of Hz, assuming the blowdown period is on the order of a few milliseconds. In order to attain such a high pulse frequency, one should consider how the volume (length and diameter) of the PD affects the time required to fill and exhaust. In addition, the latency period associated with opening and closing the injectors needs to be considered. Aerodynamic valves provide valveless operation of a detonation tubes, and may be essential in achieving such high pulse frequencies.

2. The experimental portion of this study revealed how sensitive the combustion enhancement offered by the PD was to the specific details of the flow field,

by varying the primary jet momentum flux ratio J_j . The PD device has the potential to significantly modify the velocity and pressure distribution of a supersonic flow field. Therefore, the exact details of how it is configured/oriented in a system will have a large role on the impact and extent of coupling it has with the combustion system. For example, varying the spacing between the staged primary jet and PD will change the flow dynamics in the recirculation region between them as well as influence the augmentation of entrainment and mixing with the generated CVPs. One may want to answer whether or not it is better to exhaust the PD products upstream of a JSICF system, which may modify the influence on transport phenomena differently than if they were exhausted downstream. Is it better to exhaust the PD products along a fuel-air interface? One may want to explore a base supersonic combustion system that is more suitable for combustion augmentation via a PD device such as a strut injector or a cavity based flame holder. Understanding what is the best orientation for the PD device in any of these configurations is challenging but rests upon understanding the mechanisms the PD provides (hydrodynamic, thermal, or kinetic) and how to take advantage of them. The latter requires an understanding of how the PD exhaust will couple with the specific configuration being considered.

9.2.2 Future Study

Based on the results of the present experiments and numerical analyses, the following recommendations for future study are suggested:

1. One of the largest constraints of the current study was the limited field of view in the stream-wise direction. This limitation stems from the size of the core flow which is issued as a free jet over the test model. Extending the field of view provides an unbiased evaluation of the total combustion enhancement as

certain processes require more time to develop, especially with the variation of J_j between cases.

2. While the experimental and theoretical analyses of the present study reveal the role and impact of several mechanisms on combustion enhancement, there is no understanding of the losses that are incurred by issuing the detonation wave and gases into the flow field. While the increased shock-heating and formation of recirculation regions enhance the reactivity of the system, they inevitably come at a cost. The unsteady pulsed nature of the detonation tube may reduce pressure losses as compared to a steady jet. However, a study is required to completely evaluate the use of a PD device in enhancing combustion by determining if and by what extent the combustion enhancement exceeds the incurred losses.

3. The detonation device used in this study exhibited severe non-ideal properties within the post-detonation gas. The measured pressure profiles revealed a significantly greater expansion of the post-detonation gas, which resulted in lower exhaust temperatures as well as a significantly shorter blowdown period. While the measured detonation speeds matched well with CJ-theory, owing to operation of the device well within the detonation limits, the properties downstream of the CJ plane were significantly different than what is predicted from isentropic calculations. Further experiments should use a detonation device with a $\beta \leq 50$ such that the developed model can be used to predict the temporal exhaust properties of the PD. A stronger quantitative evaluation of the impact of the PD device on the reacting flow field requires knowledge of the unsteady exhaust properties (temperature, pressure, composition, mass flow rate, momentum flux ratio) in order to better understand the reasons behind the experimentally observed flow and combustion phenomena.

4. The advantages that expansion tube facilities provide over other high-enthalpy flow-generating facilities come at a cost. The generated flows have short test times, typically on the order of hundreds of microseconds, limiting the amount of acquirable data during each test run. Moreover, the facility used for this dissertation required 30-40 minutes of turnaround time between shots. The experimental data of this study was carefully acquired, repeated, monitored, and processed to ensure that the observations were repeatable. However, a statistical analysis of the various phenomena was not possible because of the limited amount of acquired data from the impulse facility. The three-dimensional and time-transient nature of the present configuration results in large test matrices. In order to enhance our understanding, statistically converged data should be acquired and processed to confirm the observations of this study and allow for a more quantitative assessment. For example, the temporal variation of several quantities such as shear layer penetration, stability of reactions along the shear layer, and locations of reaction zones and post reaction zones, can be quantified. This would necessitate the use of high-enthalpy blowdown facilities with longer test times.

APPENDICES

APPENDIX A

Expansion Tube Solvers

A.1 Expansion Tube Solvers

Two zero-dimensional expansion tube solvers are used in this study. The solvers are both inviscid, equilibrium, temperature-dependent property models. The first solver requires experimentally measured shock speeds (primary and secondary), and initial fill conditions of each section, (composition, temperature, and pressure) as inputs to solve for the thermodynamic properties of the various states of gas. The model solves for the jump conditions across the primary and secondary shock waves, and matches conditions across the secondary unsteady expansion wave assumed to be an isentropic centered expansion. The model follows a treatment (and nomenclature) similar to what was given by Trimpi [14]. The semi-theoretical properties reported in this study were computed using this solver.

The model numerically solves for the Rankine-Hugoniot (R-H) jump conditions [114] across a moving shock wave using equilibrium, temperature-dependent properties. The properties are approximated using the NASA polynomial fits to the gas thermodynamic properties, such as the specific heats [150]. For the changes across a

normal shock moving at a speed W and processing a gas at an initial state ① to a final state ②, the R-H conditions can be written as:

$$\left(\frac{P_2 - P_1}{\rho_2 - \rho_1}\right) - \frac{\rho_1}{\rho_2} W^2 = 0 \tag{A.1}$$

$$(h_2 - h_1) - \frac{P_2 - P_1}{2}\left(\frac{1}{\rho_1} - \frac{1}{\rho_2}\right) = 0 \tag{A.2}$$

Along with the equation of state $h = \tilde{h}(T)$ given by the NASA polynomial fits [150], Eq. A.1 and A.2 are two equations where the two unknowns P_2 and T_2, and are numerically solved using a least-squares minimization scheme. This solution is implemented for both the primary and secondary shock waves.

The secondary expansion wave is modeled using the method of characteristics for one-dimensional, unsteady, isentropic wave propagation imposing that pressure and speed across the secondary contact surface is constant. Since the solution of the secondary shock wave (from the measured shock speed) effectively gives the values of P_5 and U_5, the model reduces to solving the isentropic condition $s_2 - s_5 = 0$ for the final temperature T_5 using an equilibrium, temperature-dependent expression for entropy ($s = \tilde{s}(T, P)$) derived from the NASA polynomial fits [150]. The solution is found numerically using a least-squares minimization method.

The second solver is used to design test gas conditions without any knowledge or measurement of the shock speeds. It only requires the initial fill conditions of each section. In this case, the compatibility equation

$$du + \frac{dh}{a} = 0 \tag{A.3}$$

is integrated across the expansion wave to solve for the additional unknown variable.

APPENDIX B

Combustor Entry Conditions

B.1 Constant Inlet Compression Ratio

A procedure outlined in Ref. [103] was used to estimate the combustor entry properties of a hypothetical supersonic vehicle. The method approximates the compression process across the inlet to be adiabatic, and constant over a flight envelope with a constant dynamic pressure. There are a number of considerations to make when designing flow conditions for supersonic propulsion systems. The altitude and Mach number at which these vehicles fly should lie within certain bounds determined by the dynamic pressure exerted onto the aircraft as well as the achievable mass flow rate of oxidizer into the engine. The dynamic pressure defined as, $q = 1/2\rho U_f^2$, should generally be taken between the values of 50 and 100 kPa, to generate sufficient lift while subjecting the vehicle to acceptable levels of structural loading [103]. As a result, for a hypersonic aircraft to increase its flight Mach number it must fly at higher altitudes, and is therefore generally confined to altitudes between 20 and 40 km. The combustor entry pressure as a function of flight altitude for a few flight envelopes that satisfy this criteria are given in Fig. B.1.

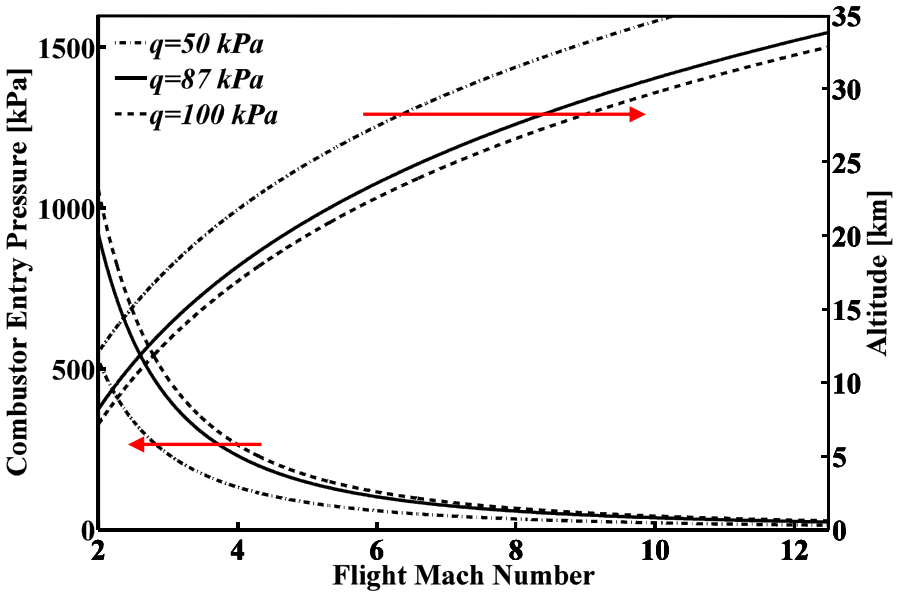

Figure B.1: Combustor entry pressure and flight altitude as a function of flight Mach number for several constant dynamic pressure trajectories.

The objective of a supersonic inlet is to decelerate the air to a speed that is sufficient for mixing and combustion. This includes increasing the residence time through the combustor to efficiently mix the fuel and oxidizer streams and allow sufficient residence time for ignition, and stable flame holding. The inlet compression process increases the air pressure and temperature and can be approximated as an adiabatic process that occurs through a complex shock system prior to the combustor. Generally, the temperature of the air entering the combustor should be greater than 1000 K but should not exceed 1500 K in order to reduce the amount of radicals produced in the exhaust and give way to a more complete and therefore efficient combustion process [103]. This confines the inlet adiabatic compression ratio T_c/T_f to values ranging between 4 and 7, where the subscripts c and f correspond to combustor and freestream, respectively. By approximating the stagnation temperature T_0 to be constant between the freestream and the combustor, the compression across the inlet is given by

$$\frac{T_c}{T_f} = \frac{1 + [(\gamma_f - 1)/2]M_f^2}{1 + [(\gamma_c - 1)/2]M_c^2} \tag{B.1}$$

where M_f is the freestream Mach number, M_c is the combustor entry Mach number, γ_f and γ_c are the ratio of specific heats of the freestream and combustor, respectively. When parameters such as the dynamic pressure and adiabatic compression ratio are fixed, the combustor entry pressure can be estimated by the following relation

$$\frac{P_c}{P_f} = \left(\frac{T_c/T_f}{T_c/T_f(1 - \eta_c) + \eta_c} \right)^{(\gamma_c/(\gamma_c - 1))} \tag{B.2}$$

where η_c is the compression efficiency of the inlet, P_c is the combustor entry pressure, and P_f is the freestream pressure. For the design of flow conditions A and B (Chapter IV), the dynamic pressure, adiabatic compression ratio, and inlet compression efficiency were taken to be 87 kPa, 5, and 0.70, respectively.

B.2 Variable Inlet Compression Ratio (Fixed Inlet Geometry)

This section outlines how the combustor entry conditions of a hypothetical scramjet vehicle with a fixed inlet geometry are computed. As the vehicle accelerates, it maintains a flight envelope with a constant dynamic pressure. Therefore, the inlet compression process (or ratio) will vary over the course of the flight and will depend on the flight Mach number. A generic two-shock inward-turning inlet is chosen for the hypothetical vehicle and is shown schemtically in Fig. B.2.

The solution involves solving for the jump conditions across an oblique shock considering real gas effects. It accounts for fully excited translational and rotational energy modes, a partially excited vibrational mode, and neglects chemistry. The solution procedure is followed twice, the first between states ① and ②, and the second between states ② and ③. Freestream air ① is turned by an angle θ (taken to be 20

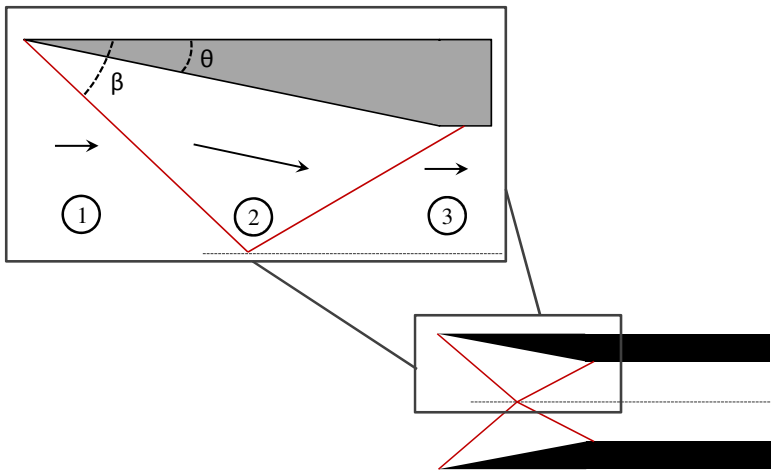

Figure B.2: Schematic of the two-shock inward-turning inlet of a hypothetical scramjet vehicle discussed in Chapter 4.3.

degress in the analysis of Chap. 4.3) and is processed by an oblique shock with an unknown angle of β. The gas in state ② is compressed again by a second oblique shock in order to turn it back by θ degrees and maintain a symmetric flow condition across the inlet. The gas in state ③, taken to be the combustor entry condition, is then moving parallel to the freestream air in state ①. The following outlines the solution process across the first oblique shock, which can then be repeated to solve for the combustor entry conditions in state ③.

First, after geometric considerations and the conservation of mass, one may show

$$\frac{u_1}{u_2} = \frac{\rho_2}{\rho_1} = \frac{\tan(\beta)}{\tan(\beta - \theta)} \tag{B.3}$$

where the subscripts 1 and 2 correspond the pre and post shock states, respectively. The second important consideration is realizing that the changes in flow properties are governed only by the flow that is normal to the shock. Therefore, in addition to Eqn. B.3, the governing equations across the shock are given by

$$u_{1,||} = u_{2,||} \tag{B.4}$$

$$p_1 + \rho_1 u_{1,\perp}^2 = p_2 + \rho_2 u_{2,\perp}^2 \tag{B.5}$$

$$h_1 + \frac{1}{2} u_{1,\perp}^2 = h_2 + \frac{1}{2} u_{2,\perp}^2 \tag{B.6}$$

where the enthalpy is evaluated by

$$h(T) = e(T) + \mathcal{R}T = \frac{7}{2}\mathcal{R}T + \frac{T_{vib}}{e^{T_{vib}/T} - 1} \tag{B.7}$$

where T_{vib} is the characteristics vibrational temperature with a value of 2270 K and 3390 K for oxygen and nitrogen, respectively and $\mathcal{R}$ is the specific gas constant. The enthalpy of air is then,

$$h_{air}(T) = Y_{O_2} h_{O_2}(T) + Y_{N_2} h_{N_2}(T) \tag{B.8}$$

where Y represents mass fraction. Finally, the ideal gas law holds in this regime and can be expressed by

$$p = \rho \mathcal{R} T \tag{B.9}$$

Given a value of M_1 and θ, the solution can then be found using an iterative procedure such as the following:

1. Guess a value of $\eta = \frac{\rho_2}{\rho_1}$.
2. Find β from Eqn. B.3.
3. Find $u_{1,\perp}$ since $u_{1,\perp} = a_1 M_1 \sin\beta$.
4. Find p_2 and h_2 from from Eqns. B.5 and B.6.
5. Find T_2 from h_2.

6. Evaluate ρ_2 given p_2 and T_2.

7. Iterate on the value of η until the solution converges.

APPENDIX C

PCB Sensor Calibration

This appendix is designed to serve as a guide for calibration of piezoelectric PCB pressure sensors with the MHExT facility. Furthermore, it serves to document calibration data for several sensors. The sensor to be calibrated is surface mounted into a custom made plug that is then fixed to a 1 inch thick aluminum end wall. The end wall replaces the secondary diaphragm of the expansion tube and is clamped between the driven and expansion sections. The sensor is calibrated by measuring the signal voltage output during the post-reflected shock state. A solver similar to the one described in Appendix A, and the measured incident shock speed along the driven section, are used to determine the thermodynamic properties of the post-reflected shock state. Assuming linearity in the sensor, the signal of the post shock conditions are averaged over a steady portion of the signal, and are subsequently compared with the ideal computed post shock pressure to construct a calibration curve. Table C.1 provides the serial numbers and resulting calibration coefficients for 7 PCB sensors. The corresponding calibration curves are given in Fig. C.1. The error bars correspond to the root mean square of the signal over the calibration window. All sensors show similar SNR values, evaluated as RMS/Signal. However, the SN 13456 sensor shows a large deviation from linearity.

Serial Number	Model	Range [psi]	Sensitivity [V/kPa]
13456	111A26	500	0.001427
14950	111A26	500	0.001530
13455	111A26	500	0.001508
20210	111B26	500	0.001570
19053	113A26	500	0.001597
28248	112A22	50	0.015795
28210	112A22	50	0.015395

Table C.1: Calibration data for PCB pressure sensors.

There are number of aspects to consider when designing conditions for pressure sensor calibration:

1. If calibrating multiple sensors, the number of experimental runs can easily add up requiring a great deal of time as well as becoming an expensive experimental campaign. Therefore, it is best to design the run conditions so they require minimal turn-around times between shots. Two ways of doing this are by designing the run conditions such that a simple diaphragm setup is required, and by using air as both the driver and driven gas compositions. Choosing a diaphragm setup that does not require pre-scoring will save time. Therefore, using 0.01 inch thick polycarbonate sheets are the easiest to manage and are also the least expensive. Furthermore, the use of thinner diaphragms leads to less energy loss during the rupturing process. The resulting measured shock wave speeds are closer to the ideal predicted values as compared with thicker diaphragms. This reduces the need to increase the driver fill pressure to compensate for losses incurred by the rupturing process, and allows the initial fill pressures to remain relatively low. Using shop air and room air as the gas compositions of the driver and driven sections is also inexpensive. Furthermore, it eliminates the long turn-around times required to evacuate the sections before filling with other gas compositions.

2. The conditions should be designed to provide a sufficiently long test time over

Case	Driver Pressure [psia]	Driven Pressure [torr]	Nominal Shock Mach Number	Nominal Post-Shock Pressure [kPa]
1	85	450	1.5	280
2	85	150	1.8	200
3	85	75	2.0	150
4	85	18.8	2.5	70
5	80	3.8	3	30

Table C.2: Nominal conditions used for PCB sensor calibration. The driver and driven gases were both air, and the diaphragm was 0.01 inch thick polycarbonate.

which the measured pressure trace can be averaged. Fig. C.2 is an example of a pressure trace acquired with sensor SN14950. The first four traces correspond to the shock counters along the driven section, and provide a measure of the incident shock speed. The pressure trace reveals how the test condition provides a test time that is on the order of several milliseconds. The arrival of the expansion tail or reflected expansion head are not observed. This is an additional advantage of using air as the driver composition, as it results in a relatively lower gas sound speed, and therefore delays the arrival of the test time terminating waves. The window of time in which the signal was averaged is indicated as the "calibration window." This period of time is not influenced by the initial noisy measurements induced by the arrival of the shock, and is free of compression due to boundary layer growth. The effect of boundary layer growth is observed as a gradual increase in pressure over the test time.

3. The conditions should be designed to span the range of pressures that the sensors will be used to measure. While this is an obvious point, it can be challenging to simultaneously satisfy with the previous few points.

Table C.2 provides the initial fill conditions for the test conditions that were used for calibration.

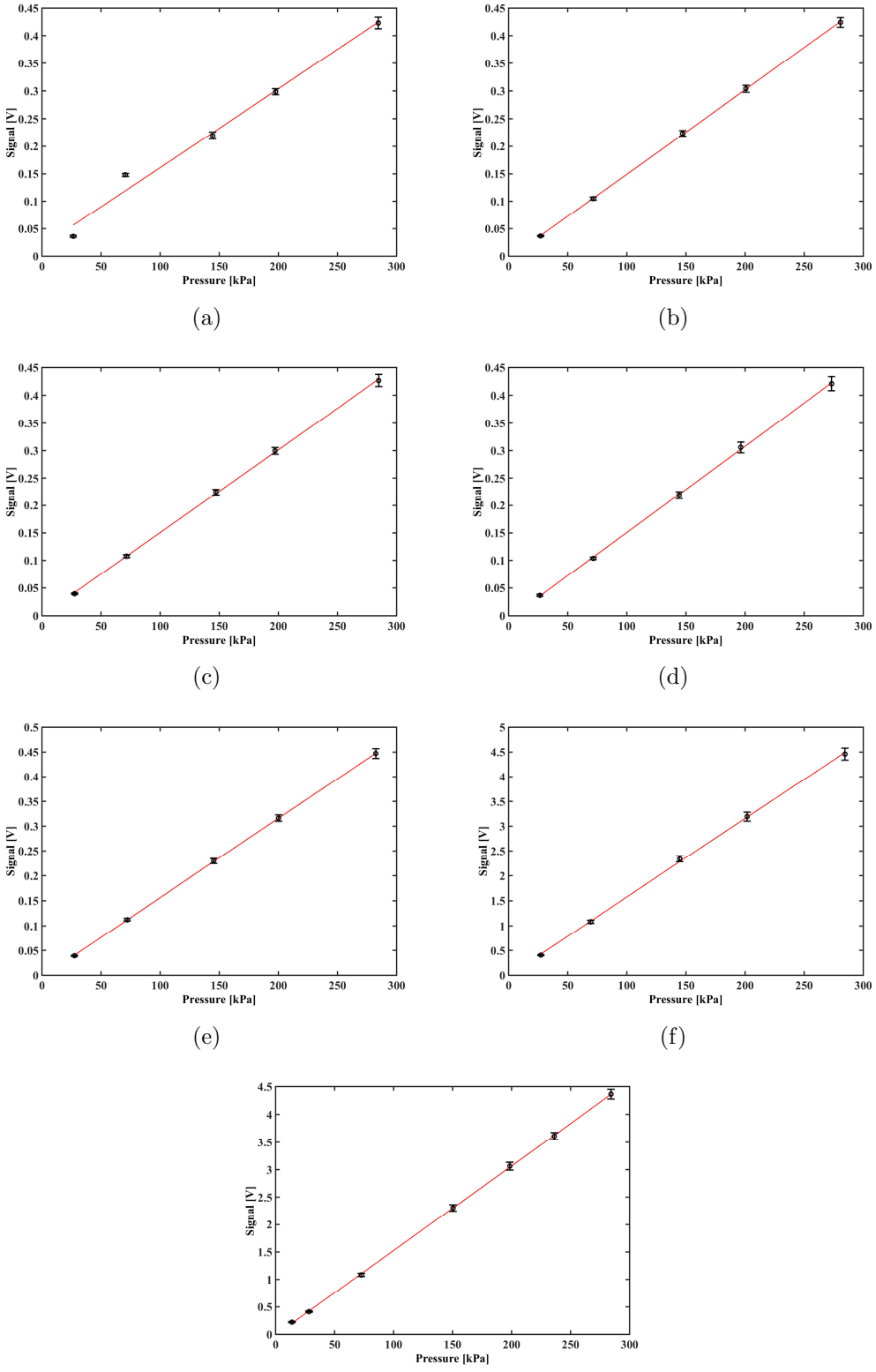

Figure C.1: Calibration curves for PCB sensors SN (a) 13456 (b) 14950 (c) 13455 (d) 20210 (e) 19053 (f) 28248 (g) 28210. The error bars correspond to the root mean square of the signal.

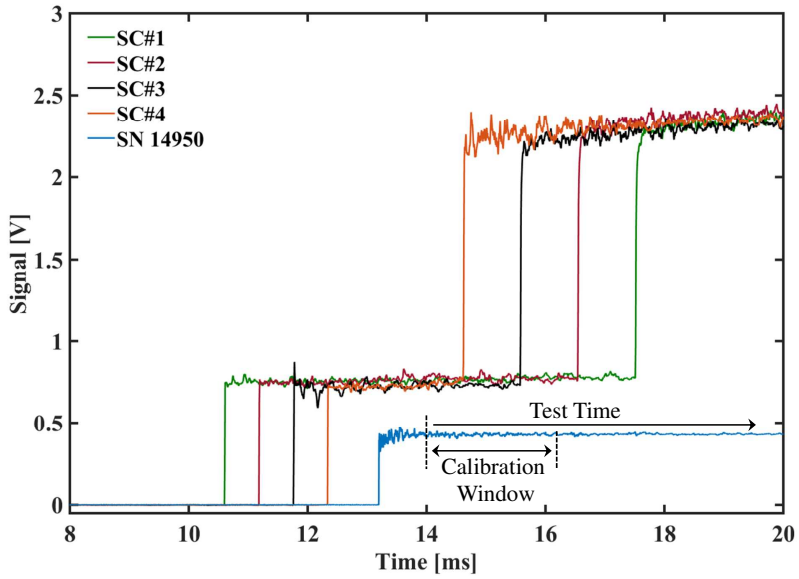

Figure C.2: Example of acquire voltage signal from PCB Sensor SN 14950 mounted in the end wall.

APPENDIX D

Derivation of Compatibility Equations

D.1 Introduction

The following derivation of the compatibility equations follows that of Refs. [171, 172]. The derivation is specific to flows of calorically perfect gases, with unity Prandtl number, through constant area ducts, and whose flow parameters are a function of position and time. The instantaneous flow properties at any position and time can be specified when three independent parameters are known. The parameters are conveniently chosen to be two thermodynamic state properties being the speed of sound (a), the specific entropy (s), and a flow property being the flow velocity (u) relative to the lab reference frame. First, the basic equations are rewritten in terms of these chosen parameters. Then the governing equations, which are expressed in Cartesian coordinates, are written in terms of a natural coordinate system, referred to as the characteristic directions. Finally, the transport of momentum and heat due to the flow interaction with the wall is described. The energy transfer processes are treated as a set of source terms, that lump the effects of gradients in momentum and temperature, and are used to determine the entropy change of a fluid element along a pathline.

D.2 Compatibility Equations

For a steady, inviscid, and constant area flow, the one-dimensional conservation equations for mass and momentum are given by

$$\frac{\partial \rho}{\partial t} + u\frac{\partial \rho}{\partial x} + \rho\frac{\partial u}{\partial x} = 0 \tag{D.1}$$

$$\frac{\partial u}{\partial t} + u\frac{\partial u}{\partial x} = -\frac{1}{\rho}\frac{\partial P}{\partial x} + f \tag{D.2}$$

where the last term in Eqn. D.2 considers contributions from body forces. Then, from the first law of thermodynamics the Gibbs relation can be expressed in terms of density or pressure as

$$\mathrm{d}s = C_\nu \frac{\mathrm{d}T}{T} - R\frac{\mathrm{d}\rho}{\rho} \tag{D.3}$$

$$\mathrm{d}s = C_p \frac{\mathrm{d}T}{T} - R\frac{\mathrm{d}P}{P} \tag{D.4}$$

By differentiation and substitution of the definition of the speed of sound, the Gibbs relations can be expressed in a more convenient form as

$$\mathrm{d}(\ln \rho) = \frac{2}{\gamma - 1}\frac{\mathrm{d}a}{a} - \frac{\mathrm{d}s}{R} \tag{D.5}$$

$$\mathrm{d}(\ln P) = \frac{2\gamma}{\gamma - 1}\frac{\mathrm{d}a}{a} - \frac{\mathrm{d}s}{R} \tag{D.6}$$

By combining Eqns. D.1 and D.5 and eliminating density, we obtain

$$\frac{2}{\gamma - 1}\frac{\partial a}{\partial t} + \frac{2}{\gamma - 1}u\frac{\partial a}{\partial x} + a\frac{\partial u}{\partial x} = \frac{a}{R}\frac{\mathrm{D}s}{\mathrm{D}t} \tag{D.7}$$

where the substantial derivative is given by

$$\frac{\mathrm{D}}{\mathrm{D}t} = \frac{\partial}{\partial t} + u\frac{\partial}{\partial x} \tag{D.8}$$

Similarly, by combining Eqns. D.2 and D.6 the pressure terms can be terminated to obtain

$$\frac{\partial u}{\partial t} + u\frac{\partial u}{\partial x} + \frac{2}{\gamma - 1}a\frac{\partial a}{\partial x} = \frac{a^2}{\gamma R}\frac{\partial s}{\delta x} + f \tag{D.9}$$

The expressions given by Eqns. D.7 and D.9 are now expressed in terms of a and s, instead of ρ and P. Next, they are added and subtracted from one another to form the following two non-linear partial differential equations.

$$\frac{\partial}{\partial t}\left(\frac{2}{\gamma - 1}a \pm u\right) + (u \pm a)\frac{\partial}{\partial x}\left(\frac{2}{\gamma - 1}a \pm u\right) = \frac{a}{R}\left(\frac{\mathrm{D}s}{\mathrm{D}t} \pm \frac{a}{\gamma}\frac{\partial s}{\partial x}\right) \pm f \tag{D.10}$$

The terms on the left describe the rate of change of the Reimann variables, in the $x - t$ plane through a substantial derivative. From this, it is easy to identify that the

slopes of the directions they describe are given by $\frac{dx}{dt} = u \pm a$. These lines move along a preferred coordinate system and are referred to as characteristic lines. Therefore, the Reimann variables described along the $C_\pm$ characteristic lines are given by

$$C_+ : P = \frac{2}{\gamma - 1} a + u \tag{D.11}$$

$$C_- : Q = \frac{2}{\gamma - 1} a - u \tag{D.12}$$

respectively. The slope of the $C_\pm$ characteristic lines are given by

$$C_+ : \ \frac{\mathrm{d}x}{\mathrm{d}t} = u + a \tag{D.13}$$

$$C_- : \ \frac{\mathrm{d}x}{\mathrm{d}t} = u - a \tag{D.14}$$

respectively. Physically, these two characteristic lines describe the propagation of an acoustic disturbance. Similarly, a third characteristic line, referred to as C_0, can be used to describe the pathline of a fluid element, and is given by

$$C_0 : \ \frac{\mathrm{d}x}{\mathrm{d}t} = u \tag{D.15}$$

This curve also describes the entropy integration path. The solution of the flow field is sought along this family of three characteristic lines. Therefore, a more convenient form of Eqn. D.10 can be obtained by letting

$$\frac{\mathrm{D}_\pm}{\mathrm{D}t} = \frac{\partial}{\partial t} + (u \pm a) \frac{\partial}{\partial x} \tag{D.16}$$

represent a substantial derivative along the $C_\pm$ characteristic lines. Then after sub-

stitution one obtains,

$$\frac{\mathrm{D}_{\pm}}{\mathrm{D}t}\left(\frac{2}{\gamma-1}a \pm u\right) = \frac{a}{R}\left(\frac{\mathrm{D}s}{\mathrm{D}t} \pm \frac{a}{\gamma}\frac{\partial s}{\partial x}\right) \pm f \tag{D.17}$$

To express the $\frac{\partial}{\partial x}$ component in terms of a characteristic direction, the quantity

$$\frac{a}{R}\frac{\mathrm{D}s}{\mathrm{D}t}\frac{1-\gamma}{\gamma} \tag{D.18}$$

is added and subtracted to the right side of the equation. Then the terms can be grouped in a convenient manner to obtain

$$\frac{\mathrm{D}_{\pm}}{\mathrm{D}t}\left(\frac{2}{\gamma-1}a \pm u\right) = \frac{a}{\gamma R}\frac{\mathrm{D}_{\pm}s}{\mathrm{D}t} + \frac{\gamma-1}{\gamma R}a\frac{\mathrm{D}s}{\mathrm{D}t} \pm f \tag{D.19}$$

Furthermore, to make the characteristic equations D.19 more convenient to use in practice, the variables are non-dimensionalized in the following manner

$$A = \frac{a}{a_0} \tag{D.20}$$

$$U = \frac{u}{u_0} \tag{D.21}$$

$$S = \frac{s_0}{\gamma R} \tag{D.22}$$

$$\xi = \frac{x}{L_0} \tag{D.23}$$

$$\tau = \frac{a_0 t}{L_0} \tag{D.24}$$

$$\Psi = \frac{L_0 f}{a_0^2} \tag{D.25}$$

where L_0 is a reference length and the subscript 0 denotes a reference state, typically taken to be the CJ-state. After non-dimensionalizing and using the definitions of the Reimann variables given in Eqns. D.11 andD.12, Eqns. D.19 become

$$\frac{\mathrm{D}_+ P}{\mathrm{D}\tau} = A\frac{\mathrm{D}_+ S}{\mathrm{D}\tau} + (\gamma - 1)\, A\frac{\mathrm{D}S}{\mathrm{D}\tau} + \Psi \tag{D.26}$$

$$\frac{\mathrm{D}_- Q}{\mathrm{D}\tau} = A\frac{\mathrm{D}_+ S}{\mathrm{D}\tau} + (\gamma - 1)\, A\frac{\mathrm{D}S}{\mathrm{D}\tau} - \Psi \tag{D.27}$$

Equations D.26 and D.27 are the compatibility equations which describe the rate of change of the P and Q Reimann variables and entropy S along the C_+ and C_- characteristics, respectively. The rate of change of entropy ($\mathrm{D}S/\mathrm{D}\tau$) along the C_0 characteristic or particle path line is given by the following general expression

$$\frac{\mathrm{D}S}{\mathrm{D}\tau} = \mathcal{F}(\xi, \tau, A, U, S) \tag{D.28}$$

The change in entropy of a fluid element depends on the process it is undergoing and therefore can be expressed as a substantial derivative of several parameters. Then, the specific entropy can be calculated by integration of Eqn. D.28 along a particle path. Equations D.26, D.27, and D.28 close the system of equations required to solve for A, U, and S in the flow field.

D.3 Entropy Change Due to Heat Transfer

The rate of specific entropy change of a gas due to heat transfer is given by the energy equation as,

$$\frac{\mathrm{D}s}{\mathrm{D}t} = \frac{1}{T}\frac{\mathrm{D}q}{\mathrm{D}t} \tag{D.29}$$

where q is the amount of heat transferred from the system. We consider the convective form of heat transfer along a pipe, and express the heat transfer per unit mass, across a surface of area πdL, as

$$\frac{1}{\pi dL}\frac{dq}{dt} = -h(T_0 - T_w) \tag{D.30}$$

where h is the convective heat transfer coefficient and T_0 and T_w are the stagnation and wall temperatures, respectively. The rate of heat transfer per unit mass of gas is then

$$\frac{\mathrm{d}q}{\mathrm{d}t} = \frac{-4h(T_0 - T_w)}{\rho d} \tag{D.31}$$

The Reynolds analogy is used to relate the film coefficient of heat transfer h and the friction coefficient C_f as,

$$\frac{h}{\rho C_p u} = \frac{C_f}{2} \tag{D.32}$$

By combining Eqns. D.32, D.31, and D.29, using the definition of stagnation temperature, and non-dimensionalizing, one obtains

$$\left.\frac{\mathrm{D}S}{\mathrm{D}\tau}\right|_{Heat\ Transfer} = -\frac{2C_f U\beta}{A^2(\gamma-1)}\left[A^2 + \frac{\gamma-1}{2}U^2 - A_w^2\right] \tag{D.33}$$

D.4 Entropy Change Due to Friction

The change in specific entropy can be calculated by integration of Eqn. D.28 along a particle path. First we consider the contributions due to momentum losses. The wall shear stress based on a friction coefficient C_f, is given by

$$\tau_w = \frac{1}{2} C_f \rho u^2 \tag{D.34}$$

Then the force per unit mass of fluid along a tube with diameter d, is given by

$$f = \frac{-2C_f u^2}{d} \tag{D.35}$$

When the force is non-dimensionalized, one obtains

$$\Psi = -2C_f U^2 \beta \tag{D.36}$$

where the parameter β is the ratio between the length and diameter of the tube ($\beta = L/d$).

The rate of change in work on a fluid element is the product of the net force applied and speed it is moving. If the energy dissipated by friction is converted to heat then one can relate the heat transfer to the rate of change in work by

$$q = fu \tag{D.37}$$

Then, combining Eqns. D.37 and D.29 and non-dimensionalizing yields a relation that describes the rate of change in entropy of a fluid element subject to friction forces,

$$\left.\frac{\mathrm{D}S}{\mathrm{D}\tau}\right|_{Friction} = -\frac{U}{A^2}\Psi \tag{D.38}$$

D.5 Total Entropy Change

The expression given by Eqn. D.28 is then the summation of the contributions due to momentum losses (Eqn. D.38) and heat losses (Eqn. D.33). This is conveniently given as,

$$\frac{\mathrm{D}S}{\mathrm{D}\tau} = -\frac{2C_f U\beta}{A^2(\gamma-1)}\left[A^2-(\gamma-1)U^2-A_w^2\right] \tag{D.39}$$

This expression describes the change of entropy of a fluid element along a pathline due to the dissipation of kinetic energy to the wall from friction and heat transfer. The last term in the brackets is the non-dimensionalized sound speed evaluated at the wall temperature.

APPENDIX E

Control and Operation of MHExT

This appendix is designed to give readers necessary information on operation and control of the MHExT facility. Figure E.1 is a schematic of the facility and includes layout details of multiple high and low pressure systems, as well as illustrates the timing system used to trigger and synchronize equipment. A total of nine (up to sixteen) PCB pressure sensors are fixed along the length of the expansion tube. The high-impedance charge output of the pressure sensors are converted to low-impedance voltage signals through the use of two signal conditioners. The voltage signals are then fed into analog input modules which are operated by a labview program.

The labview program serves three functions; 1) it provides remote control over numerous solenoid valves for convenient filling and evacuation of the expansion tube sections 2) it initiates the experimental runs and records the analog voltage outputs of the conditioned PCB charge during the experimental runs 3) it outputs the required signals to trigger a digital delay generator which then provides the timing and synchronization for numerous devices and hardware. The digital delay generator (Berkeley Nucleonics Model 725 - Multi-Trigger Digital Delay Generator) has a total of eight inputs $1-8$ and outputs $A-H$. Output H is the only channel that is not capable of triggering other channels unless it is connected externally to an input

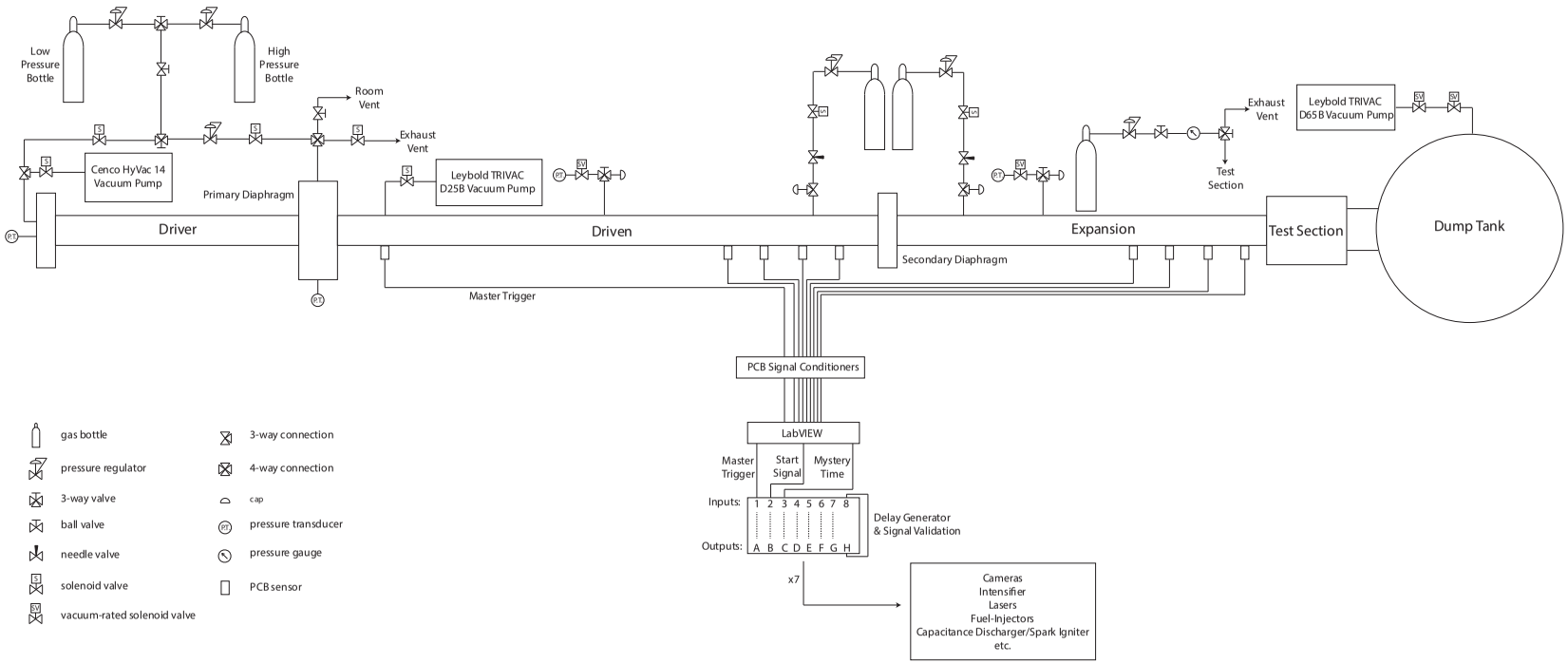

Figure E.1: Diagram of the MHExT facility which includes piping for high and low pressure systems as well as the layout for the timing system used to trigger and synchronize equipment.

(as is shown in Fig. E.1). The delay generator has a graphic user interface which is used to set the function and specifications of each channel. The function of each channel is set by choosing from a list of *timing modes*, such as "delayed pulse after trigger", "clocked pulse stream", "validated trigger input", "dynamically delayed pulse", "toggled output mode", and more (see online user manual or hard copy in lab).

A schematic of the sequence of events that occur during an experimental run is given by Fig. E.2. In order to initiate an experimental run, the **Fire Button** is pressed via the labview GUI. The solenoid valve separating the buffer section from the exhaust vent is signaled to open after 70 ms. This lengthy delay ensures that the laser pulse that is used to acquire experimental data is triggered after atleast 100 ms from the previous pulse. It was determined that as long as this criteria was satisfied, the laser pulse used for data acquisition will have a near ideal energy profile. Figure E.3 reveals how the temporal laser energy profile (width and magnitude) does not change significantly when the delay between pulses are greater than or equal to 100 ms. However, if the time between pulses is less than 100 ms (red curve), the laser pulse exhibits a significant reduction in power which would adversely affect any acquired experimental PLIF image. Each of the curves were acquired by initially running the laser on a 10 Hz clock before it was subsequently taken off and triggered after the indicated delay time. The pulse energies were measured with a photodiode, and the collected signal for each delay was repeated several times and showed negligible variations between runs.

The primary diaphragm rupturing process is given by Δt_1, and is a consequence of the increasing pressure differential imposed across the diaphragm by the venting buffer. Typically, the value of Δt_1 ranges between 10s of milliseconds to 100s of milliseconds. A good rule of thumb is to use primary diaphragm configurations and fill pressures that result in values with $200 < \Delta t_2\ [\text{ms}] < 500$, where $\Delta t_2 = 70\ [\text{ms}] + \Delta t_1$.

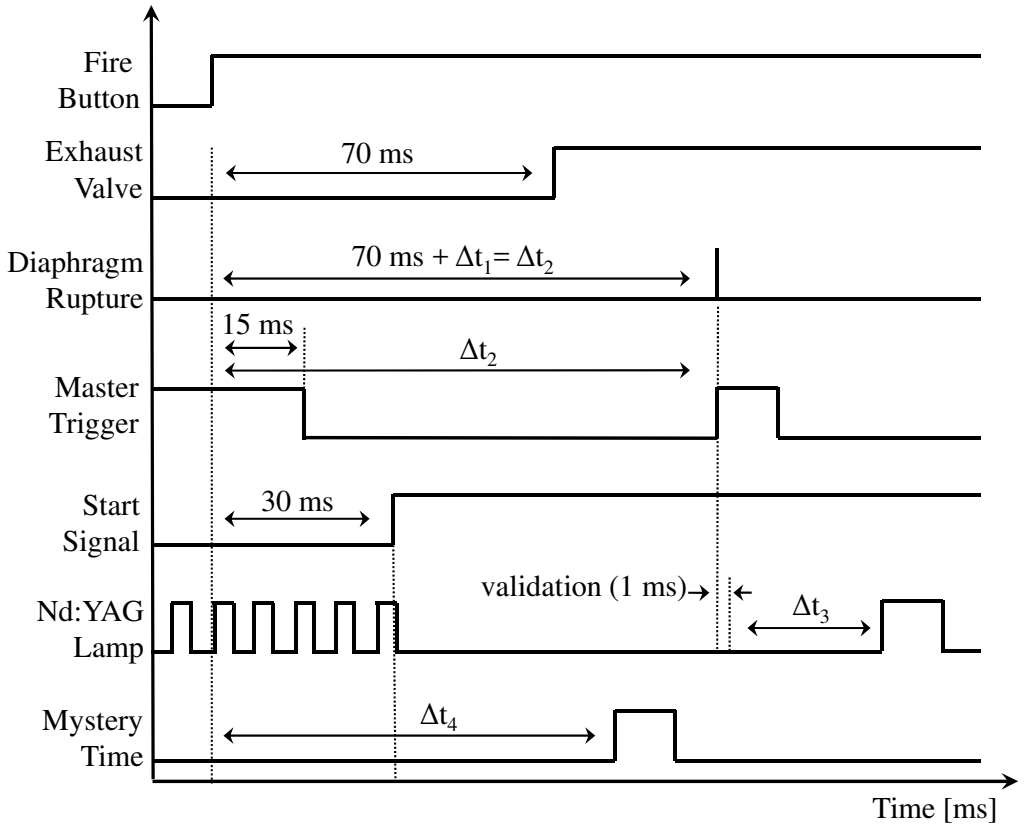

Figure E.2: Schematic illustrating the timing and sequence of events communicated between labview, delay generator, and hardware. The periods of time are not drawn to scale.

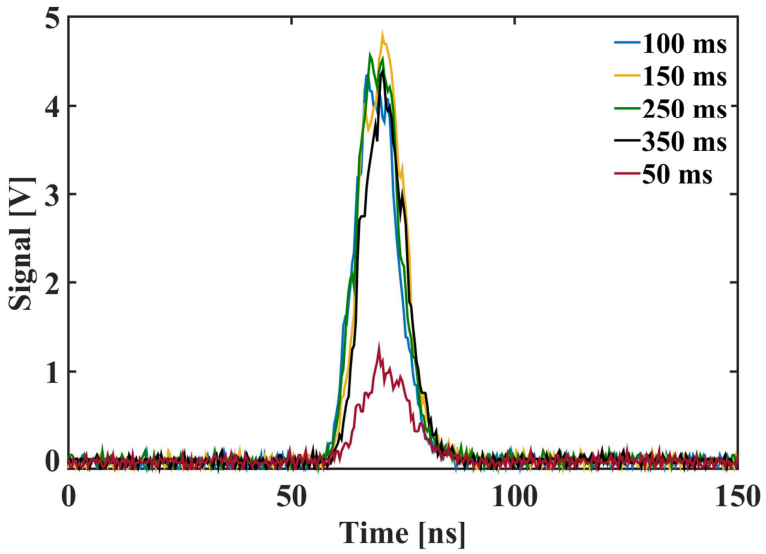

Figure E.3: Laser pulse energy profiles measured with a photodiode. The curves correspond to various delays set between the measured laser pulse and the one preceding it.

Values that are smaller than this imply that the diaphragms were over-stressed and the setup has a very small margin for error, which can lead to pre-mature rupturing. Values larger than this result in substantial energy losses during the rupturing process and yield significantly lower primary shock speeds as compared to the predicted values.

Shortly after the primary diaphragm is ruptured, a developing primary shock wave begins to propagate downstream. As long as the pressure rise across the developing wave exceeds a set threshold (typically taken to be 0.05 volts), a **Master Trigger** signal is generated via labview. This is when data acquisition and recording begins and is given by Δt_2 and referenced from the push of the **Fire Button**. In Fig. E.2, it is shown to correspond to the exact time as the diaphragm rupture, however in reality, there is a delay on the order of 10s of microseconds between the diaphragm rupturing and the high-pressure wave passing over the first PCB sensor. When the first PCB sensor is triggered, labview generates a TTL pulse which is subsequently output to the delay generator. Hardware such as cameras, fast-acting solenoid valves,

and lasers can then be triggered and referenced off of this signal. The time between when the **Master Trigger** pulse is sent to the delay generator and when the test gas arrives at the test section can range anywhere between 5 and 15 ms.

Unfortunately, activating any of the solenoid valves along the facility generates sufficient noise to falsely trigger the delay generator. Therefore, it was necessary to validate the **Master Trigger** signal being sent from labview to the delay generator. This was done by generating an additional signal, referred to as the **Start Signal** and dedicating one of the delay generator channels to validation. The logic was to only deem the **Master Trigger** true if and only if it was accompanied by a high state of the **Start Signal**. The **Start Signal** was programmed to go high after 30 ms from the push of the **Fire Button**. The reason for this choice of delay was to ensure that there was sufficient time for the **Master Trigger** signal to go low after the run was initiated. The **Master Trigger** output by labview is inherently and by default high before it subsequently drops to low after approximately 15 ms of initiating the run. It was not understood how to minimize or eliminate this fixed and inherent delay in the system. Nevertheless, the **Master Trigger** and **Start Signal** are connected to inputs 1 and 2 of the delay generator, respectively. Channel H is used to validate the signal through the following logic

$$\text{inH} = \text{in1\&in2} \tag{E.1}$$

and is required to be satisfied for atleast 1 ms. The remaining channels (with the exception of A and C) are set to generate TTL pulses that are referenced off of channel H (delayed pulse after trigger). For example, the logic for channel B which can be used to trigger the Phanton Camera and/or Valvetech solenoid valve is given by

$$\text{inB} = \text{in8} \tag{E.2}$$

This means that channel B will be triggered if and only if the validation of channel H was successful. The variable in8 refers to the input 8, which has been externally hardwired from outH (see Fig. E.1). Channel A is designated to generating a 10 Hz pulse stream that is used to trigger the Nd: YAG flash lamps (channel F). The laser follows the pulse stream until the **Start Signal** goes high, where it then waits for the validation signal output of channel H (input 8). The logic is given by

$$\text{inF} = (!\text{in1}\&\text{outA}) \mid \text{in8} \tag{E.3}$$

The !, &, and | symbols refer to *not*, *and*, and *or*, respectively. The signal to trigger the lamp for the experimental run is delayed off of the validation signal (in8). This is also illustrated in Fig. E.2, where the delay is given by Δt_3.

In the present study, the time between the master trigger being validated and the arrival of the test gas (Δt_3) was approximately 6 ms. This was sufficient time to turn on the solenoid valve (ValveTech) used for the JISCF and generate a fully established flow before arrival of the test gas. However, it was an insufficient amount of time to fill the detonation tube with a H_2-O_2 mixture since the filling process required nearly 15 ms. Therefore, unlike all of the other hardware, the automotive fuel injectors used to fill the PD had to be triggered sometime between when the fire button was pressed and when the **Master Trigger** was validated. To resolve this issue, a third output from labview, referred to as **Mystery Time**, was generated to turn on the fuel injectors well before the **Master Trigger** was validated. Channel C is programmed to output a signal to turn on the fuel injectors when both the **Start Signal** and **Mystery Time** are simultaneously true, using the *toggle output mode*. This requirement acts as a validation without having to designate another channel for signal validation. The signal to the injectors remains high until the sparker is sent a signal to ignite the mixture, where it is then toggled off. In practice, this is accomplished by the specific settings and options available within the channel.

The difficulty arises in trying to determine the appropriate delay (given by Δt_4 in Fig. E.2), and therefore the choice of when the **Mystery Time** signal is output from labview to the delay generator. The choice depends on the time it takes for a diaphragm to rupture (Δt_1) to take place. It was determined that for a given test gas condition (initial fill parameters and diaphragm setup), the diaphragm rupture times (Δt_1) vary by only 10s of milliseconds. The value of Δt_2 can be monitored after each run and it is output inside of the red box shown in Fig. E.4. An average value can be determined over the course of several runs to help guide the choice of setting Δt_4. Once a value is determined, the time in which the **Mystery Time** signal is output to the delay generator can be set in the green box of Fig. E.4.

It is important to note that the repeatability of the diaphragm rupturing time is dependent on the details of how the diaphragms are prepared and how the sections are filled. Minor variations associated with using diaphragms from different batches (provided by the manufacturer), the scoring process, and the steps taken to fill the driver and driven sections, will result in a larger spread in Δt_1 or Δt_2 between shots. Moreover, this can have implications on the shot-to-shot variations in test gas properties since they depend on the primary shock strength which can be sensitive to the rupturing process. Therefore, it is essential to be as methodical and systematic as possible when preparing for each test run.

The yellow box in Fig. E.4 indicates where the sample rate, sample time, and master trigger threshold are set. The sample rate is typically set to 2 MHz and provides sufficient resolution to infer the generated shock speeds. The sample time refers to the length of time in which data is recorded and is reference from the moment the pressure wave passes across the first PCB sensor. A threshold level of 0.05 volts corresponds to approximately 35 kPa, and is sufficient to be triggered by weaker primary shocks for low enthalpy operation.

A spreadsheet titled "Expansion Tube Layout" is used to keep track of where

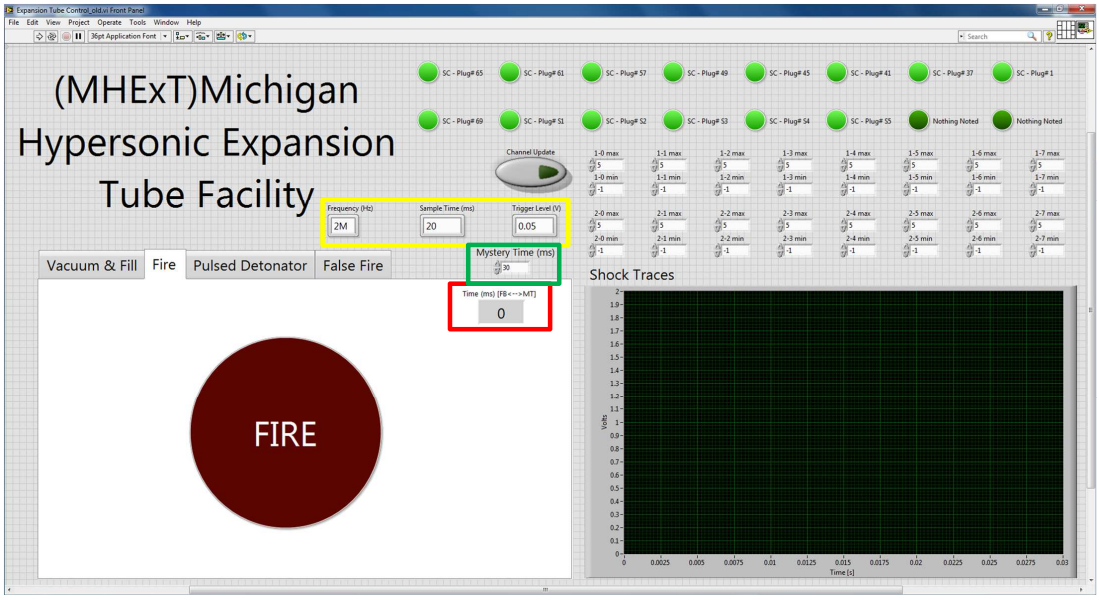

Figure E.4: Front panel of the labview code used to control the MHExT facility.

each PCB sensor is connected by their respective serial number. The file is saved in the *My Documents* folder. It is necessary to note the configuration and location of each sensor between experiments, since their arrangement may vary between experiments as different test models are used. As different layouts are used, they can be numbered and saved for later use or for reference during post-processing. Figure E.5 is a screenshot of an examplar Expansion Tube Layout file. The physical location of each sensor is given under the "Plug #" column. The first nine sensors refer to the shock counters along the length of the tube, while the last five refer to sensors that can be used inside the test section. The next column addresses which of the two signal conditioners is used and the input terminal. For example, 2.6 refers to signal conditioner number 2 input terminal 6. The next column follows the same convention but refers to the NI BNC blocks that are controlled by labview. Finally, the final two columns indicate the sensitivity of the sensor in V/kPa. The "Low" column refers to the sensitivity when the sensor signal output is below 1 volt. The "High" column refers to the sensitivity when the sensor signal output exceeds 1 volt. The bottom half of the spread sheet describes the electrical layout of power and control between

	A	B	C	D	E	F	G
1	1	Shock Counter Serial Number	Plug #	PCB Signal Conditioner	NI Channel	V/kPa Low	V/kPa High
2		27177	1	1.1	1.7	0.007785	0.007826
3		27179	37	1.2	1.6	0.007659	0.007688
4		27180	41	1.3	1.5	0.007773	0.007788
5		27288	45	1.4	1.4	0.007539	0.00755
6		27287	49	1.5	1.3	0.007541	0.007553
7		27181	57	1.6	1.2	0.007723	0.007754
8		27182	61	1.7	1.1	0.007772	0.007809
9		27184	65	1.8	1.0	0.007365	0.007395
10		27178	69	2.8	2.0	0.007737	0.007755
11		30477	S1	2.7	2.1	0.00145	0.001439
12		30623	S2	2.6	2.2	0.00141	0.00142
13		20210	S3	2.5	2.3	0.0014339	0.0014339
14		13456	S4	2.4	2.4	0.0014339	0.0014339
15		14950	S5	2.3	2.5	0.001402	0.001402
16							
17	2	Relay #	Module #	Solenoid #	Purpose	Plug #	
18		0	1	9	Driver Fill		
19		1	1	10	Expansion Vaccum D		
20		2	1	6	Buffer Fill		
21		3	1	7	Buffer Exhaust		
22		4	1	8	Driver Vaccum		
23		5	1	4	Driven Fill	51	
24		6	1	5	Driven Vaccum		
25		7	1	1	Driven Sensor Shield	35	
26		8	1	2	Expansion Sensor Shield	53	
27		9	1	3	Expansion Fill	55	
28		17	2	11	Expansion Vaccum U		

Sheet1 Sheet2 Sheet3

Figure E.5: An exemplar Expansion Tube Layout file that is used to denote the location and configuration of an experimental run for later reference or during post-processing.

labview and the various solenoid valves.

The Expansion Tube Layout File should be saved in .txt format within the *My Documents* folder. After each experimental run, the acquired data is written and saved to a `Run_XXXXX.xlsx` file in a folder named "MHExT Test Data". The files are automatically named in increasing numerical order, and XXXXX are place holders. The information in the Expansion Tube Layout.txt file is referred to by labview to organize the information saved for each experimental run, such that the data from each sensor is designated under its corresponding column. An example of the very beginning of the saved experimental data of `Run_00524.xlsx` is shown in Fig. E.6. In the first column, the numbers from top to bottom refer to the set sample rate in Hz, the set sample length in milliseconds, and the measured value of Δt_2. The

A	B	C	D	E	F	G	H	I	J	K	L	M	N	O
Untitled	27184	27182	27181	27287	27288	27180	27179	27177	27178	30477	30623	20210	13456	14950
2000000	0	0.00061	0.00061	0.00061	0	-0.00061	0	0.06958	0.00061	-0.00305	-0.00305	0.00061	0.00061	0.00061
20	0.00061	0.001221	0.001221	0.00061	0	-0.00061	0	0.240479	0	-0.00244	-0.00244	0	0.00061	0.00061
269	0.00061	0.00061	0	0.00061	-0.00061	-0.00061	0.00061	0.471191	-0.00122	-0.00366	-0.00305	0	0	0.001221
	0	0	0.00061	0.00061	-0.00061	-0.00061	0.00061	0.423584	-0.00061	-0.00366	-0.00427	0	-0.00061	0.001221
	0	0	0	0.00061	-0.00061	0	0.001221	0.531006	-0.00061	-0.00244	-0.00305	0	0	0.00061
	0	0.001221	0.00061	0.00061	0	0	0	0.598755	0	-0.00305	-0.00366	0.00061	0	0.001221
	0	0	0.00061	0	-0.00122	0	0	0.549316	-0.00061	-0.00244	-0.00305	-0.00061	-0.00061	0.00061
	0.00061	0.00061	0.001221	0.00061	-0.00061	0.00061	0	0.593872	0.00061	-0.00244	-0.00305	0.00061	0.001221	0.00061
	0.001221	0.00061	0.00061	0	0	-0.00061	0.00061	0.604858	-0.00122	-0.00305	-0.00366	-0.00061	0	0
	0	0.00061	0.00061	0.00061	-0.00061	-0.00061	0	0.55542	0	-0.00244	-0.00305	0.00061	0.00061	0.001221
	0	0.00061	0.001221	0	-0.00061	-0.00061	0	0.708008	0	-0.00366	-0.00305	0	-0.00061	0.00061
	0.00061	0	0.001221	0	-0.00061	0	-0.00122	0.606079	0	-0.00305	-0.00244	0	0	0.001221
	0	0.001221	0.00061	0.00061	0.00061	0.00061	0.00061	0.476074	0	-0.00183	-0.00244	0.00061	0.001831	0.00061

Figure E.6: Example of a portion of the test data that is acquired and saved by labview during an experimental run. The data is automatically saved in the *MHExT Test Data* folder in increasing numerical order.

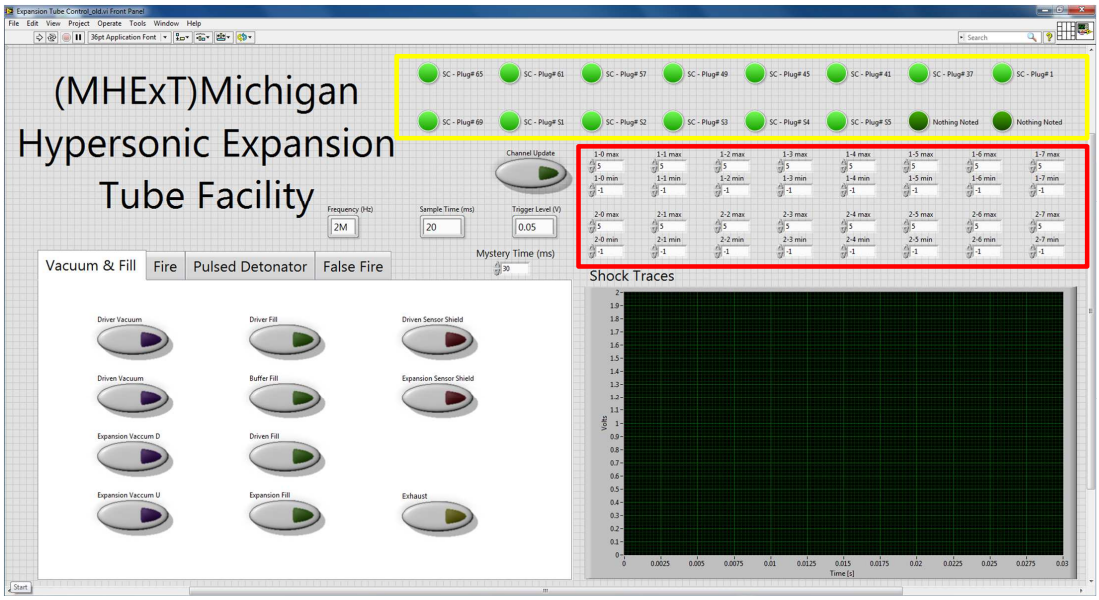

Figure E.7: Front panel of the labview code used to control the MHExT facility.

remaining fourteen columns correspond to data acquired from the fourteen different PCB sensors. For each column, the first row denotes the sensor serial number while the remaining rows denote the voltage signal at each sampled time step.

The yellow box in Fig. E.7 indicates the active (bright green) and inactive (dark green) sensors. The labview program provides this visual information based on the information that is provided and saved in the Expansion Tube Layout.txt file. The options provided within the red box in Fig. E.7 allow the user to vary the resolution of the measured signals by setting a maximum and minimum measurable voltage levels.

BIBLIOGRAPHY

BIBLIOGRAPHY

[1] T. Fric, A. Roshko, Vortical structure in the wake of a transverse jet, Journal of Fluid Mechanics 279 (1994) 1–47.

[2] J. Crafton, A. Forlines, S. Palluconi, K.-Y. Hsu, C. Carter, M. Gruber, Investigation of transverse jet injections in a supersonic crossflow using fast-responding pressure-sensitive paint, Experiments in Fluids 56 (2) (2015) 27.

[3] M. Gamba, M. G. Mungal, Ignition, Flame Structure and Near-Wall Burning in Transverse Hydrogen Jets in Supersonic Crossflow, Journal of Fluid Mechanics 780 (2015) 226–273.

[4] S. Hollo, J. McDaniel, R. Hartfield Jr., Quantitative Investigation of Compressible Mixing : Staged Transverse Injection into Mach 2 Flow, AIAA Journal 32 (3) (1994) 528–534.

[5] H. Johari, Scaling of Fully Pulsed Jets in Crossflow, AIAA Journal 44 (11) (2006) 2719–2725.

[6] R. Sau, K. Mahesh, Optimization of pulsed jets in crossflow, Journal of Fluid Mechanics 653 (2010) 365–390.

[7] M. W. Evans, C. M. Ablow, Theories of Detonation, Chemical Reviews 61 (2) (1961) 129–178.

[8] R. Strehlow, C. Engel, Transverse Waves in Detonations: II. Structure and Spacing in H2-O2, C2H2-O2, 2H4-O2, and CH4-O2 Systems, AIAA Journal 7 (3) (1969) 492–496.

[9] V. I. Manzhalei, V. V. Mitrofanov, V. A. Subbotin, Measurement of inhomogeneities of a detonation front in gas mixtures at elevated pressures, Combustion, Explosion, and Shock Waves 10 (1) (1974) 89–95.

[10] Y. Denisov, T. Ya, Structure of gaseous detonation in tubes, Sov. Phys. Tech. Phys. 5 (4) (1960) 419–431.

[11] D. Desbordes, Aspects stationnaires et transitoires de la detonation dans les gaz: relation avec la structure cellulaire du front (1990).

[12] R. Zitoun, D. Desbordes, C. Guerraud, B. Deshaies, Direct initiation of detonation in cryogenic gaseous H2-O2 mixtures, Shock Waves 4 (6) (1995) 331–337.

[13] H. Wang, X. You, A. Joshi, S. Davis, A. Laskin, F. Egolfopoulos, C. Law, USC Mech Version II. High-Temperature Combustion Reaction Model of H2/CO/C1-C4 Compunds., http://ignis.usc.edu/USC_Mech_II.htm, May 2007.

[14] R. Trimpi, Preliminary Theoretical Study of the Expansion Tube, A New Device for Producing High Enthalpy Short Duration Hypersonic Gas Flows, NASA Technical Report-133.

[15] J. L. Palmer, R. K. Hanson, Application of Method of Characteristics to Underexpanded, Freejet Flows with Vibrational Nonequilibrium, AIAA Journal 36 (2) (1998) 193–200.

[16] K. R. Jackson, M. R. Gruber, S. Buccellato, Mach 6-8+ Hydrocarbon-Fueled Scramjet Flight Experiment: The HIFiRE Flight 2 Project, Journal of Propulsion and Power 31 (1) (2014) 36–53.

[17] M. K. Smart, N. E. Hass, A. Paull, Flight Data Analysis of the HyShot 2 Scramjet Flight Experiment, AIAA Journal 44 (10) (2006) 2366–2375.

[18] K. Jackson, M. Gruber, S. Buccellato, HIFiRE Flight 2 Overview and Status Update 2011, AIAA Paper 2011-2202, 2011.

[19] S. Laurence, J. M. Schramm, S. Karl, K. Hannemann, An Experimental Investigation of Steady and Unsteady Combustion Phenomena in the Hyshot II Combustor, AIAA Paper 2011-2310, 2011.

[20] J. M. Seiner, Historical Survey on Enhanced Mixing in Scramjet Engines, Journal of Propulsion and Power 17 (6) (2001) 1273–1286.

[21] E. J. Gutmark, K. C. Schadow, K. Yu, Mixing Enhancement in Supersonic Free Shear Flows, Annual Review Fluid Mechanics 27 (1) (1995) 375–417.

[22] K. Yu, K. Wilson, K. Schadow, Effect of Flame-Holding Cavities on Supersonic-Combustion Performance, Journal of Propulsion and Power 17 (6) (2001) 1287–1295.

[23] K.-Y. Hsu, C. D. Carter, M. R. Gruber, T. Barhorst, S. Smith, Experimental Study of Cavity-Strut Combustion in Supersonic Flow, Journal of Propulsion and Power 26 (6) (2010) 1237–1246.

[24] R. L. Panton, Excitation by Grazing Flow, AIAA Journal 28 (1) (1990) 60–65.

[25] H. Do, S. Im, M. Cappelli, G. Mungal, Plasma assisted flame ignition of supersonic flows over a flat wall, Combustion and Flame 157 (12) (2010) 2298–2305.

[26] T. Ombrello, C. Carter, J. McCall, F. Schauer, A. Naples, J. Hoke, K.-Y. Hsu, Enhanced Mixing in Supersonic Flow Using a Pulse Detonator, Journal of Propulsion and Power 31 (2) (2015) 654–663.

[27] T. Ombrello, C.-j. Tam, W. Haw, C. Carter, Transient Mixing Enhancement of a Transverse Jet in Supersonic Cross Flow Using Pulse Detonation 127 (2015) 247–264.

[28] F. J. Malo-Molina, Three Dimensional Analysis of a Single Hydrocarbon-Air Pulse Detonation in a Supersonic Combustor, in: 52nd Aerospace Sciences Meeting, AIAA-2014-0626, 2014.

[29] F. J. Malo-Molina, E. Dreyer, Analysis of a Single H 2 -Air Pulse Detonation in a Supersonic Combustor, in: AIAA, 51st Aerospace Sciences Meeting including the New Horizons Forum and Aerospace Exposition, no. January, 2013.

[30] A. Karagozian, Transverse Jets and their Control, Progress in Energy and Combustion Science 36 (5) (2010) 531–553.

[31] M. P. Lee, B. K. Mcmillin, J. L. Palmer, R. K. Hansont, Planar Fluorescence Imaging of a Transverse Jet in a Supersonic Crossflow, Journal of Propulsion and Power 8 (4) (1992) 729–735.

[32] C. Rodgers, Mixing of Hydrogen Injected From Multiple Injectors Normal to a Supersonic Airstream, Tech. Rep. NASA TN D-6476, Langley Research Center, Hampton, Va 23365 (1971).

[33] B. K. Mcmillin, J. M. Seitzman, R. K. Hanson, Comparison of NO and OH Planar Fluorescence Temperature Measurements in Scramjet Model Flowfields, AIAA Journal 32 (10).

[34] M. G. Allen, T. E. Parker, W. G. Reinecke, H. H. Legner, R. R. Foutter, W. T. Rawlins, S. J. Davis, Fluorescence Imaging of OH and NO in a Model Supersonic Combustor, AIAA Journal 31 (3).

[35] M. R. Gruber, A. S. Nejadt, T. H. Chen, Mixing and Penetration Studies of Sonic Jets in a Mach 2 Freestream, Journal of Propulsion and Power 11 (2).

[36] J. A. Schetz, P. F. Hawkins, H. Lehmanf, Structure of Highly Underexpanded Transverse Jets in a Supersonic Stream, AIAA Journal 5 (5) (1966) 882–884.

[37] S. H. Smith, M. G. Mungal, Mixing, structure and scaling of the jet in crossflow, J. Fluid Mech 357 (1998) 83–122.

[38] J. D. Holdeman, Mixing of multiple jets with a confined subsonic crossflow, Progress in Energy and Combustion Science 19 (1) (1993) 31–70.

[39] H. Kolla, R. W. Grout, A. Gruber, J. H. Chen, Mechanisms of flame stabilization and blowout in a reacting turbulent hydrogen jet in cross-flow, Combustion and Flame 159 (2012) 2755–2766.

[40] D. Papamoschou, D. G. Hubbard, Visual observations of supersonic transverse jets, Experiments in Fluids 14 (1993) 468–476.

[41] J. A. Schetz, F. S. Billig, Penetration of Gaseous Jets Injected into a Supersonic Stream, Journal of Spacecraft 3 (11) (1966) 1658–1665.

[42] R. M. Kelso, A. J. Smits, Horseshoe vortex systems resulting from the interaction between a laminar boundary layer and a transverse jet, Physics of Fluids 7 (1) (1995) 153–158.

[43] M. R. Gruber, L. P. Goss, Surface Pressure Measurements in Supersonic Transverse Injection Flowfields, Journal of Propulsion and Power 15 (5) (1999) 633–641.

[44] H. Kolla, R. W. Grout, A. Gruber, J. H. Chen, Mechanisms of flame stabilization and blowout in a reacting turbulent hydrogen jet in cross-flow, Combustion and Flame 159 (8) (2012) 2755–2766.

[45] E. Gutheil, G. Balakrishnan, F. A. Williams, Structure and Extinction of Hydrogen-Air Diffusion Flames, in: Reduced kinetic mechanisms for applications in combustion systems, Springer Berlin Heidelberg, 1993, Ch. 11, pp. 177–195.

[46] Z. M. Moussa, J. W. Trischka, D. S. Eskinazi, The near field in the mixing of a round jet with a cross-stream, Journal of Fluid Mechanics 80 (1) (1977) 49–80.

[47] I. Papamoschou, A. Roshko, The compressible turbulent shear layer : an experimental study, Journal of Fluid Mechanics 197 (1988) 453–477.

[48] S. D. Stouffer, N. R. Baker, D. P. Capriotti, Effects of Compression and Expansion-Ramp Fuel Injector Configurations on Scramjet Combustion and Heat Transfer, in: 31st Aerospace Sciences Meeting, AIAA Paper 1993-0609, 1993.

[49] A. Ben-Yakar, R. K. Hanson, Cavity Flame-Holders for Ignition and Flame Stabilization in Scramjets: An Overview, Journal of Propulsion and Power 17 (4).

[50] F. Vergine, M. Crisanti, L. Maddalena, V. Miller, M. Gamba, Supersonic Combustion of Pylon-Injected Hydrogen in High-Enthalpy Flow with Imposed Vortex Dynamics, Journal of Propulsion and Power 31 (1) (2015) 89–103.

[51] A. Waitz, F. E. Marblet, E. E. Zukoskij, Investigation of a Contoured Wall Injector for Hypervelocity Mixing Augmentation, AIAA Journal 31 (6) (1993) 1014–1021.

[52] H. Do, M. Cappelli, G. Mungal, Plasma assisted cavity flame ignition in supersonic flows, Combustion and Flame 157 (9) (2010) 1783–1794.

[53] S. B. Leonov, D. A. Yarantsev, A. P. Napartovich, I. V. Kochetov, Plasma-Assisted Combustion of Gaseous Fuel in Supersonic Duct, IEEE Transactions on Plasma Science 34 (6) (2006) 2514–2525.

[54] J.Lepicovsky, K.K.Ahuja, W.H.Brown, M.Salikuddin, P.J.Morris, Acoustically Excited Heated Jets I-Internal Excitation, in: NASA Contractor Report 4129-PT-1, 1988.

[55] D. W. Bogdanoff, Advanced Injection and Mixing Techniques for Scramjet Combustors, Journal of Propulsion and Power 10 (2) (1994) 183–190.

[56] T. Ombrello, X. Qin, Y. Ju, C. Carter, Combustion Enhancement via Stabilized Piecewise Nonequilibrium Gliding Arc Plasma Discharge, AIAA Journal 44 (1).

[57] H. Takahashi, G. Masuya, M. Hirota, Supersonic Turbulent Mixing Structure in Staged Injection Flowfields, in: 48th AIAA Aerospace Sciences Meeting, AIAA Paper 2010-753, 2010.

[58] S.-H. Lee, Characteristics of Dual Transverse Injection in Scramjet Combustor, Part 1: Mixing, Journal of Propulsion and Power 22 (5) (2006) 1012–1019.

[59] R. C. Rogers, Mixing of Hydrogen Injected from Multiple Injectors Normal to a Supersonic Airstream, NASA TND-6476.

[60] R. C. Rogers, A Study of the Mixing of Hydrogen Injected Normal to a Supersonic Airstream, NASA TND-6114.

[61] T. Kouchi, K. Sasaya, J. Watanabe, H. Sibayama, G. Masuya, Penetration Characteristics of Pulsed Injection into Supersonic Crossflow, in: 46th AIAA/ASME/SAE/ASEE Joint Propulsion Conference & Exhibit, AIAA 2010-6645, 2010.

[62] H. Randolph, L. Chew, H. Johari, Pulsed Jets in Supersonic Crossflow, Journal of Propulsion and Power 10 (5) (1994) 746–748.

[63] A. Eroglu, R. E. Breidenthal, Structure, Penetration, and Mixing of Pulsed Jets in Crossflow, AIAA Journal 39 (3) (2001) 417–423.

[64] R. Vernet, L. Thomas, L. David, Analysis and reconstruction of a pulsed jet in crossflow by multi-plane snapshot POD, Experiments in Fluids 47 (2009) 707–720.

[65] D. L. Chapman, On the Rate of Explosion in Gases, Philosophical Magazine 47 (1899) 90–104.

[66] E. Jouguet, On the propagation of chemical reactions in gases, Journal de Mathematiques Pures et Appliquees 1 (1905) 347.

[67] P. A. Thompson, Compressible Fluid Dynamics, advanced e Edition, thompson1988, 1988.

[68] Y. B. Zel'dovich, On the theory of the propagation of detonations in gaseous systems, Journal of Experimental and Theoretical Physics1 10 (1940) 542–568.

[69] J. von Neumann, T. A, The Collected Works of John von Neumann: 6-Volume Set, 1942.

[70] D. W, On Detonation Processes in Gases, Ann. Phys 43 (1943) 421–436.

[71] D. G. Goodwin, H. K. Moffat, R. L. Speth, Cantera: An object- oriented software toolkit for chemical kinetics, thermodynamics, and transport processes. (2017).

[72] C. Smith, G.P., Golden, D.M., Frenklach, M., Moriarty, N.W., Eiteneer, B., Goldenberg, M., Bowman, Z. Hanson, R.K., Song, S., Gardiner, W.C. Jr., Lissianski, V.V. and Qin, GRI 3.0 Mechanism.

[73] F. W, D. W, Detonation Theory and Experiment, Dover Publications Inc., 2001.

[74] I. Schelkin, Y. Troshin, Gas Dynamics of Combustion, Mono Book Corp., Baltimore, MD, 1965.

[75] E. Wintenberger, J. M. Austin, M. Cooper, S. Jackson, J. E. Shepherd, Analytical Model for the Impulse of Single-Cycle Pulse Detonation Tube, Journal of Propulsion and Power 19 (1) (2003) 22–38.

[76] T. Endo, J. Kasahara, A. Matsuo, S. Sato, K. Inaba, T. Fujiwara, Pressure History at the Thrust Walls of a Simplified Detonation Engine, AIAA Journal 42 (9) (2004) 1921–1930.

[77] T. Ombrello, S. H. Won, Y. Ju, S. Williams, Flame propagation enhancement by plasma excitation of oxygen. Part II: Effects of O2(a1Δg), Combustion and Flame 157 (10) (2010) 1916–1928.

[78] P. J. Morris, K. Takita, G. Masuya, T. Sato, Y. Ju, Effect of Addition of Radicals on Burning Velocity, AIAA Journal 39 (4) (2001) 724–744.

[79] A. Starikovskii, Plasma supported combustion, Proceedings of the Combustion Institute 30 (2005) 2405–2417.

[80] A. Firsov, K. V. Savelkin, D. A. Yarantsev, S. B. Leonov, Plasma-enhanced mixing and flameholding in supersonic flow., Philosophical transactions. Series A, Mathematical, physical, and engineering sciences 373 (2048).

[81] G. L. Pellett, C. Bruno, W. Chinitz, Review of air vitiation effects on scramjet ignition and flameholding combustion proocesses, in: 38th AIAA/ASME/SAE/ASEE Joint Propulsion Conference & Exhibit, AIAA Paper 2002-3880, 2002.

[82] C. Law, Combustion Physics, Cambridge University Press, 2006.

[83] S. Bozhenkov, S. Starikovskaia, A. Starikovskii, Nanosecond gas discharge ignition of H2 and CH4 containing mixtures, Combustion and Flame 133 (2003) 133–146.

[84] S. M. Starikovskaia, Plasma assisted ignition and combustion, Journal of Physics D: Applied Physics 39 (16) (2006) R265–R299.

[85] K. Ramohalli, Y. Yang, A. Cort, Further results from free radicals-augmented high-speed turbulent combustion, in: 26th Joint Propulsion Conference, AIAA Paper 1990-42016, 1990.

[86] V. I. Golovitchev, M. L. Piliaf, Autoignition of Methane Mixtures: The Effect of Hydrogen Peroxide, Journal of Propulsion and Power 12 (4) (1996) 699–707.

[87] G.-B. Chen, Y.-H. Li, T.-S. Cheng, H.-W. Hsu, Y.-C. Chao, Effects of hydrogen peroxide on combustion enhancement of premixed methane/air flames, International Journal of Hydrogen Energy 36 (23) (2011) 15414–15426.

[88] D. S.-K. Ting, G. T. Reader, Hydrogen peroxide for improving premixed methaneair combustion, Energy 30 (2) (2005) 313–322.

[89] F. Lu, M. Dan, Advanced Hypersonic Test Facilities, American Institute of Aeronautics and Astronautics, Reston, VA, 2002.

[90] J. Lukasiewicz, Experimental Methods of Hypersonics, Marcel Dekker Inc., New York, 1973.

[91] A. Dufrene, M. Maclean, T. Wadhams, Characterization of the New LENS Expansion Tunnel Facility, AIAA Paper 2010-1564, 2010.

[92] J. Calleja, J. Tamagno, Calibration of HYPULSE for Hypervelocity Mach Air Flows Corresponding to Flight Numbers 13.5, 15, and 17, NASA Contractor Report 191578.

[93] I. John, R. J. Bakos, A. Castrogiovanni, R. C. Rogers, R. C. Rogers, Dual Mode Shock-Expansion / Reflected-Shock Tunnel, in: 35th AIAA Aerospace Sciences Meeting, AIAA Paper 97-0560, 1997.

[94] A. Paull, R. Stalker, Scramjet Testing in the T3 and T4 Hypersonic Impulse Facilities, in: Scramjet Propulsion, Reston, VA, 2000, Ch. 1, pp. 1–46.

[95] A. Neely, R. Morgan, The Superorbital Expansion Tube Concept, Experiment and Analysis, The Aeronatutical Journal 98 (973) (1994) 97–105.

[96] R. Stalker, A. Paull, M. D.J, R. G. Morgan, P. Jacobs, Scramjets and Shock Tunnels - The Queensland Experience, Progress in Aerospace Sciences 41 (6) (2005) 471–513.

[97] H. Hornung, B. Sturtvant, J. Belanger, S. Sanderson, M. Brouillette, M. Jenkins, Performance data of the New Free-Piston Shock Tunnel T5 at GALCIT, in: Shock Waves, 1992, pp. 603–610.

[98] a. Dufrene, M. Sharma, J. M. Austin, Design and Characterization of a Hypervelocity Expansion Tube Facility, Journal of Propulsion and Power 23 (6) (2007) 1185–1193.

[99] A. Sasoh, Y. Ohnishi, K. Koremoto, K. Takayama, Operation Design and Performance of a Free-Piston-Driven Expansion Tube, in: 37th Aerospace Sciences Meeting and Exhibit, AIAA Paper 99-16672, 1999.

[100] K. Itoh, S. Ueda, T. Komuro, K. Sato, M. Takahashi, H. Miyajima, H. Tanno, H. Muramoto, Improvemnt of a Free Piston Driver for a High-Enthalpy Shock Tunnel, Shock Waves 8 (4) (1998) 215–233.

[101] K. Itoh, S. Ueda, T. Komuro, K. Sato, H. Tanno, M. Takahashi, Hypersonic Aerothermodynamic and Scramjet Research Using High Enthalpy Shock Tunnel, Shock Waves 12 (2) (2002) 93–98.

[102] K. Hannemann, S. Karl, J. M. Schramm, J. Steelant, Methodology of a Combined Ground Based Testing and Numerical Modelling Analysis of Supersonic Combustion Flow Paths, Shock Waves 20 (5) (2010) 353–366.

[103] D. T. Heiser, W. H. and Pratt, Hypersonic Airbreathing Propulsion, sixth Edition, American Institute of Aeronautics and Astronautics, 1994.

[104] F. Luo, W. Song, Z. Zhang, W. Li, J. Li, Experimental and Numerical Studies of Vitiated Air Effects on Hydrogen-fueled Supersonic Combustor Performance, Chinese Journal of Aeronautics 25 (2) (2012) 164–172.

[105] V. A. Miller, M. Gamba, M. G. Mungal, R. K. Hanson, Secondary Diaphragm Thickness Effects and Improved Pressure Measurements in an Expansion Tube, AIAA Journal 52 (2) (2014) 451–456.

[106] T. Furukawa, T. Aochi, A. Sasoh, Expansion Tube Operation with Thin Secondary Diaphragm, AIAA Journal 45 (1) (2007) 214–217.

[107] H. Ashkenas, F. Sherman, Structure and Utilization of Supersonic Free Jets in Low Density Wind Tunnels, NASA CR-60423 222 (45).

[108] S. Crist, P. M. Sherman, D. R. Glass, Study of the Highly Underexpanded Sonic Jet, AIAA Journal 4 (1) (1966) 68–71.
URL `Crist1966`

[109] S. Gordon, B. McBride, Computer Program for Calculation of Complex Chemical Equilibrium Compositions and Applications, Tech. rep. (1996).

[110] S. Gordon, B. McBride, Computer Program for Calculation of Complex Chemical Equilibrium Compositions and Applications, NASA-Reference Publication 1311 (1994).

[111] M. McGilvray, J. M. Austin, M. Sharma, P. a. Jacobs, R. G. Morgan, Diagnostic Modeling of an Expansion Tube Operating Condition, Shock Waves 19 (1) (2009) 59–66.

[112] M. A. Sutcliffe, R. G. Morgan, The Measurement of Pitot Pressure in High Enthalpy Expansion Tubes, Measurement Science and Technology 12 (3) (2001) 327–334.

[113] F. Orley, A Study of Expansion Tube Gas Flow Conditions for Scramjet Combustor Model Testing, Ph.D. thesis, Technische Universitat Munchen (2011).

[114] H. W. Liepmann, A. Roshko, Elements of Gas Dynamics, John Wiley and Sons, 1957.

[115] A. Gazi, G. Vourliotakis, G. Skevis, M. A. Founti, Assessment of Chemical Markers for Heat-Release Rate Correlations in Laminar Premixed Flames, Combustion Science and Technology 185 (10) (2013) 1482–1508.

[116] B. O. Ayoola, R. Balachandran, J. H. Frank, E. Mastorakos, C. F. Kaminski, Spatially resolved heat release rate measurements in turbulent premixed flames, Combustion and Flame 144 (2006) 1–16.

[117] J. G. Lee, D. A. Santavicca, Experimental Diagnostics for the Study of Combustion Instabilities in Lean Premixed Combustors, Journal of Propulsion and Power 19 (5) (2003) 735–750.

[118] A. Eckbreth, Laser Diagnostics for Combustion Temperature and Species, Gordon and Breach Publishers, Amsterdam, The Netherlands, 1996.

[119] J. Luque, D. Crosley, Lifbase.database and spectral simulation for diatomic molecules. Tech. rep., SRI International Report MP-99-009 (1999).

[120] J. Zonglin, W. Bo, G. Yunliang, W. Zhao, H. Zongmin, Development of the detonation-driven expansion tube for orbital speed experiments, Science China Technological Sciences 58 (4) (2015) 695–700.

[121] R. Bakos, J. Erdos, Options for Enhancement of the Performance of Shock-Expansion Tubes and Tunnels, in: 33rd Aerospace Sciences Meeting and Exhibit, AIAA 95-0799, 1995.

[122] G. Anderson, A. Kumar, J. Erdos, Progress in Hypersonic Combustion Technology with Computation and Experiment, AIAA Paper 1990-5254, 1990.

[123] H. Pergament, A Theoretical Analysis of Non-Equilibrium Hydrogen-Air Reactions in Flow Systems, in: AIAA/ASME Hypersonic Ramjet Conference, AIAA Paper 63113, 1963.

[124] V. P. Zhukov, V. A. Sechenov, A. Y. Starikovskiy, Autoignition of Kerosene (Jet-A)/ Air Mixtures Behind Reflected Shock Waves, Fuel 126 (2014) 169–176.

[125] A. De Toni, M. Werler, R. Hartmann, L. Cancino, R. Schießl, M. Fikri, C. Schulz, A. Oliveira, E. Oliveira, M. Rocha, Ignition Delay Times of Jet A-1 Fuel: Measurements in a High-Pressure Shock Tube and a Rapid Compression Machine, Proceedings of the Combustion Institute 36 (3) (2016) 3695–3703.

[126] K. Kumar, C.-J. Sung, An Experimental Study of the Autoignition Characteristics of Conventional Jet Fuel/Oxidizer Mixtures: Jet-A and JP-8, Combustion and Flame 157 (4) (2010) 676–685.

[127] W. Davies, L. Bernstein, Heat Transfer and Transition to Turbulence in the Shock- Induced Boundary Layer on a Semi-Infinite Flat Plate, Journal of Fluid Mechanics 36 (1) (1969) 87–112.

[128] M. S. Holden, Boundary-Layer Displacement and Leading-Edge Bluntness Effects on Attached and Separated Laminar Boundary Layers in a Compression Corner . Part II : Experimental Study, AIAA Journal 9 (1) (1971) 84–93.

[129] M. S. Holden, Establishment Time of Laminar Separated Flows, AIAA Journal 9 (11) (1971) 2296–2298.

[130] J. Miles, H. Mirels, H. Wang, Time Required for Establishing Detached Bow Shock, AIAA Journal 4 (6) (1966) 1127–1128.

[131] S. G. Mallinson, S. L. Gai, N. R. Mudford, Establishment of Steady Separated Flow Over a Compression - Corner in a Free - Piston Shock Tunnel, Shock Waves 7 (4) (1997) 249–253.

[132] M. H. Farris, C. T. Russell, Determining the Standoff Distance of the Bow Shock: Mach Number Dependence and Use of Models, Journal of Geophysical Research 99 (A9) (1994) 17681–17689.

[133] H. Mirels, Shock Tube Test Time Limitation Due to Turbulent-Wall Boundary Layer, AIAA Journal 2 (1) (1964) 84–93.

[134] H. Mirels, Flow Nonuniformity in Shock Tubes Operating at Maximum Test Times, Physics of Fluids 9 (10) (1966) 1907–1912.

[135] V. Andronov, Turbulent Mixing at Contact Surface Accelerated by Shock Waves, Journal of Experimental and Theoretical Physics 44 (2) (1977) 424–427.

[136] C. L. Strand, R. K. Hanson, Quantification of Supersonic Impulse Flow Conditions via High-Bandwidth Wavelength Modulation Absorption Spectroscopy, AIAA Journal 53 (10) (2015) 2978–2987.

[137] A. Ben-Yakar, R. K. Hanson, Characterization of Expansion Tube Flows for Hypervelocity Combustion Studies, Journal of Propulsion and Power 18 (4) (2002) 943–952.

[138] R. Hartunian, A. Russo, P. Marrone, Boundary-Layer Transition and Heat Transfer in Shock Tubes, Journal of the Aerospace Sciences 27 (1960) 587–594.

[139] F. White, Viscous Fluid Flow, 2nd Edition, McGraw-Hill, 1991.

[140] A. Paull, R. Stalker, Test Flow Disturbances in an Expansion Tube, Journal of Fluid Mechanics 245 (1992) 493–521.

[141] A. Paull, R. J. Stalker, The Effect on an Acoustic Wave as it Traverses an Unsteady Expansion, Physics of Fluids 3 (4) (1991) 717.

[142] Maskell E, A Theory of the Blockage Effects on Bluff Bodies and Stalled Wings in a Closed Wind Tunnel, Aeronautical Research Council Reports and Memoranda R&M 3400.

[143] G. West, C. J. Apelt, The effects of tunnel blockage and aspect ratio on the mean flow past a circular cylinder with Reynolds numbers between 10 4 and 10 5, Journal of Fluid Mechanics 114 (1982) 361–377.

[144] M. McGilvray, P. A. Jacobs, R. G. Morgan, R. J. Gollan, C. M. Jacobs, Helmholtz Resonance of Pitot Pressure Measurements in Impulsive Hypersonic Test Facilities, AIAA Paper 2009-1157, 2009.

[145] N. Sudani, B. Valiferdowsi, H. Hornung, Test time increase by delaying driver gas contamination for reflected shock tunnels, AIAA journal 38 (9) (2000) 1497–1503.

[146] R. Stalker, K. Crane, Driver gas contamination in a high-enthalpy reflected shock tunnel, AIAA Technical Note 16 (3) (1978) 277–279.

[147] Y. Burtschell, M. Cardoso, D. Zeitoun, Numerical analysis of reducing driver gas contamination in impulse shock tunnels, AIAA Journal 39 (12) (2001) 2357–2365.

[148] Y. M. Abul-Huda, M. Gamba, Flow Characterization of a Hypersonic Expansion Tube Facility for Supersonic Combustion Studies, Journal of Propulsion and Power (article in advance).

[149] W. Heltsley, J. Snyder, A. Houle, D. Davidson, M. Mungal, R. Hanson, Design and Characterization of the Stanford 6 Inch Expansion Tube, in: 42nd AIAA/ASME/SAE/ASEE Joint Propulsion Conference & Exhibit, AIAA Paper 2006-4443, 2006.

[150] B. McBridge, S. Gordon, M. Reno, Coefficients for Calculating Thermodynamic and Transport Properties of Individual Species, NASA TM-4513.

[151] W. Sheeran, D. Darshan, Observations on jet flows from a two- dimensional, underexpanded, sonic nozzle, AIAA Journal 6 (3) (1967) 540–542.

[152] G. Ben-Dor, O. Igra, T. Elperin, A. Lifshitz, Shock Wave Interaction and Propagation; Handbook of Shock Waves; vol. 2., 2001.

[153] B. W. Chester, The propagation of shock waves in a channel of non-uniform width, The Quarterly Journal of Mechanics and Applied Mathematics 6 (4) (1953) 440–452.

[154] R. F. Chisnell, The motion of a shock wave in a channel, with applications to cylindrical and spherical shock waves, Journal of Fluid Mechanics 2 (3) (1957) 286–298.

[155] G. B. Whitham, On the propagation of shock waves through regions of non-uniform area or flow, Journal of Fluid Mechanics 4 (4) (1958) 337–360.

[156] D. Russel, Shock-wave strengthening by area convergence, Journal of Fluid Mechanics 27 (2) (1967) 305–314.

[157] G. Bird, The effect of wall shape on the degree of reinforcement of a shock wave moving into a converging channel, Journal of Fluid Mechanics 05 (1) (1959) 60–66.

[158] O. Laporte, On the Interaction of a Shock with Constriction, University of California, Los Alamos Scientific Lab. Report LA-1740.

[159] Y. M. Abul-Huda, M. Gamba, Design and Characterization of the Michigan Hypersonic Expansion Tube Facility (MHExT), in: 53rd AIAA Aerospace Sciences Meeting, no. January, Reston, Virginia, 2015.

[160] D. H. Edwards, B. D. R, H. G, A. T. Jones, The influence of wall heat transfer on the expansion following a C-J detonation wave, Journal of Physics D: Applied Physics 3 (3) (1970) 365–376.

[161] M. Sichel, T. David, Transfer behind detonations in H2-O2 mixtures, AIAA Journal 4 (6) (1966) 1089–1090.

[162] S. J. H, Friction and Heat-Transfer Effects on the Non-stedy Flow Behind a Detonation, AIAA Journal 5 (11) (1967) 2069–2071.

[163] J. P. Laviolette, C. B. Kiyanda, A. J. Higgins, The Effect of Friction and Heat Transfer on Impulse in Detonation Tube, in: Canadian Section of Combustion Institute, 2002.

[164] G. B. Kistiakowsky, W. G. Zinman, Gaseous Detonations. VII. A Study of Thermodynamic Equilibration in Acetylene-Oxygen Waves, The Journal of Chemical Physics 23 (10) (1955) 1889–1894.

[165] J. A. Fay, Two-Dimensional Gaseous Detonations: Velocity Deficit, Physics of Fluids 2 (1959) 283–289.

[166] M. I. Radulescu, R. K. Hanson, Effect of Heat Loss on Pulse-Detonation-Engine Flow Fields and Performance, Journal of Propulsion and Power 21 (2) (2005) 274–285.

[167] K. Kawane, S. Shimada, J. Kasahara, A. Matsuo, The influence of heat transfer and friction on the impulse of a detonation tube, Combustion and Flame 158 (10) (2011) 2023–2036.

[168] B. D. H. Edwards, G. T. Williams, J. C. Breeze, Pressure and velocity measurements on detonation waves in hydrogen-oxygen mixtures, Journal of Fluid Mechanics 6 (4) (1959) 497–517.

[169] J. Dove, B. Scroggie, H. Semerjian, Velocity deficits and detonability limits of hydrogen-oxygen detonations, Acta Astronautica 1 (3-4) (1974) 345–359.

[170] G. L. Agafonov, S. M. Frolov, Computation of the detonation limits in gaseous hydrogen-containing mixtures, Combustion, Explosion, and Shock Waves 30 (1) (1994) 91–100.

[171] J. V. Foa, Elements of flight propulsion, New York,, 1960.

[172] R. George, Wave Diagrams for Nonstedy Flow in Ducts, D. Van Nostrand Company, Inc, New York, NY, 1955.

[173] K. Ajmani, K. J. Breisacher, Qualitative Study of Cooling methods for Pulse Detonation Engine, 51st JANNAF Propulsion Meeting.

[174] X. He, A. R. Karagozian, Numerical simulation of pulse detonation engine phenomena, Journal of Scientific Computing 19 (1-3) (2003) 201–223.

[175] Y. Gao, B. Zhang, H. D. Ng, J. H. Lee, An experimental investigation of detonation limits in hydrogen-oxygen-argon mixtures, International Journal of Hydrogen Energy 41 (14) (2016) 6076–6083.

[176] Z. C. Owens, R. K. Hanson, The Influence of Wall Heat Transfer, Friction, and Condensation on Detonation Tube Performance, Combustion Science and Technology 182 (8) (2010) 1104–1140.

[177] E. A. Barbour, R. K. Hanson, Chemical nonequilibrium, heat transfer, and friction in a detonation tube with nozzles, Journal of Propulsion and Power 26 (2) (2010) 230–239.

[178] R. M. Kelsot, T. T. Lims, A. E. Perry, An experimental study of round jets in cross-flow, Journal of Fluid Mechanics 306 (1996) 111–144.

[179] L. L. Yuan, R. L. Street, J. H. Ferziger, Large-eddy simulations of a round jet in crossflow, Journal of Fluid Mechanics 379 (1999) 71–104.

[180] P. Paul, A model for temperature-dependent collisional quenching of OHA2+, Journal of Quantitative Spectroscopy and Radiative Transfer 51 (3) (1994) 511–524.

[181] I. B. Pollack, Y. Lei, T. A. Stephenson, M. I. Lester, Electronic quenching of OH A2S+ radicals in collisions with molecular hydrogen, Chemical Physics Letters 421 (4-6) (2006) 324–328.

[182] D. E. Heard, D. A. Henderson, Quenching of OH (A2Σ+) by several collision partners between 200 and 344 K. Cross-section measurements and model comparisons, Physical Chemistry Chemical Physics 2 (1) (2000) 67–72.

[183] P. Boivin, Reduced-kinetic mechanisms for hydrogen and syngas combustion including autoignition, Ph.D. thesis, Universidad Carlos III de Madrid (2011).

[184] J. Hoke, R. Bradley, F. Schauer, Heat transfer and thermal management in a pulsed detonation engine, in: 41th AIAA Aerospace Sciences Meeting and Exhibit, AIAA Paper 2003-0852, 2003.

[185] C. Donaldson, R. Snedeker, A study of free jet impingement. Part 1. Mean properties of free and impinging jets, Journal of Fluid Mechanics 45 (2) (1971) 281–319.

[186] D. C. Pack, On the formation of shock-waves in supersonic gas jets, The Quarterly Journal of Mechanics and Applied Mathematics.

[187] W. J. Sheeran, D. S. Dosanjh, Observations on jet flows from a two- dimensional, underexpanded, sonic nozzle., AIAA Journal 6 (3) (1968) 540–542.

[188] A. Vick, E. Andrew, J. Dennard, C. Craidon, Comparisons of experimental free-jet boundaries with theoretical results obtained with the method of characteristics, NASA TN D2327.